

**NUMERICAL STUDY ON NATURAL CONVECTION IN
ENCLOSURES WITH DIFFERENT GEOMETRIES**

CHEONG HUEY TYNG

**FACULTY OF SCIENCE
UNIVERSITY OF MALAYA
KUALA LUMPUR**

2017

**NUMERICAL STUDY ON NATURAL CONVECTION IN
ENCLOSURES WITH DIFFERENT GEOMETRIES**

CHEONG HUEY TYNG

**THESIS SUBMITTED IN FULFILMENT OF THE
REQUIREMENTS FOR THE DEGREE OF
DOCTOR OF PHILOSOPHY**

**INSTITUTE OF MATHEMATICAL SCIENCES
FACULTY OF SCIENCE
UNIVERSITY OF MALAYA
KUALA LUMPUR**

2017

UNIVERSITY OF MALAYA
ORIGINAL LITERARY WORK DECLARATION

Name of Candidate: **Cheong Huey Tyng**

Matric No: **SHB140002**

Name of Degree: **Doctor of Philosophy (Mathematics and Science Philosophy)**

Title of Project Paper/Research Report/Dissertation/Thesis (“this Work”):

Numerical Study on Natural Convection in Enclosures with Different Geometries

Field of Study: **Numerical Method and Mathematical Modelling**
(Applied Mathematics)

I do solemnly and sincerely declare that:

- (1) I am the sole author/writer of this Work;
- (2) This Work is original;
- (3) Any use of any work in which copyright exists was done by way of fair dealing and for permitted purposes and any excerpt or extract from, or reference to or reproduction of any copyright work has been disclosed expressly and sufficiently and the title of the Work and its authorship have been acknowledged in this Work;
- (4) I do not have any actual knowledge nor do I ought reasonably to know that the making of this work constitutes and infringement of any copyright work;
- (5) I hereby assign all and every rights in the copyright to this Work to the University of Malaya (“UM”), who henceforth shall be owner of the copyright in this Work and that any reproduction or use in any form or by any means whatsoever is prohibited without the written consent of UM having been first had and obtained;
- (6) I am fully aware that if in the course of making this Work I have infringed any copyright whether intentionally or otherwise, I may be subject to legal action or any other action as may be determined by UM.

Candidate’s Signature

Date:

Subscribed and solemnly declared before,

Witness’s Signature

Date:

Name:

Designation:

ABSTRACT

Natural convection is a heat transfer process which occurs due to temperature differences between a surface and surrounding fluids. Together with fluid flow, natural convective heat transfer has been an important interest for energy-related applications and production industries. The present study deals with natural convection in enclosures with different geometries, which are rectangular, triangular, trapezoidal, oblique and wavy enclosures. Different thermal boundary conditions are taken into account as well. The enclosure is two-dimensional and hence the governing equations are derived using two-dimensional Cartesian coordinate system. The enclosure is filled with fluid-saturated porous medium. Darcy model is used to describe the fluid flow through the porous medium. Different temperature profiles are applied on the sidewall of the enclosure, and appropriate boundary conditions are formulated for all sidewalls. The governing equations and boundary conditions are dimensional, and hence dimensionless method is employed to reduce the equations to dimensionless form. Grid generation method is used to map the non-rectangular domain to a rectangular computational domain. Finite difference approximations are then used to discretize the dimensionless governing equations and boundary conditions. A numerical algorithm is developed to implement the numerical methods proposed. The discretized governing equations and boundary conditions are solved iteratively until the convergence is reached. The solutions are obtained graphically to show the fluid flow and temperature distribution inside the enclosure at steady state. Also, heat transfer rate is calculated to determine the significance of the model. It is observed that the geometry and thermal boundary conditions affect the fluid flow and temperature distribution, as well as the heat transfer rate inside the enclosure. The heat transfer rate increases with Darcy-Rayleigh number. Also, the raise of internal heat generation reduces the heat transfer rate inside the porous enclosure at high Darcy-Rayleigh number. The wavy porous enclosure has the highest heat transfer rate among all enclosure shapes considered. Constant heating also gives higher heat transfer rate compared to other temperature profiles (sinusoidal and linear heating).

ABSTRAK

Olakan tabii merupakan suatu proses pemindahan haba yang wujud akibat perbezaan suhu pada suatu permukaan dengan bendalir di sekelilingnya. Bersama dengan aliran bendalir, pemindahan haba olakan tabii telah menjadi begitu penting bagi tenaga berkaitan aplikasi serta industri pengeluaran. Kajian semasa ini tertumpu kepada olakan tabii dalam kurungan dengan pelbagai geometri, seperti kurungan segi empat, segi tiga, trapezium, serong dan berombak. Syarat sempadan suhu berlainan juga akan dikaji. Kurungan tersebut adalah berdimensi dua, jadi persamaan menakluk diterbitkan dengan menggunakan sistem koordinat Cartesan dua dimensi. Kurungan adalah diisi dengan medium berliang yang ditepu dengan bendalir. Model Darcy diguna pakai untuk menghuraikan aliran bendalir melalui medium berliang. Profil suhu yang berlainan akan diguna pakai di dinding sisi kurungan tersebut, dan syarat sempadan dirumus untuk dinding sisi. Persamaan menakluk dan syarat sempadan adalah bermatra, oleh itu kaedah tak bermatra diguna pakai untuk menurunkan persamaan tersebut ke bentuk tidak bermatra. Penghampiran beza terhingga diguna pakai bagi menjelmakan persamaan menakluk dan syarat sempadan. Kaedah penjanaan grid diguna pakai untuk memetakan domain bukan segi empat ke domain pengiraan bersegi empat. Algoritma berangka bersesuaian dibangunkan untuk melaksanakan kaedah penyelesaian yang dicadangkan. Persamaan menakluk dan syarat sempadan yang terjelma diselesaikan secara lelaran sehingga keputusan tertumpu dicapai. Keputusan berangka dipaparkan secara grafik untuk menunjukkan aliran bendalir dan taburan suhu dalam kurungan dalam keadaan mantap. Selain itu, kadar pemindahan haba dikira bagi memastikan keberkesanan model. Hasil kajian mendapati bahawa geometri dan syarat sempadan suhu mempengaruhi aliran bendalir dan taburan suhu, serta kadar pemindahan haba kurungan tersebut. Kadar pemindahan suhu meningkat dengan nombor Darcy-Rayleigh. Selain itu, peningkatan penjana haba dalaman mengurangkan kadar pemindahan haba pada nombor Darcy-Rayleigh yang tinggi. Kurungan berliang berombak didapati mempunyai peningkatan kadar pemindahan haba paling tinggi antara kurungan bentuk lain. Pemanasan malar juga didapati memberi kadar pemindahan haba yang lebih tinggi berbanding dengan profil suhu yang lain (pemanasan sinus dan linear).

ACKNOWLEDGEMENTS

First and foremost, I would like to express my greatest gratitude and respect to my supervisor, Dr. Sivanandam Sivasankaran, for his excellent guidance, valuable comments and endless support throughout my research study. I also would like to thank my supervisor, Dr. Zailan Siri, for his advices and grant management. I am very thankful to them for giving me various ideas and suggestions to improve my knowledge about my research topic.

I also would like to thank my family for their endless support for allowing me to further my study. Without their understanding, encouragement and sacrifices, it would have been impossible for me to complete this work. Special thanks to my grandparents and my uncle for their endless motivation and encouragement throughout the years.

I gratefully acknowledge Institute of Mathematical Sciences and University of Malaya for accepting me to pursue my higher degree and providing me excellent facilities and work environment. I also would like to thank Faculty of Science for the financial support for attending conferences. Moreover, I would like to appreciate the financial support from the Postgraduate Research Grant (PG083-2014B) for aiding me to carry out my research smoothly. Greatest appreciation is expressed to the Ministry of Higher Education of Malaysia for the scholarship and allowance through the MyPhD Programme.

Last but not least, I would like to thank my friends and roommates for their concern and support throughout my years of study. Their proactive spirit has motivated me to complete my work in pace and on time.

TABLE OF CONTENTS

Abstract.....	iii
Abstrak	iv
Acknowledgements	v
Table of Contents	vi
List of Figures.....	x
List of Tables.....	xiv
List of Symbols and Abbreviations	xv
CHAPTER 1: INTRODUCTION.....	1
1.1 Fluid Dynamics.....	2
1.2 Convective Heat Transfer	3
1.3 Porous Medium.....	4
1.4 Problem Statement	5
1.5 Scope and Limitations.....	6
1.6 Research Objectives	6
1.7 Thesis Organization.....	7
CHAPTER 2: LITERATURE REVIEW.....	8
2.1 Natural Convection Through Porous Medium.....	8
2.2 Enclosures with Different Geometries	10
2.3 Various Thermal Boundary Conditions.....	14
2.4 Convection in Inclined Enclosures.....	19
2.5 Research Questions	21

CHAPTER 3: MATHEMATICAL FORMULATION AND METHODS OF SOLUTION	23
3.1 Mathematical Formulation.....	23
3.1.1 Continuity equation	23
3.1.2 Momentum equations	25
3.1.3 Energy equation.....	28
3.1.4 Stream Function	33
3.1.5 Boundary Conditions.....	34
3.1.6 Rate of Heat Transfer.....	36
3.2 Method of Solution	37
3.2.1 Dimensionless Equations	37
3.2.2 Grid Generation.....	40
3.2.3 Transformation of Governing Equations and Boundary Conditions	44
3.2.4 Discretization Method: Finite Difference Approximations	46
3.2.5 Iterative Method	48
3.2.6 Discretization of Governing Equations and Boundary Conditions	50
3.2.7 Numerical Procedure	53
3.2.8 Grid Independence Test and Code Validation	54
 CHAPTER 4: NATURAL CONVECTION IN A TRIANGULAR POROUS ENCLOSURE.....	 57
4.1 Introduction	57
4.2 Problem Statement	57
4.3 Solution Approach	59
4.4 Results and Discussion.....	60
4.5 Conclusion.....	67

CHAPTER 5: NATURAL CONVECTION IN SQUARE, TRAPEZOIDAL AND TRIANGULAR POROUS ENCLOSURES	68
5.1 Introduction	68
5.2 Problem Statement	68
5.3 Solution Approach	70
5.4 Results and Discussion	70
5.5 Conclusion	76
CHAPTER 6: NATURAL CONVECTION IN AN OBLIQUE POROUS ENCLOSURE WITH SINUSOIDAL HEATING.....	77
6.1 Introduction	77
6.2 Problem Statement	77
6.3 Solution Approach	79
6.4 Results and Discussion	79
6.5 Conclusion	85
CHAPTER 7: NATURAL CONVECTION IN AN OBLIQUE POROUS ENCLOSURE WITH LOCALIZED HEATING	86
7.1 Introduction	86
7.2 Problem Statement	86
7.3 Solution Approach	88
7.4 Results and Discussion	90
7.4.1 Effect of Different Heating Locations	90
7.4.2 Effect of Different Heating Lengths	97
7.5 Conclusion	103

CHAPTER 8: NATURAL CONVECTION IN A WAVY POROUS ENCLOSURE WITH SINUSOIDAL HEATING.....	104
8.1 Introduction	104
8.2 Problem Statement	104
8.3 Solution Approach	106
8.4 Results and Discussion.....	107
8.4.1 Effects of Wall Waviness	108
8.4.2 Effects of Internal Heat Generation/Absorption.....	115
8.4.3 Effects of Inclination	120
8.5 Conclusion	133
CHAPTER 9: NATURAL CONVECTION IN A WAVY POROUS ENCLOSURE WITH LOCALIZED HEATING	134
9.1 Introduction	134
9.2 Problem Statement	134
9.3 Solution Approach	136
9.4 Results and Discussion.....	138
9.4.1 Effects of Heater Location	138
9.4.2 Effects of Enclosure Inclination	146
9.5 Conclusion	154
CHAPTER 10:SUMMARY AND CONCLUSION	155
10.1 Summary.....	155
10.2 Conclusion.....	156
10.3 Future Work	157
References	167
List of Publications and Papers Presented	168

LIST OF FIGURES

Figure 1.1: Streamlines visualization of laminar and turbulent flow through a channel	2
Figure 1.2: Examples of (a) natural convection and (b) forced convection.....	3
Figure 1.3: Fluid flow through a porous medium	4
Figure 3.1: Fluid flow for a two-dimensional control volume.....	24
Figure 3.2: Buoyancy force components.....	26
Figure 3.3: Schematic diagram of a square porous enclosure	34
Figure 3.4: A demonstration of (a) a physical domain with uneven step sizes and (b) an associated computational domain with constant step sizes	40
Figure 3.5: Illustration of grid points used in backward, forward and central difference approximations for first order derivative.....	47
Figure 3.6: Grid points employed in Gauss-Seidel iteration method.....	48
Figure 3.7: Flow chart for the numerical procedure	53
Figure 3.8: Grid independency test at $Ra_D = 10^3$ with (a) $ \Psi _{\max}$ and (b) \overline{Nu}	55
Figure 3.9: Streamlines (left) and isotherms (right) for natural convection in square porous enclosures heated with constant temperature on the left sidewall ..	56
Figure 4.1: Schematic diagram of a triangular porous enclosure	57
Figure 4.2: Streamlines and isotherms for various inclination angles with different temperature profiles at $Ra_D = 10^2$	60
Figure 4.3: Streamlines and isotherms for various inclination angles with different temperature profiles at $Ra_D = 10^3$	61
Figure 4.4: Local Nusselt number for different temperature profiles at (a) $Ra_D =$ 10, (b) $Ra_D = 10^2$ and (c) $Ra_D = 10^3$	63
Figure 4.5: Average Nusselt number for different inclination angles and Darcy-Rayleigh numbers.....	63
Figure 5.1: Schematic diagram of a trapezoidal porous enclosure	68
Figure 5.2: Streamlines for various enclosure shapes and thermal boundary conditions at $Ra_D = 10^3$	71
Figure 5.3: Isotherms for various enclosure shapes and thermal boundary conditions at $Ra_D = 10^3$	72

Figure 5.4: Local Nusselt number for various enclosure shapes and thermal boundary conditions at $Ra_D = 10^3$	73
Figure 5.5: Average Nusselt number for various enclosure shapes and thermal boundary conditions	75
Figure 6.1: Schematic diagram of an oblique porous enclosure.....	77
Figure 6.2: Isotherms for various walls inclination at $Ra_D = 10^3$	81
Figure 6.3: Streamlines for various walls inclination at $Ra_D = 10^3$	81
Figure 6.4: Local Nusselt number for various internal heat generation parameters at $Ra_D = 10^3$	83
Figure 6.5: Average Nusselt number at various Darcy-Rayleigh numbers	84
Figure 7.1: Schematic diagram of an oblique porous enclosure with localized heating	86
Figure 7.2: Streamlines for enclosure of different wall inclinations and heater positions with $L_h = L/2$ at $Ra_D = 10^3$	91
Figure 7.3: Isotherms for enclosure of different wall inclinations and heater positions with $L_h = L/2$ at $Ra_D = 10^3$	92
Figure 7.4: Local Nusselt number for different wall inclinations and heater positions with $L_h = L/2$ at $Ra_D = 10^3$	95
Figure 7.5: Average Nusselt number for different wall inclinations and heater locations with $L/2$ heater length at various Darcy-Rayleigh numbers.....	96
Figure 7.6: Streamlines of middle heating enclosure with different wall inclinations and heater lengths at $Ra_D = 10^3$	98
Figure 7.7: Isotherms of middle heating enclosure with different wall inclinations and heater lengths at $Ra_D = 10^3$	99
Figure 7.8: Local Nusselt number for middle heating enclosure with different wall inclinations and heater lengths at $Ra_D = 10^3$	101
Figure 7.9: Average Nusselt number of the heater for middle heating enclosure with different wall inclinations and heater lengths at various Darcy-Rayleigh numbers	102
Figure 8.1: Schematic diagram of a wavy porous enclosure	104

Figure 8.2: Isotherms for various amplitudes and undulations with $\varphi = 0^\circ$ and $Q = 0$ at $Ra_D = 10^3$	109
Figure 8.3: Streamlines for various amplitudes and undulations with $\varphi = 0^\circ$ and $Q = 0$ at $Ra_D = 10^3$	110
Figure 8.4: Mid-height velocity for different amplitudes and undulations with $\varphi = 0^\circ$ and $Q = 0$ at various Darcy-Rayleigh numbers.....	111
Figure 8.5: Local Nusselt number for different amplitudes and undulations with $\varphi = 0^\circ$ and $Q = 0$ at $Ra_D = 10$	112
Figure 8.6: Local Nusselt number for different amplitudes and undulations with $\varphi = 0^\circ$ and $Q = 0$ at $Ra_D = 10^3$	112
Figure 8.7: Average Nusselt number for various Darcy-Rayleigh numbers with different amplitudes and number of undulations when $\varphi = 0^\circ$	114
Figure 8.8: Isotherms for various internal heat generation/absorption parameters with different combinations of amplitudes and undulations at $\varphi = 0^\circ$ and $Ra_D = 10^3$	115
Figure 8.9: Streamlines for various internal heat generation/absorption parameters with different combinations of amplitudes and undulations at $\varphi = 0^\circ$ and $Ra_D = 10^3$	116
Figure 8.10:Local Nusselt number for various internal heat generation/absorption parameters with different combinations of amplitudes and undulations at $\varphi = 0^\circ$ and $Ra_D = 10^3$	118
Figure 8.11:Variation of average Nusselt number with internal heat generation/absorption parameters with different combinations of amplitudes and undulations at various Darcy-Rayleigh numbers when $\varphi = 0^\circ$	119
Figure 8.12:Streamlines for various enclosure inclination with different combinations of amplitude and undulation at $Q = 0$ and $Ra_D = 10^3$	121
Figure 8.13:Isotherms for various enclosure inclination with different combinations of amplitude and undulation at $Q = 0$ and $Ra_D = 10^3$	122

Figure 8.14:Local Nusselt numbers for various enclosure inclination with different combinations of amplitude and undulation at different Darcy-Rayleigh numbers when $Q = 0$	124
Figure 8.15:Local Nusselt number for various amplitudes with different number of undulations and enclosure inclination at $Q = 0$ and $Ra_D = 10^3$	125
Figure 8.16:Local Nusselt number for various number of undulations with different amplitudes and enclosure inclination at $Q = 0$ and $Ra_D = 10^3$	126
Figure 8.17:Variation of average Nusselt numbers with enclosure inclination for various amplitudes at different Darcy-Rayleigh numbers when $Q = 0$	127
Figure 8.18:Variation of average Nusselt numbers with enclosure inclination for various undulations at different Darcy-Rayleigh numbers when $Q = 0$	128
Figure 9.1: Schematic diagram of a wavy porous enclosure with localized heating	134
Figure 9.2: Isotherms for various heating locations, amplitude and undulation of the wavy right wall with $\varphi = 0^\circ$ at $Ra_D = 10^3$	139
Figure 9.3: Streamlines for various heating locations, amplitude and undulation of the wavy right wall with $\varphi = 0^\circ$ at $Ra_D = 10^3$	140
Figure 9.4: Local Nusselt numbers for different heating locations and waviness of right wall when $\varphi = 0^\circ$ at $Ra_D = 10^3$	143
Figure 9.5: Variation of average Nusselt number with different undulations, amplitudes, Darcy-Rayleigh numbers and heating locations when $\varphi = 0^\circ$	144
Figure 9.6: Isotherms for various heating locations and enclosure inclinations with $a = 0.15$, $\lambda = 3$ at $Ra_D = 10^3$	147
Figure 9.7: Streamlines for various heating locations and enclosure inclinations with $a = 0.15$, $\lambda = 3$ at $Ra_D = 10^3$	148
Figure 9.8: Local Nusselt number for different heating locations and waviness of right wall at $Ra_D = 10^3$	151
Figure 9.9: Variation of average Nusselt number with enclosure inclination at different heating locations when $a = 0.15$ at various Darcy-Rayleigh numbers	152

LIST OF TABLES

Table 3.1: Comparison of \overline{Nu} results for natural convection in a square porous enclosure.....	54
Table 4.1: Grid independence test at $Ra_D = 10^3$ with \overline{Nu} for triangular porous enclosures with different temperature profiles.....	59
Table 4.2: Comparison of \overline{Nu} between sinusoidal heating and linear heating for various values of Ra_D and φ	65
Table 7.1: Grid independence test for square and oblique enclosures at $Ra_D = 10^3$..	89
Table 8.1: Grid independency test for wavy and square enclosures with sinusoidal heating	107
Table 9.1: Grid independency test for wavy and square enclosures at $Ra_D = 10^3$ with different heating lengths	138

LIST OF SYMBOLS AND ABBREVIATIONS

A	: area
a	: dimensionless amplitude
\vec{a}	: acceleration in any direction
c_p	: specific heat capacity at constant pressure
D	: dimensionless length of the hot wall
d	: length of the hot wall
E	: extra term
\vec{F}	: net force in any direction
f	: a continuous and analytical function
g	: gravitational acceleration
I	: enthalpy
J	: Jacobian of transformation
K	: permeability of the porous medium
k	: thermal conductivity
L	: width and height of the enclosure
L_h	: length of the heater
m	: mass
N, S	: dimensionless normal and tangent plane of a surface
n, s	: normal and tangent plane of a surface
Nu	: Nusselt number
\overline{Nu}	: average Nusselt number
P	: pressure
\vec{p}	: momentum in any direction
P_h	: position of the heater
Q	: internal heat generation/absorption parameter
q'''	: volumetric heat generation/absorption
q	: heat transfer rate
\bar{q}	: average heat transfer rate
R	: ratio of element width to element height

r	: relaxation parameter
Ra_D	: Darcy-Rayleigh number
S	: source term
T	: temperature
t	: time
u, v	: velocity components in the x - and y -directions, respectively
ΔV	: element volume
\vec{v}	: velocity in any direction
X, Y	: dimensionless Cartesian coordinates
x, y	: Cartesian coordinates
$\Delta x, \Delta y, \Delta z$: element width, height and depth, or step sizes in the respective directions

Greek Symbols

α	: thermal diffusivity
β	: coefficient of thermal expansion
λ	: number of undulations
μ	: dynamic viscosity
ν	: kinematic viscosity
ϕ	: inclination of left wall from the vertical plane
ϕ	: porosity of the porous medium
Ψ	: dimensionless stream function
ψ	: stream function
ρ	: density
Θ	: dimensionless temperature
φ	: inclination angle of x -axis from the horizontal plane
ξ, η	: computational space coordinates
$n\xi, n\eta$: number of grids in the ξ - and η -directions, respectively
$\Delta\xi, \Delta\eta$: element width and height in the ξ - and η -directions respectively

Subscripts/Superscripts

c	:	cold
h	:	hot/heater
i, j	:	indices for a nodal point in the horizontal and vertical directions, respectively
(k)	:	iteration number
max	:	maximum
ref	:	reference

Abbreviations

CFD	:	computational fluid dynamics
CSCM	:	Chebyshev spectral collocation method
FDM	:	finite difference method
FVM	:	finite volume method
SOR	:	Successive-Over-Relaxation
SUR	:	Successive-Under-Relaxation

CHAPTER 1: INTRODUCTION

Fluids (both liquids and gases) are abundant, and yet the essential matters that support life on the earth. The streaming of rivers, air flow inside a room and blood flow in the human cardiovascular system are the examples that involve fluid flow in nature. The flow of a fluid, in view of microscopic scale, is the movement of fluid particles due to concentration gradient, pressure gradient or enthalpy difference. The diffusion process, is the movement with mixing of fluid particles arises from different quantities or precisely, concentrations between two locations. Unlike diffusion process, advection process is the bulk movement of fluid, and energy can be advected in this process. Heat is a form of energy that can be transferred through mediums, and the subject deals with the rate of heat flow is called heat transfer. Fluid flow couples with heat transfer process have been the important happenings in our daily life. To name a few, boiling of water, air ventilation and petrol combustion do involve fluid flow with heat transfer. These phenomena are common, yet if the energy waste can be minimized by proper thermal management, the risk of global warming can be slightly reduced.

Over the past decades, scientists and engineers have been working on finding the optimal solutions for heat transfer related situations and applications. Numerous approaches have been developed, and mathematical modelling is one of the ways to obtain predictions or approximate solutions. That is, mathematical equations are developed to describe the fluid flow and heat transfer processes under different occasions and circumstances. Various numerical methods are also developed to approximate the solutions of mathematical equations that are difficult to solve. With the advancement of technology, computers with greater computation capacity and memory allow virtual simulations to be performed using self-programmed codes or softwares available. Hence, engineers and scientists can save timely observations and costly experiments by implementing proper modelling and numerical methods on the problems. In fluid dynamics, the modelling of fluid flow with numerical analysis is called computational fluid dynamics (CFD). It has been mainly used for the design of aircraft, submarines and automobiles.

1.1 Fluid Dynamics

Mechanics is a subject that deals with forces and motion of physical bodies, and dynamics is a branch of classical mechanics that concerns the causes of forces and their effect on motion. Fluid mechanics is a branch of applied mechanics that concerned with the statics and dynamics of fluids, both liquids and gases (Brewster, 2009). The subject that deals with fluids in motion (or fluid flow) is called fluid dynamics. It is a branch of fluid mechanics that concerns the causes and effect of fluids in motion. It has several sub-disciplines, to name a few, aerodynamics that studies air or gases in motion, and hydrodynamics which focus on the study of liquid flow.

Fluid flow can be classified based on the fluid properties, such as compressibility and viscosity of the fluid. The flow is compressible if the fluid density varies with pressure and temperature, otherwise it is incompressible. The flow is viscous when the effect of fluid friction is significant on the fluid motion, and the flow is inviscid when the fluid possess zero viscosity. Fluid flow also can be classified according to the nature of flow, which are steady and unsteady flow. Depending on the reference frame, the flow is considered to be steady when the properties of the fluid at a point do not vary with time, otherwise the flow is unsteady. Also, laminar flow happens when the fluid flows in parallel layers without mixing between layers, whereas turbulent flow occurs with the formation of swirls and eddies as depicted in Figure 1.1. Fluid flow also can be classified as subsonic, transonic, supersonic and hypersonic, relies on the fluid velocity (precisely, the Mach number).

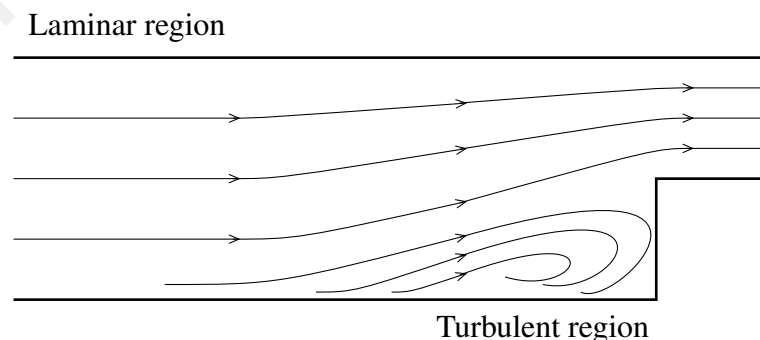


Figure 1.1: Streamlines visualization of laminar and turbulent flow through a channel

1.2 Convective Heat Transfer

Heat transfer (or heat) is thermal energy in transit due to a spatial temperature difference (Incropera et al., 2007). Heat can be transferred by three modes, namely, conduction, convection and radiation. In the presence of temperature gradient in a medium, conduction is a mode of heat transfer in solid and stationary fluid, whereas radiation is the emission of energy from a surface in the form of electromagnetic wave. Convection heat transfer occurs when there exists temperature difference between a surface and a moving fluid. It involves the random motion of fluid particles (diffusion) and bulk motion of fluid (advection). Convection heat transfer can be further classified as natural and forced convection, and examples are illustrated in Figure 1.2. Natural (or free) convection flow is driven by buoyancy force, which is caused by the density difference due to temperature difference in the fluid. Forced convection flow is driven by external forces, such as a fan, pump or atmospheric winds. Mixed convection occurs when the effect of buoyancy and external forces are equally important to drive the heat transfer.

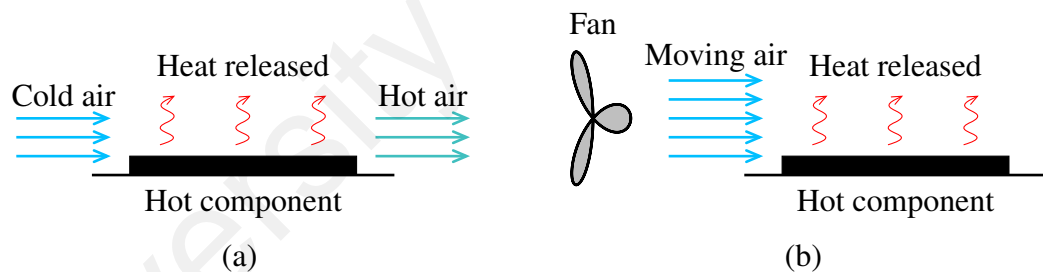


Figure 1.2: Examples of (a) natural convection and (b) forced convection

There are many practical uses of natural convection in our daily life. Boiling and condensation are the convection processes associated with phase change of a fluid. Geothermal reservoirs are usually built on volcanic rocks for electricity generation. Heat steam is produced when water is boiled by the volcanic rocks. It is used to turn the turbines in the reservoir. Geothermal water also can be used for residential heating, green house and agriculture. The solar energy collector absorbs the incoming solar radiation, converts it into heat energy and, transfers to fluid flowing through the panel. Heat energy carried by the circulating fluid is then transferred to a thermal energy storage tank. Solar energy collectors are common for water heating, space heating system and solar refrigeration.

1.3 Porous Medium

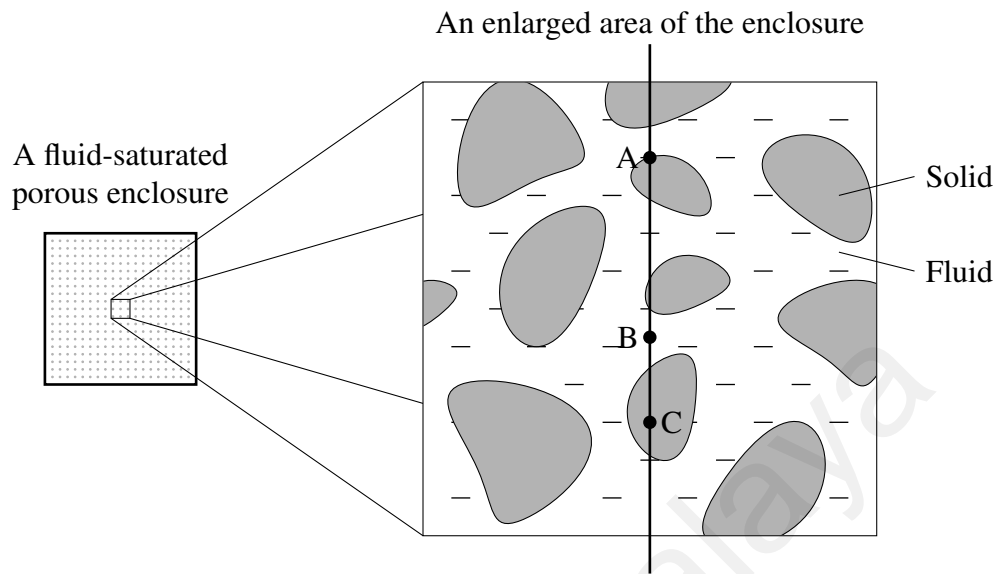


Figure 1.3: Fluid flow through a porous medium

A porous medium is a material consisting of a solid matrix with an interconnected void (Nield & Bejan, 2013). Usually, the solid matrix is rigid, or it can undergoes small deformation. Fluid can flow freely through the interconnected void (or the pores), as illustrated in Figure 1.3. In a naturally existed porous medium, the pores are usually of irregular shape and size. Soil, sand, limestone, bread, wood, sponge, the human lungs and bones are the examples of natural porous media. Ceramic and metallic foams are the man-made porous media. Artificial porous media can have evenly distributed pores with fixed shape and size.

The porosity (ϕ) is the ratio of the volume of void space to the total volume of the medium. Hence, $1 - \phi$ is the fraction occupied by the solid of the porous medium. The permeability of the porous medium (K) is determined by the nature of the pores, which are the shape and size, and also their arrangement. The values of K are varied widely for natural porous media, for example, $10^{-12}\text{m}^2 \sim 10^{-9}\text{m}^2$ for clean sand and $10^{-13}\text{m}^2 \sim 10^{-11}\text{m}^2$ for soil. However, geophysicists often use *Darcy* as a unit of permeability, which is $0.987 \times 10^{-12}\text{m}^2$ (Nield & Bejan, 2013). The porous medium is isotropic if the permeability of the porous medium is equal in each direction, that is, the pores are of the same shape and size and they are evenly distributed. The porous medium is anisotropic when the pores are of irregular arrangement, variable shapes and sizes.

Darcy's law was derived to describe the fluid flow through porous media. It was originated from Henry Darcy's work in 1856 on the hydrology of water supply (Nield & Bejan, 2013). His experiments revealed the proportionality between the flow rate and pressure difference. Darcy's law holds when the fluid velocity is low, i.e. Reynold number of the flow is small. As the fluid velocity increases, the drag force due to solid particles is now comparable with the surface force due to fluid friction. Hence, Forchheimer term (the inertial term) is added to the Darcy's equation to take care the drag force in high velocity fluid flow. Another variant is the Brinkman's equation where the viscous forces are considered for the case of high permeability. The Darcy model can be coupled with the Forchheimer's and Brinkman's extensions for the consideration of more complex flow through a porous medium.

There are numerous applications of fluid flow through porous media in the engineering and production industries. Porous medium can be used as a catalyst for chemical reaction in fluids, such as the catalytic converter is invented to reduce toxic gases released from petrol combustion. Packed beds are designed for drying of liquids and gases. The water flow in the geothermal reservoirs is also an example of fluid flow through porous media. The injection and withdrawal of water from the plant, oil and gas extraction, gas reservoir storage and landmine detection do involve fluid flow through porous media.

1.4 Problem Statement

Convective flow and heat transfer in porous enclosures have been of great importance to provide better understanding and improvement on the drying technology, geothermal reservoirs, artificial bones and many more. Rectangular enclosures have been common, but to serve different purposes and for the seek of space saving, non-rectangular enclosures might be more practical. Hence, the present study addresses natural convection in porous enclosures of different geometries. Shading and the presence of obstacle also will affect the temperature distribution on a surface. Therefore, different thermal boundary conditions on the enclosure are also considered. The orientation of the enclosure and the presence of internal heat generation and absorption will be investigated as well.

1.5 Scope and Limitations

This study focuses on natural convective flow and heat transfer in different enclosures. The enclosure is filled with a fluid-saturated porous medium. The porous medium is homogeneous and in thermal equilibrium with the surrounding fluid. The Darcy model is used to describe the fluid flow through the porous medium inside the enclosure. By the adoption of the Darcy's model, the porous medium is taken as sand, and water will be the fluid. The fluid has constant properties and Newtonian, and the flow will be viscous, laminar and incompressible. The porous medium is also isotropic and it is saturated by a fluid only, so there will be a single-phase flow.

The problem is considered on two-dimensional Cartesian coordinate system. The u - and v -velocities are in the direction of x - and y -axes, respectively. The gravity acts in vertical downwards direction and the Boussinesq approximation is valid for the density variation. Steady flow is considered and the dissipations due to viscous forces and Darcy flow are negligible for the enclosure problem.

1.6 Research Objectives

This research study intends to:

1. Construct a mathematical model of natural convection in porous enclosures with:
 - (a) various enclosure shapes and orientations,
 - (b) different thermal boundary conditions, and
 - (c) other effects such as the presence of heat generation/absorption.
2. Derive mathematical formulation to describe the fluid flow and heat transfer in porous enclosures as stated in objective 1.
3. Derive the initial and boundary conditions for the problems in objective 1.
4. Develop a numerical algorithm to solve the convective flow and heat transfer in porous enclosures. An iterative method with finite difference technique is considered to find the numerical solution. Then, the algorithm will be formed by stating the initial conditions for each solution by implementing the formulae obtained from objectives 2 and 3.

5. Find numerical prediction of heat transfer and fluid flow in porous enclosures.
The numerical algorithm achieved in objective 4 will be used to develop a functional numerical simulation. Later, numerical simulations will be performed for different values of parameters involved in the study.
6. Analyze the results obtained from the numerical simulations in objective 5.
The results will be presented in the form of streamlines, isotherms and Nusselt numbers which will respectively demonstrate the flow patterns, temperature distributions and heat transfer rate inside the porous enclosures.

1.7 Thesis Organization

This thesis consists of ten chapters, followed by a list of references and publications. Chapter 1 is an introductory chapter which gives the general introduction on fluid dynamics, convective heat transfer and porous medium. Then, the research problem is stated, along with the scope and limitations, and objectives of the study. In Chapter 2, a comprehensive literature review is presented.

Chapter 3 provides the details on mathematical formulation of the equations and boundary conditions that are governing the fluid flow and heat transfer in the porous enclosure. Then, the numerical methods and algorithms are described.

In the next six chapters, i.e. Chapters 4 to 9, the numerical solutions of convective flow and heat transfer in porous enclosures of different geometries with different conditions, such as, various thermal boundary conditions, inclination of the enclosure and the presence of internal heat generation/absorption, are given. Chapter 4 focuses on isosceles triangular enclosure with inclination and different temperature profiles. The comparison on square, trapezoidal and right-angled triangular enclosures with different temperature profiles is presented in Chapter 5. Chapters 6 and 7 discuss the fluid flow and heat transfer in the oblique enclosure with sinusoidal and localized heating, respectively. The wavy enclosure with sinusoidal heating and localized heating is demonstrated in Chapters 8 and 9.

Chapter 10 provides the summary of the overall results obtained. Contributions of the thesis and future research topics are briefly discussed as well.

CHAPTER 2: LITERATURE REVIEW

Over the past four decades, natural convection in enclosures has been an enthralling subject interested by most industries and researchers. In this chapter, a brief study on the literatures related to the research questions is reported. It is presented based on the different aspects of the research questions, in the respective sections of this chapter.

2.1 Natural Convection Through Porous Medium

Henry Darcy formulated Darcy's law in 1856 from his column experiments on the flow of water through sand (Chery & de Marsily, 2007). Darcy's law is a constitutive equation that proposed the proportional relation between the rate of fluid flow and pressure difference. His findings have served as a beginning for numerous experimental verification and theories developed in support of the Darcy's law. Most studies reported fluid flow through porous media by taking constitutive assumptions to obtain the closure and extensions of the equation. However, without making any constitutive assumptions, Whitaker (1986) used the volume averaging method to derive Darcy's law for flow of an incompressible fluid through homogenous and spatially periodic porous media with no abrupt changes in the structure of a porous medium. Until now, Darcy's law still serves as the fundamental equation that describe the fluid flow through a porous medium.

Together with heat transfer, fluid flow through porous medium has been studied extensively over the past years. There are plenty of literatures and books available for the study on convection process through porous medium. Oosthuizen and Naylor (1999) discussed the convective heat transfer through porous medium for duct flow, boundary layer flow and also enclosure with inclination. They stated that the convection process occurs when the Darcy-Rayleigh number exceeds 39.5 in the case of enclosure heated from below. While Oosthuizen and Naylor (1999) considered the problem using steady state equations, Saeid and Pop (2004) analyzed natural convection process in a square porous enclosure by using transient approach. They observed that the average heat transfer undershoots during transient period. They also found that low Darcy-Rayleigh number requires longer time than high Darcy-Rayleigh number to achieve the steady state.

The modelling of convection process in a porous medium for different applications are also discussed in Vafai (2000, 2005, 2010) and Nield and Bejan (2013). In particular, Vafai (2010) reported various studies on the applications of a porous medium in the modelling of blood flow, transport through tissues, biofilms, and many more. Nield and Bejan (2013) reported the applications in geophysical aspects.

The porous medium is anisotropic when the permeability of the porous medium is not equal for all basis direction. Ni and Beckermann (1991) considered natural convective flow and heat transfer in a porous enclosure using Darcy flow model with anisotropic permeability and thermal conductivity. They found that the average Nusselt number increases with the permeability ratio, but it decreases with the thermal conductivity ratio. Zheng et al. (2001) considered convection process of water near its density maximum inside a square porous enclosure with anisotropic medium where the permeability of each direction is related by the anisotropic angle. Costa (2003) analyzed the fluid flow inside a square porous enclosure with anisotropic medium. It is observed that the variation of thermal conductivity and permeability of the porous medium affect the fluid flow and temperature distribution along the thermally active sidewalls.

Using Darcy flow model, local thermal non-equilibrium between fluid and solid phases has been investigated by several researchers. Baytas and Pop (2002), Kayhani et al. (2011) and Chen et al. (2016) studied it using a square porous enclosure. Baytas and Pop (2002) found that the local thermal non-equilibrium model affects the flow and local heat transfer inside the square enclosure. Kayhani et al. (2011) derived a correlation equation for the average Nusselt number with the Rayleigh number, conductivity ratio and inter-phase heat transfer coefficient. While Baytas and Pop (2002) and Kayhani et al. (2011) used finite volume method (FVM), Chen et al. (2016) solved the problem using Chebyshev spectral collocation method (CSCM) and they compared the results with exact solutions. Badruddin et al. (2007) considered the effect of radiation on the square porous enclosure and they found that for the cold wall, the average heat transfer rate of the fluid phase decreases with the inter-phase heat transfer coefficient but the heat transfer rate of the solid phase increases with the coefficient.

For comparison purposes, the present study uses Darcy flow model for the momentum equations. The porosity and permeability of the porous medium are taken to be constant and local thermal equilibrium is considered for the thermal conductivity of fluid and porous medium.

2.2 Enclosures with Different Geometries

Natural convection in square or rectangular enclosures has been extensively studied over the past decades. To meet the needs and demands for some industrial and engineering applications, enclosure with non-rectangular shape has been developed. For example, triangular enclosure is used for the modelling of the roof of buildings, green houses, and solar collecting systems. Right-angled triangular porous enclosure has been studied by several researchers using Darcy flow model, such as Varol et al. (2006, 2007) and Oztop et al. (2009). They have also considered different aspect ratio of the enclosure. They reported that multiple flow inside the porous enclosure occurs at high Darcy-Rayleigh number. The effect of different heating-cooling walls of the porous enclosure also examined by Varol et al. (2007).

Basak et al. (2010b, 2013a), Zeng et al. (2013) and Sheremet and Pop (2015b) investigated convection process inside the triangular porous enclosure using non-Darcy flow model. Isosceles triangular porous enclosure was considered by Basak et al. (2010b). Having high temperature on the inclined sidewalls and low temperature on the top wall, symmetrical flow and temperature distributions are observed. Zeng et al. (2013) also considered isosceles triangular porous enclosure. The hot wall is located at the bottom and the inclined sidewalls are cold. Right-angled triangular porous enclosure was investigated by Basak et al. (2013a) and Sheremet and Pop (2015b). Basak et al. (2013a) studied the curvature of the hypotenuse on the heat transfer of the system and found that the overall heat transfer rate is high when the hypotenuse is concave. Sheremet and Pop (2015b) added nanoparticles into the porous enclosure to study the overall heat performance.

Trapezoidal enclosure can be used for the modelling of solar collectors and geothermal reservoirs. Natural convection inside trapezoidal porous enclosures has been studied by several researchers using Darcy flow model, for example Singh et al. (2000), Rathish

Kumar and Kumar (2004), Varol et al. (2009b, 2010), Tiwari et al. (2012) and Varol (2012). Singh et al. (2000) constructed the trapezoidal porous enclosure by varying the inclination of the adiabatic top wall from the horizontal plane. They found that the average Nusselt number increases with the inclination of the top wall. Rathish Kumar and Kumar (2004) studied the trapezoidal porous enclosure by changing the inclination of both thermally active sidewalls from the top wall with Darcy and non-Darcy flow models. Right-angled trapezoidal porous enclosure with a hot and thick left wall was investigated by Varol et al. (2009b). The right wall is cold and inclined. Varol et al. (2010) considered differential heating and cooling on the horizontal walls of the trapezoidal porous enclosure. The inclined sidewalls are adiabatic. Different aspect ratio of the enclosure was also considered and they found that the maximum density effect of water reduces the convective strength and average Nusselt number.

Using the same configurations for the enclosure as in Singh et al. (2000), Tiwari et al. (2012) considered the effect of anisotropic porous medium inside the trapezoidal enclosure. Varol (2012) reported a study on the trapezoidal porous enclosure with a hot wall entrapped between the horizontal walls of the trapezoidal enclosure. They also considered the effect of aspect ratio and they found that the effect of Darcy-Rayleigh number is insignificant on the fluid flow inside the upper trapezoidal porous enclosure. Using non-Darcy flow model, Ramakrishna et al. (2014) studied thermal management on the trapezoidal porous enclosure with thermally active inclined sidewalls. They concluded that the trapezoidal enclosure with sidewall inclination of 60° or more from the horizontal plane may give optimal thermal effect for food processing applications.

Besides rectangular, triangular and trapezoidal enclosures, oblique enclosure is also useful for engineering applications such as the cooling of electronic devices. The study on natural convective fluid flow and heat transfer in an oblique porous enclosure was first reported by Baytas and Pop (1999). They found that the computations are getting difficult as the walls inclination increases. Also, they observed that a series of sub-vortices of flow and temperatures at the sharp corners of the enclosure grow in size as the walls inclination and Darcy-Rayleigh number increase. Baytas and Pop (1999) considered the oblique enclosure with inclined thermally active sidewalls, but Costa (2004) investigated the

parallelogrammic enclosure with bottom and top walls which are inclined and adiabatic. Effect of aspect ratio was also considered and it is observed that the adiabatic walls which are inclined upward have higher heat transfer rate than the enclosure with walls inclined downward in the same magnitude of inclination angle. Both Baytas and Pop (1999) and Costa (2004) studied the convection process inside the trapezoidal porous enclosure using Darcy flow model.

Using non-Darcy flow model, the turbulence of convective flow in an oblique porous enclosure was investigated by Braga and de Lemos (2008). They found that the enclosure slanted to the left has higher heat transfer compared to a right-slanted enclosure with the same magnitude of inclination angle. Anandalakshmi and Basak (2013a,c) performed numerical studies on the rhombic porous enclosures with differential heating and Rayleigh-Benard heating. They reported that Rayleigh-Benard heating gives higher heat transfer rate than differential heating when the rhombic enclosure is greatly skewed.

Within the same region, a wavy surface has a larger area compared to a flat surface, and hence the larger surface area for heat exchange. Therefore, enclosure with irregular or wavy wall(s) can be used for the improvement and study of the cardiovascular system, design of solar collector, geothermal plant, cooking appliances and many more. Natural convective flow and heat transfer in a wavy porous enclosure have been considered by several researchers, particularly, the Darcy flow model is summarized. Murthy et al. (1997) and Rathish Kumar et al. (1998) investigated the porous enclosure with a wavy bottom wall. Rayleigh-Benard heating is applied on the enclosure. They reported that the wavy wall reduces the heat transfer rate into the enclosure. Rathish Kumar et al. (1998) also studied the effect of aspect ratio of the wavy porous enclosure and they reported that the heat transfer rate also reduces on raising the aspect ratio. The porous enclosure with a wavy left wall was examined by Rathish Kumar (2000) and Rathish Kumar and Shalini (2005). Rathish Kumar (2000) applied heat flux on the wavy wall, whereas Rathish Kumar and Shalini (2005) considered thermal stratification on the wavy wall. Rathish Kumar (2000) found that more undulations will enhance the convection process in the wavy porous enclosure. Rathish Kumar and Shalini (2005) observed that the presence of secondary flow in the hull of wavy wall reduces the heat transfer along the heated wall.

Besides enclosure with a wavy wall, porous enclosure with two wavy walls was also reported in some articles. The porous enclosure with in-phase wave on the left and right walls was examined by Misirlioglu et al. (2005). Differential heating is applied on the wavy walls. For such case, it is observed that the average Nusselt number of the hot wall is the highest when the waviness and aspect ratio of the enclosure are moderate at high Darcy-Rayleigh number. Later, Misirlioglu et al. (2006) considered the wavy porous enclosure with convex shape, and inclination of the enclosure was taken into account as well. They found that the heat transfer rate is highly dependent on the wall waviness and Darcy-Rayleigh number.

Natural convection in a concave porous enclosure with wavy top and bottom walls was numerically investigated by Mansour et al. (2011a). Rayleigh-Benard heating is applied, with radiation and local thermal non-equilibrium are considered as well on the concave porous enclosure. They observed that the average Nusselt number for fluid decreases with increasing wall waviness, but for solid phase, the average Nusselt number increases. Sojoudi et al. (2014) performed transient observation on natural convection process in a differentially heated in-phase wavy porous enclosure. They concluded that the change in the amplitude affects the flow field in the main flow whereas the alteration of the number of undulations affects the flow pattern along the walls. Sheremet et al. (2016) examined the convection process inside the nanofluid-filled porous enclosure with Rayleigh-Benard heating applied on the wavy bottom and top walls. The remaining vertical sidewalls are maintained at the same temperature as the cold top wall. It is observed that the flow is double cell for such configurations on the wavy enclosure.

Wavy enclosure also has been reported for non-Darcy flow model. Rathish Kumar and Shalini (2003) investigated convective flow and heat transfer in the differentially heated porous enclosure with a wavy left wall. They found that rough wavy surface causes secondary circulation zones in the region adjacent to the wavy wall, which leads to a decrease in the heat transfer due to convection. The similar problem was studied by Khanafer et al. (2009), by considering different models of convective flow through porous medium. They reported that the amplitude and number of undulations affect the heat transfer inside the enclosure. Sultana and Hyder (2007) performed numerical study on

natural convection in a differentially heated convex porous enclosure. They found that the effect of walls waviness on the heat transfer is less significant as compared to Darcy and Rayleigh numbers.

2.3 Various Thermal Boundary Conditions

Most of the works discussed in the previous sections have considered heating and cooling with constant temperatures on the porous enclosure. However, in most of the real life situations, shading or presence of a heat conducting body on the thermal active wall would result in non-uniform temperature distribution along the wall. Hence, it is essential to study the effect of non-uniform heating on the temperature dependent devices as it may affect the overall performance of the devices. Various thermal boundary conditions can be formulated based on the nature of the heat source under different conditions. In this section, linear wall temperature, sinusoidal heating and partial heating are discussed.

Using Darcy flow model, Rathish Kumar et al. (2002) performed a numerical study on the square porous enclosure with linear wall temperature applied on the right wall while the opposite wall is cooled at a constant temperature. It is observed that the average Nusselt number of the cold wall decreases with thermal stratification (the slope of the linear function of the temperature profile) for aiding flows, and it increases for opposing flows. For non-Darcy flow model, natural convection in a square porous enclosure with linearly heated sidewall(s) was investigated by Sathiyamoorthy et al. (2007). The bottom wall is isothermally heated and the top wall is adiabatic. It is noticed that the presence of secondary circulation causes the oscillation of local Nusselt number along the walls.

Linear heating has been considered on the right-angled triangular porous enclosure by Anandalakshmi et al. (2011) and Basak et al. (2012). Linear wall temperature is applied on the vertical left wall or on the inclined right wall of the right-angled triangular porous enclosure. It can be noticed that linear heating on the vertical left wall has higher heat transfer rate than linear heating on the inclined right wall. Also, the tall right-angled triangular porous enclosure possesses the highest heat transfer rate for both wall heating cases.

Trapezoidal porous enclosure with linear heating on the inclined sidewall(s) was examined by Basak et al. (2009c) and Ramakrishna et al. (2013). Isothermal heating is applied on the bottom wall while the top wall is adiabatic. It is observed that the average Nusselt number of the bottom wall is higher with linear heating on an inclined sidewall than that of linear heating on both inclined sidewalls. Also, it can be noticed that the average Nusselt number of the square porous enclosure is the highest compared to other trapezoidal porous enclosures.

Sinusoidal heating is used to model a heat source with non-uniform temperatures using sine or cosine function. Sinusoidal heating on the porous enclosure with Darcy flow model has been explored by Saeid and Mohamad (2005), Saeid (2005), Zahmatkesh (2008) and Varol et al. (2008c). Saeid and Mohamad (2005) examined the effect of sinusoidal heating on the left wall of the square porous enclosure. They found that the average Nusselt number increases with the amplitude of the temperature profile. Then, Saeid (2005) studied the rectangular porous enclosure with partially sinusoidal heating applied on the bottom wall. The opposite top wall is cold and the left and right sidewalls are adiabatic. From the study, the average heat transfer rate increases with the heat source length and amplitude of the temperature profile. Natural convection in a rectangular enclosure with sinusoidal temperature variation on the bottom wall was investigated by Varol et al. (2008c). Multiple flows are observed inside the enclosure for all Darcy-Rayleigh numbers, aspect ratios and amplitudes considered. The effect of aspect ratio is significant when the amplitude of the temperature profile is high. Zahmatkesh (2008) reported a study on the square porous enclosure with sinusoidal heating on the bottom wall and sinusoidal cooling on the sidewalls with a adiabatic top wall. The article concluded that constant heating and cooling have higher heat transfer rate than non-uniform cooling.

Several researchers have reported sinusoidal heating on a porous enclosure using non-Darcy flow model. Basak et al. (2006) investigated natural convection in a square porous enclosure with sinusoidal heating on the bottom wall and constant cooling on the sidewalls. Sinusoidal heating has higher local heat transfer at the middle of the bottom wall, but the average heat transfer along the wall is much lower compared to

constant heating. Later, Basak et al. (2007) added sinusoidal heating on the left wall of the square porous enclosure as well. They reported that the average heat transfer rate is low for non-uniform heating. Kumar and Bera (2009) and Khandelwal et al. (2012) also considered sinusoidal heating on the bottom wall of the square enclosure with anisotropic porous medium. Kumar and Bera (2009) applied constant cooling on the sidewalls whereas Khandelwal et al. (2012) applied thermal insulation on the walls. Khandelwal et al. (2012) found that the wave number of the sinusoidal temperature profile affects the number of convective cells inside the porous enclosure. Mansour et al. (2012) investigated the effect of the amplitude of sinusoidal temperature profile and they found that the raise of the amplitude increases the heat transfer rate. Sinusoidal heating on both sidewalls of the square porous enclosure was examined by Sivasankaran and Bhuvaneshwari (2013) and they concluded that sinusoidal heating on both sidewalls gives higher heat transfer rate than sinusoidal heating on one sidewall only.

Varol et al. (2008b) investigated sinusoidal heating on the bottom wall of a right-angled triangular porous enclosure using Darcy flow model. It is observed that the heat transfer rate of the bottom wall is higher when the sidewalls are differentially heated. Basak et al. (2008a,b) considered sinusoidal heating on the isosceles triangular porous enclosure with non-Darcy flow model. Basak et al. (2008a) studied the triangular porous enclosure with sinusoidal heating applied on the bottom wall and the inclined walls are cooled at a constant temperature. However, Basak et al. (2008b) focused on the opposite way, i.e. sinusoidal heating is applied on the inclined walls and constant cooling is applied on the bottom wall. Both results show that the average Nusselt number of the bottom wall is $\sqrt{2}$ times of the average Nusselt number of the inclined wall.

Sinusoidal heating on the bottom wall of the trapezoidal porous enclosure with non-Darcy flow model has been reported by Basak et al. (2009a,b, 2010a, 2013b). The inclined sidewalls are cooled with constant temperature and the top wall is thermally insulated. They observed that non-uniform heating has lower heat transfer rate than uniform heating and square porous enclosure has higher heat transfer rate than trapezoidal porous enclosure.

Then, sinusoidal heating on the rhombic porous enclosure was reported by Anandalakshmi and Basak (2012a,b, 2013b) with non-Darcy flow model. They applied sinusoidal temperature profile on the bottom wall with opposite top wall is adiabatic. Anandalakshmi and Basak (2012a,b) applied constant cooling on the inclined sidewalls whereas Anandalakshmi and Basak (2013b) considered linear heating on the inclined sidewalls. Anandalakshmi and Basak (2012a,b) highlighted that the average Nusselt number of the bottom wall is higher for rhombic porous enclosure at low Darcy number, however the square porous enclosure gives higher value at high Darcy number. Anandalakshmi and Basak (2013b) observed that the average Nusselt number of the bottom wall decreases with the raise of thermal aspect ratio of linear heating on the inclined sidewalls.

For wavy porous enclosure, sinusoidal heating has been published by Sheremet and Pop (2015a). The Darcy porous enclosure is concave with wavy bottom and top walls. Sinusoidal heating is applied on both vertical sidewalls and the wavy walls are adiabatic. It can be seen that the flow is multicellular inside the wavy porous enclosure with sinusoidal heating on both sidewalls. Right-angled triangular porous enclosure with a wavy left wall was documented by Bhardwaj et al. (2015) and Bhardwaj and Dalal (2015). Sinusoidal heating is applied on the bottom wall with constant cooling on the wavy left wall. For the inclined right wall, Bhardwaj et al. (2015) applied adiabatic condition on it whereas Bhardwaj and Dalal (2015) considered constant cooling. Non-Darcy flow model is used, and it is observed that the average Nusselt number increases with the number of undulations on the left wall.

A wall is partially heated if a heater is placed on some part of the wall with thermal insulation on the remaining unheated portion. Varol et al. (2008a) have placed three heaters on the left wall of a square Darcy porous enclosure with constant cooling on the right wall. It can be noticed that the position of heaters affect the overall average Nusselt number of the left wall. Zhao et al. (2007, 2008) placed a heater on the right wall with constant cooling on the left wall of the square porous enclosure. Zhao et al. (2007) used Darcy flow model whereas Zhao et al. (2008) considered non-Darcy flow model. It is observed that the average Nusselt number is low when the heater is placed at a higher

position on the right wall. Kaluri and Basak (2010, 2011a,b) considered partial heating on the bottom, left and right walls with adiabatic top wall of the square porous enclosure. However, in their study, the unheated portions are cooled with constant temperature. It can be seen that the flow is symmetrical when the heaters on the left and right walls are placed at the same height.

Sankar et al. (2011) and Bhuvaneshwari et al. (2011) examined five different heating and cooling locations on the square and rectangular porous enclosures, respectively. They found that middle-middle thermally active location gives higher heat transfer rate. Sankar et al. (2011) also concluded that enclosure with partially heated/cooled walls produces higher heat transfer rate than fully heated/cooled walls. Bhuvaneshwari et al. (2011) added that the heat transfer rate decreases with the raise of aspect ratio. Then, Sivasankaran et al. (2011) made an analysis on convective process in a rectangular porous enclosure with two isoflux heaters on the left wall. The average heat transfer rate is found to be higher at the bottom heater than that of the top heater. A brief review on natural convection in enclosures with various types and locations of the heat sources was analyzed by Öztop et al. (2015).

Partial heating on the right-angled triangular porous enclosure was investigated by Sun and Pop (2011). The heater is placed on the vertical left wall with constant cooling on the inclined right wall and the bottom wall is adiabatic. They found out that longer heater and lower heater position produce better heat transfer. Right-angled trapezoidal Darcy porous enclosure with partial cooling on the inclined right wall was examined by Varol et al. (2009a). The vertical left wall is isothermally heated and the bottom and top walls are adiabatic. It is observed that the heat transfer rate of the right wall is higher when the cooler is placed the top of the wall.

For wavy enclosure, partial heating has been reported by Hussain et al. (2011), Singh and Bhargava (2014) and Cho (2014). Convective flow and heat transfer inside an in-phase wavy enclosure with an isoflux heater placed at the bottom wall was numerically studied by Hussain et al. (2011). Singh and Bhargava (2014) considered partial heating at the bottom-right corner of the enclosure with constant cooling on the wavy left wall. Cho (2014) examined natural convection inside a square enclosure with partially heated wavy

left wall. Uniform heat flux is applied on the wavy portion and the remaining portion of the left wall is insulated. It is noticed that the waviness of the heated portion reduces the average Nusselt number of the wavy wall.

2.4 Convection in Inclined Enclosures

The inclination of the enclosure, which changes the orientation of heat source(s) and heat sink(s) applied on the enclosure, may affect the flow field and temperature distribution inside the enclosure. Natural convection in an inclined rectangular porous enclosure using Darcy flow model has been investigated by Moya et al. (1987), Baytaş (2000), Liu et al. (2002), Báez and Nicolás (2006) and Selamat et al. (2012). At 0° inclination from the horizontal plane, the rectangular porous enclosures of Moya et al. (1987) and Liu et al. (2002) are experiencing Rayleigh-Benard heating, that is, the enclosure is isothermally heated and cooled on the bottom and top walls, respectively. It can be observed that the flow is multicellular with Rayleigh-Benard heating. Moya et al. (1987) also found the existence of multiple solutions when the bottom wall is close to or on the horizontal plane. Baytaş (2000) considered differential heating on the square porous enclosure. The flow is multicellular at high Darcy-Rayleigh number when the enclosure is inclined to Rayleigh-Benard heating condition, but it is single cell at low Darcy-Rayleigh number. Báez and Nicolás (2006) investigated convective flow inside the inclined rectangular enclosure with and without the presence of porous medium. Sinusoidal heating on the inclined square porous enclosure has been reported by Selamat et al. (2012). The average Nusselt number is low when the enclosure is heated from above.

Chen and Lin (1997), Hsiao (1998), Chamkha and Al-Naser (2001), Chamkha and Al-Mudhaf (2008), Al-Farhany and Turan (2012), Basak et al. (2013c), Oztop (2007) and Ahmed et al. (2014) have performed numerical study on the inclined rectangular porous enclosure using non-Darcy flow model. Chen and Lin (1997) considered a rectangular enclosure with equal division of a fluid layer and a heat generating porous layer. Then, Hsiao (1998) studied the effect of porosity and thermal dispersion on the inclined square porous enclosure. Chamkha and Al-Naser (2001), Chamkha and Al-Mudhaf (2008) and Al-Farhany and Turan (2012) performed numerical study on the inclined tall porous

enclosure. It is noticed that the flow is multicellular when the enclosure is heated from below. Later, Basak et al. (2013c) studied thermal management on the inclined square porous enclosure. They concluded that the inclined enclosure with $\varphi \leq 30^\circ$ gives efficient thermal processing for low Prandtl number fluid. Partial cooling on the inclined porous enclosure was considered by Oztop (2007) whereas Ahmed et al. (2014) studied corner heating on the inclined porous enclosure. Oztop (2007) stated that partial cooling does not give plume like flow structure like in the case of partial heating. Ahmed et al. (2014) found that the highest heat transfer rate is obtained when the corner heater is at west and it is lowest when the corner heater is at the northeast direction.

Varol et al. (2008d, 2009c) considered natural convection inside the inclined triangular enclosure using Darcy flow model. Varol et al. (2008d) applied constant heating on the vertical left wall of the right-angled triangular enclosure whereas Varol et al. (2009c) used sinusoidal heating on the top wall of the isosceles triangular enclosure. Varol et al. (2008d) found the maximum and minimum average Nusselt number at $\varphi = 330^\circ$ and 210° , respectively. Varol et al. (2009c) observed that the flow and temperature are symmetrical at 0° and 180° of inclination. Convective flow in an inclined right-angled triangular porous enclosure with heat generation and sinusoidal heating on the bottom wall was investigated by Mansour et al. (2011b). They concluded that the increase of enclosure inclination leads to the rise of horizontal velocity and Nusselt number. Then, Sun and Pop (2014) applied partial heating on the vertical left wall of the inclined right-angled triangular porous enclosure. The highest average Nusselt number is found at 150° of inclination.

Baytaş and Pop (2001) and Varol et al. (2008e) performed numerical study on the inclined trapezoidal Darcy porous enclosure. To be precise, Baytaş and Pop (2001) used polar coordinates to construct the trapezoidal enclosure with cylindrical top and bottom wall. Rayleigh-Benard heating is applied at 0° inclination. Varol et al. (2008e) applied heating and cooling on the left and right inclined walls of the isosceles trapezoidal enclosure respectively. They found that the flow is multicellular and the heat transfer rate is low at $\varphi = 90^\circ$.

There is not much literature available for inclined porous enclosure with a wavy wall, however without the presence of porous medium, natural convective flow and heat transfer inside an inclined wavy enclosure have been examined by Adjlout et al. (2002), Aounallah et al. (2007), Dalal and Das (2005), Varol and Oztop (2007, 2008) and Sabeur-Bendehina et al. (2011). Adjlout et al. (2002) and Aounallah et al. (2007) applied differential heating on the wavy right wall and vertical left wall. Adjlout et al. (2002) found that the undulations of the hot wall reduce the heat transfer rate when it is near the horizontal plane. Rayleigh-Benard heating was considered on the wavy bottom wall and flat top wall in the study of Varol and Oztop (2007, 2008). Varol and Oztop (2008) found that the average Nusselt number decreases with the enclosure inclination for wavy enclosure, but it increases in the case of shallow enclosure. Also, sinusoidal heating was considered, with Dalal and Das (2005) applied it on the vertical right wall whereas Sabeur-Bendehina et al. (2011) used it on the wavy right wall. Dalal and Das (2005) also found that the average Nusselt number is high when the heated wall is near the horizontal wall.

2.5 Research Questions

Literatures available on convection in porous enclosures are abundant. However, the comparisons between different geometries and boundary conditions are still hardly available. Hence, such comparison will be addressed in the present study as the following;

1. Unlike the thermal boundary conditions considered by Basak et al. (2008a,b) and Varol et al. (2009c) on the isosceles triangular porous enclosure, how do the fluid flow and temperature inside the inclined isosceles triangular porous enclosure with different types of heating on the inclined left wall and constant cooling on the inclined right wall affect the heat transfer of the porous enclosure?
2. What are the differences on the fluid flow and temperature between square, trapezoidal and triangular enclosures? Also, how do the different thermal boundary conditions of these enclosures affect the overall heat transfer rate?
3. Besides square porous enclosure, what happen if sinusoidal heating is applied on the inclined left wall with constant cooling on the inclined right wall of the oblique porous enclosure? How about partial heating on the bottom wall?

4. For wavy porous enclosure, most study focused on the heating of the wavy wall of the enclosure. However, cooling on the wavy wall has not been considered. So, what happen if sinusoidal heating or partial heating is applied on the vertical left wall with constant cooling on the opposite wavy right wall?
5. Which geometry, square, rectangular, oblique, trapezoidal, triangular or wavy is giving the highest heat transfer rate? Also, which thermal boundary condition and enclosure inclination do provide the best performance in view of heat transfer rate?

These unattended problems are the focuses and goals to achieve in this study.

University of Malaya

CHAPTER 3: MATHEMATICAL FORMULATION AND METHODS OF SOLUTION

3.1 Mathematical Formulation

The convective fluid flow and heat transfer through porous media are governed by the continuity, momentum and energy equations. These equations are derived based on their respective conservation laws, and they serve as the fundamental governing equations of this work. The boundary conditions that constitute the enclosure problem and the heat transfer rate will be addressed as well.

3.1.1 Continuity equation

From Figure 1.3, we can see that when the fluid is flowing through a porous medium, the fluid velocity will not be uniform over an area. That is, the fluid velocity will be zero on the intersection of the solid particles (point A and C), but it can flow freely between the gaps of the solid particles (point B). Since the size of the solid particles is small compared with the overall size of the system, the details of the fluid local velocity variation are too complicated for comparison with the overall size of the system. However, the mean velocity of an area is sufficient as it has a comparable size larger than the size of solid particles, but it is small compared with the overall size of the system (Oosthuizen & Naylor, 1999).

Consider a two-dimensional control volume, ΔV of a porous medium. The control volume has height Δy , length Δx and a unit depth $\Delta z = 1$ ($\Delta V = \Delta x \cdot \Delta y \cdot 1$). The mean velocities (u and v) over the rectangular areas $\Delta y \cdot 1$ and $\Delta x \cdot 1$ respectively are,

$$u = \frac{1}{\Delta y} \int_0^{\Delta y} u_p \, dy, \quad v = \frac{1}{\Delta x} \int_0^{\Delta x} v_p \, dx,$$

where u_p and v_p are the fluid local velocities in the porous medium in the x - and y -directions, respectively. Since, Δx and Δy are small compared with the overall size of the system, the mean velocities are considered as the area-averaged velocity components at a point in the flow. Hence, in this study, u and v are taken as the velocity components for fluid flow through a porous medium.

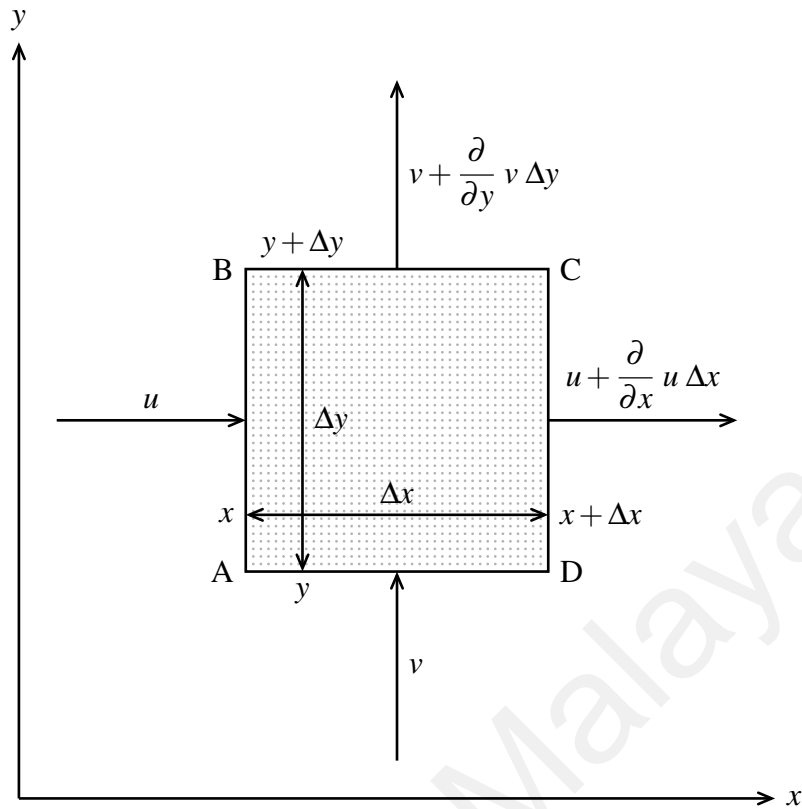


Figure 3.1: Fluid flow for a two-dimensional control volume

The continuity equation is derived from the law of conservation for mass. This principle states that mass can be neither created nor destroyed (Incropera et al., 2007). Consider the same control volume with a fixed mass m . By the law of mass conservation,

$\text{rate of change of mass in } \Delta V = \text{rate of mass convected into } \Delta V - \text{rate of mass convected out of } \Delta V$	(3.1)
--	-------

According to Archimedes' Principle,

$$\rho = \frac{m}{\Delta V} \Rightarrow m = \rho \Delta V,$$

where ρ is the fluid density.

Now, consider the fluid is flowing through the control volume across any surface of an area, $A \equiv \Delta x \cdot 1$ or $\Delta y \cdot 1$. At a certain velocity \vec{v} that is perpendicular to the surface, the rate of change of mass in ΔV is equal to the mass flow through the area A , that is,

$$\frac{\partial m}{\partial t} = \Delta V \frac{\partial \rho}{\partial t} = \rho A \vec{v}. \quad (3.2)$$

Based on the information in Figure 3.1 and equation (3.2), equation (3.1) can be mathematically written as,

$$\Delta V \frac{\partial \rho}{\partial t} = \rho \Delta y u + \rho \Delta x v - \rho \Delta y \left(u + \frac{\partial}{\partial x} u \Delta x \right) - \rho \Delta x \left(v + \frac{\partial}{\partial y} v \Delta y \right),$$

and becomes,

$$\frac{\partial \rho}{\partial t} = - \left[\frac{\partial}{\partial x} (\rho u) + \frac{\partial}{\partial y} (\rho v) \right],$$

or,

$$\frac{\partial \rho}{\partial t} + \nabla \cdot (\rho \vec{v}) = 0. \quad (3.3)$$

In this study, steady and incompressible fluid flow is considered. That is, the density of the fluid is constant at any time. Therefore, the two-dimensional continuity equation for the present study is,

$$\frac{\partial u}{\partial x} + \frac{\partial v}{\partial y} = 0. \quad (3.4)$$

3.1.2 Momentum equations

The momentum equations are obtained by applying the law of conservation for momentum to the fluid flow with the assumption that mass of fluid is conserved in any closed system. This principle is known as Newton's second law of motion which states that,

$$\vec{F} = \frac{d\vec{p}}{dt} = \frac{d}{dt} (m \vec{v}) = m \frac{d\vec{v}}{dt} = m \vec{a},$$

where \vec{F} is the net force in any direction, \vec{p} is the momentum and \vec{a} is the acceleration of the fluid in the direction that the force is acting.

The conservation of momentum is considered separately for each flow direction. For example, the net force acting on the control volume in the x -direction can be summarized as,

net force acting on the control volume in the x -direction	=	rate of u -momentum leaves the control volume	-	rate of u -momentum enters the control volume	(3.5)
--	---	---	---	---	-------

The net force acting on the control volume in any of the direction, consists of two types of external force which are the surface force and body force. The surface force arises from the pressure force and shearing force acting on the faces of the control volume, whereas the body force comprises of the gravity, g , acting on the body.

Consider the control volume shown in Figure 3.1. In the x -direction, the net pressure forces acting on the control volume will be,

$$P \Delta y - \left(P + \frac{\partial}{\partial x} P \Delta x \right) \Delta y = -\frac{\partial}{\partial x} P \Delta x \Delta y. \quad (3.6)$$

The viscous shearing forces comprises of two orthogonal forces, which are the normal shear stress and tangential shear stress that act on a surface. When the fluid flows through a porous medium, the solid particles exert a force on the fluid that is equal and opposite to the drag force on the solid particles. Also, in the Darcy model of flow through a porous medium, the flow velocities are assumed to be low, and hence the viscous forces acting on the fluid particles are negligible compared to the drag force on the solid particles. Hence, the drag force acting on the control volume in the x -direction will be,

$$-D_{F_x}. \quad (3.7)$$

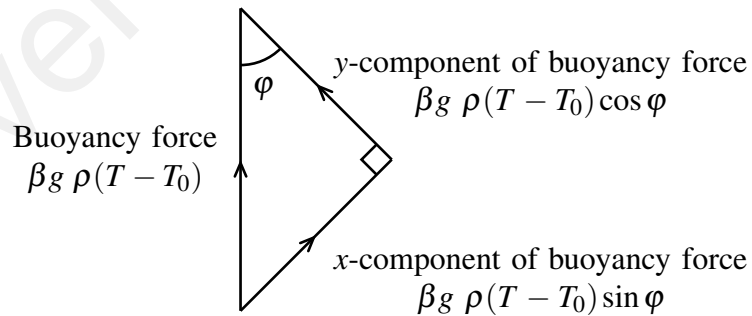


Figure 3.2: Buoyancy force components

Finally, the body force acting on the control volume will be the gravity force. Natural convective flow arises due to the changes of fluid density with temperature. Hence, in order for thermal convection to occur, the density of the fluid must be a function of temperature, i.e.

$$\rho = \rho_0 [1 - \beta (T - T_0)],$$

where ρ_0 is the fluid density at the reference temperature T_0 and β is the coefficient of thermal expansion. By Oberbeck-Boussinesq approximation, the density changes in the fluid is sufficiently small to be neglected except that its variation with temperature that gives rise to buoyancy force (Nield & Bejan, 2013). Therefore, based on Figure 3.2, the body force acting on the control volume in the x -direction will be,

$$\beta g \rho (T - T_0) \sin \varphi \Delta x \Delta y, \quad (3.8)$$

where φ is the inclination angle between x -axis and horizontal plane.

Adding up terms (3.6) – (3.8), the net force acting on the control volume in the x -direction will be,

$$-\frac{\partial}{\partial x} P \Delta x \Delta y - D_{F_x} + \beta g \rho (T - T_0) \sin \varphi \Delta x \Delta y.$$

By Darcy flow model, the momentum changes in fluid particles are also negligible compared to the drag force of solid particles. Therefore, equation (3.5) now can be written as;

$$-\frac{\partial}{\partial x} P \Delta x \Delta y - D_{F_x} + \beta g \rho (T - T_0) \sin \varphi \Delta x \Delta y = 0,$$

and simplifying becomes,

$$-\frac{\partial P}{\partial x} + \beta g \rho (T - T_0) \sin \varphi = \frac{D_{F_x}}{\Delta x \Delta y} = D_x, \quad (3.9)$$

where D_x is the drag force per unit volume in the x -direction.

Since the flow velocity is low in Darcy flow model, the fluid velocity over the solid particles is also small. Viscosity of the fluid will be large in relative to the size of the solid particles. This type of flow will be a “creeping” or “Stokes” type of flow (Oosthuizen & Naylor, 1999). For such type of flow, the drag force on a body is proportional to the velocity over the body and the dynamic viscosity of the fluid, μ . That is, $D_x \propto u \mu$. Hence, equation (3.9) now becomes,

$$K_x \left[-\frac{\partial P}{\partial x} + \beta g \rho (T - T_0) \sin \varphi \right] = u \mu,$$

and rearranging,

$$u = -\frac{K_x}{\mu} \frac{\partial P}{\partial x} + \frac{K_x}{\mu} \beta g \rho (T - T_0) \sin \varphi,$$

where K_x is the permeability of the porous medium in the x -direction. It depends on the number of solid particles per unit volume of the porous medium and also on the shape and size of the solid particles.

Similarly, the v -momentum equation in the y -direction is derived using the same procedure as in deriving the u -momentum equation. Generally, the Darcy's law or the Darcy's equation with Boussinesq approximation can be written as,

$$\vec{v} = -\frac{1}{\mu} \vec{K} \cdot \nabla P + \frac{1}{\mu} \vec{K} \cdot \vec{F}.$$

In this study, the porous medium is assumed to be isotropic, that is, the permeability of the porous medium will be the same in all directions, i.e. $K_x = K_y = K$. Therefore, the velocity components for two-dimensional Darcy flow through an isotropic porous medium are,

$$u = -\frac{K}{\mu} \frac{\partial P}{\partial x} + \frac{K}{\mu} \beta g \rho (T - T_0) \sin \varphi, \quad (3.10)$$

$$v = -\frac{K}{\mu} \frac{\partial P}{\partial y} + \frac{K}{\mu} \beta g \rho (T - T_0) \cos \varphi. \quad (3.11)$$

3.1.3 Energy equation

The energy equation is derived based on the law of conservation for energy. By First Law of Thermodynamics (Wendt, 2009),

rate of change of energy inside the control volume	=	net flux of heat into the control volume	+	rate of work done on the control volume due to body and surface forces	(3.12)
--	---	--	---	--	--------

It is assumed that the fluid and solid particles of the porous medium are in thermal equilibrium, that is, the fluid and solid particles in contact are at the same temperature locally, i.e. $T_s = T_f = T$, where T_s and T_f are temperatures of solid and fluid phases,

respectively. Also, it is assumed that heat conduction in the solid and fluid phases is parallel, so that there is no net heat transfer from one phase to another, that is,

$$k = \phi k_f + (1 - \phi) k_s,$$

where k_f and k_s are the thermal conductivities of fluid and solid particles, respectively, and ϕ is the porosity of the porous medium.

The total enthalpy, I , per unit mass of a control volume can be defined as follow,

$$I = \text{specific enthalpy} = c_p T, \quad (3.13)$$

The rate of change of enthalpy within the control volume ΔV of a fixed mass m is,

$$\begin{aligned} \frac{\partial}{\partial t} (m I) &= \frac{\partial m}{\partial t} I + m \frac{\partial I}{\partial t}, \\ &= \frac{\partial m}{\partial t} I + \rho \Delta V \frac{\partial I}{\partial t}, \\ &= \frac{\partial m}{\partial t} I + \rho \frac{\partial I}{\partial t} \Delta x \Delta y. \end{aligned} \quad (3.14)$$

From equation (3.2), $\frac{\partial m}{\partial t}$ is the mass flow rate through the surface of the control volume with area A . Then, the difference between the rate at which the sum of enthalpy and kinetic energy leave and enter the control volume in the x -direction is,

$$\left[\frac{\partial m}{\partial t} I + \frac{\partial}{\partial x} \left(\frac{\partial m}{\partial t} I \right) \Delta x \right] - \frac{\partial m}{\partial t} I = \frac{\partial}{\partial x} \left(\frac{\partial m}{\partial t} I \right) \Delta x,$$

or it can be rewritten as,

$$\left[\frac{\partial}{\partial x} (\rho u I) \right] \Delta x \Delta y. \quad (3.15)$$

The same arguments are used for y -direction,

$$\left[\frac{\partial}{\partial y} (\rho v I) \right] \Delta x \Delta y. \quad (3.16)$$

Then, adding up equations (3.14) – (3.16), and substitute with equation (3.13), it can be shown that the left-hand side of equation (3.12) is,

$$\begin{aligned} & \left[\frac{\partial}{\partial x} (\rho u I) \right] \Delta x \Delta y + \left[\frac{\partial}{\partial y} (\rho v I) \right] \Delta x \Delta y + \rho \frac{\partial I}{\partial t} \Delta x \Delta y \\ & = \frac{\partial}{\partial x} (\rho u c_P T) \Delta x \Delta y + \frac{\partial}{\partial y} (\rho v c_P T) \Delta x \Delta y + \rho \frac{\partial}{\partial t} (c_P T) \Delta x \Delta y. \end{aligned} \quad (3.17)$$

The heat flux occurred on the control volume is due to two factors, which are the volumetric heating such as absorption or emission of radiation, and the heat transfer across the surface due to temperature gradients, i.e. thermal conduction (Wendt, 2009). Let q''' be the rate of volumetric heat generation per unit mass. The volumetric heat generation of the control volume will be,

$$q''' \Delta x \Delta y \cdot 1 = q''' \Delta x \Delta y. \quad (3.18)$$

Based on Figure 3.1, q_x is the rate at which heat is transferred into the control volume in the x -direction through the left-hand face. The difference between the rate at which heat is transferred into the control volume in the x -direction and the rate at which the heat is conducted out in this direction is,

$$q_x - \left(q_x + \frac{\partial}{\partial x} q_x \Delta x \right) = -\frac{\partial}{\partial x} q_x \Delta x. \quad (3.19)$$

By Fourier's Law, the heat transfer rate, q_n , which is measured normal to a surface is,

$$q_n = -k A \frac{\partial T}{\partial n},$$

where k is the thermal conductivity.

The control volume has a unit depth ($\Delta z = 1$). Therefore, the net rate of heat transferred into the control volume in the x -direction through the left-hand face is,

$$q_x = -k \Delta y \frac{\partial T}{\partial x},$$

and substitute into equation (3.19) gives,

$$-\frac{\partial}{\partial x} \left(-k \Delta y \frac{\partial T}{\partial x} \right) \Delta x = \left[\frac{\partial}{\partial x} \left(k \frac{\partial T}{\partial x} \right) \right] \Delta x \Delta y. \quad (3.20)$$

Similarly, for y-direction,

$$\left[\frac{\partial}{\partial y} \left(k \frac{\partial T}{\partial y} \right) \right] \Delta x \Delta y, \quad (3.21)$$

then, combining equations (3.18), (3.20) and (3.21), the net flux of heat into the control volume is,

$$\begin{aligned} q''' \Delta x \Delta y + \left[\frac{\partial}{\partial x} \left(k \frac{\partial T}{\partial x} \right) \right] \Delta x \Delta y + \left[\frac{\partial}{\partial y} \left(k \frac{\partial T}{\partial y} \right) \right] \Delta x \Delta y \\ = q''' \Delta x \Delta y + k \left(\frac{\partial^2 T}{\partial x^2} + \frac{\partial^2 T}{\partial y^2} \right) \Delta x \Delta y. \end{aligned} \quad (3.22)$$

For Darcy model of flow through a porous medium, the rate at which work is done on the control volume due to viscous force that gave rises the viscous dissipation effects is neglected. However, the rate at which work is done on the control volume due to the pressure acting on the control volume will be,

$$\begin{aligned} \left\{ (u P) \Delta y - \left[(u P) \Delta y + \frac{\partial}{\partial x} (u P) \Delta x \Delta y \right] \right\} \\ + \left\{ (v P) \Delta x - \left[(v P) \Delta x + \frac{\partial}{\partial y} (v P) \Delta x \Delta y \right] \right\} \\ = -\frac{\partial}{\partial x} (u P) \Delta x \Delta y - \frac{\partial}{\partial y} (v P) \Delta x \Delta y. \end{aligned}$$

Expand and rearrange,

$$\begin{aligned} - \left(u \frac{\partial P}{\partial x} + P \frac{\partial u}{\partial x} \right) \Delta x \Delta y - \left(v \frac{\partial P}{\partial y} + P \frac{\partial v}{\partial y} \right) \Delta x \Delta y \\ = u \left(-\frac{\partial P}{\partial x} \right) \Delta x \Delta y + v \left(-\frac{\partial P}{\partial y} \right) \Delta x \Delta y - P \left(\frac{\partial u}{\partial x} + \frac{\partial v}{\partial y} \right) \Delta x \Delta y, \end{aligned}$$

and compare with equations (3.10) and (3.11), it can be rewritten as,

$$\begin{aligned} u \left[\frac{\mu}{K} u - \beta g \rho (T - T_0) \sin \varphi \right] \Delta x \Delta y + v \left[\frac{\mu}{K} v - \beta g \rho (T - T_0) \cos \varphi \right] \Delta x \Delta y \\ = \frac{\mu}{K} (u^2 + v^2) \Delta x \Delta y - \beta g \rho (T - T_0) (u \sin \varphi + v \cos \varphi) \Delta x \Delta y. \end{aligned} \quad (3.23)$$

From the derivation of momentum equations, the body force acting on the control volume will be the gravity force. Therefore, based on Figure 3.2, the rate at which work is done on the control volume due to body force is,

$$\begin{aligned} u \beta g \rho (T - T_0) \sin \varphi \Delta x \Delta y + v \beta g \rho (T - T_0) \cos \varphi \Delta x \Delta y \\ = \beta g \rho (T - T_0) (u \sin \varphi + v \cos \varphi) \Delta x \Delta y. \end{aligned} \quad (3.24)$$

From equations (3.23) and (3.24), the rate at which work is done on the control volume will be,

$$\begin{aligned} \frac{\mu}{K} (u^2 + v^2) \Delta x \Delta y - \beta g \rho (T - T_0) (u \sin \varphi + v \cos \varphi) \Delta x \Delta y \\ + \beta g \rho (T - T_0) (u \sin \varphi + v \cos \varphi) \Delta x \Delta y \\ = \frac{\mu}{K} (u^2 + v^2) \Delta x \Delta y. \end{aligned} \quad (3.25)$$

From equations (3.17), (3.22) and (3.25), and dividing by $\Delta x \Delta y$, equation (3.12) can be mathematically written as,

$$\begin{aligned} \frac{\partial}{\partial x} (\rho u c_P T) + \frac{\partial}{\partial y} (\rho v c_P T) + \rho \frac{\partial}{\partial t} (c_P T) \\ = q''' + k \left(\frac{\partial^2 T}{\partial x^2} + \frac{\partial^2 T}{\partial y^2} \right) + \frac{\mu}{K} (u^2 + v^2), \end{aligned} \quad (3.26)$$

ρ and c_P are the properties which are being assumed constant, then equation (3.25) can be written as,

$$\rho c_P \frac{\partial T}{\partial t} + \rho c_P \frac{\partial}{\partial x} (u T) + \rho c_P \frac{\partial}{\partial y} (v T) = k \left(\frac{\partial^2 T}{\partial x^2} + \frac{\partial^2 T}{\partial y^2} \right) + q''' + \frac{\mu}{K} (u^2 + v^2),$$

and simplifying,

$$\frac{\partial T}{\partial t} + \frac{\partial}{\partial x}(uT) + \frac{\partial}{\partial y}(vT) = \left(\frac{k}{\rho c_P}\right) \left(\frac{\partial^2 T}{\partial x^2} + \frac{\partial^2 T}{\partial y^2}\right) + \frac{q'''}{\rho c_P} + \left(\frac{\mu}{\rho c_P}\right) \frac{u^2 + v^2}{K}, \quad (3.27)$$

where the last term of on the right-hand side of the equation is the Darcy dissipation term.

In general, the energy equation with volumetric heat generation can be simplified as,

$$\frac{\partial T}{\partial t} + \nabla \cdot (\vec{v}T) = \alpha \nabla^2 T + \frac{q'''}{\rho c_P} + \frac{\mu}{\rho c_P} \frac{\vec{v} \cdot \vec{v}}{K},$$

where $\alpha \equiv \frac{k}{\rho c_P}$ is the thermal diffusivity.

Since the flow velocities are low in Darcy model of flow, the dissipation term can be ignored. Therefore, the steady two-dimensional energy equation with volumetric heat generation is,

$$u \frac{\partial T}{\partial x} + v \frac{\partial T}{\partial y} = \alpha \left(\frac{\partial^2 T}{\partial x^2} + \frac{\partial^2 T}{\partial y^2} \right) + \frac{q'''}{\rho c_P}. \quad (3.28)$$

3.1.4 Stream Function

The lines of constant stream function, ψ , represent streamlines, and the difference in the values of ψ between two streamlines gives the volumetric flow rate between them (Hoffman & Chiang, 2000). Thus, the plot of streamlines can illustrate the flow direction of a particle.

Eliminate the pressure term between the two momentum equations (3.10) and (3.11). That is, subtract y -derivative of equation (3.10) and x -derivative of equation (3.11) yields,

$$\frac{\partial v}{\partial x} - \frac{\partial u}{\partial y} = \frac{K}{\mu} \beta g \rho \left[\frac{\partial}{\partial x}(T - T_0) \cos \varphi - \frac{\partial}{\partial y}(T - T_0) \sin \varphi \right]. \quad (3.29)$$

Therefore, equations (3.4) and (3.29) are governing the velocity components in Darcy flow.

The stream function, ψ , is introduced as follows,

$$u = \frac{\partial \psi}{\partial y} \quad \text{and} \quad v = -\frac{\partial \psi}{\partial x}. \quad (3.30)$$

It is noticed that equation (3.4) is always satisfied with equation (3.30). Substitute equation (3.30) into equation (3.29) to get the stream function equation, that is,

$$\frac{\partial^2 \psi}{\partial x^2} + \frac{\partial^2 \psi}{\partial y^2} = -\frac{K\beta g}{\nu} \left(\cos \phi \frac{\partial T}{\partial x} - \sin \phi \frac{\partial T}{\partial y} \right), \quad (3.31)$$

where $\nu \equiv \frac{\mu}{\rho}$ is the kinematic viscosity.

Also, the energy equation (3.28) in terms of stream function will be,

$$\frac{\partial \psi}{\partial y} \frac{\partial T}{\partial x} - \frac{\partial \psi}{\partial x} \frac{\partial T}{\partial y} = \alpha \left(\frac{\partial^2 T}{\partial x^2} + \frac{\partial^2 T}{\partial y^2} \right) + \frac{q'''}{\rho c_P}. \quad (3.32)$$

3.1.5 Boundary Conditions

The governing equations are important to explain the dynamics or motion of the flow. However, the flow fields are quite different for various cases of heat transfer even though the governing equations are the same. So, the boundary conditions are important to govern the flow field for different cases. For natural convection in enclosures, the boundary conditions are derived based on three criteria, the velocity, pressure and temperature of the flow. However, with stream function formulation, the boundary conditions for pressure is not necessary required for solving the governing equations.

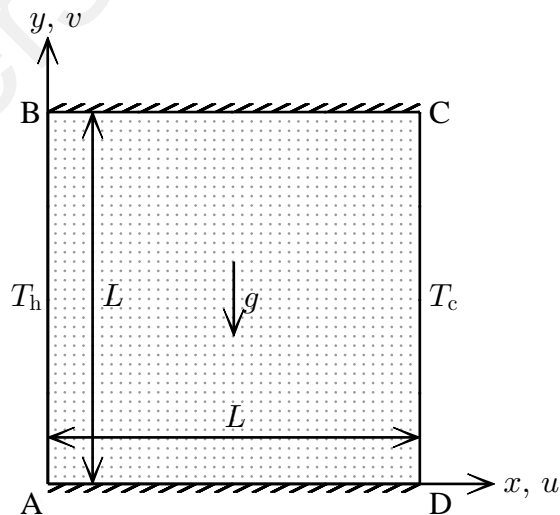


Figure 3.3: Schematic diagram of a square porous enclosure

From Figure 3.3, u and v are the velocity components of the flow in the x - and y -directions, respectively. The boundaries AB, BC, CD and DA are the solid surfaces of the enclosure. On a solid surface, fluid flow experiences no-slip condition, that is, at

the point of contact between a viscous fluid and a solid surface, the fluid velocity is the same as the solid surface. So, the fluid particle at the boundary is of zero velocity in relative to the boundary. This is the Dirichlet condition which indicates that for all solid surfaces,

$$u = v = 0. \quad (3.33)$$

Also, mass is conserved in a closed system, that is, no fluid flows in or out from the system. This implies that there is no velocity gradient on every solid wall. This is the Neumann condition which implies that,

$$\begin{aligned} \text{on AB and CD} & : \frac{\partial u}{\partial y} = 0, \\ \text{on BC and DA} & : \frac{\partial v}{\partial x} = 0. \end{aligned} \quad (3.34)$$

Based on equation (3.30), the boundary conditions of stream function is depending on the boundary conditions of u - and v -velocities at the boundaries. From the derivation of equations (3.33) and (3.34), the boundary conditions for Figure 3.3 are,

$$\begin{aligned} \text{on AB, BC, CD and DA} & : \frac{\partial \psi}{\partial y} = \frac{\partial \psi}{\partial x} = 0, \\ \text{on AB and CD} & : \frac{\partial^2 \psi}{\partial y^2} = 0, \\ \text{on BC and DA} & : \frac{\partial^2 \psi}{\partial x^2} = 0. \end{aligned} \quad (3.35)$$

The actual value of ψ is unknown because only the derivatives of ψ are available in hand. However, from Figure 3.3, the value of ψ at point A can be arbitrary taken as $\psi_A = 0$. Since $\frac{\partial \psi}{\partial y} = 0$ along AB, this suggests that $\psi = 0$ along AB and $\psi_B = 0$. Similarly, $\frac{\partial \psi}{\partial x} = 0$ along BC, this also implies that $\psi = 0$ along BC and $\psi_C = 0$. Using the same arguments for walls CD and DA, it can be concluded that on all walls,

$$\psi = 0, \quad \frac{\partial \psi}{\partial n} = 0, \quad (3.36)$$

where n is the normal of the surface being considered.

From Figure 3.3, the enclosure is heated at temperature T_h on the left wall. The enclosure can be uniformly or non-uniformly heated along the wall AB. It is cooled at a constant temperature T_c along the wall CD. However, the thermal boundary conditions on the walls BC and DA are depending on whether they are thermally insulated (or adiabatic) or perfectly conducting. In this study, the BC and DA walls are considered to be adiabatic. Therefore, the temperature conditions on the sidewalls are,

$$\begin{aligned} \text{on AB} & : T = T_h \text{ or } T(y), \\ \text{on CD} & : T = T_c, \\ \text{on BC and DA} & : \frac{\partial T}{\partial y} = 0. \end{aligned} \quad (3.37)$$

3.1.6 Rate of Heat Transfer

The heat transfer distribution is used to monitor on how the heat is transferred across a surface into the system. It is also important to figure out the occurrence of conductive or convective heat transport across the boundary.

The heat transfer rate is obtained by applying Fourier's law at the walls. From Figure 3.3 and temperature boundary conditions (3.37), the calculation is needed for thermally active sidewalls only, because the heat transfer rate is zero for adiabatic bottom and top walls. Therefore, Fourier's law suggests that the local heat transfer rates along the hot and cold walls are,

$$q_n = -k \frac{\partial T}{\partial n}, \quad (3.38)$$

where n is the normal of the sidewall being measured.

The average heat transfer rate gives the overall heat transfer that happens across the boundary. Hence, the average heat transfer rate of the hot and cold walls are,

$$\bar{q}_n = \frac{1}{d} \int_d q_n \, ds, \quad (3.39)$$

where d is the length of the sidewall and s is tangential to the sidewall being measured.

3.2 Method of Solution

The stream function and energy equations with the corresponding boundary conditions are governing natural convective flow and heat transfer inside the porous enclosure. The two equations, (3.31) and (3.32) are depending on the solutions of each other, hence the equations have to be solved simultaneously to obtain the results over the domain considered. The present work uses finite difference method (FDM) to solve the governing equations and boundary conditions. The details of solution approaches are discussed briefly in the following subsections.

3.2.1 Dimensionless Equations

The governing equations for convective flow and heat transfer comprises of a system of partial differential equations. The equations are dimensional and the physical quantities involved are depending on the properties of the fluid considered. Thus, dimensionless method is introduced to reduce the complexity in solving the equations. For natural convection in a square porous enclosure with width and height L as illustrated in Figure 3.3, the dimensionless variables are introduced as follow,

$$X = \frac{x}{L}, \quad Y = \frac{y}{L}, \quad \Psi = \frac{\psi}{\alpha}, \quad \Theta = \frac{T - T_c}{T_h - T_c}, \quad Q = \frac{q''' L^2}{k(T_h - T_c)}, \quad (3.40)$$

From equation (3.40), the terms involve in the governing equations can be expressed in dimensionless form as the following,

$$\begin{aligned} \frac{\partial \psi}{\partial x} &= \left(\frac{\alpha}{L}\right) \frac{\partial \Psi}{\partial X}, & \frac{\partial \psi}{\partial y} &= \left(\frac{\alpha}{L}\right) \frac{\partial \Psi}{\partial Y}, \\ \frac{\partial^2 \psi}{\partial x^2} &= \left(\frac{\alpha}{L^2}\right) \frac{\partial^2 \Psi}{\partial X^2}, & \frac{\partial^2 \psi}{\partial y^2} &= \left(\frac{\alpha}{L^2}\right) \frac{\partial^2 \Psi}{\partial Y^2}, \\ \frac{\partial T}{\partial x} &= \left(\frac{T_h - T_c}{L}\right) \frac{\partial \Theta}{\partial X}, & \frac{\partial T}{\partial y} &= \left(\frac{T_h - T_c}{L}\right) \frac{\partial \Theta}{\partial Y}, \\ \frac{\partial^2 T}{\partial x^2} &= \left(\frac{T_h - T_c}{L^2}\right) \frac{\partial^2 \Theta}{\partial X^2}, & \frac{\partial^2 T}{\partial y^2} &= \left(\frac{T_h - T_c}{L^2}\right) \frac{\partial^2 \Theta}{\partial Y^2}. \end{aligned}$$

Substitute the dimensionless terms into the stream function equation (3.31),

$$\left(\frac{\alpha}{L^2}\right) \frac{\partial^2 \Psi}{\partial X^2} + \left(\frac{\alpha}{L^2}\right) \frac{\partial^2 \Psi}{\partial Y^2} = -\frac{K\beta g}{\nu} \left[\cos \varphi \left(\frac{T_h - T_c}{L}\right) \frac{\partial \Theta}{\partial X} - \sin \varphi \left(\frac{T_h - T_c}{L}\right) \frac{\partial \Theta}{\partial Y} \right],$$

and simplify to obtain the dimensionless stream function equation,

$$\frac{\partial^2 \Psi}{\partial X^2} + \frac{\partial^2 \Psi}{\partial Y^2} = -Ra_D \left(\cos \varphi \frac{\partial \Theta}{\partial X} - \sin \varphi \frac{\partial \Theta}{\partial Y} \right), \quad (3.41)$$

where $Ra_D = \frac{K\beta g(T_h - T_c)L}{\alpha \nu}$ is the Darcy-Rayleigh number based on the enclosure width L . It is the multiplication of Darcy number, $Da = \frac{K}{L^2}$ and Rayleigh number, $Ra = \frac{\beta g(T_h - T_c)L^3}{\alpha \nu}$. The Darcy number shows the permeability of the porous medium per unit area whereas the Rayleigh number shows the relative magnitude of buoyancy and viscous forces acting on the fluid. The Darcy-Rayleigh number is a dimensionless number associated with natural convection heat transfer to determine whether the fluid-saturated porous medium undergoes conductive or convective transport.

The dimensionless energy equation (3.32) is,

$$\begin{aligned} \left(\frac{\alpha}{L}\right) \frac{\partial \Psi}{\partial Y} \left(\frac{T_h - T_c}{L}\right) \frac{\partial \Theta}{\partial X} - \left(\frac{\alpha}{L}\right) \frac{\partial \Psi}{\partial X} \left(\frac{T_h - T_c}{L}\right) \frac{\partial \Theta}{\partial Y} \\ = \alpha \left[\left(\frac{T_h - T_c}{L^2}\right) \frac{\partial^2 \Theta}{\partial X^2} + \left(\frac{T_h - T_c}{L^2}\right) \frac{\partial^2 \Theta}{\partial Y^2} \right] + \left(\frac{k}{\rho c_p}\right) \left(\frac{T_h - T_c}{L^2}\right) Q, \end{aligned}$$

and the simplified form is,

$$\frac{\partial \Psi}{\partial Y} \frac{\partial \Theta}{\partial X} - \frac{\partial \Psi}{\partial X} \frac{\partial \Theta}{\partial Y} = \frac{\partial^2 \Theta}{\partial X^2} + \frac{\partial^2 \Theta}{\partial Y^2} + Q. \quad (3.42)$$

Besides governing equations, the boundary conditions also have to express in dimensionless form. Based on dimensionless variables (3.40), the boundary conditions of the stream function equation (3.36) will be,

$$\Psi = 0, \quad \frac{\partial \Psi}{\partial N} = 0, \quad (3.43)$$

where $N \equiv \frac{n}{L}$ is the dimensionless coordinate for the normal of the surface being considered.

The dimensionless form of temperature conditions (3.37) is,

$$\begin{aligned} \text{on } X = 0, \quad 0 \leq Y \leq 1 & : \Theta = 1, \\ \text{on } X = 1, \quad 0 \leq Y \leq 1 & : \Theta = 0, \\ \text{on } Y = 0 \text{ and } 1, \quad 0 \leq X \leq 1 & : \frac{\partial \Theta}{\partial Y} = 0, \end{aligned} \quad (3.44)$$

for the case with constant wall temperature $T = T_h$ along the left wall.

The dimensionless governing equations (3.41) and (3.42) with the corresponding boundary conditions (3.43) and (3.44) are now can be solved simultaneously inside the dimensionless domain, that is the region bounded by the inequalities $0 \leq X \leq 1$ and $0 \leq Y \leq 1$. This dimensionless domain is obtained by reducing the dimensions of the square porous enclosure in Figure 3.3 with the characteristic length L , which is the width and height of the enclosure as given by equations in (3.40).

Apply dimensionless variables (3.40) to equations of rate of heat transfer, (3.38) and (3.39), it gives,

$$\begin{aligned} q_n &= -k \left(\frac{T_h - T_c}{L} \right) \frac{\partial \Theta}{\partial N}, \\ \bar{q}_n &= \frac{L}{d} \int_{\frac{d}{L}} q_n \, dS, \end{aligned}$$

and simplifying,

$$Nu_N = -\frac{\partial \Theta}{\partial N}, \quad (3.45)$$

$$\overline{Nu}_N = \frac{1}{D} \int_D Nu_N \, dS, \quad (3.46)$$

where $Nu = \frac{q_n L}{k(T_h - T_c)}$ is the Nusselt number, $D = \frac{d}{L}$ is the dimensionless length of the sidewall and $S \equiv \frac{s}{L}$ is the tangent of the sidewall being considered. The Nusselt number is a dimensionless number which shows the ratio of convective to conductive heat transfer across the boundary. It is an important parameter in the present study to determine the significance of the models proposed in the point of view on the rate of heat transfer. The Nusselt number is close to 1 when conduction heat transfer is dominant, otherwise it shows the intensity of convective heat transfer.

3.2.2 Grid Generation

In order to solve the equations numerically, approximations to the partial derivatives are introduced to discretize the governing equations and boundary conditions. This discretization process will result in the partitioning of the physical domain into a set of grid points. The equations are then subsequently solved at discrete points within the domain. Usually, the computational domain is chosen to be rectangular so that the interior points as well as the boundary grid points are evenly distributed. However, in this study, different enclosure shapes will be considered. The partitioning of non-rectangular shape of physical domain using uniform spacing will result in grid points that do not coincide with the boundary of the physical domain. Therefore, with an appropriate interpolation from the boundaries of the physical domain, a rectangular computational domain with uniform spacing can be imposed on the non-rectangular physical domain that is not evenly partitioned. This implies that there is a relation between the physical domain and the computational domain, so that such transformation can be done. This is the grid generation technique that uses algebraic equations to map the non-rectangular grid system in the physical domain to a rectangular computational grids with uniform spacing as illustrated in Figure 3.4.

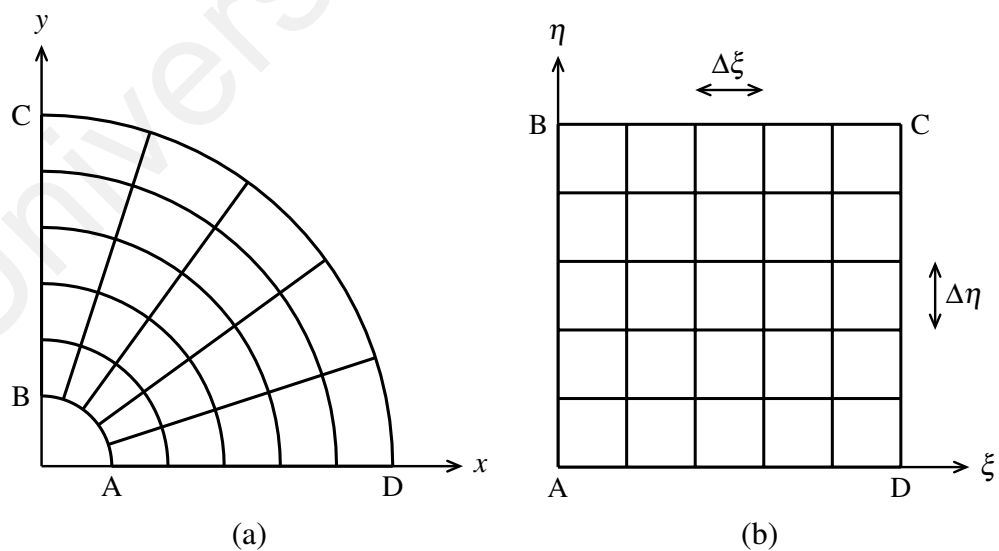


Figure 3.4: A demonstration of (a) a physical domain with uneven step sizes and (b) an associated computational domain with constant step sizes

Define the relations between the physical space (x,y) and computational space (ξ,η) ,

$$\xi = \xi(x,y), \quad \eta = \eta(x,y). \quad (3.47)$$

Apply chain rule for partial differentiation yields the following first order partial derivatives,

$$\frac{\partial}{\partial x} = \frac{\partial \xi}{\partial x} \frac{\partial}{\partial \xi} + \frac{\partial \eta}{\partial x} \frac{\partial}{\partial \eta} = \xi_x \frac{\partial}{\partial \xi} + \eta_x \frac{\partial}{\partial \eta}, \quad (3.48)$$

$$\frac{\partial}{\partial y} = \frac{\partial \xi}{\partial y} \frac{\partial}{\partial \xi} + \frac{\partial \eta}{\partial y} \frac{\partial}{\partial \eta} = \xi_y \frac{\partial}{\partial \xi} + \eta_y \frac{\partial}{\partial \eta}. \quad (3.49)$$

To obtain second order partial derivatives, let

$$A = \frac{\partial}{\partial x} = \frac{\partial}{\partial \xi} \frac{\partial \xi}{\partial x} + \frac{\partial}{\partial \eta} \frac{\partial \eta}{\partial x}, \quad (3.50)$$

then,

$$\begin{aligned} \frac{\partial^2}{\partial x^2} &= \frac{\partial}{\partial x} \cdot \frac{\partial}{\partial x} = \frac{\partial A}{\partial x} = \frac{\partial}{\partial x} \left(\frac{\partial}{\partial \xi} \frac{\partial \xi}{\partial x} + \frac{\partial}{\partial \eta} \frac{\partial \eta}{\partial x} \right) \\ &= \frac{\partial}{\partial \xi} \frac{\partial^2 \xi}{\partial x^2} + \frac{\partial \xi}{\partial x} \frac{\partial^2}{\partial x \partial \xi} + \frac{\partial}{\partial \eta} \frac{\partial^2 \eta}{\partial x^2} + \frac{\partial \eta}{\partial x} \frac{\partial^2}{\partial x \partial \eta}. \end{aligned} \quad (3.51)$$

Again, let

$$B = \frac{\partial^2}{\partial x \partial \xi} = \frac{\partial}{\partial x} \cdot \frac{\partial}{\partial \xi} = \left(\frac{\partial}{\partial \xi} \frac{\partial \xi}{\partial x} + \frac{\partial}{\partial \eta} \frac{\partial \eta}{\partial x} \right) \frac{\partial}{\partial \xi} = \frac{\partial^2}{\partial \xi^2} \frac{\partial \xi}{\partial x} + \frac{\partial^2}{\partial \xi \partial \eta} \frac{\partial \eta}{\partial x}, \quad (3.52)$$

$$C = \frac{\partial^2}{\partial x \partial \eta} = \frac{\partial}{\partial x} \cdot \frac{\partial}{\partial \eta} = \left(\frac{\partial}{\partial \xi} \frac{\partial \xi}{\partial x} + \frac{\partial}{\partial \eta} \frac{\partial \eta}{\partial x} \right) \frac{\partial}{\partial \eta} = \frac{\partial^2}{\partial \xi \partial \eta} \frac{\partial \xi}{\partial x} + \frac{\partial^2}{\partial \eta^2} \frac{\partial \eta}{\partial x}. \quad (3.53)$$

Substitute the results from equations (3.52) and (3.53) into equation (3.51),

$$\begin{aligned} \frac{\partial^2}{\partial x^2} &= \frac{\partial}{\partial \xi} \frac{\partial^2 \xi}{\partial x^2} + \frac{\partial \xi}{\partial x} \left(\frac{\partial^2}{\partial \xi^2} \frac{\partial \xi}{\partial x} + \frac{\partial^2}{\partial \xi \partial \eta} \frac{\partial \eta}{\partial x} \right) + \frac{\partial}{\partial \eta} \frac{\partial^2 \eta}{\partial x^2} + \frac{\partial \eta}{\partial x} \left(\frac{\partial^2}{\partial \xi \partial \eta} \frac{\partial \xi}{\partial x} + \frac{\partial^2}{\partial \eta^2} \frac{\partial \eta}{\partial x} \right) \\ &= \frac{\partial}{\partial \xi} \frac{\partial^2 \xi}{\partial x^2} + \frac{\partial}{\partial \eta} \frac{\partial^2 \eta}{\partial x^2} + \frac{\partial^2}{\partial \xi^2} \left(\frac{\partial \xi}{\partial x} \right)^2 + \frac{\partial^2}{\partial \eta^2} \left(\frac{\partial \eta}{\partial x} \right)^2 + 2 \frac{\partial^2}{\partial \xi \partial \eta} \frac{\partial \xi}{\partial x} \frac{\partial \eta}{\partial x}, \end{aligned}$$

and simplify,

$$\frac{\partial^2}{\partial x^2} = \xi_{xx} \frac{\partial}{\partial \xi} + \eta_{xx} \frac{\partial}{\partial \eta} + \xi_x^2 \frac{\partial^2}{\partial \xi^2} + \eta_x^2 \frac{\partial^2}{\partial \eta^2} + 2\xi_x \eta_x \frac{\partial^2}{\partial \xi \partial \eta}. \quad (3.54)$$

Similarly, second order partial derivative with respect to y is,

$$\frac{\partial^2}{\partial y^2} = \xi_{yy} \frac{\partial}{\partial \xi} + \eta_{yy} \frac{\partial}{\partial \eta} + \xi_y^2 \frac{\partial^2}{\partial \xi^2} + \eta_y^2 \frac{\partial^2}{\partial \eta^2} + 2\xi_y \eta_y \frac{\partial^2}{\partial \xi \partial \eta}. \quad (3.55)$$

For example, consider a model first order partial differential equation,

$$\frac{\partial f}{\partial x} + a \frac{\partial f}{\partial y} = 0,$$

where a is a constant. Transform this equation from physical space to computational space by using equations (3.48) and (3.49),

$$\left(\xi_x \frac{\partial f}{\partial \xi} + \eta_x \frac{\partial f}{\partial \eta} \right) + a \left(\xi_y \frac{\partial f}{\partial \xi} + \eta_y \frac{\partial f}{\partial \eta} \right) = 0,$$

and rearrange,

$$(\xi_x + a\xi_y) \frac{\partial f}{\partial \xi} + (\eta_x + a\eta_y) \frac{\partial f}{\partial \eta} = 0. \quad (3.56)$$

Also, consider a model second order partial differential equation,

$$\frac{\partial^2 f}{\partial x^2} + a \frac{\partial^2 f}{\partial y^2} = 0,$$

where a is a constant. Transform this equation from physical space to computational space by using equations (3.54) and (3.55),

$$\begin{aligned} & \left(\xi_{xx} \frac{\partial f}{\partial \xi} + \eta_{xx} \frac{\partial f}{\partial \eta} + \xi_x^2 \frac{\partial^2 f}{\partial \xi^2} + \eta_x^2 \frac{\partial^2 f}{\partial \eta^2} + 2\xi_x \eta_x \frac{\partial^2 f}{\partial \xi \partial \eta} \right) \\ & + a \left(\xi_{yy} \frac{\partial f}{\partial \xi} + \eta_{yy} \frac{\partial f}{\partial \eta} + \xi_y^2 \frac{\partial^2 f}{\partial \xi^2} + \eta_y^2 \frac{\partial^2 f}{\partial \eta^2} + 2\xi_y \eta_y \frac{\partial^2 f}{\partial \xi \partial \eta} \right) = 0, \end{aligned}$$

and rearrange,

$$\begin{aligned} & (\xi_x^2 + a\xi_y^2) \frac{\partial^2 f}{\partial \xi^2} + (\eta_x^2 + a\eta_y^2) \frac{\partial^2 f}{\partial \eta^2} \\ & + (\xi_{xx} + a\xi_{yy}) \frac{\partial f}{\partial \xi} + (\eta_{xx} + a\eta_{yy}) \frac{\partial f}{\partial \eta} + 2(\xi_x \eta_x + a\xi_y \eta_y) \frac{\partial^2 f}{\partial \xi \partial \eta} = 0. \end{aligned} \quad (3.57)$$

ξ_x , ξ_y , η_x and η_y are transformation derivatives and are defined as the metrics of transformation (Hoffman & Chiang, 2000). Consider the following approximation,

$$\xi_x = \frac{\partial \xi}{\partial x} \cong \frac{\Delta \xi}{\Delta x}.$$

The expression shows that the metrics are the ratio of arc lengths in the computational space (ξ, η) to that of the physical space (x, y) . Now, consider the total derivatives of computational space variables (ξ, η) in equation (3.47),

$$d\xi = \frac{\partial \xi}{\partial x} dx + \frac{\partial \xi}{\partial y} dy = \xi_x dx + \xi_y dy, \quad (3.58)$$

$$d\eta = \frac{\partial \eta}{\partial x} dx + \frac{\partial \eta}{\partial y} dy = \eta_x dx + \eta_y dy, \quad (3.59)$$

or in compact form,

$$\begin{pmatrix} d\xi \\ d\eta \end{pmatrix} = \begin{pmatrix} \xi_x & \xi_y \\ \eta_x & \eta_y \end{pmatrix} \begin{pmatrix} dx \\ dy \end{pmatrix}. \quad (3.60)$$

Now, reverse the role of independent variables in equation (3.47),

$$x = x(\xi, \eta), \quad y = y(\xi, \eta). \quad (3.61)$$

The total derivatives of physical space variables (x, y) are,

$$dx = \frac{\partial x}{\partial \xi} d\xi + \frac{\partial x}{\partial \eta} d\eta = x_\xi d\xi + x_\eta d\eta, \quad (3.62)$$

$$dy = \frac{\partial y}{\partial \xi} d\xi + \frac{\partial y}{\partial \eta} d\eta = y_\xi d\xi + y_\eta d\eta. \quad (3.63)$$

In compact form,

$$\begin{pmatrix} dx \\ dy \end{pmatrix} = \begin{pmatrix} x_\xi & x_\eta \\ y_\xi & y_\eta \end{pmatrix} \begin{pmatrix} d\xi \\ d\eta \end{pmatrix}. \quad (3.64)$$

Comparing equations (3.60) and (3.64),

$$\begin{pmatrix} \xi_x & \xi_y \\ \eta_x & \eta_y \end{pmatrix} = \begin{pmatrix} x_\xi & x_\eta \\ y_\xi & y_\eta \end{pmatrix}^{-1} \\ = \frac{1}{x_\xi y_\eta - x_\eta y_\xi} \begin{pmatrix} y_\eta & -x_\eta \\ -y_\xi & x_\xi \end{pmatrix}. \quad (3.65)$$

This implies that,

$$\begin{aligned} \xi_x &= Jy_\eta, & \xi_y &= -Jx_\eta, \\ \eta_x &= -Jy_\xi, & \eta_y &= Jx_\xi, \end{aligned}$$

where $J = \frac{1}{x_\xi y_\eta - x_\eta y_\xi} = \xi_x \eta_y - \xi_y \eta_x$ is the Jacobian of the transformation. It is the ratio of areas in the computational space (ξ, η) to that of the physical space (x, y) .

The second order derivatives of the transformation metrics are then calculated as,

$$\begin{aligned} \xi_{xx} &= \frac{\partial \xi_x}{\partial x} = \xi_x \frac{\partial \xi_x}{\partial \xi} + \eta_x \frac{\partial \xi_x}{\partial \eta}, \\ \xi_{yy} &= \frac{\partial \xi_y}{\partial y} = \xi_y \frac{\partial \xi_y}{\partial \xi} + \eta_y \frac{\partial \xi_y}{\partial \eta}, \\ \eta_{xx} &= \frac{\partial \eta_x}{\partial x} = \xi_x \frac{\partial \eta_x}{\partial \xi} + \eta_x \frac{\partial \eta_x}{\partial \eta}, \\ \eta_{yy} &= \frac{\partial \eta_y}{\partial y} = \xi_y \frac{\partial \eta_y}{\partial \xi} + \eta_y \frac{\partial \eta_y}{\partial \eta}. \end{aligned}$$

3.2.3 Transformation of Governing Equations and Boundary Conditions

Using an appropriate algebraic relation, the non-rectangular dimensionless physical domain (X, Y) is transformed into a rectangular computational domain (ξ, η) . Hence, in order to carry out calculation in the computational domain, the governing equations and boundary conditions of the physical domain are required to transform to the computational domain.

The transformation on the dimensionless stream function equation (3.41) and energy equation (3.42) will be,

$$a \frac{\partial^2 \Psi}{\partial \xi^2} + b \frac{\partial^2 \Psi}{\partial \eta^2} + c \frac{\partial \Psi}{\partial \xi} + d \frac{\partial \Psi}{\partial \eta} + 2e \frac{\partial^2 \Psi}{\partial \xi \partial \eta} = -Ra_D \left[(\xi_X \cos \varphi - \xi_Y \sin \varphi) \frac{\partial \Theta}{\partial \xi} + (\eta_X \cos \varphi - \eta_Y \sin \varphi) \frac{\partial \Theta}{\partial \eta} \right], \quad (3.66)$$

$$a \frac{\partial^2 \Theta}{\partial \xi^2} + b \frac{\partial^2 \Theta}{\partial \eta^2} + c \frac{\partial \Theta}{\partial \xi} + d \frac{\partial \Theta}{\partial \eta} + 2e \frac{\partial^2 \Theta}{\partial \xi \partial \eta} = J \left(\frac{\partial \Psi}{\partial \eta} \frac{\partial \Theta}{\partial \xi} - \frac{\partial \Psi}{\partial \xi} \frac{\partial \Theta}{\partial \eta} \right) - Q, \quad (3.67)$$

where,

$$\begin{aligned} a &= \xi_X^2 + \xi_Y^2, & b &= \eta_X^2 + \eta_Y^2, \\ c &= \xi_{XX} + \xi_{YY}, & d &= \eta_{XX} + \eta_{YY}, \\ e &= \xi_X \eta_X + \xi_Y \eta_Y. \end{aligned}$$

The transformation on the dimensionless boundary conditions (3.43) and (3.44) are,

$$\begin{aligned} &\text{on all solid walls} : \Psi = 0, \\ &\text{on } \xi = 0, \quad 0 \leq \eta \leq 1 : \Theta = 1, \\ &\text{on } \xi = 1, \quad 0 \leq \eta \leq 1 : \Theta = 0, \\ &\text{on } \eta = 0 \text{ and } 1, \quad 0 \leq \xi \leq 1 : \xi_Y \frac{\partial \Theta}{\partial \xi} + \eta_Y \frac{\partial \Theta}{\partial \eta} = 0. \end{aligned} \quad (3.68)$$

So now, the transformed governing equations (3.66) and (3.67) with the boundary conditions (3.68) can be solved inside the rectangular computational domain, which is the region bounded by the inequalities $0 \leq \xi \leq 1$ and $0 \leq \eta \leq 1$.

Also, the Nusselt numbers will be,

$$Nu_N = (N_X \xi_X + N_Y \xi_Y) \frac{\partial \Theta}{\partial \xi} + (N_X \eta_X + N_Y \eta_Y) \frac{\partial \Theta}{\partial \eta}, \quad (3.69)$$

$$\overline{Nu}_N = \frac{1}{D} \int_D \frac{1}{J} (S_Y \xi_X - S_X \xi_Y) Nu_N \, d\eta, \quad (3.70)$$

where $N = N(X, Y)$ and $S = S(X, Y)$ are the normal and tangent of the sidewall considered.

3.2.4 Discretization Method: Finite Difference Approximations

In general, a finite difference approximation approximates the derivatives of a function $f(x)$ at point x in its domain with sample function values of nearby points. Given an analytical function $f(x)$, $f(x + \Delta x)$ can be expressed in a Taylor series about x as,

$$f(x + \Delta x) = f(x) + (\Delta x) \frac{\partial f}{\partial x} + \frac{(\Delta x)^2}{2!} \frac{\partial^2 f}{\partial x^2} + \frac{(\Delta x)^3}{3!} \frac{\partial^3 f}{\partial x^3} + \dots \quad (3.71)$$

Solve for $\frac{\partial f}{\partial x}$,

$$\frac{\partial f}{\partial x} = \frac{f(x + \Delta x) - f(x)}{\Delta x} + O(\Delta x),$$

where $O(\Delta x)$ is the terms of order Δx . This is the forward difference approximation of $\frac{\partial f}{\partial x}$ with order Δx . Now, expand $f(x + 2\Delta x)$ about x ,

$$f(x + 2\Delta x) = f(x) + (2\Delta x) \frac{\partial f}{\partial x} + \frac{(2\Delta x)^2}{2!} \frac{\partial^2 f}{\partial x^2} + \frac{(2\Delta x)^3}{3!} \frac{\partial^3 f}{\partial x^3} + \dots \quad (3.72)$$

Multiply equation (3.71) by 4, then subtract with equation (3.72), and later solve for $\frac{\partial f}{\partial x}$,

$$\frac{\partial f}{\partial x} = \frac{-f(x + 2\Delta x) + 4f(x + \Delta x) - 3f(x)}{2\Delta x} + O(\Delta x)^2.$$

This is the forward difference approximation for $\frac{\partial f}{\partial x}$ of order $O(\Delta x)^2$. Second order approximation gives more accurate derivative, by adding more terms from the series.

Now, consider the Taylor series expansion of $f(x - \Delta x)$ and $f(x - 2\Delta x)$ about x ,

$$f(x - \Delta x) = f(x) + (-\Delta x) \frac{\partial f}{\partial x} + \frac{(-\Delta x)^2}{2!} \frac{\partial^2 f}{\partial x^2} + \frac{(-\Delta x)^3}{3!} \frac{\partial^3 f}{\partial x^3} + \dots \quad (3.73)$$

$$f(x - 2\Delta x) = f(x) + (-2\Delta x) \frac{\partial f}{\partial x} + \frac{(-2\Delta x)^2}{2!} \frac{\partial^2 f}{\partial x^2} + \frac{(-2\Delta x)^3}{3!} \frac{\partial^3 f}{\partial x^3} + \dots \quad (3.74)$$

Using similar approaches with equations (3.73) and (3.74), the first and second order backward difference approximations of $\frac{\partial f}{\partial x}$ are,

$$\begin{aligned} \frac{\partial f}{\partial x} &= \frac{f(x - \Delta x) - f(x)}{-\Delta x} + O(\Delta x), \\ \frac{\partial f}{\partial x} &= \frac{-f(x - 2\Delta x) + 4f(x - \Delta x) - 3f(x)}{-2\Delta x} + O(\Delta x)^2. \end{aligned}$$

Subtract equation (3.73) from (3.71), the central difference approximation of $\frac{\partial f}{\partial x}$ is,

$$\frac{\partial f}{\partial x} = \frac{f(x + \Delta x) - f(x - \Delta x)}{2\Delta x} + O(\Delta x)^2.$$

To approximate expressions for higher order derivatives of the function f , say $\frac{\partial^2 f}{\partial x^2}$, adding up equations (3.71) and (3.73), then solve for $\frac{\partial^2 f}{\partial x^2}$, the central difference approximation for second order derivative of f is,

$$\frac{\partial^2 f}{\partial x^2} = \frac{f(x + \Delta x) - 2f(x) + f(x - \Delta x)}{(\Delta x)^2} + O(\Delta x)^2.$$

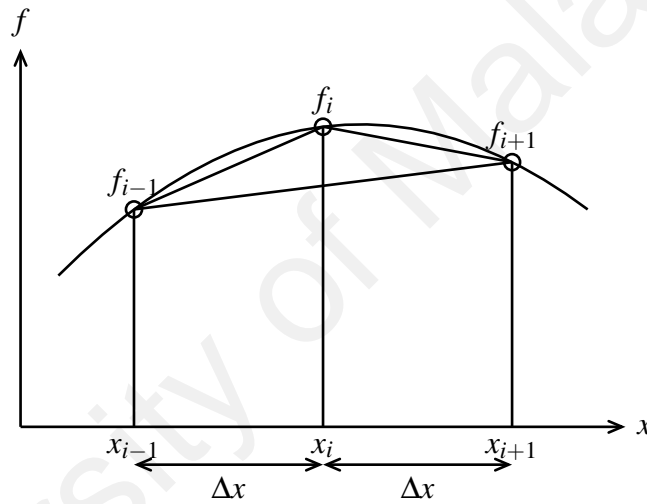


Figure 3.5: Illustration of grid points used in backward, forward and central difference approximations for first order derivative

If the subscript index i is used to represent the discrete point in the x -direction, Figure 3.5 illustrates the grid points adopted for first order derivative. In short, the finite difference approximations of f can be written as the following,

$$\begin{aligned} \text{1st order forward difference} & : \frac{\partial f}{\partial x} \approx \frac{f_{i+1} - f_i}{\Delta x}, \\ \text{1st order backward difference} & : \frac{\partial f}{\partial x} \approx \frac{f_{i-1} - f_i}{-\Delta x}, \\ \text{2nd order forward difference} & : \frac{\partial f}{\partial x} \approx \frac{-f_{i+2} + 4f_{i+1} - 3f_i}{2\Delta x}, \\ \text{2nd order backward difference} & : \frac{\partial f}{\partial x} \approx \frac{-f_{i-2} + 4f_{i-1} - 3f_i}{-2\Delta x}, \\ \text{2nd order central difference} & : \frac{\partial f}{\partial x} \approx \frac{f_{i+1} - f_{i-1}}{2\Delta x}, \\ \text{2nd order derivative} & : \frac{\partial^2 f}{\partial x^2} \approx \frac{f_{i+1} - 2f_i + f_{i-1}}{(\Delta x)^2}. \end{aligned} \quad (3.75)$$

3.2.5 Iterative Method

Finite difference approximations are used to discretize the partial differential equations. Consider a two-dimensional elliptic equation,

$$\frac{\partial^2 f}{\partial x^2} + a \frac{\partial^2 f}{\partial y^2} = S_f(x, y),$$

where a is a constant. Using central difference approximation for second order derivatives from equation (3.75),

$$\frac{f_{i+1,j} - 2f_{i,j} + f_{i-1,j}}{(\Delta x)^2} + a \frac{f_{i,j+1} - 2f_{i,j} + f_{i,j-1}}{(\Delta y)^2} = (S_f)_{i,j},$$

and rearranging, we obtain,

$$f_{i,j} = \frac{1}{2(1+aR^2)} [(f_{i+1,j} + f_{i-1,j}) + aR^2(f_{i,j+1} + f_{i,j-1}) - (\Delta x)^2(S_f)_{i,j}], \quad (3.76)$$

where $R = \frac{\Delta x}{\Delta y}$.

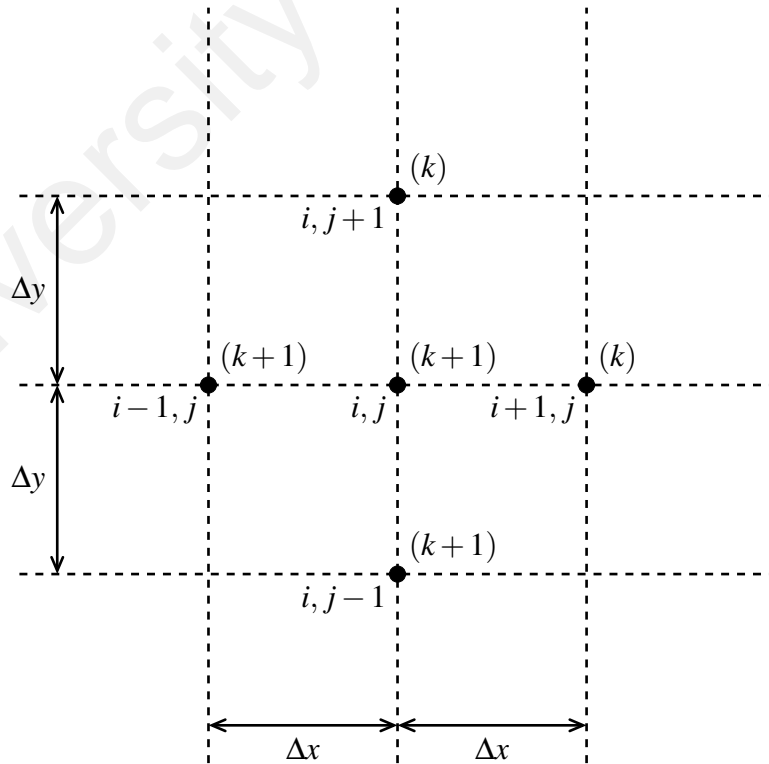


Figure 3.6: Grid points employed in Gauss-Seidel iteration method

To solve equation (3.76) within a chosen domain with large amount of nodal points, it is more appropriate to use iterative methods than that of direct methods such as Cramer's rule and Gaussian elimination (Hoffman & Chiang, 2000). In order to obtain the value of f at the grid point i, j , the values of f on the right-hand side of equation (3.76) must be available. If the current values of f are used to compute the neighbouring points as soon as they are available,

$$f_{i,j}^{(k+1)} = \frac{1}{2(1+aR^2)} \left[\left(f_{i+1,j}^{(k)} + f_{i-1,j}^{(k+1)} \right) + aR^2 \left(f_{i,j+1}^{(k)} + f_{i,j-1}^{(k+1)} \right) - (\Delta x)^2 (S_f)_{i,j}^{(k)} \right], \quad (3.77)$$

this gives the Gauss-Seidel iteration method as illustrated in Figure 3.6. Here, the computation is assumed to start from left to right and from bottom to top, and the superscript (k) is the iteration number. The Gauss-Seidel iteration method increases the convergence rate over the Jacobi method which uses initial guessed values of neighbouring points or previously computed values.

Perform $f_{i,j}^{(k+1)} - f_{i,j}^{(k)}$ to the right-hand side of equation (3.77), and rearrange,

$$f_{i,j}^{(k+1)} = f_{i,j}^{(k)} + \frac{1}{2(1+aR^2)} \left[\left(f_{i+1,j}^{(k)} + f_{i-1,j}^{(k+1)} \right) + aR^2 \left(f_{i,j+1}^{(k)} + f_{i,j-1}^{(k+1)} \right) - 2(1+aR^2) f_{i,j}^{(k)} - (\Delta x)^2 (S_f)_{i,j}^{(k)} \right].$$

As the computation proceeds, $f_{i,j}^{(k)}$ will approach to $f_{i,j}^{(k+1)}$. To accelerate the convergence, the square bracket terms on the right-hand side is multiplied by relaxation parameter, r_f , and obtain,

$$f_{i,j}^{(k+1)} = (1-r_f) f_{i,j}^{(k)} + \frac{r_f}{2(1+aR^2)} \left[\left(f_{i+1,j}^{(k)} + f_{i-1,j}^{(k+1)} \right) + aR^2 \left(f_{i,j+1}^{(k)} + f_{i,j-1}^{(k+1)} \right) - (\Delta x)^2 (S_f)_{i,j}^{(k)} \right]. \quad (3.78)$$

The values of relaxation parameter r_f must be in the range of $0 < r_f < 2$ for convergence. If $0 < r_f < 1$, it is called the Successive-Under-Relaxation (SUR) method and the range $1 < r_f < 2$ gives the Successive-Over-Relaxation (SOR) method. For $r_f = 1$, equation (3.78) reduces to Gauss-Seidel iteration method.

3.2.6 Discretization of Governing Equations and Boundary Conditions

The dimensionless governing equations (3.66) – (3.67) and boundary conditions (3.68) are discretized using finite difference approximations and then are solved using the iterative methods discussed in the previous section.

In general, the dimensionless stream function equation (3.66) and energy equation (3.67) can be discretized as,

$$a_{i,j} \frac{\zeta_{i+1,j} - 2\zeta_{i,j} + \zeta_{i-1,j}}{(\Delta\xi)^2} + b_{i,j} \frac{\zeta_{i,j+1} - 2\zeta_{i,j} + \zeta_{i,j-1}}{(\Delta\eta)^2} + (E_\zeta)_{i,j} = (S_\zeta)_{i,j}, \quad (3.79)$$

where,

$$(E_\zeta)_{i,j} = c_{i,j} \frac{\zeta_{i+1,j} - \zeta_{i-1,j}}{2\Delta\xi} + d_{i,j} \frac{\zeta_{i,j+1} - \zeta_{i,j-1}}{2\Delta\eta} + 2e_{i,j} \frac{\zeta_{i+1,j+1} - \zeta_{i+1,j-1} - \zeta_{i-1,j+1} + \zeta_{i-1,j-1}}{4\Delta\xi\Delta\eta},$$

$$\begin{aligned} a_{i,j} &= (\xi_X)_{i,j}^2 + (\xi_Y)_{i,j}^2, & b_{i,j} &= (\eta_X)_{i,j}^2 + (\eta_Y)_{i,j}^2, \\ c_{i,j} &= (\xi_{XX})_{i,j} + (\xi_{YY})_{i,j}, & d_{i,j} &= (\eta_{XX})_{i,j} + (\eta_{YY})_{i,j}, \\ e_{i,j} &= (\xi_X)_{i,j}(\eta_X)_{i,j} + (\xi_Y)_{i,j}(\eta_Y)_{i,j}. \end{aligned}$$

ζ is Ψ for the stream function equation and Θ for the energy equation. Also,

$$(S_\Psi)_{i,j} = -Ra_D \left\{ [(\xi_X)_{i,j} \cos \varphi - (\xi_Y)_{i,j} \sin \varphi] \frac{\Theta_{i+1,j} - \Theta_{i-1,j}}{2\Delta\xi} + [(\eta_X)_{i,j} \cos \varphi - (\eta_Y)_{i,j} \sin \varphi] \frac{\Theta_{i,j+1} - \Theta_{i,j-1}}{2\Delta\eta} \right\},$$

$$(S_\Theta)_{i,j} = J_{i,j} \left[\left(\frac{\Psi_{i,j+1} - \Psi_{i,j-1}}{2\Delta\eta} \right) \left(\frac{\Theta_{i+1,j} - \Theta_{i-1,j}}{2\Delta\xi} \right) - \left(\frac{\Psi_{i+1,j} - \Psi_{i-1,j}}{2\Delta\xi} \right) \left(\frac{\Theta_{i,j+1} - \Theta_{i,j-1}}{2\Delta\eta} \right) \right] - Q,$$

are the source term of the stream function equation (3.66) and energy equation (3.67), respectively.

The iterative expression for the discretized equation (3.79) will be,

$$\zeta_{i,j}^{(k+1)} = (1 - r_\zeta) \zeta_{i,j}^{(k+1)} + \frac{r_\zeta}{2(1 + R_{i,j})} \left[\left(\zeta_{i+1,j}^{(k)} - \zeta_{i-1,j}^{(k+1)} \right) + R_{i,j} \left(\zeta_{i,j+1}^{(k)} - \zeta_{i,j-1}^{(k+1)} \right) - \frac{1}{a_{i,j}} (\Delta \xi)^2 \left(-(\mathbf{E}_\zeta)_{i,j}^{(k)} + (\mathbf{S}_\zeta)_{i,j}^{(k)} \right) \right], \quad (3.80)$$

where $R_{i,j} = \frac{b_{i,j}}{a_{i,j}} \left(\frac{\Delta \xi}{\Delta \eta} \right)^2$.

Equation (3.80) is used to solve internal nodal points, that is, for points $i = 2, \dots, n\xi$ and $j = 2, \dots, n\eta$, where $n\xi$ and $n\eta$ are number of grids in the ξ - and η -directions, respectively. The values of the boundaries are given by the boundary conditions of each variables considered. The boundary conditions of stream function (3.68) give,

$$\begin{aligned} \Psi_{1,j} = 0, \quad \Psi_{n\xi+1,j} = 0, \quad \text{for } j = 1, \dots, n\eta + 1, \\ \Psi_{i,1} = 0, \quad \Psi_{i,n\eta+1} = 0, \quad \text{for } i = 1, \dots, n\xi + 1. \end{aligned} \quad (3.81)$$

The boundary conditions for temperature (3.68) along the left and right walls are,

$$\Theta_{1,j} = 1, \quad \Theta_{n\xi+1,j} = 0, \quad \text{for } j = 1, \dots, n\eta + 1. \quad (3.82)$$

Using second order finite difference approximations, temperature boundary conditions along the top and bottom walls are,

$$\begin{aligned} \Theta_{i,1} &= \frac{1}{3} \left[\frac{(\xi_Y)_{i,1} \Delta \eta}{(\eta_Y)_{i,1} \Delta \xi} (\Theta_{i+1,1} - \Theta_{i-1,1}) + (-\Theta_{i,3} + 4\Theta_{i,2}) \right], \\ \Theta_{i,n\eta+1} &= \frac{1}{3} \left[\frac{(\xi_Y)_{i,n\eta+1} - \Delta \eta}{(\eta_Y)_{i,n\eta+1} \Delta \xi} (\Theta_{i+1,n\eta+1} - \Theta_{i-1,n\eta+1}) + (-\Theta_{i,n\eta-1} + 4\Theta_{i,n\eta}) \right], \end{aligned} \quad (3.83)$$

for $i = 2, \dots, n\xi$.

The first order forward and backward approximations are used to evaluate the local Nusselt number along the left and right walls, respectively.

Along the left wall,

$$\begin{aligned}
Nu_{1,1} &= [(N_X)_{1,1}(\xi_X)_{1,1} + (N_Y)_{1,1}(\xi_Y)_{1,1}] \frac{\Theta_{2,1} - \Theta_{1,1}}{\Delta\xi} \\
&\quad + [(N_X)_{1,1}(\eta_X)_{1,1} + (N_Y)_{1,1}(\eta_Y)_{1,1}] \frac{\Theta_{1,2} - \Theta_{1,1}}{\Delta\eta}, \\
Nu_{1,j} &= [(N_X)_{1,j}(\xi_X)_{1,j} + (N_Y)_{1,j}(\xi_Y)_{1,j}] \frac{\Theta_{2,j} - \Theta_{1,j}}{\Delta\xi} \\
&\quad + [(N_X)_{1,j}(\eta_X)_{1,j} + (N_Y)_{1,j}(\eta_Y)_{1,j}] \frac{\Theta_{1,j+1} - \Theta_{1,j-1}}{2\Delta\eta}, \\
Nu_{1,n\eta+1} &= [(N_X)_{1,n\eta+1}(\xi_X)_{1,n\eta+1} + (N_Y)_{1,n\eta+1}(\xi_Y)_{1,n\eta+1}] \frac{\Theta_{2,n\eta+1} - \Theta_{1,n\eta+1}}{\Delta\xi} \\
&\quad + [(N_X)_{1,n\eta+1}(\eta_X)_{1,n\eta+1} \\
&\quad\quad + (N_Y)_{1,n\eta+1}(\eta_Y)_{1,n\eta+1}] \frac{\Theta_{1,n\eta} - \Theta_{1,n\eta+1}}{-\Delta\eta},
\end{aligned} \tag{3.84}$$

and along the right wall,

$$\begin{aligned}
Nu_{n\xi+1,1} &= [(N_X)_{n\xi+1,1}(\xi_X)_{n\xi+1,1} + (N_Y)_{n\xi+1,1}(\xi_Y)_{n\xi+1,1}] \frac{\Theta_{n\xi,j} - \Theta_{n\xi+1,1}}{-\Delta\xi} \\
&\quad + [(N_X)_{n\xi+1,1}(\eta_X)_{n\xi+1,1} \\
&\quad\quad + (N_Y)_{n\xi+1,1}(\eta_Y)_{n\xi+1,1}] \frac{\Theta_{n\xi+1,2} - \Theta_{n\xi+1,1}}{\Delta\eta}, \\
Nu_{n\xi+1,j} &= [(N_X)_{n\xi+1,j}(\xi_X)_{n\xi+1,j} + (N_Y)_{n\xi+1,j}(\xi_Y)_{n\xi+1,j}] \frac{\Theta_{n\xi,j} - \Theta_{n\xi+1,j}}{-\Delta\xi} \\
&\quad + [(N_X)_{n\xi+1,j}(\eta_X)_{n\xi+1,j} \\
&\quad\quad + (N_Y)_{n\xi+1,j}(\eta_Y)_{n\xi+1,j}] \frac{\Theta_{n\xi+1,j+1} - \Theta_{n\xi+1,j-1}}{2\Delta\eta}, \\
Nu_{n\xi+1,n\eta+1} &= [(N_X)_{n\xi+1,n\eta+1}(\xi_X)_{n\xi+1,n\eta+1} \\
&\quad\quad + (N_Y)_{n\xi+1,n\eta+1}(\xi_Y)_{n\xi+1,n\eta+1}] \frac{\Theta_{n\xi,n\eta+1} - \Theta_{n\xi+1,n\eta+1}}{-\Delta\xi} \\
&\quad + [(N_X)_{n\xi+1,n\eta+1}(\eta_X)_{n\xi+1,n\eta+1} \\
&\quad\quad + (N_Y)_{n\xi+1,n\eta+1}(\eta_Y)_{n\xi+1,n\eta+1}] \frac{\Theta_{n\xi+1,n\eta} - \Theta_{n\xi+1,n\eta+1}}{-\Delta\eta},
\end{aligned} \tag{3.85}$$

for $j = 2, \dots, n\eta$.

3.2.7 Numerical Procedure

The set of finite difference equations and associated boundary conditions are solved by implementing the algorithm as given in Figure 3.7. A converged solution is obtained with the condition that $\max_{i,j} |\zeta_{i,j}^{(k+1)} - \zeta_{i,j}^{(k)}| < 10^{-6}$, where ζ is either Ψ or Θ and (k) represents the iteration number.

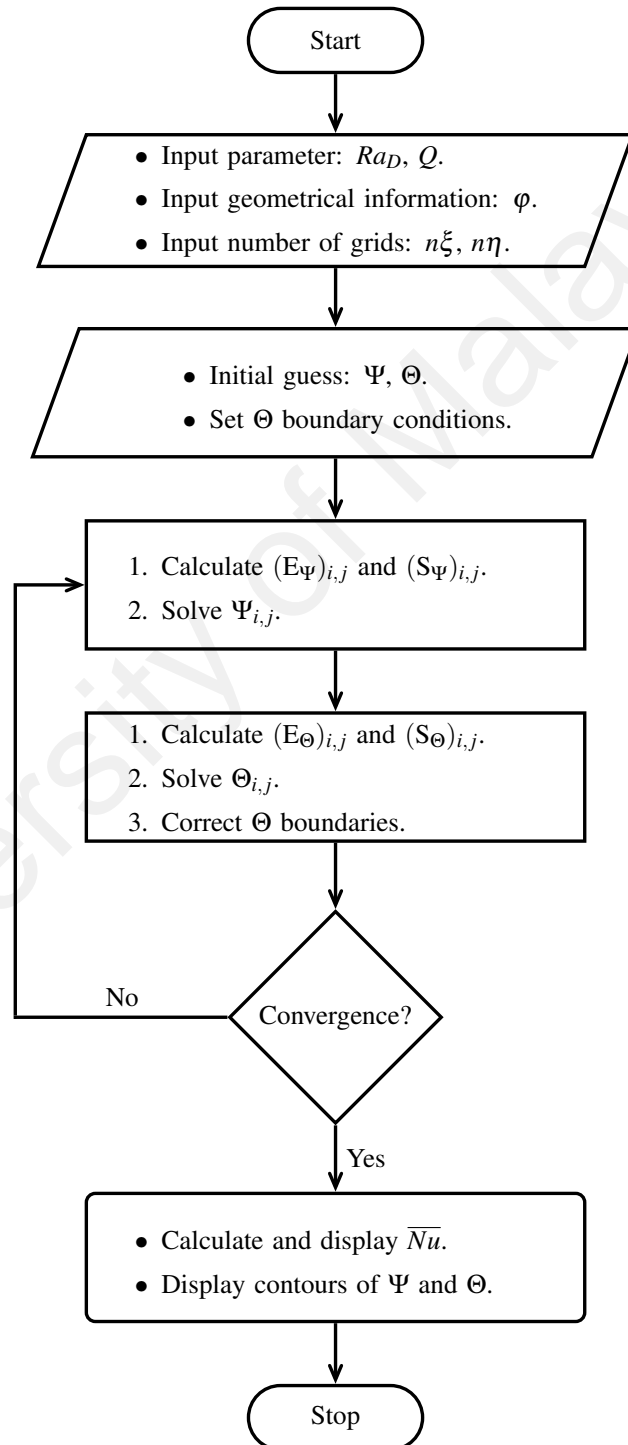


Figure 3.7: Flow chart for the numerical procedure

3.2.8 Grid Independence Test and Code Validation

Several grid sensitivity tests were performed to ensure that the results are grid independence. Uniform grid in ξ - and η -directions are used in all computations. A grid test is performed for $Ra_D = 10^3$ in the range from 40×40 to 320×320 grids. The results are shown in Figure 3.8. It is found that the grid size 200×200 is sufficient to perform as good as the finer mesh sizes and so it is used for further calculations for the case of natural convection in a square porous enclosure.

Verification of the developed computer code is very important in the numerical study. Therefore, the present results are tested to verify the code and compared with the solutions available in the literature for square porous enclosure heated with constant temperature at the sidewalls. The comparison of \overline{Nu} results for natural convection in a square porous enclosure is tabulated in Table 3.1. From Table 3.1, the results predicted by current computer code are agreed well with previous studies. This shows the confidence on our results.

Table 3.1: Comparison of \overline{Nu} results for natural convection in a square porous enclosure

References	Method	Mesh Size	$Ra_D = 10^2$	$Ra_D = 10^3$
Ni and Beckermann (1991)	FVM	50×50	3.103	13.420
Zheng et al. (2001)	FDM	80×80	3.124	13.413
Saeid and Pop (2004)	FVM	41×41	3.002	13.726
Zhao et al. (2007, 2008)	FVM	81×81	3.090	13.450
Kayhani et al. (2011)	FVM	75×75	3.117	13.721
Selamat et al. (2012)	FDM	160×160	3.106	13.498
Sojoudi et al. (2014)	FVM	200×200	3.105	13.019
Sheremet and Pop (2015b)	FDM	500×500	3.104	13.839
Chen et al. (2016)	CSCM	36×36	3.116	13.743
Present study	FDM	200×200	3.108	13.517

The streamlines (contour of Ψ) and isotherms (contour of Θ) for the validation are presented in Figure 3.9. The negative sign of stream function Ψ indicates the clockwise flow and positive sign shows counter-clockwise fluid flow. The contour of Θ shows the isoline of dimensionless temperature.

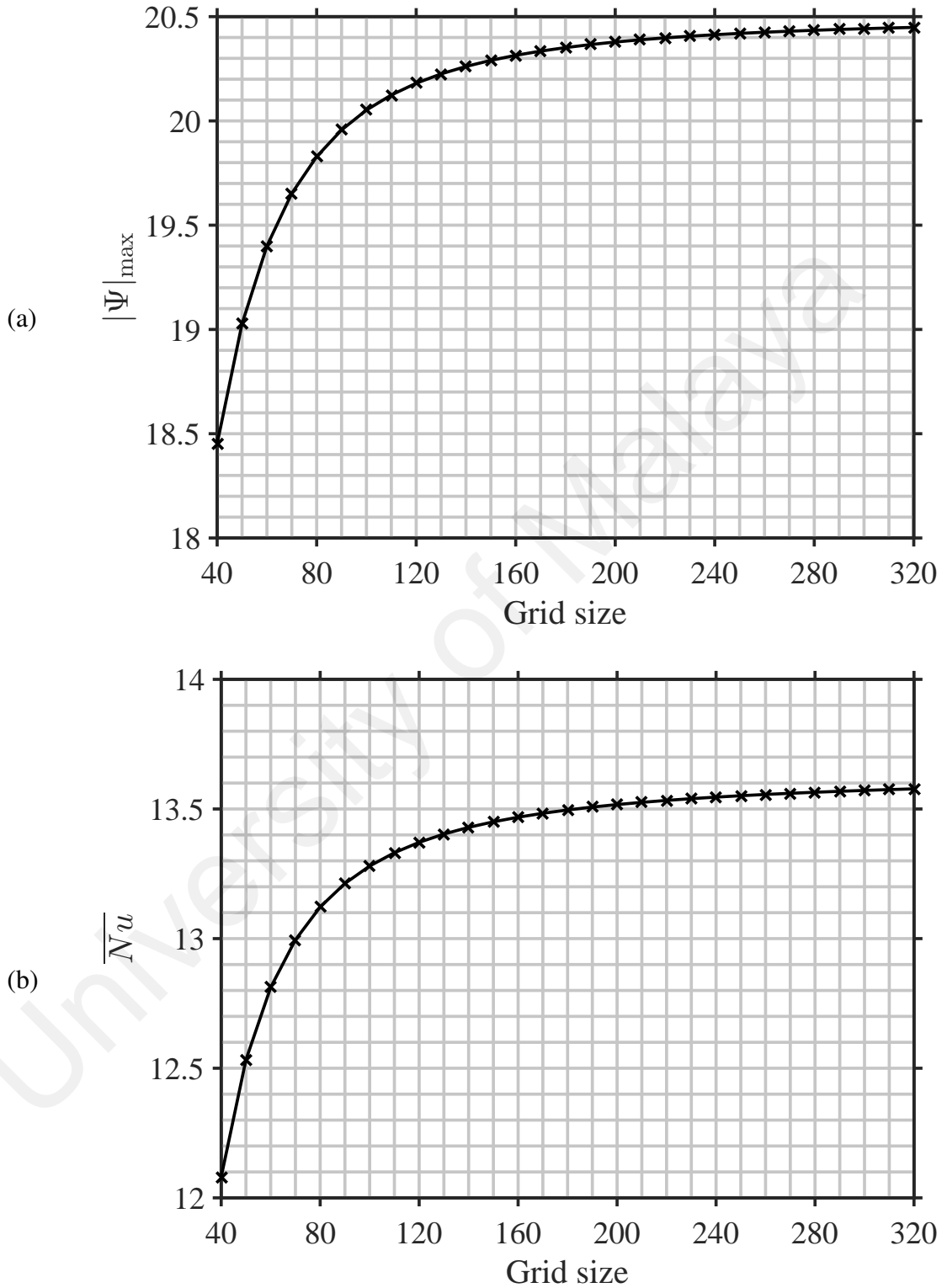


Figure 3.8: Grid independency test at $Ra_D = 10^3$ with (a) $|\Psi|_{\max}$ and (b) \overline{Nu}

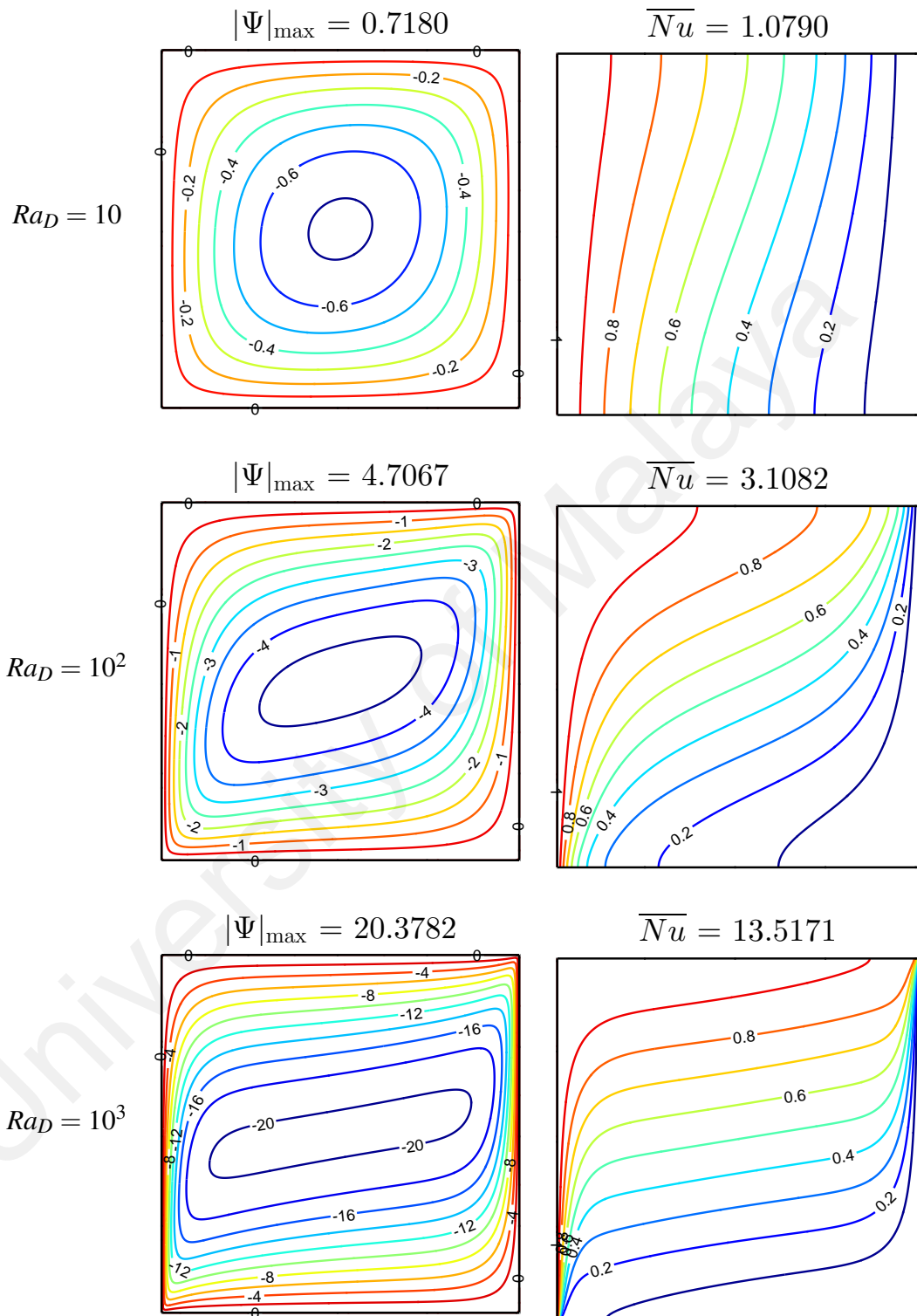


Figure 3.9: Streamlines (left) and isotherms (right) for natural convection in square porous enclosures heated with constant temperature on the left sidewall

CHAPTER 4: NATURAL CONVECTION IN A TRIANGULAR POROUS ENCLOSURE

4.1 Introduction

Natural convective flow and heat transfer inside an isosceles triangular enclosure have been investigated by several researchers. However, there is no study available on the comparison of different thermal boundary conditions and enclosure inclination of the isosceles triangular porous enclosure. Hence, the present chapter reports on natural convection in an inclined triangular porous enclosure with various thermal boundary conditions. The results may be useful in solar engineering applications.

4.2 Problem Statement

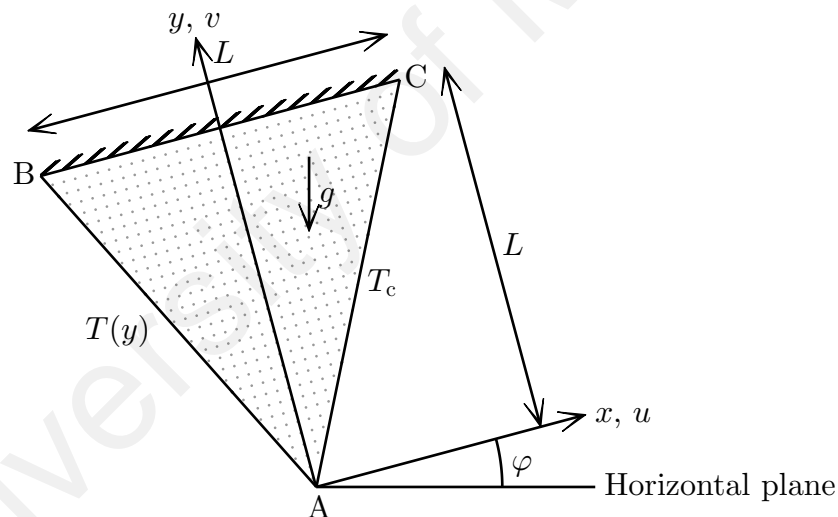


Figure 4.1: Schematic diagram of a triangular porous enclosure

Consider a two-dimensional triangular enclosure of height and width L filled with fluid saturated porous medium as shown in Figure 4.1. The top wall of the enclosure is insulated. Temperature profile $T(y)$ is applied on the left wall while the right wall is cooled with constant temperature T_c . Two cases of temperature profile are considered in this study, which are sinusoidal heating and linear heating. The inclination of the enclosure (φ) is the angle between the x -axis and the horizontal plane. The gravity acts in the vertical downward direction. The velocity components, u and v are taken in the x - and y -directions, respectively. Fluid in the enclosure is incompressible and Newtonian.

The fluid properties are constant and density variation is neglected except in the buoyancy term (by Boussinesq approximation). The porous medium is assumed to be homogeneous, isotropic and in thermal equilibrium with the fluid. Furthermore, it is assumed that the flow is steady and the viscous dissipation is negligible. Hence, Darcy model is adopted to explain the fluid flow through the porous medium. By the laws of conservation for mass, momentum, and energy, the governing equations for convective flow and heat transfer inside a porous enclosure with Darcy flow are;

$$\frac{\partial u}{\partial x} + \frac{\partial v}{\partial y} = 0, \quad (4.1)$$

$$u = -\frac{K}{\mu} \frac{\partial P}{\partial x} + \frac{K\beta g}{v} (T - T_c) \sin \varphi, \quad (4.2)$$

$$v = -\frac{K}{\mu} \frac{\partial P}{\partial y} + \frac{K\beta g}{v} (T - T_c) \cos \varphi, \quad (4.3)$$

$$u \frac{\partial T}{\partial x} + v \frac{\partial T}{\partial y} = \alpha \left(\frac{\partial^2 T}{\partial x^2} + \frac{\partial^2 T}{\partial y^2} \right) + \frac{q'''}{\rho c_P}, \quad (4.4)$$

with $q''' = 0$ for present study. The boundary conditions for the triangular porous enclosure are;

$$\text{on all solid walls} : u = v = 0,$$

$$\text{on AB} : T = \begin{cases} T_c + (T_{\text{ref}} - T_c) \sin \left(\pi \frac{y}{L} \right), \\ T_c + (T_{\text{ref}} - T_c) \frac{y}{L}, \end{cases} \quad (4.5)$$

$$\text{on CA} : T = T_c,$$

$$\text{on BC} : \frac{\partial T}{\partial y} = 0.$$

Using the solution approaches introduced in Chapter 3, u and v components in the governing equations are first expressed in terms of stream function. Then, dimensionless variables (3.40) are used to non-dimensionalize the governing equations and boundary conditions, which yields the dimensionless governing equations (3.41) and (3.42) with

$Q = 0$. The dimensionless boundary conditions are;

$$\begin{aligned}
 \text{on all solid walls} & : \Psi = 0, \\
 \text{on AB} & : \Theta = \begin{cases} \sin \pi Y, \\ Y, \end{cases} \\
 \text{on CA} & : \Theta = 0, \\
 \text{on BC} & : \frac{\partial \Theta}{\partial Y} = 0,
 \end{aligned} \tag{4.6}$$

The heat transfer rate of the porous enclosure is measured by the Nusselt number, which is defined as in equations (3.45) and (3.46).

4.3 Solution Approach

Finite difference method is used to discretize governing equations (3.41) and (3.42) subject to boundary conditions (4.6). The discretized equations are solved using SUR method. However, grid generation method is not used in the present study. In order to carry out computations using uniform grids in the X - and Y -directions, the height of a grid is the double of its width, so that the grid points are coincided with the inclined sidewalls of the triangular enclosure. A grid test is performed for $Ra_D = 10^3$ with $\phi = 0^\circ$ in the range of 80×40 to 400×200 grids. It is found that the grid size of 320×160 is sufficient to perform the computation as good as the finer mesh sizes as tabulated in Table 4.1. The converged solution is obtained by implementing the numerical procedure discussed in Chapter 3.

Table 4.1: Grid independence test at $Ra_D = 10^3$ with \overline{Nu} for triangular porous enclosures with different temperature profiles

Grid size	$\Theta = \sin \pi Y$	$\Theta = Y$
80×40	8.869	4.256
160×80	10.332	4.874
200×100	10.663	5.016
300×150	11.119	5.215
320×160	11.177	5.241
340×170	11.229	5.264
360×180	11.274	5.284
400×200	11.352	5.319

4.4 Results and Discussion

A numerical study is conducted to investigate the effect of thermal boundary conditions and enclosure inclination on convective flow and heat transfer of a porous medium filled triangular enclosure. The range of Darcy-Rayleigh number, Ra_D considered is 10 to 10^3 and the enclosure inclination is $\varphi = 0^\circ$ to 180° . There are two temperature profiles under investigation, which are sinusoidal heating ($\Theta = \sin \pi Y$) and linear heating ($\Theta = Y$).

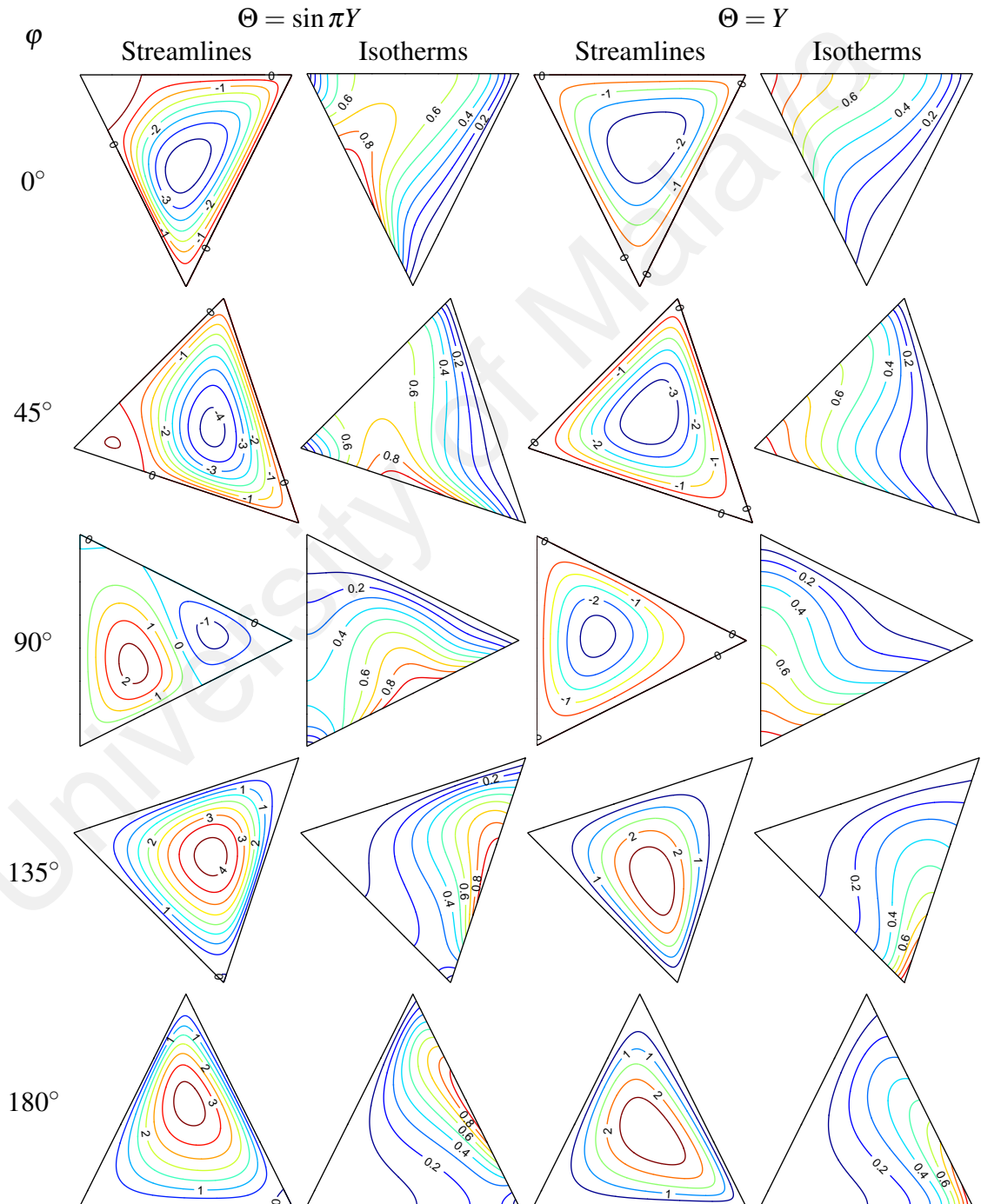


Figure 4.2: Streamlines and isotherms for various inclination angles with different temperature profiles at $Ra_D = 10^2$

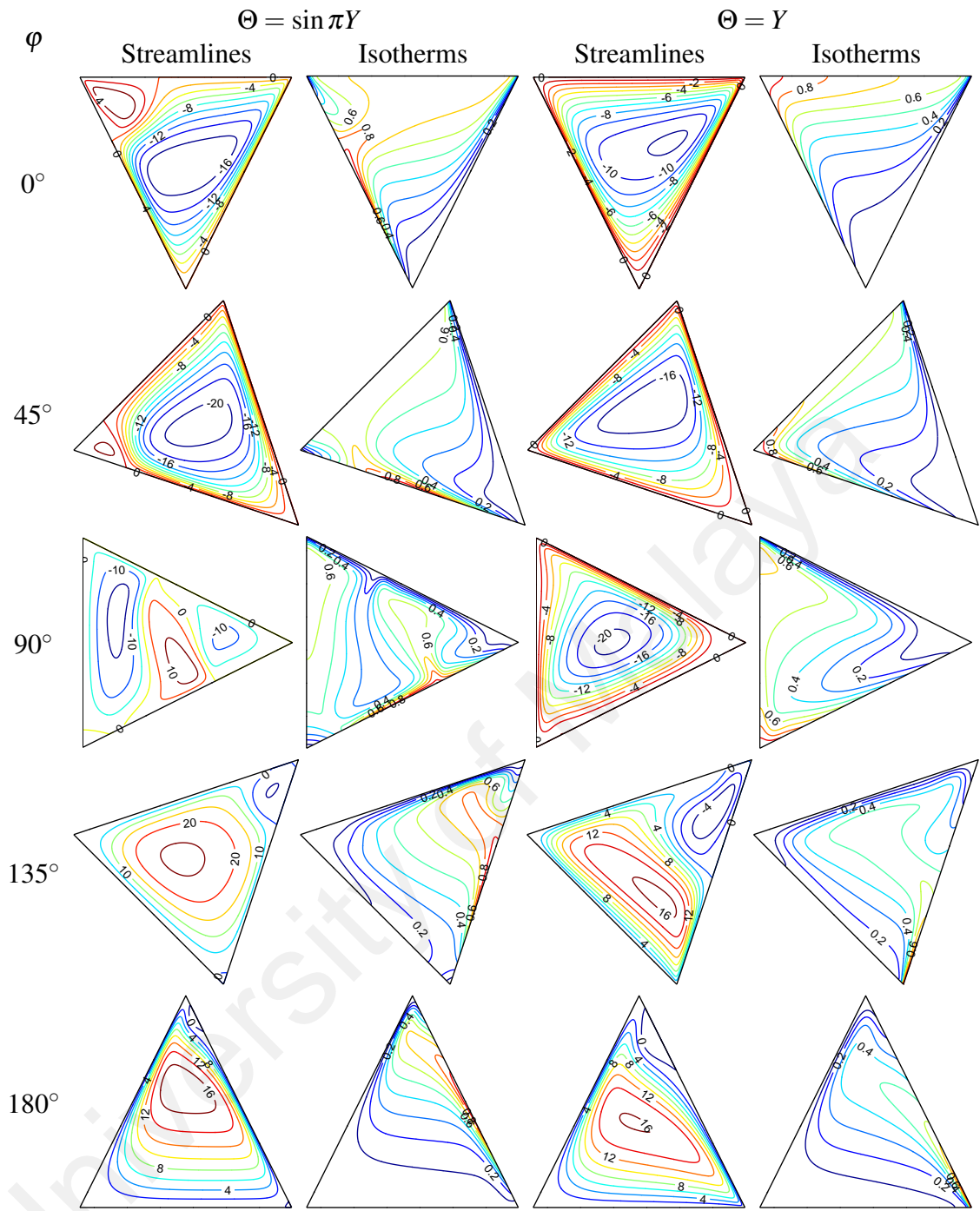


Figure 4.3: Streamlines and isotherms for various inclination angles with different temperature profiles at $Ra_D = 10^3$

Figure 4.2 shows the streamlines and isotherms at $Ra_D = 10^2$ with the comparison between sinusoidal heating and linear heating. Both temperature profiles affect the flow structure and temperature distribution inside the triangular porous enclosure. Inclination of the enclosure also is a factor for the change of flow structure and temperature distribution inside the enclosure. For sinusoidal heating, it can be seen that counter acting dual cells are formed inside the enclosure. The clockwise cell dominates and occupies

the majority of the enclosure for $\varphi = 0^\circ$ and 45° . At $\varphi = 90^\circ$, two cells of opposite flow direction are observed with larger cell flowing in counter-clockwise direction near the insulated wall. Counter-clockwise cell is dominating the enclosure for $\varphi = 135^\circ$ and 180° . A small weak cell is formed at the corner of the sidewall. The isotherms are clustered near the left wall and top corner of the right wall, and formed thermal boundary layers along the left wall and top portion of the cold wall for $\varphi = 0^\circ$ and 45° . For $\varphi \geq 90^\circ$, the isotherms are more concentrated near the hot wall and bottom part of the cold wall. Thermal boundary layers are formed near the left wall and bottom portion of the right wall. The formation of thermal boundary layer shows the convection dominant heat transfer. For the case of linear heating, single cell is formed for all enclosure inclination. The fluid flows in clockwise direction for $\varphi = 0^\circ$ to 90° . Counter-clockwise flow is formed in the enclosure with inclination $\varphi \geq 135^\circ$. The isotherms are almost evenly distributed inside the enclosure for $\varphi = 0^\circ$ to 90° . However, for $\varphi \geq 135^\circ$, the isotherms are clustered at the top portion of the hot wall, showing the formation of thermal boundary layers at the top of the left wall.

The streamlines and isotherms for both cases with $Ra_D = 10^3$ are shown in Figure 4.3. It is noticed that the Darcy-Rayleigh number affects the flow and temperature distribution inside the triangular porous enclosure in comparison between Figures 4.2 and 4.3. Increasing the Darcy-Rayleigh number increases the ratio of buoyancy force to viscous force. Increasing effect of buoyancy force due to temperature difference in the enclosure drives the hot fluid to flow upwards at higher velocity. Decreasing fluid viscosity also causes the fluid to flow near to the walls of the enclosure. Therefore, the cell with high stream value occupies a large area in the enclosure and it is closer to the boundary for $Ra_D = 10^3$ as compared to $Ra_D = 10^2$. The isotherms show that convection is dominating the heat transfer inside the porous enclosure at $Ra_D = 10^3$. The isotherms are closer to the hot and cold walls compared to $Ra_D = 10^2$, so the local heat transfer is higher for high Darcy-Rayleigh number. The flow phenomenon is similar to that of $Ra_D = 10^2$ for both cases, but there is another weak cell forming at the corner of the enclosure for $\varphi = 135^\circ$ and 180° .

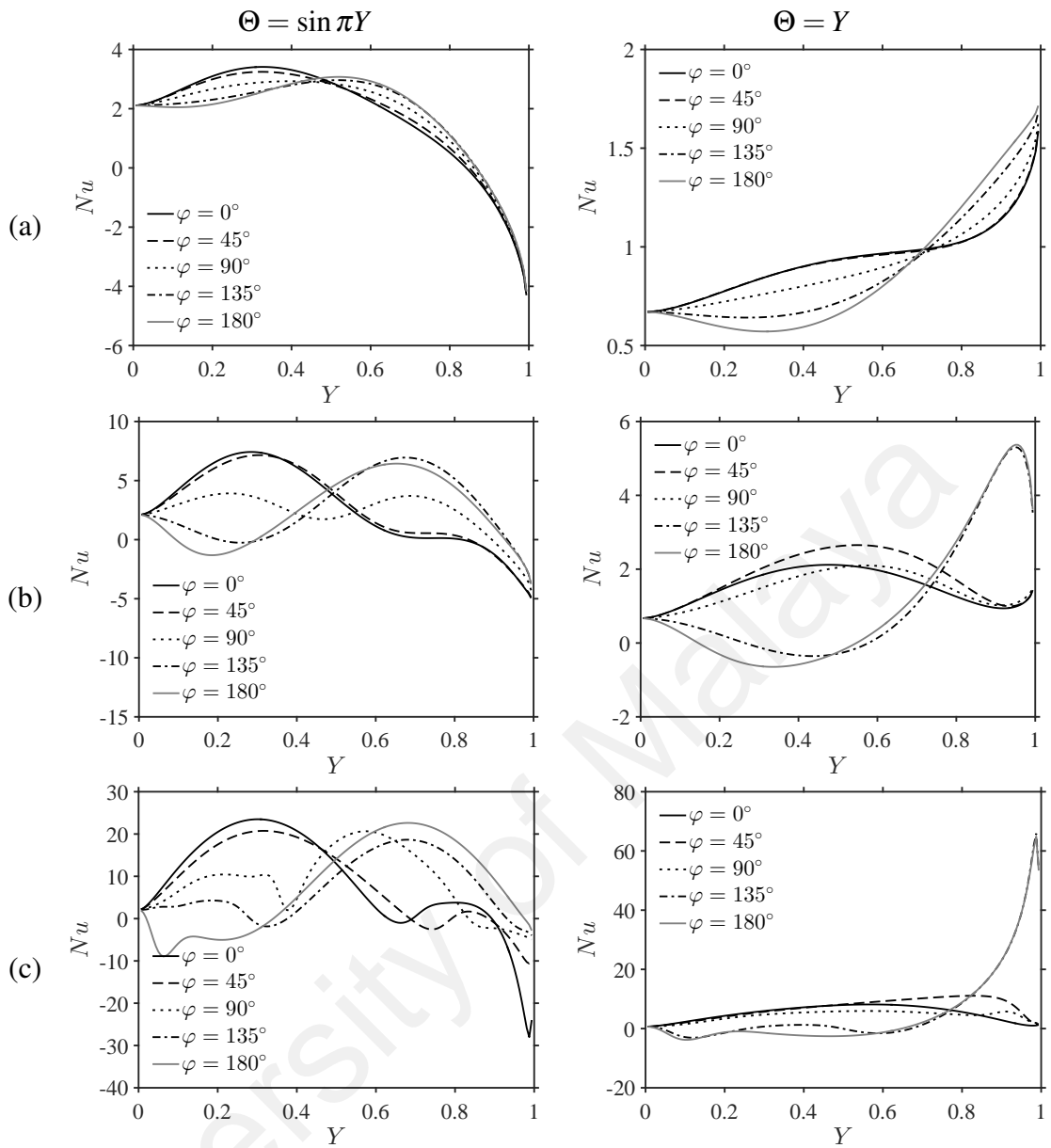


Figure 4.4: Local Nusselt number for different temperature profiles at (a) $Ra_D = 10$, (b) $Ra_D = 10^2$ and (c) $Ra_D = 10^3$

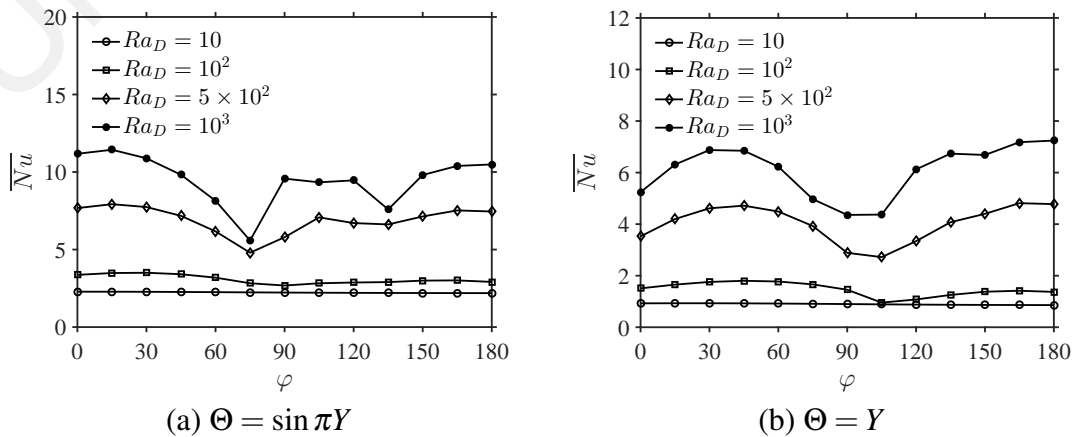


Figure 4.5: Average Nusselt number for different inclination angles and Darcy-Rayleigh numbers

Figure 4.4 shows the local heat transfer for sinusoidal heating and linear heating with $Ra_D = 10$ to 10^3 . It can be seen from both cases that the variation of heat transfer depends on the temperature profile imposed and the inclination of the enclosure. By considering sinusoidal heating, the local heat transfer slightly increases near the bottom of the sidewall, and then it decreases along the wall for $Ra_D = 10$. However, the curves of the local heat transfer for $Ra_D = 10^2$ and 10^3 are of sine wave form. For $\varphi = 0^\circ$ and 45° , the local heat transfer increases from the bottom wall to its global maximum around $Y = 0.3$, then it decreases along the wall. The trend of heat transfer for $\varphi = 135^\circ$ and 180° is opposing of $\varphi = 0^\circ$ and 45° for $Y < 0.7$, where at the bottom of the sidewall, the local heat transfer decreases to its local minimum near $Y = 0.3$. Then, the local heat transfer increases and the global maximum is found around $Y = 0.7$. The local heat transfer is then decreasing along the wall. The local heat transfer for $\varphi = 90^\circ$ is of wavy pattern, and increasing the Darcy-Rayleigh number increases the wavy sinusoidal heat transfer along the wall. Near $Y = 0.9$, the value of Nu is negative for all Ra_D and φ . This indicates that the fluid in the enclosure is of higher temperature than the wall and heat is lost to the environment near the top of the hot wall.

For linear heating, heat is transferred into the enclosure with an increasing trend for $Ra_D = 10$. The heat transfer rate increases gradually along the wall for $\varphi = 0^\circ$ to 90° . It starts to decrease around $0.5 \leq Y \leq 0.8$ and then slightly increases near the insulated wall. While for $\varphi = 135^\circ$ and 180° , the heat transfer decreases and at $Y = 0.7$, it increases rapidly to local maximum and decreases near the insulated wall. From Figure 4.4, it can be noticed that the maximum local heat transfer for sinusoidal heating is higher than linear heating for $Ra_D = 10$ and 10^2 , but for $Ra_D = 10^3$, the maximum local heat transfer is higher for linear wall temperature. For $\varphi = 0^\circ$ to 90° , heat lost from the enclosure to the environment for linear heating is lower compared to sinusoidal heating as the value of Nu is positive.

Average Nusselt numbers are shown in Figure 4.5 with various Darcy-Rayleigh number and inclination angle. The average heat transfer increases with increasing Darcy-Rayleigh number for all inclination angles. Figure 4.5 also shows that the heat transfer rates for sinusoidal heating and linear heating depend on the inclination of the

enclosure. The variation of heat transfer with enclosure inclination for $Ra_D = 10$ is almost constant, and it shows conduction-dominant regime across the fluid layer. For $Ra_D = 10^2$ to 10^3 , both cases show similar pattern for heat transfer where it behaves non-linearly with the enclosure inclination. The plot of \overline{Nu} is almost symmetrical at $\varphi = 90^\circ$ for sinusoidal heating at low Darcy-Rayleigh number. For $Ra_D = 10^2$ to 10^3 , the lowest heat transfer for both cases is found around $75^\circ \leq \varphi \leq 105^\circ$. However, the highest heat transfer for sinusoidal heating is achieved at $\varphi = 15^\circ$ and for linear heating is obtained at 45° . It can be seen from Figure 4.5 that the heat transfer is more enhanced for sinusoidal heating compared to linear heating.

Table 4.2: Comparison of \overline{Nu} between sinusoidal heating and linear heating for various values of Ra_D and φ

φ	$Ra_D = 10$			$Ra_D = 10^2$			$Ra_D = 10^3$		
	$\sin \pi Y$	Y	Difference (%)	$\sin \pi Y$	Y	Difference (%)	$\sin \pi Y$	Y	Difference (%)
0°	2.28	0.93	59.4	3.37	1.51	55.2	11.18	5.24	53.1
15°	2.28	0.93	59.2	3.49	1.65	52.6	11.43	6.31	44.8
30°	2.27	0.93	59.1	3.50	1.76	49.8	10.88	6.87	36.9
45°	2.26	0.93	59.1	3.41	1.80	47.1	9.82	6.85	30.3
60°	2.25	0.92	59.2	3.19	1.77	44.3	8.15	6.23	23.6
75°	2.24	0.91	59.4	2.83	1.66	41.2	5.58	4.97	10.9
90°	2.23	0.90	59.6	2.68	1.45	45.7	9.57	4.36	54.4
105°	2.22	0.89	60.0	2.83	0.95	66.2	9.33	4.37	53.1
120°	2.21	0.88	60.2	2.87	1.08	62.5	9.46	6.13	35.2
135°	2.20	0.87	60.4	2.90	1.25	56.8	7.59	6.74	11.2
150°	2.20	0.87	60.6	3.00	1.38	54.0	9.81	6.68	31.9
165°	2.19	0.86	60.7	3.01	1.42	53.0	10.39	7.18	30.9
180°	2.19	0.86	60.8	2.91	1.37	52.9	10.49	7.24	31.0

Table 4.2 shows the comparison of \overline{Nu} for sinusoidal heating and linear heating with various Darcy-Rayleigh number and enclosure inclination. The heat transfer of sinusoidal heating is almost double of linear heating for all inclination angle in $Ra_D = 10$. The enhancement of heat transfer depends on the enclosure inclination as shown by the differences of $Ra_D = 10^2$ and 10^3 . The variation of the difference is of wavy form with increasing inclination angle. Among all enclosure inclination considered, 0° has the highest difference and the least difference is found at 75° . For a fixed enclosure

inclination, the difference of enhancement is decreasing by increasing the Darcy-Rayleigh number. Therefore, sinusoidal heating is more enhanced than linear heating at low values of Darcy-Rayleigh number.

Correlation equations are derived based on the data of \overline{Nu} obtained from the simulations for different value of inclination angles and Darcy-Rayleigh numbers. For the case of sinusoidal heating,

$$Ra_D = 10,$$

$$\overline{Nu} = Ra_D^{-\frac{0.1}{\varphi+10}+0.45} (0.004\varphi^3 - 0.015\varphi^2 - 0.013\varphi + 0.83), \quad 0 \leq \varphi \leq \pi,$$

$$Ra_D = 10^2,$$

$$\overline{Nu} = \begin{cases} Ra_D^{-\frac{0.1}{\varphi+10}+0.45} (0.077\varphi^4 - 0.21\varphi^3 - 0.074\varphi^2 - 0.020\varphi + 0.44), & 0 \leq \varphi \leq \frac{\pi}{2}, \\ Ra_D^{-\frac{0.1}{\varphi+10}+0.45} (-0.030\varphi^2 + 0.013\varphi + 0.23), & \frac{\pi}{2} < \varphi \leq \pi, \end{cases}$$

$$500 \leq Ra_D \leq 10^3,$$

$$\overline{Nu} = \begin{cases} Ra_D^{-\frac{0.1}{\varphi+10}+0.45} (0.36\varphi^4 - 0.97\varphi^3 + 0.60\varphi^2 - 0.095\varphi + 0.50), & 0 \leq \varphi \leq \frac{\pi}{2}, \\ Ra_D^{-\frac{0.1}{\varphi+10}+0.45} (-0.22\varphi^4 + 2.24\varphi^3 - 8.53\varphi^2 + 14.37\varphi - 8.61), & \frac{\pi}{2} < \varphi \leq \pi. \end{cases}$$

The correlation equations for the case of linear heating are,

$$Ra_D = 10,$$

$$\overline{Nu} = Ra_D^{-\frac{0.1}{\varphi+10}+0.47} (0.002\varphi^3 - 0.011\varphi^2 + 0.006\varphi + 0.32), \quad 0 \leq \varphi \leq \pi,$$

$$Ra_D = 10^2,$$

$$\overline{Nu} = \begin{cases} Ra_D^{-\frac{0.1}{\varphi+10}+0.47} (-0.023\varphi^4 + 0.065\varphi^3 - 0.095\varphi^2 + 0.085\varphi + 0.18), & 0 \leq \varphi \leq \frac{7\pi}{12}, \\ Ra_D^{-\frac{0.1}{\varphi+10}+0.47} (-0.023\varphi^2 + 0.14\varphi - 0.21), & \frac{7\pi}{12} \leq \varphi \leq \pi, \end{cases}$$

$$500 \leq Ra_D \leq 10^3,$$

$$\overline{Nu} = \begin{cases} Ra_D^{-\frac{0.1}{\varphi+10}+0.47} (0.13\varphi^4 - 0.40\varphi^3 + 0.24\varphi^2 + 0.073\varphi + 0.22), & 0 \leq \varphi \leq \frac{7\pi}{12}, \\ Ra_D^{-\frac{0.1}{\varphi+10}+0.47} (-0.070\varphi^2 + 0.42\varphi - 0.38), & \frac{7\pi}{12} \leq \varphi \leq \pi. \end{cases}$$

4.5 Conclusion

Natural convection in an inclined triangular porous enclosure with sinusoidal and linearly heated wall has been studied. The governing equations and boundary conditions are solved directly by using finite difference method. From this study, multiple flow patterns are observed for the case of sinusoidal heating and single cell flow pattern is observed for linear heating. For small Darcy-Rayleigh number, heat transfer is dominated by conduction across the fluid layers, and then convection is dominated with increasing Darcy-Rayleigh number. The local Nusselt number is affected by the temperature boundary conditions. The local Nusselt number is also affected by the enclosure inclination for $10^2 \leq Ra_D \leq 10^3$. The average Nusselt number behaves non-linearly with inclination of the enclosure for all Darcy-Rayleigh number. The lowest heat transfer for sinusoidal heating and linear heating is found around $75^\circ \leq \varphi \leq 105^\circ$ while the highest heat transfer is found around $\varphi = 15^\circ$ for sinusoidal heating and $\varphi = 45^\circ$ for linear heating. It can be observed that the heat transfer is enhanced in the case of sinusoidal heating than that of linear heating. This study is useful for the understanding of convection process in the green houses and solar heaters.

CHAPTER 5: NATURAL CONVECTION IN SQUARE, TRAPEZOIDAL AND TRIANGULAR POROUS ENCLOSURES

5.1 Introduction

In previous chapter, natural convection process inside an isosceles triangular porous enclosure is reported. However, from a careful review on the literatures available, there is no study to compare convection process inside the square, right-angled trapezoidal and right-angled triangular porous enclosure. Of course, there is also no study conducted on the comparison of different thermal boundary conditions for these enclosures. Hence, these features are the focus of this chapter. The outcomes of this study can be beneficial in the design of heat transfer related systems, such as solar collectors, air ventilation system, cooking appliances and more.

5.2 Problem Statement

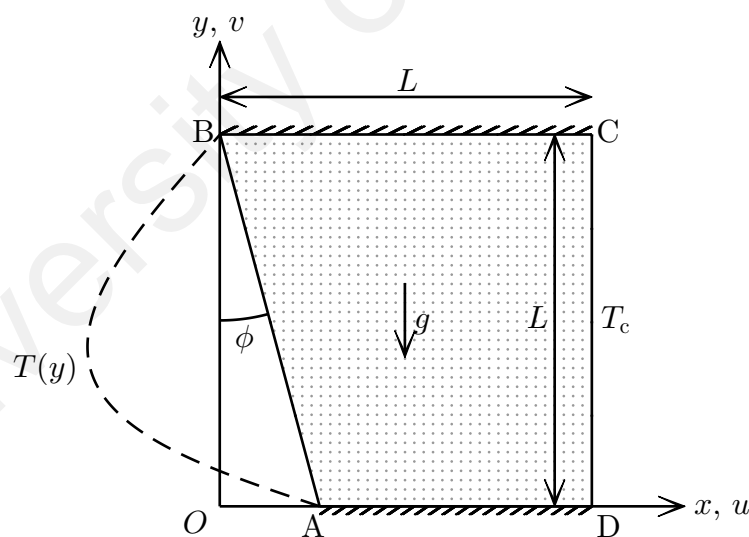


Figure 5.1: Schematic diagram of a trapezoidal porous enclosure

Consider a right-angled trapezoidal enclosure of size L filled with fluid-saturated porous medium as shown in Figure 5.1. The inclination of the left wall (ϕ) is the angle bounded between the y -axis and the left wall, which gives different geometry of the enclosure. Three enclosure shapes will be considered, which are square ($\phi = 0^\circ$), right-angled trapezoidal ($\phi = 30^\circ$) and right-angled triangular ($\phi = 45^\circ$) enclosures. The different temperature profiles, which are constant, sinusoidal and linear, are applied on

the left wall while the vertical right wall is cooled with a constant temperature T_c . The bottom and top walls are insulated. The velocity components, u and v are taken in the x - and y -directions, respectively. The gravity acts in the negative y -direction. Darcy model is adopted to describe fluid flow in the enclosure and Boussinesq approximation is valid for density variation. The porous medium is assumed to be homogeneous, isotropic and in thermal equilibrium with the fluid. The governing equations for conservations of mass, momentum and energy are given by equations (4.1) to (4.4) with $\phi = 0^\circ$ and $Q = 0$. The boundary conditions of the trapezoidal porous enclosure are;

$$\begin{aligned}
 &\text{on all solid walls} : u = v = 0, \\
 &\text{on AB} : T = \begin{cases} T_h, \\ T_c + (T_{\text{ref}} - T_c) \sin\left(\pi \frac{y}{L}\right), \\ T_c + (T_{\text{ref}} - T_c) \left(1 - \frac{y}{L}\right), \\ T_c + (T_{\text{ref}} - T_c) \left(\frac{y}{L}\right), \end{cases} \quad (5.1) \\
 &\text{on CD} : T = T_c, \\
 &\text{on BC and DA} : \frac{\partial T}{\partial y} = 0,
 \end{aligned}$$

where T_{ref} is a reference temperature of each temperature profile that is having higher temperature than T_c . For the case of constant temperature, it is simply $T_h = T_{\text{ref}}$.

After applying dimensionless variables (3.40), the governing equations are equations (3.41) and (3.42) with $\phi = 0^\circ$ and $Q = 0$. The dimensionless boundary conditions for the problem can be written as;

$$\begin{aligned}
 &\text{on all solid walls} : \Psi = 0, \\
 &\text{on AB} : \Theta = 1, \sin \pi Y, 1 - Y \text{ or } Y, \\
 &\text{on CD} : \Theta = 0, \\
 &\text{on BC and DA} : \frac{\partial \Theta}{\partial Y} = 0.
 \end{aligned} \quad (5.2)$$

The heat transfer rate along the wall is evaluated by defining the Nusselt number, which is given by equations (3.45) and (3.46).

5.3 Solution Approach

Finite difference approximations are used to discretize governing equations (3.41) and (3.42) subject to boundary conditions (5.2). The discretized equations are solved using SUR method. However, grid generation method is not used in the present study. Uniform grids in X - and Y -directions are used for all computations, where 80×80 for square and triangular enclosures and 138×80 for trapezoidal enclosure. Numerical procedure discussed in Chapter 3 is used to obtain the numerical results for present study.

5.4 Results and Discussion

Natural convection in the square enclosure ($\phi = 0^\circ$), trapezoidal enclosure ($\phi = 30^\circ$) and right-angled triangular enclosure ($\phi = 45^\circ$) filled with fluid-saturated porous medium is investigated numerically. The Darcy-Rayleigh number, Ra_D which determines the importance of convective heat transfer is varied from 10 to 10^3 . Different temperature profiles, which are constant ($\Theta = 1$), sinusoidal ($\Theta = \sin \pi Y$) and linear ($\Theta = 1 - Y$ and $\Theta = Y$) are applied on the left wall of the enclosure.

The streamlines and isotherms for $Ra_D = 10^3$ with various geometries and thermal boundary conditions are shown in Figures 5.2 and 5.3. The streamlines and isotherms clearly indicate the effect of different temperature boundary conditions inside the enclosure. For the enclosure with constant heating, the main flow is circulating in clockwise direction with single cell occupied the whole enclosure for all enclosure shapes from square to triangular. Constant heating of the left wall causes the reduction of fluid density along the left wall, and the cold right wall gives raise of fluid density, and thus the fluid is flowing in clockwise direction. In the case of sinusoidal heated left wall, the main flow is clockwise circulating and a small counter-clockwise rotating cell is observed at the top corner of the left wall. The small recirculating corner cell is increasing in size as the enclosure varies from square to triangular. Low temperature at the top-left corner causes the recirculation of cold fluid upon meeting hot ascending fluid from the lower left wall. Clockwise circulating main flow and small recirculating flow at the top-left corner are also observed for the case of linear heating of the left wall with profile $\Theta = 1 - Y$. The corner cell is larger for triangular enclosure. It is also larger than the corner cell observed for

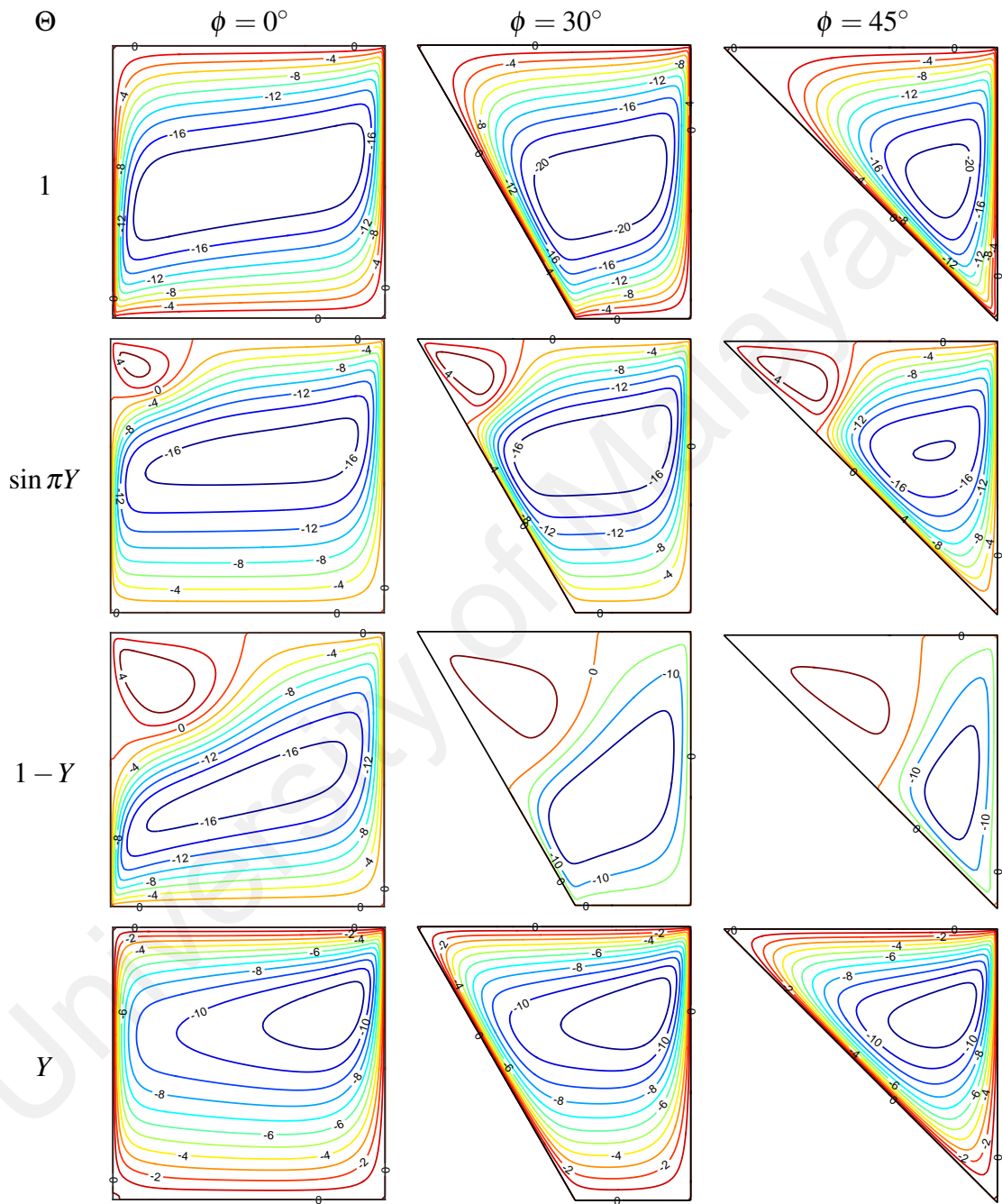


Figure 5.2: Streamlines for various enclosure shapes and thermal boundary conditions at $Ra_D = 10^3$

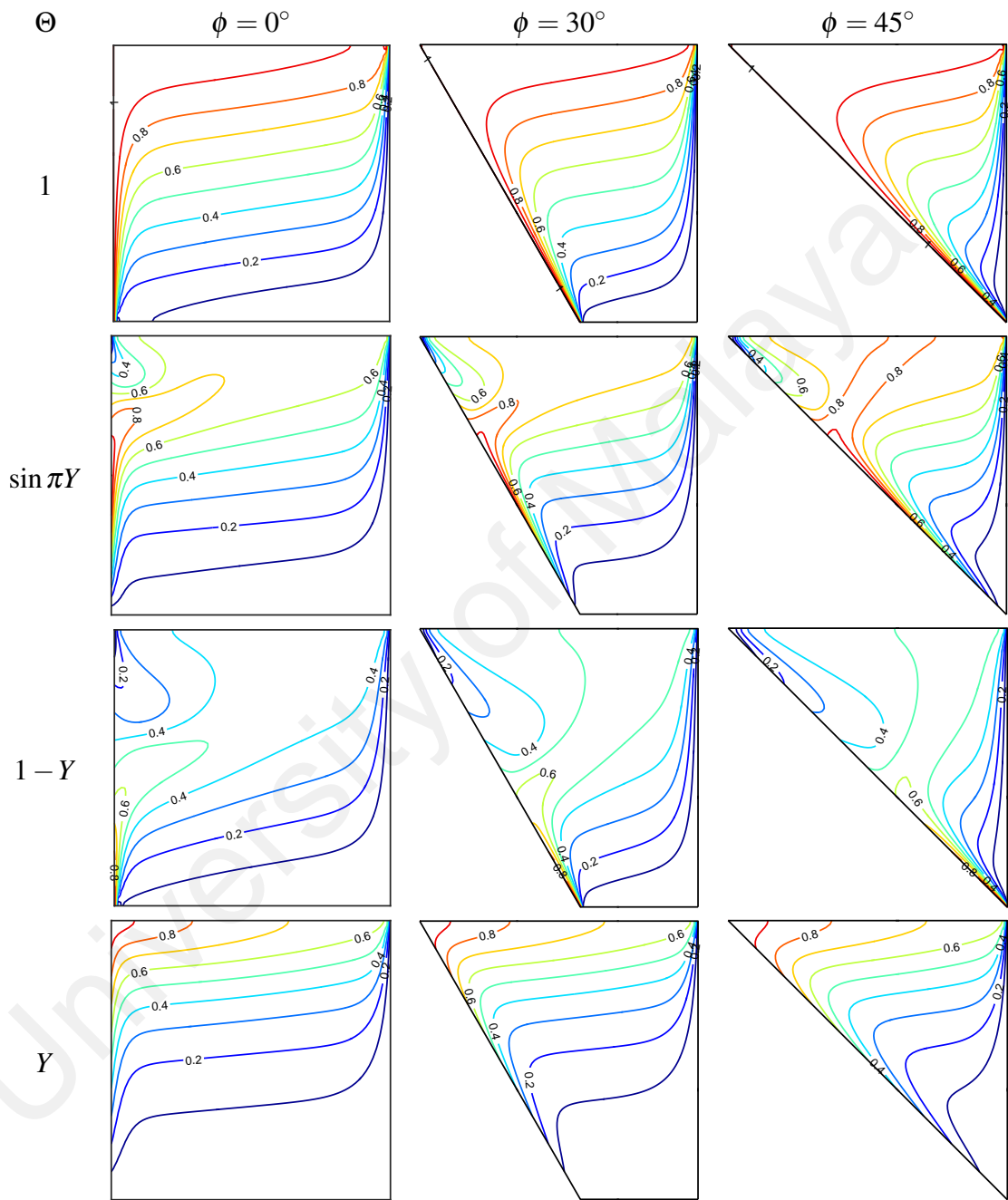


Figure 5.3: Isotherms for various enclosure shapes and thermal boundary conditions at $Ra_D = 10^3$

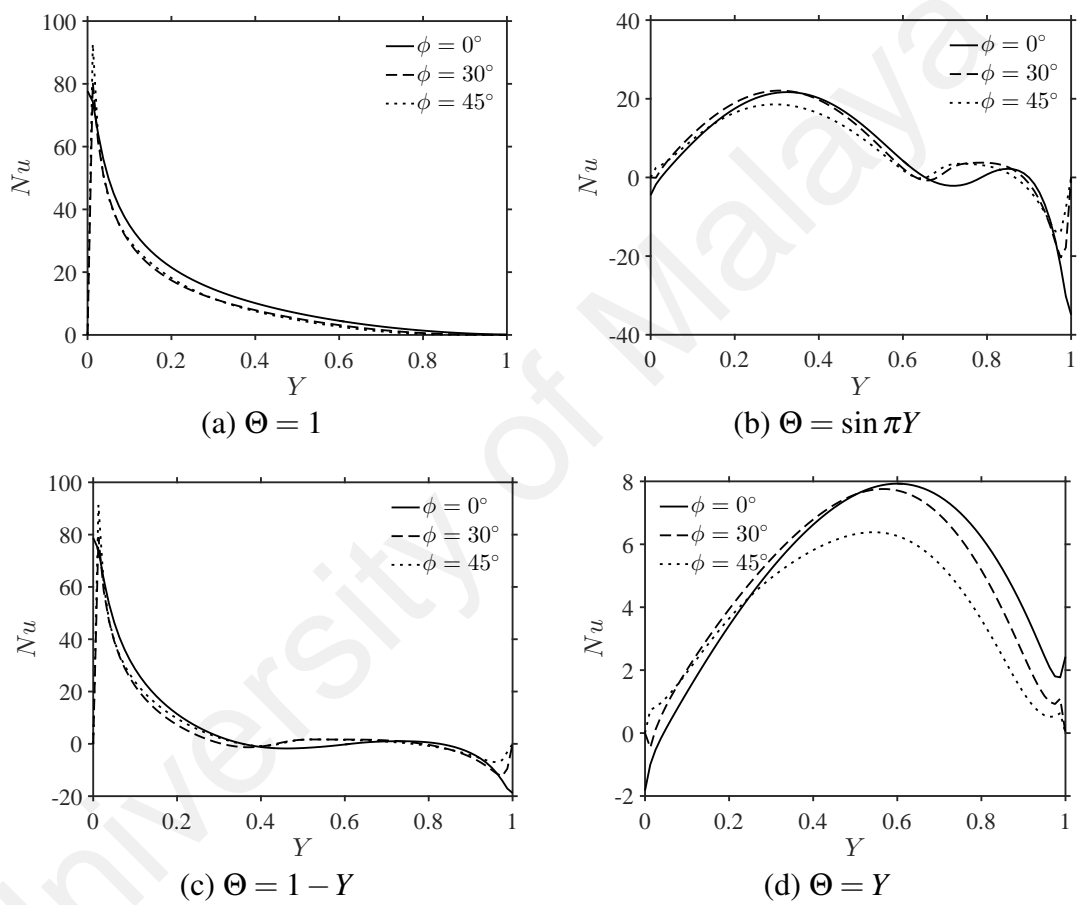


Figure 5.4: Local Nusselt number for various enclosure shapes and thermal boundary conditions at $Ra_D = 10^3$

sinusoidal case; it occupies almost half of the triangular enclosure. The isotherms reveal that the fluid of lower temperature is occupying a larger area in the enclosure with linear heating than that of sinusoidal heating of the left wall and thus the larger the area of fluid is circulating at the top-left corner. For the case of linearly heated ($\Theta = Y$) enclosures, only clockwise rotating main flow is observed. Gradually increasing of temperature along the left wall enhances the buoyancy of fluid and thus it is flowing upward along the wall, and sinks when it is cooled along the right wall. Comparing two types of linear heating, i.e., $\Theta = 1 - Y$ and Y , dual cell structure exists in all enclosures for the case of $\Theta = 1 - Y$ and single cell structure is observed in all enclosures for the latter case ($\Theta = Y$). Also, linear heating ($\Theta = Y$) gives the lowest circulation of flow (stream function value) than that of other temperature profiles.

Figure 5.4 shows the local Nusselt number along the left wall of three different enclosures with various thermal boundary conditions at $Ra_D = 10^3$. The distribution of local Nusselt number along the left wall clearly presents the effect of enclosures shapes and temperature profiles on the local heat transfer along the left wall. In the case of constant heating, the heat transfer rate is exponentially decreasing along the wall. Heat is transferred into the enclosure at the highest rate near the lower left wall and the least heat transfer rate is observed near the top of the left wall. The square enclosure is having the highest local heat transfer rate along the left wall with constant heating. Sinusoidal temperature profile gives wavy form of local heat transfer where highest heat transfer rate can be obtained near the lower half of the left wall and the lowest heat transfer rate is near the bottom and top portion of the left wall. The local Nusselt number for the temperature profile $\Theta = 1 - Y$ is decreasing along the wall and slightly increases near $Y = 0.5$, and further decreases as approaching the top wall. The local Nusselt number for $\Theta = Y$ is increasing along the wall and then decreases near $Y = 0.6$, and square enclosure is having the highest local heat transfer along the upper half of the left wall in this case. It is observed from these figures that the local Nusselt number is affected directly by the imposed temperature boundary conditions.

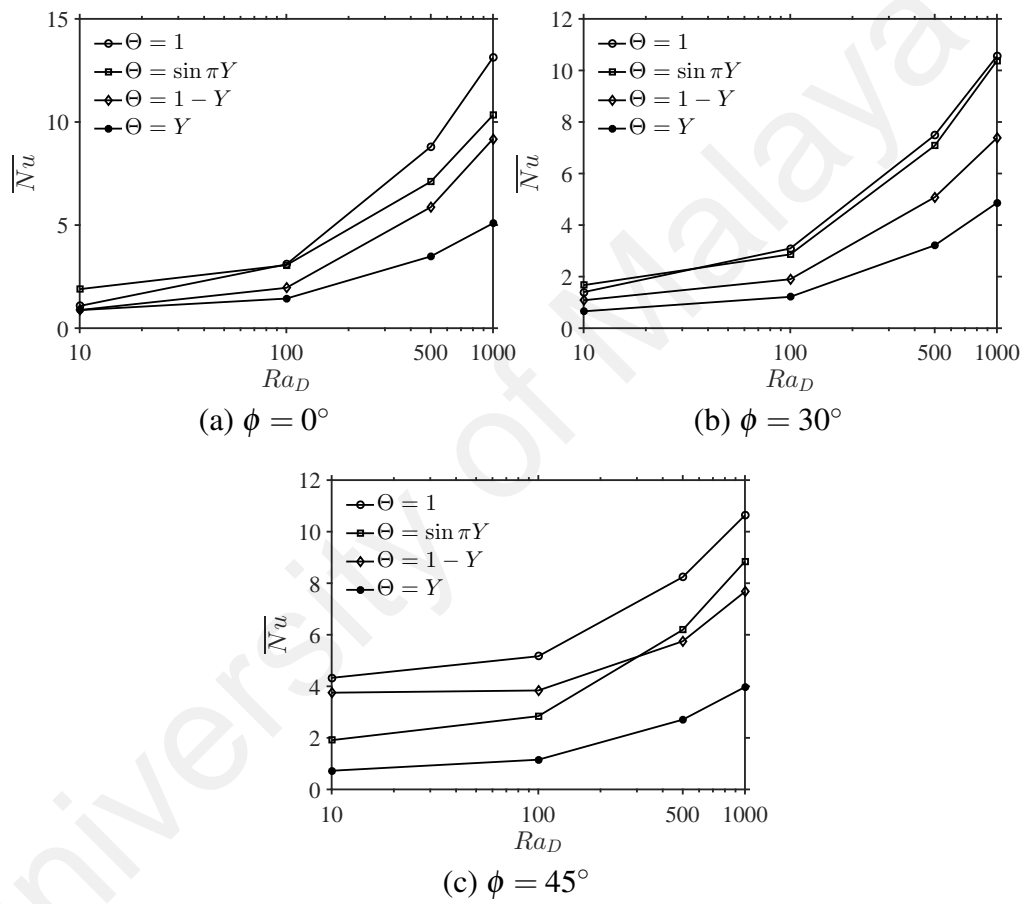


Figure 5.5: Average Nusselt number for various enclosure shapes and thermal boundary conditions

In order to find the effect of various thermal boundary conditions and geometries on the average heat transfer, average Nusselt number (\overline{Nu}) is plotted against Ra_D with different conditions. Figure 5.5 presents the plots of average Nusselt number with different thermal boundary conditions for different enclosure shapes. For square enclosures, sinusoidal profile gives the highest average heat transfer at $Ra_D = 10$ and constant heating gives the highest heat transfer at $Ra_D \geq 10$. The average heat transfer rate of the trapezoidal enclosure is higher at $Ra_D = 10$ in the case of sinusoidal heating while constant heating gives higher heat transfer when $Ra_D > 10$. Constant heating produces highest heat transfer in the triangular enclosure for all Ra_D . Both linear heating give the lowest average heat transfer for all enclosure shapes especially for temperature profile $\Theta = Y$. Comparing the three enclosure shapes, the enhancement of heat transfer rate is obtained in the triangular enclosure at low Darcy-Rayleigh number and in the square enclosure at high Darcy-Rayleigh number.

5.5 Conclusion

Natural convection heat transfer in square, trapezoidal and triangular enclosures filled with fluid-saturated porous medium has been studied numerically using finite difference method. Different temperature profiles, constant, sinusoidal and linear temperatures, which are applied on the left wall, affect the fluid flow and heat transfer in the porous enclosures. Multiple flows can be observed in the case of sinusoidal and linear heating. Constant heating gives the highest heat transfer rate for all enclosure shapes at high values of Darcy-Rayleigh number whereas linear heating produces the lowest heat transfer for all enclosure shapes and Darcy-Rayleigh numbers considered. Comparing the three enclosures, the triangular porous enclosure gives higher heat transfer rate for low values of Darcy-Rayleigh number and the square porous enclosure gives higher heat transfer rate for high values of Darcy-Rayleigh number ($Ra_D \geq 500$).

CHAPTER 6: NATURAL CONVECTION IN AN OBLIQUE POROUS ENCLOSURE WITH SINUSOIDAL HEATING

6.1 Introduction

Square enclosure is typical for most heat transfer related systems, but what happen if the enclosure undergoes deformation such that now it becomes skewed? There are some studies available for convection process inside the oblique porous enclosure. However, there is no report available on sinusoidal heating on the inclined wall of the oblique porous enclosure. In this chapter, porous medium with internal heat generation and absorption is taken into consideration as well. Porous medium with heat generation or heat absorption such as packed beds have been commonly used for drying of liquids and gases.

6.2 Problem Statement

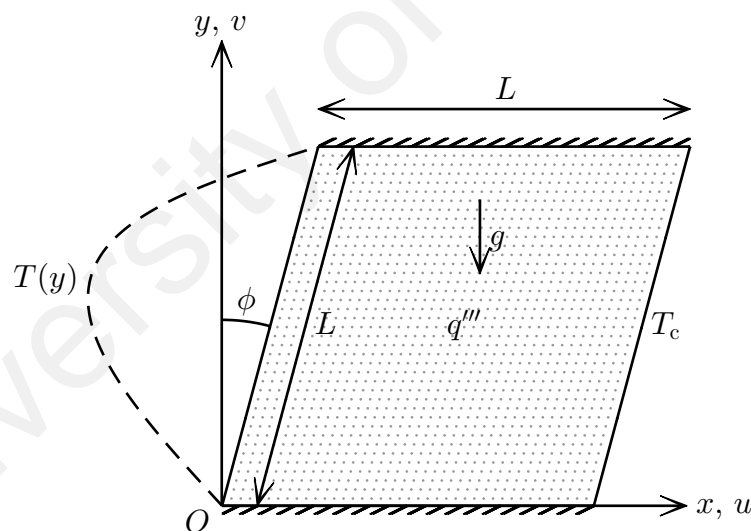


Figure 6.1: Schematic diagram of an oblique porous enclosure

Consider an oblique enclosure of width and height L , in which the vertical walls are inclined at an angle ϕ with respect to the vertical plane as presented in Figure 6.1. The enclosure is filled with fluid-saturated heat-absorbing or heat-generating porous medium and Darcy law is adopted to describe fluid flow in the enclosure. Sinusoidal temperature profile is used for the left wall while the right wall is cooled at a constant temperature T_c . The bottom and top walls are thermally insulated. The velocity components, u and v are taken in the x - and y -directions, respectively. The gravity acts in the negative

y-direction. Boussinesq approximation is valid for density variation. Fluid flow in the enclosure is assumed to be steady and viscous dissipation is negligible. The porous medium is assumed to be homogeneous, isotropic and in thermal equilibrium with the fluid. The governing equations for conservation of mass, momentum and energy are given by equations (4.1) to (4.4) with $\varphi = 0$. Also, based on the above physical configurations, the boundary conditions are;

$$\begin{aligned}
 & \text{on all solid walls} : u = v = 0, \\
 & \text{on } 0 \leq x \leq L \sin \phi, 0 \leq y \leq L \cos \phi : T = T_c + (T_{\text{ref}} - T_c) \sin \left(\pi \frac{y}{L \cos \phi} \right), \\
 & \text{on } L \leq x \leq L + L \sin \phi, 0 \leq y \leq L \cos \phi : T = T_c, \\
 & \text{on } y = 0, 0 \leq x \leq L \text{ and } y = L \cos \phi, \\
 & \quad L \sin \phi \leq x \leq L + L \sin \phi : \frac{\partial T}{\partial y} = 0,
 \end{aligned} \tag{6.1}$$

where T_{ref} is a reference temperature on the left wall that is higher than T_c .

Apply dimensionless variables (3.40) to the governing equations and boundary conditions, the dimensionless governing equations are equations (3.41) and (3.42) with $\varphi = 0$, and the corresponding boundary conditions are;

$$\begin{aligned}
 & \text{on all solid walls} : \Psi = 0, \\
 & \text{on } 0 \leq X \leq \sin \phi, 0 \leq Y \leq \cos \phi : \Theta = \sin \left(\pi \frac{Y}{\cos \phi} \right), \\
 & \text{on } 1 \leq X \leq 1 + \sin \phi, 0 \leq Y \leq \cos \phi : \Theta = 0, \\
 & \text{on } Y = 0, 0 \leq X \leq 1 \\
 & \text{and } Y = 1, \sin \phi \leq X \leq 1 + \sin \phi : \frac{\partial \Theta}{\partial Y} = 0.
 \end{aligned} \tag{6.2}$$

The dimensionless heat transfer rate along the sidewall is defined by the Nusselt number in equations (3.45) and (3.46).

6.3 Solution Approach

Grid generation method is employed to transform the non-rectangular physical domain (X,Y) to a rectangular computational domain (ξ,η) . The algebraic relations,

$$\xi = X - Y \tan \phi, \quad \eta = \frac{Y}{\cos \phi}, \quad (6.3)$$

will transform the oblique physical domain to a square computational domain.

Equations (3.66) and (3.67) are the transformed governing equations and the corresponding boundary conditions are;

$$\begin{aligned} \text{on all solid walls} & : \Psi = 0, \\ \text{on } \xi = 0, \quad 0 \leq \eta \leq 1 & : \Theta = \sin \pi \eta, \\ \text{on } \xi = 1, \quad 0 \leq \eta \leq 1 & : \Theta = 0, \\ \text{on } \eta = 0 \text{ and } 1, \quad 0 \leq \xi \leq 1 & : \xi_Y \frac{\partial \Theta}{\partial \xi} + \eta_Y \frac{\partial \Theta}{\partial \eta} = 0. \end{aligned} \quad (6.4)$$

The Nusselt numbers are calculated using equations (3.69) and (3.70).

Finite difference approximations are used to discretize the transformed governing equations (3.66) and (3.67) and boundary conditions (6.4). SUR method is used to solve the discretized stream function equation and energy equation coupled with the corresponding boundary conditions. Uniform grids in the ξ - and η -directions are used in all computations, in which 100×100 grids are sufficient to perform as good as finer meshes. An iterative process is taken to solve for each variable from the set of discretized equations. A converged solution is obtained with the numerical procedure discussed in Chapter 3.

6.4 Results and Discussion

Natural convection in an oblique enclosure filled with a fluid-saturating and heat-absorbing or heat-generating porous medium is investigated numerically. The vertical walls of the enclosure is inclined at an angle ϕ from the vertical plane, in which the wall inclination is taken in the range -45° to 45° . Negative walls inclination ($\phi < 0$) gives an oblique enclosure that is slanted to the left while positive walls inclination ($\phi > 0$)

produces the oblique enclosure slanted to the right. Square enclosure is obtained when $\phi = 0$. The heat generation parameter, Q , considered being from -10 to 10 , such that when $Q < 0$, the fluid is heat absorbing and the fluid is heat generating when $Q > 0$. The Darcy-Rayleigh number which determines the importance of convection is taken in the range of 10 to 10^3 .

The effects of walls inclination and internal heat generation parameter are presented in Figures 6.2 and 6.3. Figure 6.2 shows the isotherms for various walls inclination and internal heat generation parameter at $Ra_D = 10^3$. The contours of temperature clearly illustrate the effects of sinusoidal heating on the enclosures. Lower temperature is observed at the bottom and top corners and higher temperature is distributed around the middle section of the left wall. Also, thermal stratification in the center of the enclosures indicates the dominance of convective heat transfer in the enclosures at $Ra_D = 10^3$. The isotherms are clustered at the top right corner of the enclosures, showing the development of thermal boundary layer along the cold wall. When the effect of heat absorption/generation is absent ($Q = 0$), it can be noticed that the temperature distribution in the enclosure varies upon the variation of walls inclination. Fluid along the hot wall is flowing upward due to the reduction of density. When the enclosure is slanted to the left, the inclined hot sidewall is delivering heat in an upward direction, i.e. towards the top wall. The heating direction further aids the reduction of fluid density along the hot wall. Hence, the left-slanted enclosure has a large area of hot fluid near the top wall. On the other hand, the cold sidewall is applying the cooling effect in the downward direction, i.e. towards the bottom wall. Fluid particles lose energy along the cold wall, fluid density increases and thus the fluid flows downward along the cold wall. Hence, there is a large area of cold fluid near the bottom of the enclosure. When the enclosure is slanted to the right, the hot wall provides heat in downward direction whereas the cold wall is cooling the enclosure in an upward direction. Since sinusoidal heating of sidewall has low temperatures at the bottom and top corners, the presence of cold fluid at the top corner limits the hot fluid flows near to the top corner. Hence, the area of hot fluid is smaller for the right-slanted enclosure as compared to the left-slanted enclosure.

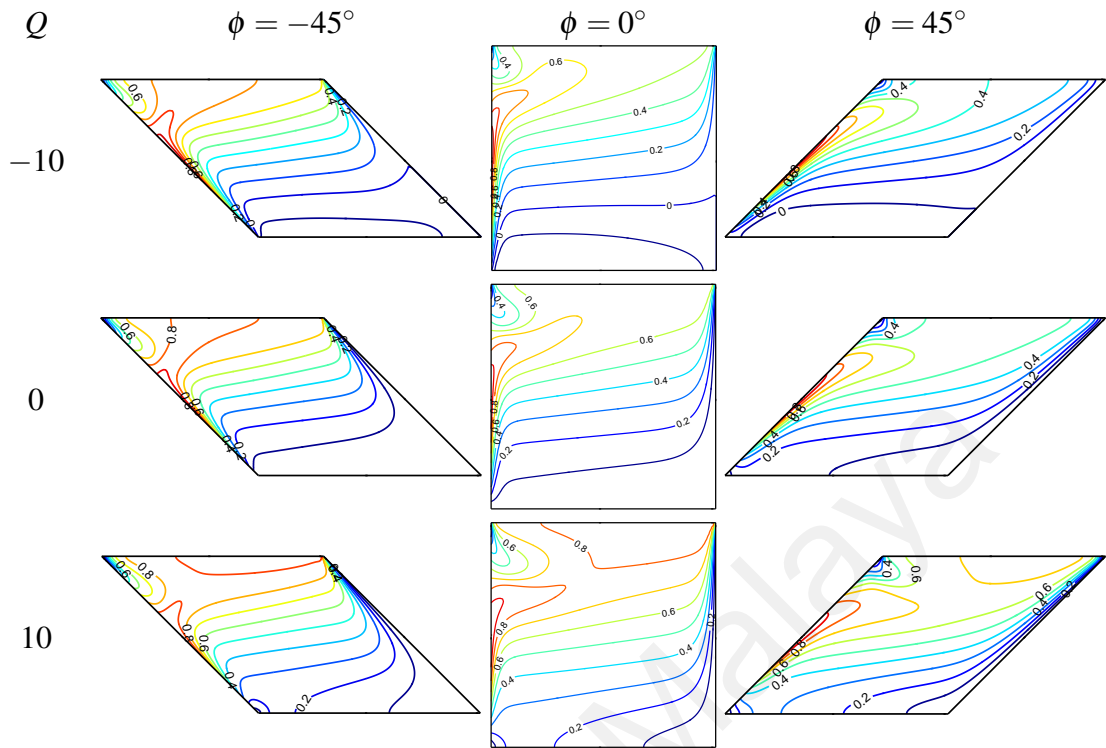


Figure 6.2: Isotherms for various walls inclination at $Ra_D = 10^3$

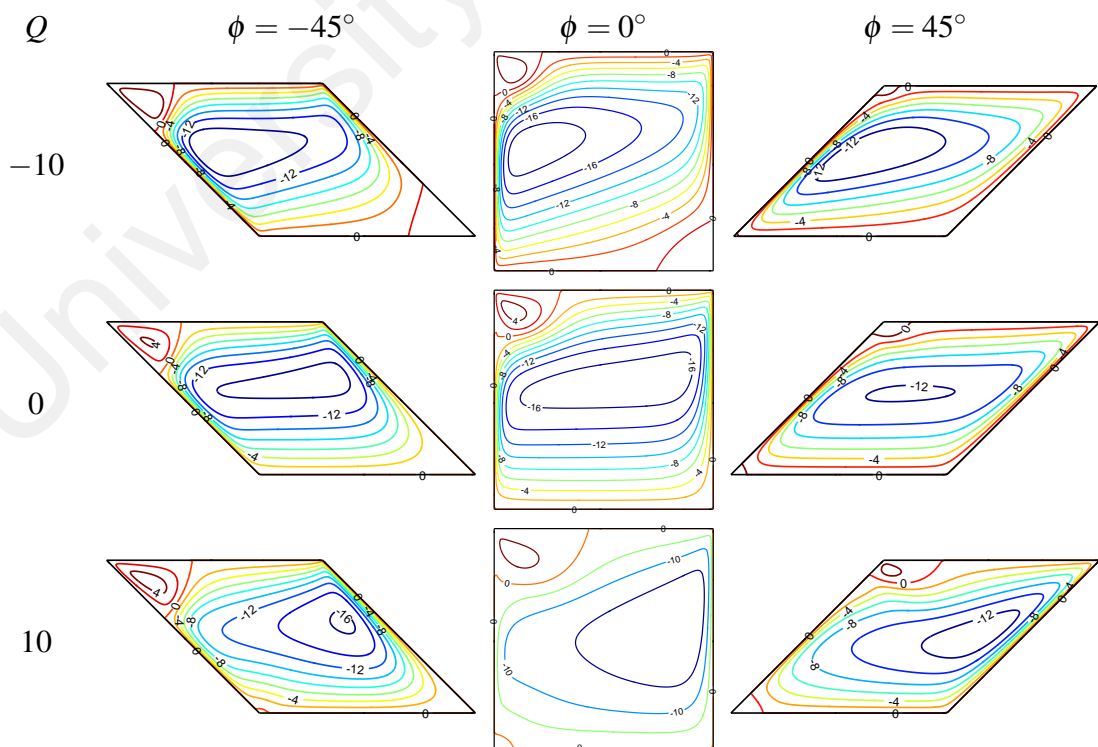


Figure 6.3: Streamlines for various walls inclination at $Ra_D = 10^3$

Figures 6.2 and 6.3 also present the effects of heat absorption and heat generation on the enclosures of different walls inclination. When the fluid in the enclosure is heat absorbing ($Q = -10$), the fluid in the enclosure is of lower temperature than the heat sources of the enclosure. Thus, there exists an area of cold fluid at the lower section of the enclosure that is lower temperature than the cold wall. The area of cold fluid is increasing in size as the walls inclination of the enclosure varies from left-slanted to right-slanted. When the effect of heat generation ($Q = 10$) is considered, the fluid itself is heat generating. Since the hot fluid is less dense in the enclosure, it can be observed that an area of hot fluid is present at the upper section of the enclosure, with the area larger than the enclosure without the presence of heat generation ($Q = 0$).

The streamlines in Figure 6.3 show the effects of walls inclination and heat generation parameter on the fluid flow in the enclosure. When the effect of heat absorption/generation is not considered ($Q = 0$), fluid flow in the enclosure consists of a clockwise flow that occupies most region of the enclosure and a secondary flow is circulating at the top left region. The primary vortex is closer to the right wall when the enclosure is left-slanted. It can be observed that the convection strength increases on shifting the enclosure shape from left-slanted to square enclosure, then the circulation strength decreases when the enclosure becomes right-slanted. On increasing of the walls inclination, the secondary flow at the top left corner is gradually reducing in size. The right-slanted enclosure is having another secondary flow at the lower left corner of the enclosure.

In addition of heat-absorbing substance inside the porous enclosure ($Q = -10$), fluid flow in the enclosure is governed by a main cell in the clockwise direction and secondary flows are present at the top-left and bottom-right corners of the enclosure. The main vortex is closer to the left wall, revealing the formation of momentum boundary layer along the left wall when the fluid in the enclosure is heat absorbing. It also can be noticed that the secondary flow at the bottom-right corner gradually vanishes when the inclination of the walls changes from left-slanted to right-slanted. In the presence of internal heat generation ($Q = 10$), there exists a clockwise circulating flow that occupies most region of the enclosure and secondary eddies at the top-left and bottom-left corners of the enclosure as presented in Figure 6.3. The primary vortex moves closer to the right wall, indicates

the formation of momentum boundary layer along the right wall. Thermal boundary layer also presences along the right wall as shown in Figure 6.2. This shows that heat exchange rate is high along the right wall. On increasing of the walls inclination, the secondary flow at the top-left corner is gradually reducing in size, but the secondary flow at the bottom-left corner is slightly increasing in size.

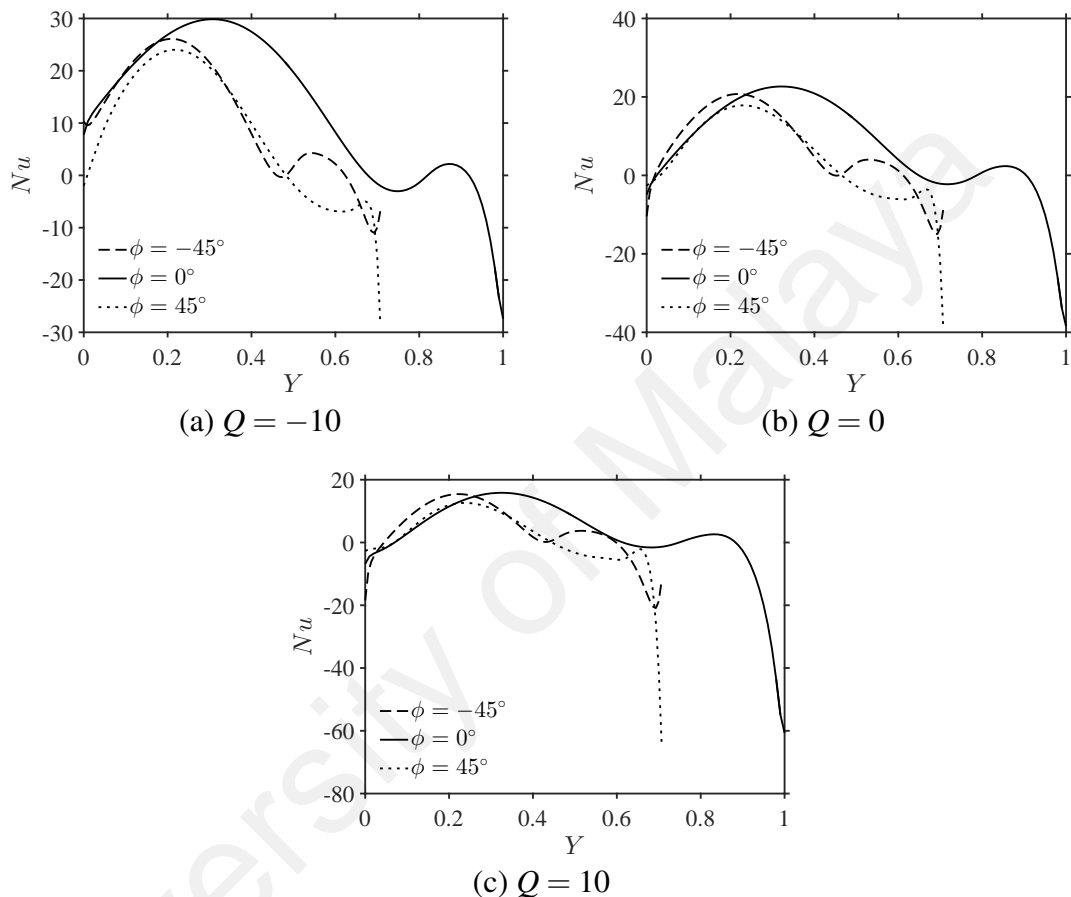


Figure 6.4: Local Nusselt number for various internal heat generation parameters at $Ra_D = 10^3$

The distributions of local heat transfer rate along the left wall are depicted in Figure 6.4 for various walls inclination and internal heat generation parameters at $Ra_D = 10^3$. The distributions of local heat transfer rate clearly exemplify the effect of sinusoidal temperature on the heat transfer along the left wall. The variation of walls inclination affects the range of local heat transfer rate along the wall, where the right-slanted enclosure shows lower heat transfer rate along the wall as compared to the left-slanted and square enclosures. The internal heat generation parameter also affects the distribution of local heat transfer rate. When the enclosure is filled with heat-absorbing porous medium, the overall local heat transfer rates are higher as compared to the enclosure with $Q = 0$.

The square enclosure is having higher heat transfer rate at the lower section of the heated wall as compared to the left-slanted and right-slanted enclosures when the enclosure is heat absorbing. Enclosures with the presence of heat-generating porous medium are having high rate of heat transfer out of the enclosures with negative values of heat transfer rate, especially near the edges of the heated wall.

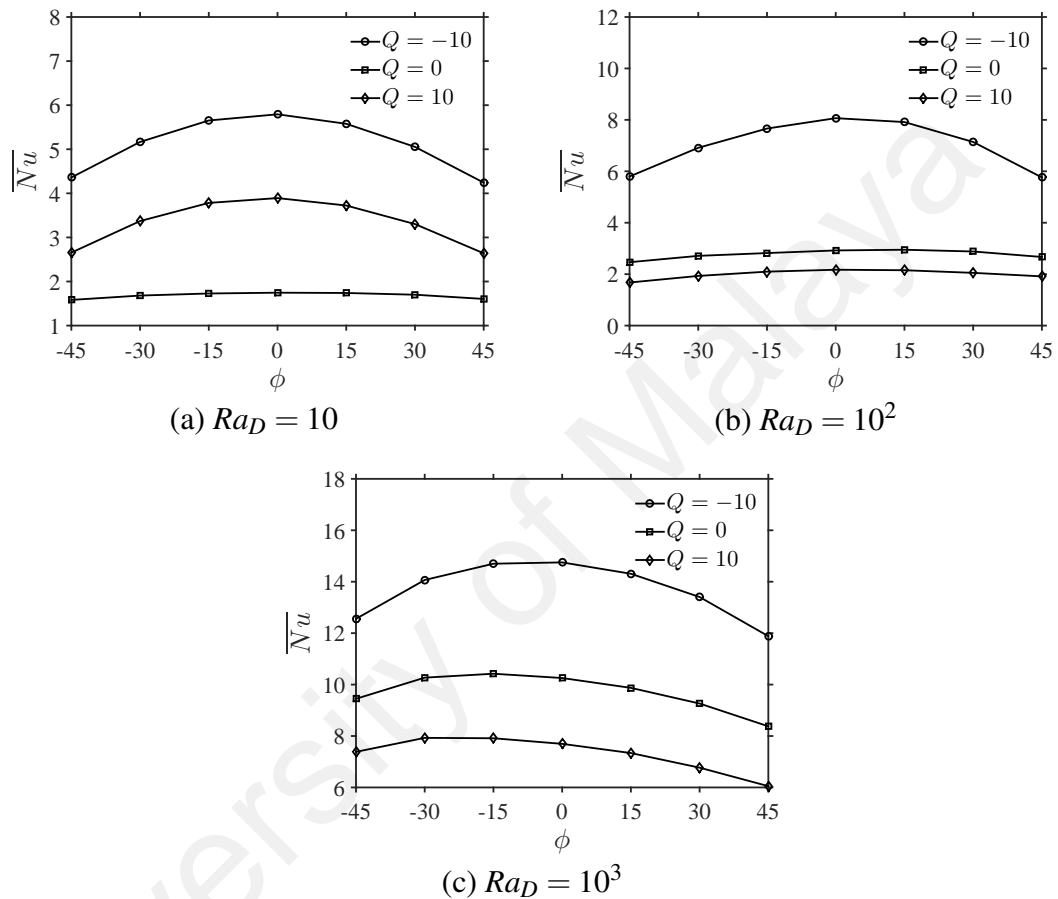


Figure 6.5: Average Nusselt number at various Darcy-Rayleigh numbers

The average heat transfer rate dissipated from the heated wall is measured by the average Nusselt number as presented in Figure 6.5 for various walls inclination, internal heat generation parameter and Darcy-Rayleigh number. The average Nusselt number is an increasing function of Darcy-Rayleigh number for all walls inclination and internal heat generation parameter considered. Also, the raise of internal heat generation parameter decreases the average Nusselt number. For $Ra_D = 10$, the variation of average Nusselt number with the walls inclination is symmetrical at $\phi = 0^\circ$, where the average Nusselt number increases when the enclosure changes from left-slanted to square, attains maximum value for the square enclosure, and then it decreases as the enclosure begins

to become right-slanted. The slightly right-slanted enclosure produces higher average Nusselt number when $Q > 0$ at $Ra_D = 10^2$. At $Ra_D = 10^3$, the left-slanted enclosure with $\phi = -15^\circ$ has the highest average Nusselt number and $\phi = 45^\circ$ gives the lowest average Nusselt number for all internal heat generation parameter considered.

6.5 Conclusion

The main aim of the present numerical study is to investigate the effect of walls inclination on natural convective flow and heat transfer in an oblique porous enclosure in the presence of internal heat generation/absorption. Sinusoidal heating is applied on the inclined left sidewall while the inclined right sidewall is maintained at a lower constant temperature. From the results presented, it can be concluded that the walls inclination of the oblique enclosure affects the fluid flow and heat transfer rate across the enclosure. The average Nusselt number increases on increasing of Darcy-Rayleigh number, but decreases when the internal heat generation parameter is increasing. The square enclosure gives the highest heat transfer rate for all internal heat generation parameter considered at $Ra_D = 10$. At $Ra_D = 10^2$ and 10^3 , the right-slanted and left-slanted walls inclination respectively, enhances the heat transfer rate into the enclosure as compared to a square enclosure.

CHAPTER 7: NATURAL CONVECTION IN AN OBLIQUE POROUS ENCLOSURE WITH LOCALIZED HEATING

7.1 Introduction

In previous chapter, oblique porous enclosure is introduced. Most literatures have considered Rayleigh-Benard heating on the oblique porous enclosure, that is, constant heating is applied on the bottom wall with constant cooling on the top wall of the oblique porous enclosure. The present study considers localized heating on the bottom wall of the oblique porous enclosure. Localized heating is common in countries with cold climate, where a heater is placed on a wall with the remaining portion of the wall is insulated or cooled.

7.2 Problem Statement

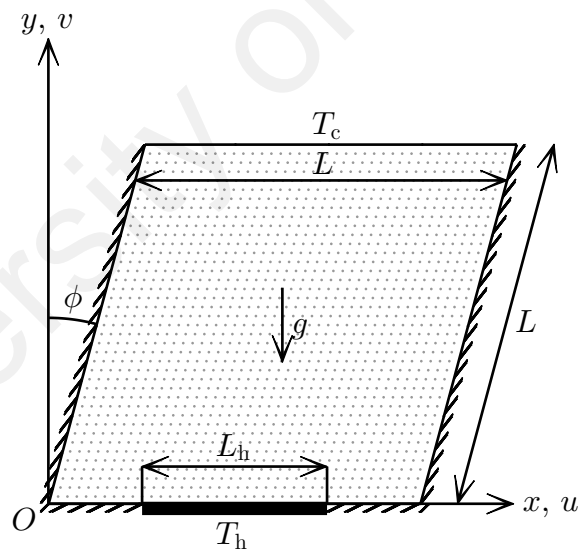


Figure 7.1: Schematic diagram of an oblique porous enclosure with localized heating

Figure 7.1 illustrates the Cartesian coordinate system with schematic diagram of the model proposed in the present study. A two-dimensional enclosure of height and width L with vertical walls are inclined at an angle ϕ from the vertical y -axis is considered. The velocity components, u and v are in the direction of the x - and y -axes, respectively and the gravitational acceleration is acting in the vertical downward direction. A fixed length of heater (L_h) with higher temperature T_h is placed at the bottom wall while the top

wall is cooled at a constant temperature T_c . With $L/2$ of heater length, the enclosure is heated discretely at three different positions (P_h) of the bottom wall, that is, left heating ($P_h = L/2$), middle heating ($P_h = L/2$) and right heating ($P_h = 3L/4$). Also, four different heater lengths ($L/4$, $L/2$, $3L/4$ and L) are considered when the heater is placed at the middle of the bottom wall. Thermal insulation is applied on the remaining non-heated portion of the bottom wall, and left and right walls.

The enclosure is filled with fluid-saturated porous medium. The fluid in the enclosure is incompressible and Newtonian. Also, the fluid is of constant properties and density variation is negligible except with the buoyancy. That is, Boussinesq approximation is valid for the body force acting on the system, in which the buoyancy force resulting from the density variation with temperature. The fluid flow is assumed to be laminar, steady and viscous dissipation is negligible. The porous medium is assumed to be homogeneous, isotropic and in thermal equilibrium with the fluid. Hence, Darcy model is used for fluid flow through the porous medium. By the laws of conservation for mass, momentum and energy, the governing equations are given by equations (4.1) to (4.4) with $\phi = 0^\circ$. Also, the boundary conditions of the model proposed are;

$$\begin{aligned}
 & \text{on all solid walls} : u = v = 0, \\
 & \text{on } \left(P_h - \frac{L_h}{2}\right) \leq x \leq \left(P_h + \frac{L_h}{2}\right), \quad y = 0 : T = T_h, \\
 & \text{on } L \sin \phi \leq x \leq L + L \sin \phi, \quad y = L \cos \phi : T = T_c, \quad (7.1) \\
 & \text{on } 0 \leq x \leq L \sin \phi \text{ and } L \leq x \leq L + L \sin \phi, \quad 0 \leq y \leq L \cos \phi : \frac{\partial T}{\partial n} = 0, \\
 & \text{on } 0 < x < \left(P_h - \frac{L_h}{2}\right) \text{ and } \left(P_h + \frac{L_h}{2}\right) < x < L, \quad y = 0 : \frac{\partial T}{\partial y} = 0,
 \end{aligned}$$

where n is the normal plane of the inclined left and right sidewalls.

The dimensional governing equations and boundary conditions are non-dimensionalized by appropriate dimensionless variables. This approach could reduce the complexity and number of physical quantities in solving the system of partial differential equations. After the substitution with dimensionless variables (3.40), the governing equations are equations (3.41) and (3.42) with $\phi = 0^\circ$, and the boundary

conditions are,

$$\begin{aligned}
& \text{on all solid walls} : \Psi = 0, \\
& \text{on } \left(\frac{P_h}{L} - \frac{L_h}{2L}\right) \leq X \leq \left(\frac{P_h}{L} + \frac{L_h}{2L}\right), \quad Y = 0 : \Theta = 1, \\
& \text{on } \sin \phi \leq X \leq 1 + \sin \phi, \quad Y = \cos \phi : \Theta = 0, \quad (7.2) \\
& \text{on } 0 \leq X \leq \sin \phi \text{ and } 1 \leq X \leq 1 + \sin \phi, \quad 0 \leq Y \leq \cos \phi : \frac{\partial \Theta}{\partial N}, \\
& \text{on } 0 < X < \left(\frac{P_h}{L} - \frac{L_h}{2L}\right) \text{ and } \left(\frac{P_h}{L} + \frac{L_h}{2L}\right) < X < 1, \quad Y = 0 : \frac{\partial \Theta}{\partial Y} = 0
\end{aligned}$$

where $N = n/L$ is the normal plane of the inclined left and right sidewalls.

The heat transfer rate is an important measurement used to determine the effectiveness of a temperature dependent system. The dimensionless heat transfer rate is calculated by the Nusselt number. It provides the ratio of convection to conduction heat transfer rate across a boundary wall. In the present study, the local Nusselt number and average Nusselt number of the heater are defined by equations (3.45) and (3.46) with D is the dimensionless length of the heater.

7.3 Solution Approach

Grid generation method is employed to partition the oblique enclosure for numerical simulations. This approach could map the slanted physical domain into a square computational domain with regular grids. Hence, in this study, the algebraic relations (6.3) will associate the physical domain of the oblique enclosure (X,Y) with a square computational region (ξ,η) . In order to perform calculations in the computational space, transformation on the relevant equations is required to map those equations from the physical domain to the computational domain. So, the transformed governing equations

are equations (3.66) and (3.67), with boundary conditions;

$$\begin{aligned}
& \text{on all solid walls} : \Psi = 0, \\
& \text{on } \left(\frac{P_h}{L} - \frac{L_h}{2L}\right) \leq \xi \leq \left(\frac{P_h}{L} + \frac{L_h}{2L}\right), \eta = 0 : \Theta = 1, \\
& \text{on } 0 \leq \xi \leq 1, \eta = 1 : \Theta = 0, \\
& \text{on } \xi = 0 \text{ and } 1, 0 \leq \eta \leq 1 : \frac{\partial \Theta}{\partial N} = 0, \\
& \text{on } 0 < \xi < \left(\frac{P_h}{L} - \frac{L_h}{2L}\right) \text{ and } \left(\frac{P_h}{L} + \frac{L_h}{2L}\right) < \xi < 1, \eta = 0 : \xi_Y \frac{\partial \Theta}{\partial \xi} + \eta_Y \frac{\partial \Theta}{\partial \eta} = 0,
\end{aligned} \tag{7.3}$$

where,

$$\frac{\partial}{\partial N} = (\xi_X \cos \phi - \xi_Y \sin \phi) \frac{\partial}{\partial \xi} + (\eta_X \cos \phi - \eta_Y \sin \phi) \frac{\partial}{\partial \eta}.$$

The Nusselt numbers in the computational space (ξ, η) are evaluated as given by equations (3.69) and (3.70).

The transformed governing equations (3.66) and (3.67) and corresponding boundary conditions (7.3) are discretised using finite difference approximations. The grids of the computational coordinate system are uniformly spaced in the ξ - and η -directions. The average Nusselt number is used as an assessment to determine a suitable grid size for the simulations. Grid independence tests are carried out for the square ($\phi = 0^\circ$) and slanted ($\phi = -45^\circ$) enclosures in the case of middle heating with $L_h = L/4$ and L at $Ra_D = 10^3$. The meshes considered are in the range of 40×40 to 200×200 and it is observed that 160×160 grids are sufficient for simulations as tabulated in Table 7.1.

Table 7.1: Grid independence test for square and oblique enclosures at $Ra_D = 10^3$

Grid size	Square ($\phi = 0^\circ$)		Oblique ($\phi = -45^\circ$)	
	$L_h = L/4$	$L_h = L$	$L_h = L/4$	$L_h = L$
40×40	17.044	-	19.657	8.648
80×80	23.530	7.824	22.986	8.616
120×120	26.612	7.893	24.849	8.561
160×160	28.533	7.914	26.160	8.518
200×200	29.897	7.922	27.159	8.483

SUR method is used to solve the discretized stream function equation and energy equation along with their respective boundary conditions. An iterative process is taken to solve for dimensionless stream function (Ψ) and temperature (Θ) until the convergence is reached as described by the numerical procedure in Chapter 3.

7.4 Results and Discussion

Natural convection in an oblique porous enclosure with partial heating on the bottom wall has been studied numerically to investigate the effects of sidewalls inclinations, heater lengths and positions on the flow field and heat transfer rate inside the porous enclosure. The enclosure considered is left-slanted, vertical or right-slanted, where the sidewalls inclination from the vertical plane is in the range of $-45^\circ \leq \phi \leq 45^\circ$. A fixed portion of the bottom wall (L_h) is heated at a higher temperature with the remaining portion is thermally insulated. The bottom wall of the enclosure is heated at three different locations, namely, left heating ($P_h = L/4$), middle heating ($P_h = L/2$) and right heating ($P_h = 3L/4$) with heater length of $L_h = L/2$. Also, in the case of middle heating, different heating lengths are considered, which are $L/4$, $L/2$, $3L/4$ and L to study the variation of heater length on the fluid flow and heat transfer of the oblique enclosure. The Darcy-Rayleigh number is taken from 10 to 10^3 to determine natural convective strength inside the porous enclosure.

7.4.1 Effect of Different Heating Locations

Figures 7.2 and 7.3 present the flow field and temperature inside the oblique enclosures with heater length of $L/2$ for three different heating locations on the bottom wall at $Ra_D = 10^3$. The streamlines in Figure 7.2 show that the sidewalls inclination and heating location affect the flow pattern inside the porous enclosure at steady state. When the enclosure is slanted to the left ($\phi = -30^\circ$ and -45°), it is observed that the main flow is circulating in counter-clockwise direction for all heating locations considered. For square enclosure ($\phi = 0^\circ$), left heating on the bottom wall produces clockwise flow whereas right heating gives counter-clockwise flow inside the enclosure. It is noticed that the flow field inside left heating enclosure is the reflection of right heating enclosure along the vertical plane,

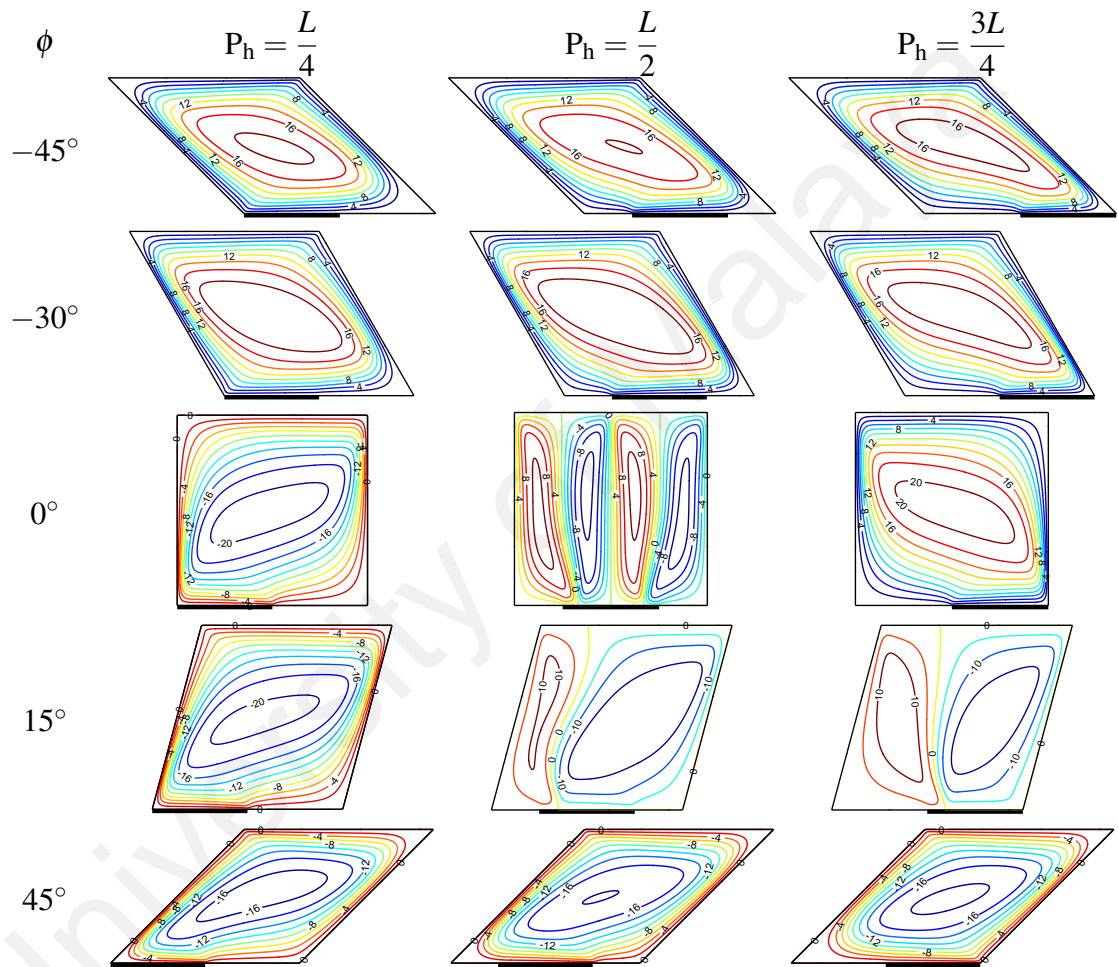


Figure 7.2: Streamlines for enclosure of different wall inclinations and heater positions with $L_h = L/2$ at $Ra_D = 10^3$

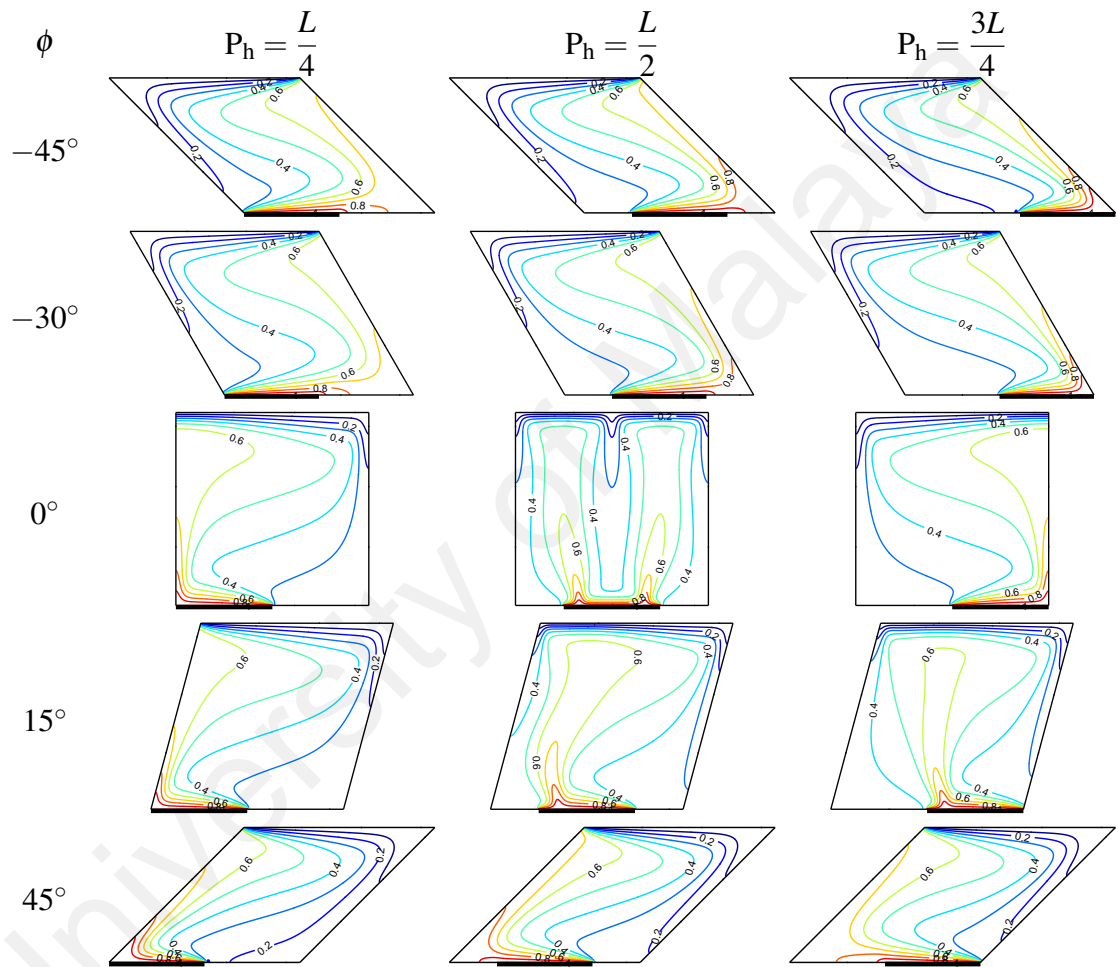


Figure 7.3: Isotherms for enclosure of different wall inclinations and heater positions with $L_h = L/2$ at $Ra_D = 10^3$

and vice versa as well. Also, vertical symmetric flow of opposing direction are observed when the enclosure is heated at middle portion. When the enclosure is slanted to the right ($\phi = 15^\circ$ and 45°), the main cell inside the enclosure is clockwise circulating. Dual cell flow is present in the slightly-right-slanted enclosure ($\phi = 15^\circ$) with middle or right heating. Also, it is observed that the -45° slanted enclosure with left(right) heating is the reflection of the 45° slanted enclosure with right(left) heating, and the same statement is valid for middle heating enclosure. Based on above observation, it can be concluded that, the main cell is flowing in the direction of the inclined sidewalls, i.e. the main flow is counter-clockwise when the enclosure is left-slanted, and vice versa. Also, the presence of secondary flow is depending on the sidewalls inclination and heating location, that is left(right)-slanted enclosure with left(right) heating has secondary flow on the right(left) of the heater.

The isotherms in Figure 7.3 show the temperature distribution inside the enclosure of different sidewalls inclinations and heating locations. Thermal stratification inside the enclosure shows that convection is the dominated mode of heat transfer at $Ra_D = 10^3$, as it is clear to see that the isotherms are extended from the heater to the cold wall, showing heat diffusion inside the enclosure. The clustering of isotherms along the heater and top wall shows the formation of thermal boundary layers, and it also indicates the occurrence of steep temperature gradient in those region. The formation of thermal boundary layer along the heater also co-exists with momentum boundary layer as presented in Figure 7.2. A plume like structure of isotherms is existed inside the enclosure and it is coincide with the formation of multiple flow inside the enclosure as shown in Figure 7.2. The stretching of the plume also shows the direction of main flow, that is, when the plume is slanted to the right(left), the convective cell is flowing in the counter-clockwise(clockwise) direction. When left heating is applied on the right-slanted enclosure, the acute angle between the heater and the adjacent adiabatic sidewall produces an area of hot fluid around the vertex, and fluid is flowing up along the adiabatic inclined sidewall due to the reduction of density. The hot fluid is gradually cooled by the top wall and then it begins to sink along another

sidewall. A small region of cold fluid is gathered along the adiabatic portion of the bottom wall, and the fluid is stagnant around the obtuse vertex of the adiabatic sidewall and bottom wall as illustrated in Figure 7.2.

Figure 7.4 displays the local Nusselt number along the horizontal walls of the oblique enclosure with different wall inclinations and heating locations at $Ra_D = 10^3$. For local heat transfer rate along the heater at the bottom wall of the left-slanted enclosure, it is observed that there is a steep decrease of heat transfer rate at the leading edge of the heater and it is gradually decreasing to minimum along the heater for the three different heating locations considered. The local heat transfer of the left and middle heating enclosure is then increasing sharply near the trailing edge of the heater. The local heat transfer along the top wall of the left-slanted enclosure is gradually increasing and then it hikes near the top-right corner of the enclosure. It is observed that the local heat transfer rate of the square enclosure is symmetrical about the mid-length of the enclosure, that is the heat transfer rate decreases sharply from the left end of the heater to the mid-length of the enclosure, then it increases rapidly to the right end of the heater for middle heating enclosure. Similarly, the local heat transfer rate along the top wall is symmetrical about the mid-length of the enclosure with convex trend along the half left of the top wall. Left heating gives enhanced heat transfer rate along the heater whereas right heating produces reduced heat transfer rate when square enclosure is considered. A reverse trend is observed for the heat transfer rate along the top wall, that is, the local Nusselt number is decreasing with left heating and it is increasing when right heating is applied on the square enclosure. For right-slanted enclosure, it is observed that the local heat transfer rate along the heater and the top wall is the reflection of the left-slanted enclosure, that is, the trend of the right-slanted enclosure with left heating is similar as the reflection of the left-slanted enclosure with right heating.

The variation of average heat transfer rate of the heater with different wall inclinations and heating locations is presented in Figure 7.5 for three different Darcy-Rayleigh numbers. At $Ra_D = 10$, it is observed that the average heat transfer rate for the case of left heating is decreasing for the transition of the enclosure from left-slanted to right-slanted, and it is increasing when right heating is applied. However, in the case of middle heating,

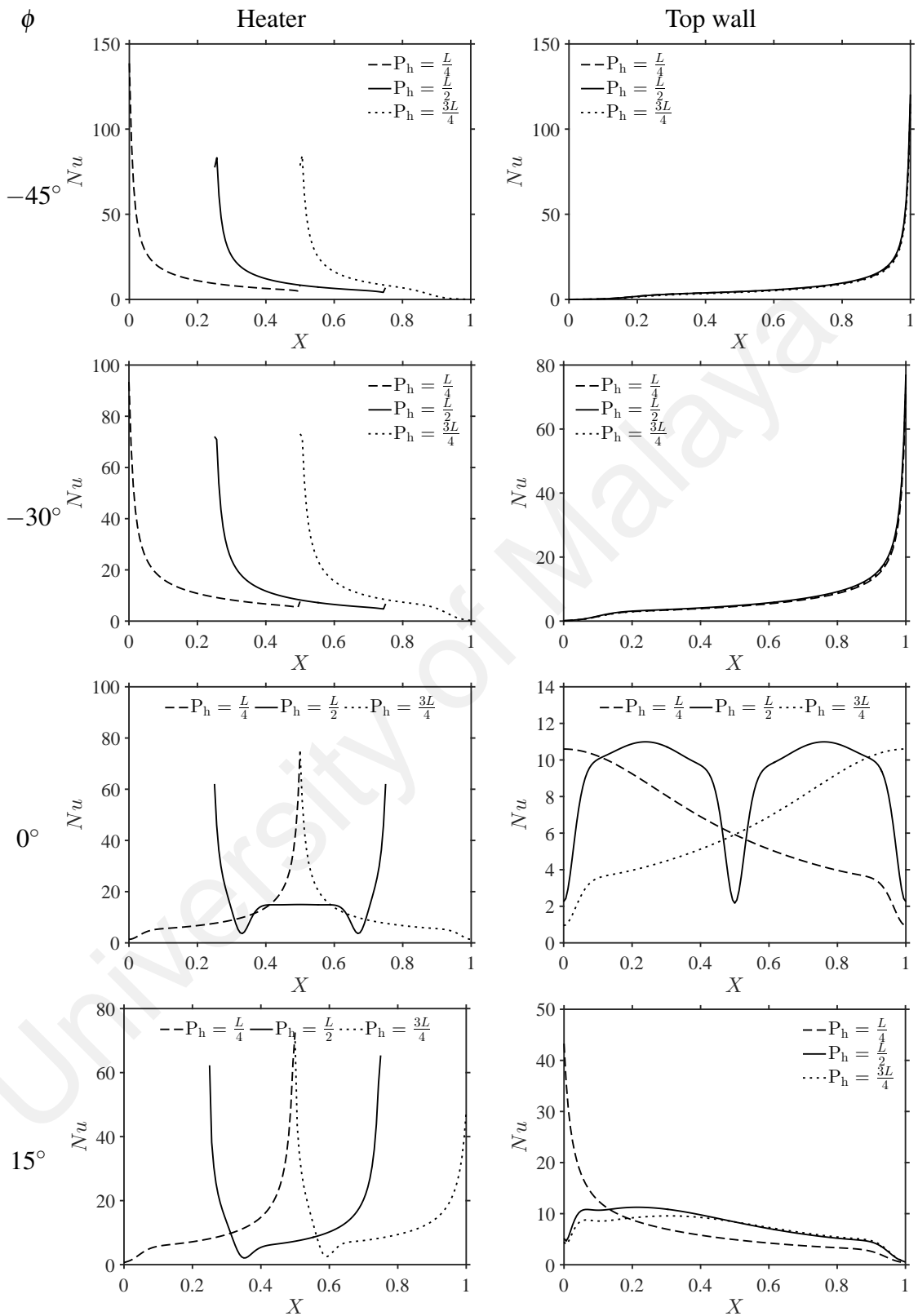


Figure 7.4: Local Nusselt number for different wall inclinations and heater positions with $L_h = L/2$ at $Ra_D = 10^3$

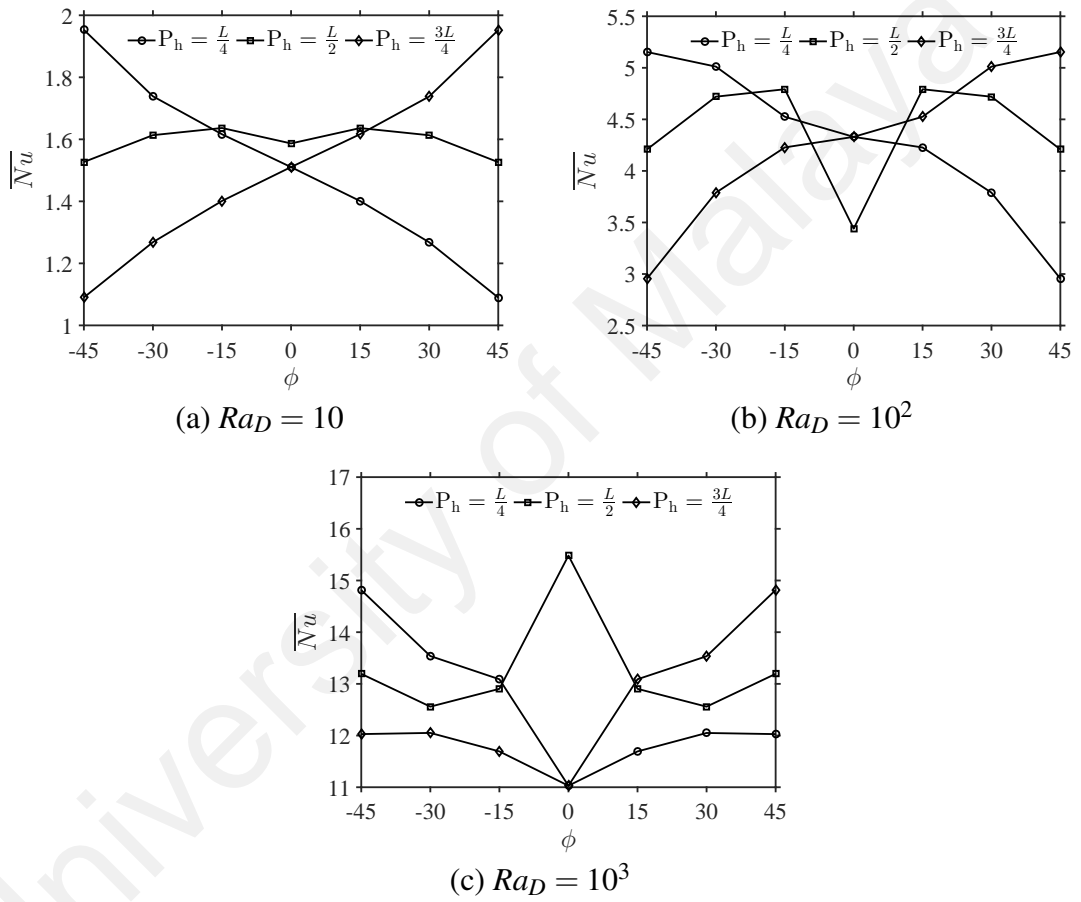


Figure 7.5: Average Nusselt number for different wall inclinations and heater locations with $L/2$ heater length at various Darcy-Rayleigh numbers

the heat transfer rate is increasing to maximum at $\phi = -15^\circ$ for the transition from left-slanted to square, and then it is increasing to maximum again at $\phi = 15^\circ$ from square to right-slanted enclosure. For all Darcy-Rayleigh numbers considered, it is observed that the average heat transfer rate is symmetrical about $\phi = 0^\circ$ (square enclosure) when middle heating is considered, that is, the left- and right-slanted enclosures with the same magnitude of walls inclination are having the same average heat transfer rate along the heater. Also, it can be observed that the left-slanted enclosure with left(right) heating is having the same average Nusselt number as the right-slanted enclosure with right(left) heating. The average Nusselt number increases on the raise of Darcy-Rayleigh number. It is observed in Figure 7.2 that the enclosure with $|\phi| \leq 15^\circ$ is having dual cell structure, that is, the flow separation at a point of the heater produces a plume like structure along the heater (Figure 7.3). The thin thermal boundary layers adjacent to the plume structure indicates steep temperature gradient in the region (Figure 7.4), and thus the higher average heat transfer rate of the heater. Also, it is observed that the square enclosure with left and right heating have similar average heat transfer rate. It is because the left heating enclosure is the reflection of the right heating enclosure along the vertical plane as presented in Figures 7.2 and 7.3, as well as the local heat transfer rate as shown in Figure 7.4. Furthermore, it can be noticed that the left-slanted enclosure with left heating and right-slanted enclosure with right heating are having the highest heat transfer for the two heating locations considered. The square enclosure gives the highest at $Ra_D = 10^3$ due to the presence of dual cell structure.

7.4.2 Effect of Different Heating Lengths

The streamlines and isotherms for the oblique and square enclosures with different heater lengths on the middle of bottom wall are presented in Figures 7.6 and 7.7. Figure 7.6 depicts that the heater length affects the flow pattern inside the middle heating enclosure. It is observed that the left-slanted and right-slanted enclosures are the reflection of each other along the vertical plane regardless of the heater length. When the enclosure is slanted, it is occupied by a main circulating cell. Also, it can be observed that momentum boundary layer is formed along the heater, as the fluid flow is parallel along

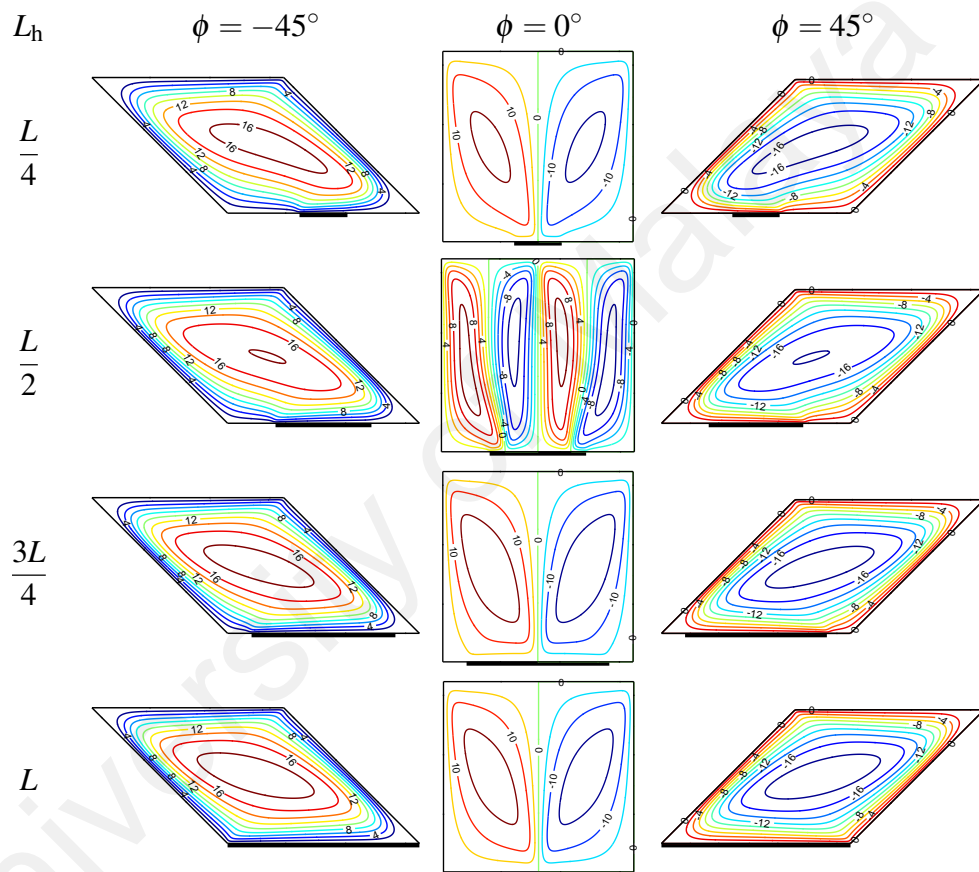


Figure 7.6: Streamlines of middle heating enclosure with different wall inclinations and heater lengths at $Ra_D = 10^3$

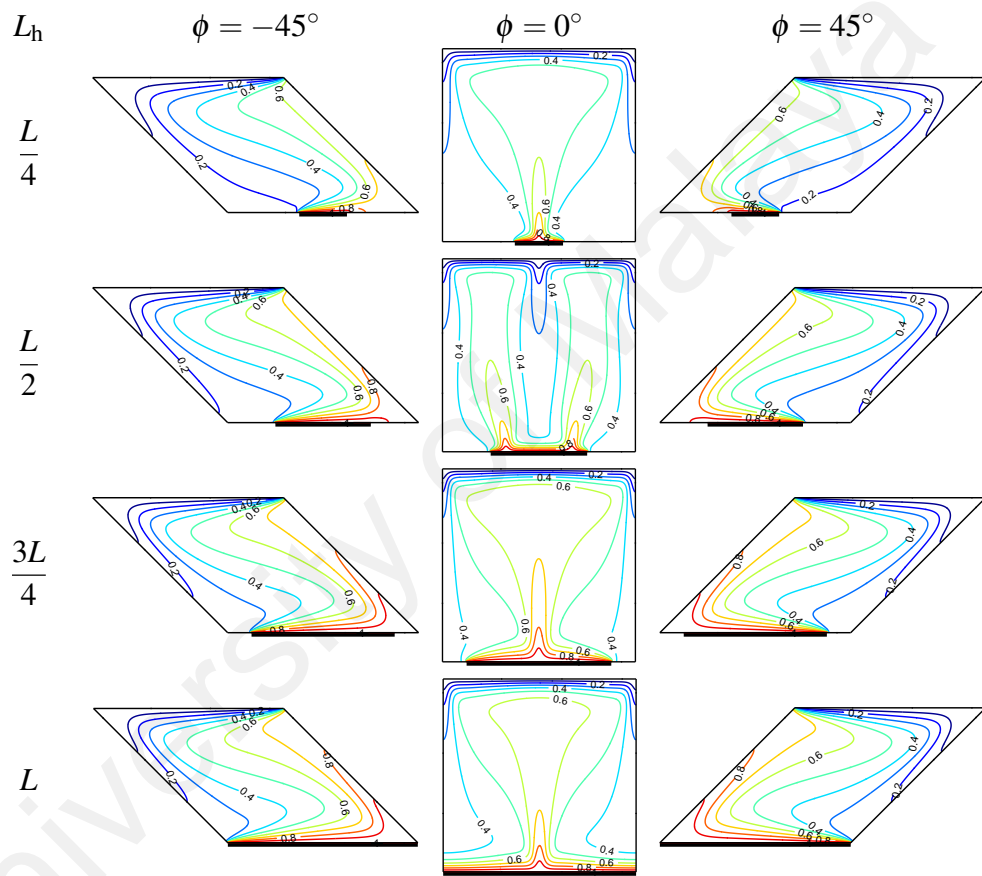


Figure 7.7: Isotherms of middle heating enclosure with different wall inclinations and heater lengths at $Ra_D = 10^3$

the heater, and fluid flow is stagnant at the adiabatic portions of the bottom wall. The strength of circulation of the main core is increasing when the heating length increases. It is because the raise of heating length on the bottom wall increases the thermal active area for heat exchange between the heater and fluid that induces a large area of less dense fluid along the heater. A greater amount of light fluid particles along the heater trigger a more intensive flow inside the enclosure. Middle heating on the square enclosure produces multiple cell structure inside the enclosure. Fluid flow is dual cell when the heating lengths are $L/4$, $3L/4$ and L , and quad cell when $L_h = L/2$ is used. The strength of circulation inside the quad cell enclosure is reduced as compared to dual cell enclosures.

The isotherms in Figure 7.7 shows that the heater length influences the temperature distribution inside the porous enclosure, especially along the bottom and top walls. The formation of thermal boundary layer along the heater is thinner when heating length is shorter. Also, a plume like structure is formed and it is coincide with the formation of multiple cells inside the square enclosure. The plume structure is increasing in size when the heater length is increased. Also, the cold fluid by the sides of the heater is reducing in area as the heater length increases and thus the area of stagnant fluid by the adiabatic portions of the bottom wall is reducing. It is interesting to note that a plume like structure also forms at the top wall of the square enclosure with heater length $L/2$, and hence it produces quad cells inside the enclosure as shown in Figure 7.6.

Figure 7.8 pictures the local Nusselt number along the heater and top wall of the oblique enclosure with middle heating. Again, it can be noticed that the local heat transfer rate along the heater and top wall of the left- and right-slanted enclosures are the reflection of each other along the vertical plane. For left-slanted enclosure with $L_h \leq 3L/4$, the local heat transfer rate is decreasing sharply at the leading edge of the heater, and then slowly decreasing along the heater. However, for $L_h = L$, the local heat transfer rate is decreasing sharply from the left corner and it is gradually reaching zero at the right corner of the bottom wall. The trend of local heat transfer rate for the top wall is similar for all heater lengths considered, that is, it is gradually increasing along the wall and it hikes at the right end of the wall. Also, it is observed that the local heat transfer rate of the top wall is increasing on the raise of heater length. For square enclosure, the local heat transfer

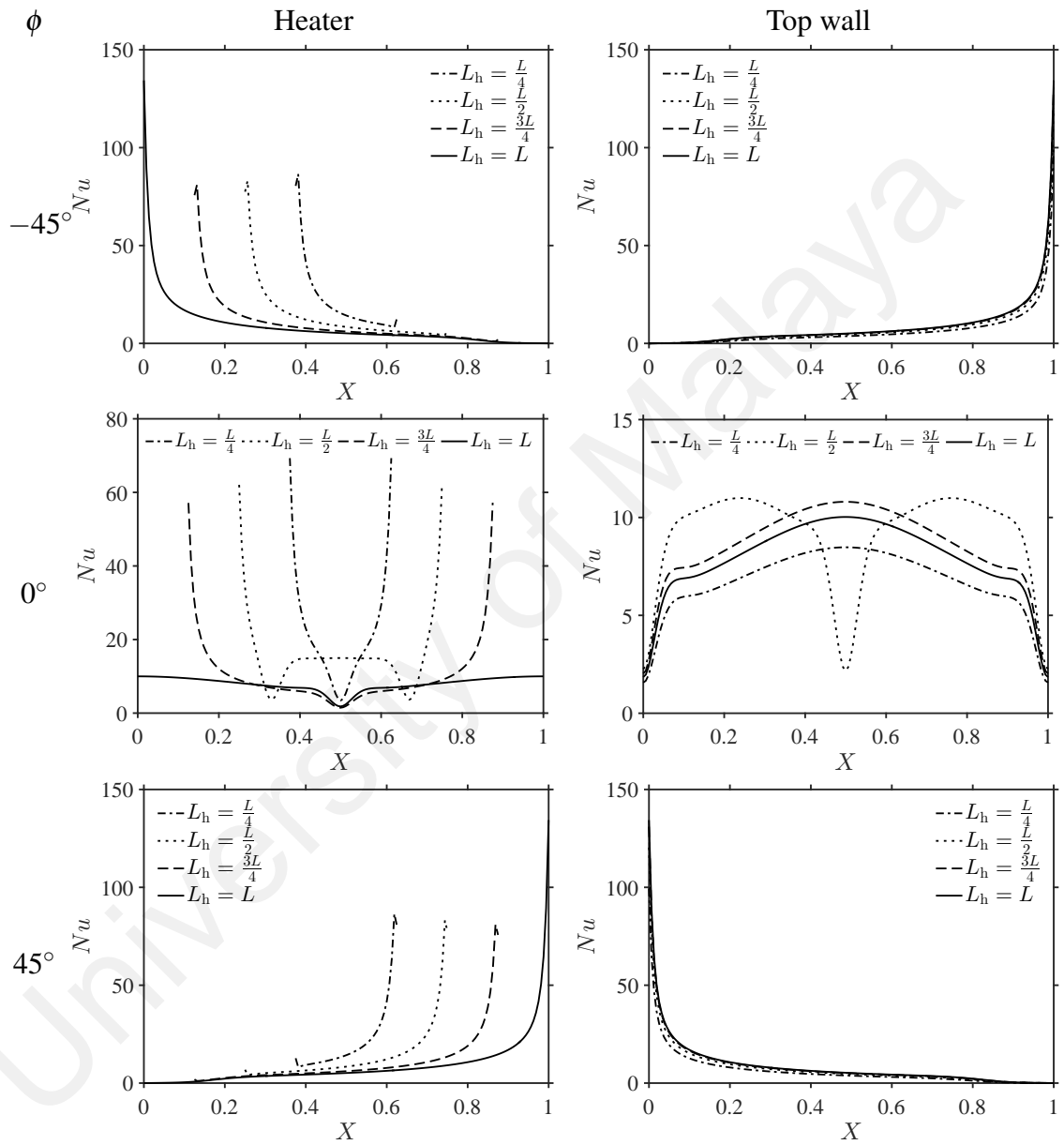


Figure 7.8: Local Nusselt number for middle heating enclosure with different wall inclinations and heater lengths at $Ra_D = 10^3$

rates of the heater and top wall are symmetrical about the mid-length of the enclosure. The range of heat transfer for the heater is decreasing on the increase of heater length. It is observed that the lowest heat transfer rate of a heater is corresponding to the point that the plume structure is appeared as pictured in Figure 7.7.

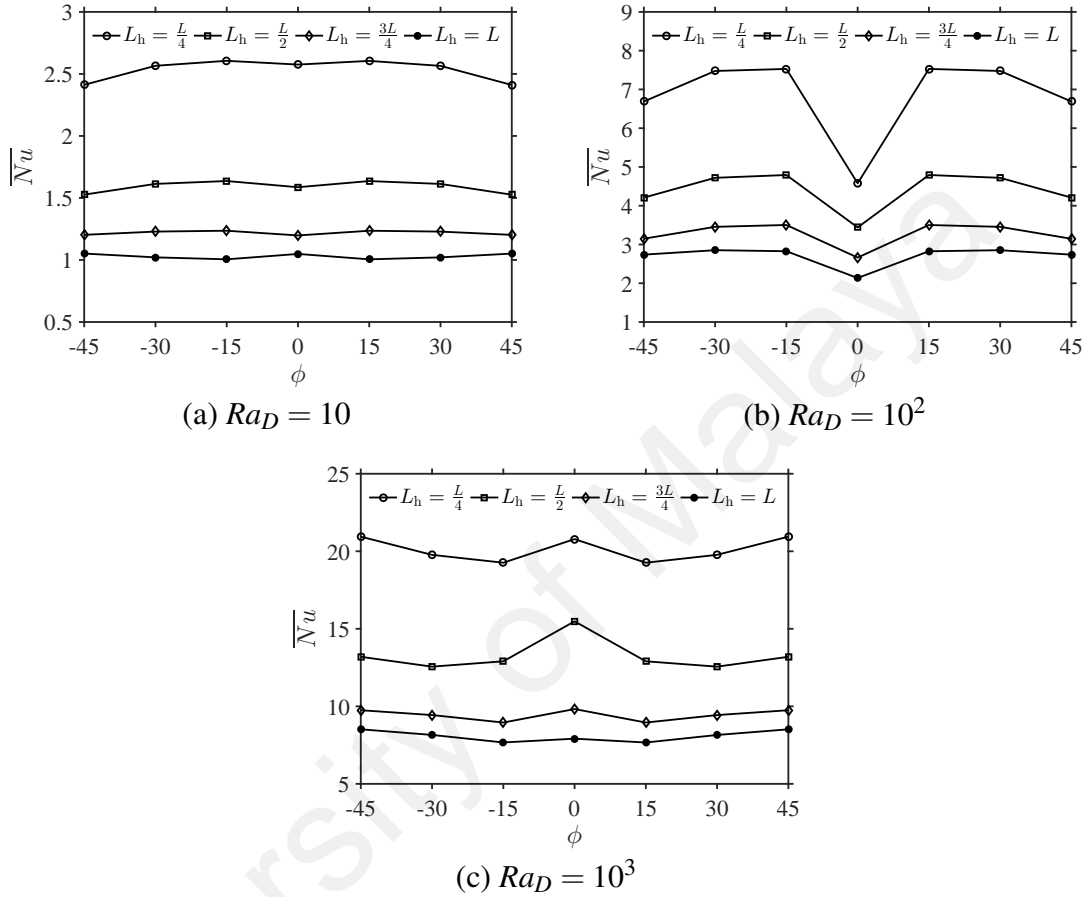


Figure 7.9: Average Nusselt number of the heater for middle heating enclosure with different wall inclinations and heater lengths at various Darcy-Rayleigh numbers

The variation of Nusselt number with the walls inclination for different heater lengths and Darcy-Rayleigh numbers is presented in Figure 7.9. The average heat transfer rate is symmetrical at $\phi = 0^\circ$, that is, the left- and right-slanted enclosures with the same magnitude of walls inclination are going to have the same value of average heat transfer rate in the case of middle heating. The average heat transfer rate of the heater is decreasing with the raise of heater length. For $Ra_D = 10$ and 10^2 , it is observed that the oblique enclosure with $|\phi| = 15^\circ$ is having the highest heat transfer rate whereas square enclosure gives the lowest heat transfer rate. However, at $Ra_D = 10^3$, the square enclosure is giving the highest heat transfer performance when the heater length on the bottom wall is finite, that is $L_h \leq 3L/4$.

7.5 Conclusion

Natural convection in an oblique porous enclosure with partial heating on the bottom wall is investigated numerically. The left-slanted, right-slanted and square enclosures are considered. The bottom wall of the enclosure is heated at three different locations, namely left heating, middle heating and right heating with heating length of $L/2$. Also, different heater lengths are considered in the case of middle heating on the bottom wall. Based on the results obtained, the flow field and temperature distribution inside the enclosure are influenced by walls inclination, heating location and heater length. The flow field and temperature inside the left-slanted enclosure are similar as the vertical reflection of the right-slanted enclosure with the same magnitude of walls inclination. The slanted enclosure has higher heat transfer rate than that of square enclosure. Middle heating with $L_h = L/2$ heater length is producing higher heat transfer rate than left and right heating on the porous enclosure. However, at $Ra_D = 10^3$, the square enclosure is giving the best heat transfer enhancement as compared to the oblique enclosure with different heater lengths. Short heater length also promotes high heat transfer rate in the porous enclosure with middle heating. In view of application, this study suggests that a shorter heating length can increase the heat transfer rate of the solar collector if sunlight intensity is low during daytime.

CHAPTER 8: NATURAL CONVECTION IN A WAVY POROUS ENCLOSURE WITH SINUSOIDAL HEATING

8.1 Introduction

From a careful study on the literature available, most studies reported on convection process inside the wavy enclosure with heating on the wavy wall. There is no study available on cooling of the wavy wall. Hence, the present chapter deals with numerical study on natural convection inside the wavy porous enclosure with sinusoidal heating on vertical left wall and constant cooling on wavy right sidewall. Porous medium with internal heat generation or absorption is taken into as well. Enclosure with wavy surface have greater surface area for heat transfer, hence it may enhance or reduce the overall performance of a heat dependent device.

8.2 Problem Statement

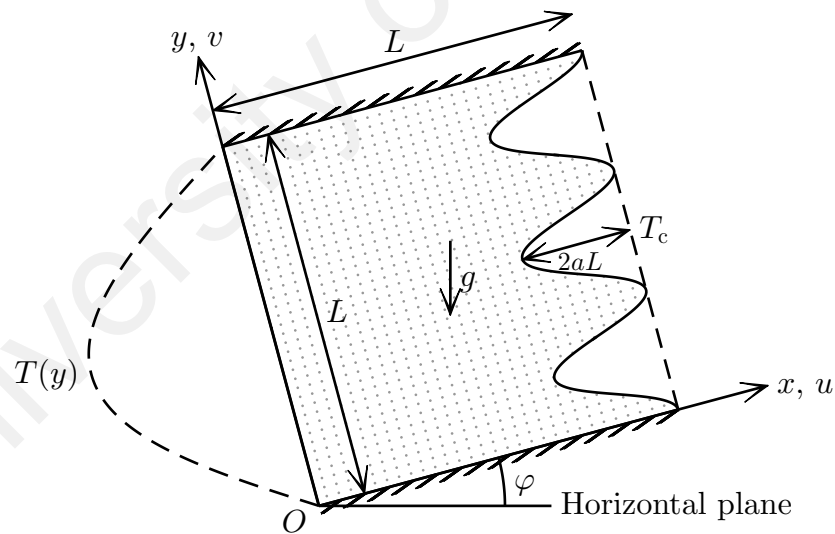


Figure 8.1: Schematic diagram of a wavy porous enclosure

A two-dimensional enclosure of width and height L shown in Figure 8.1 is considered. The right wall of the enclosure is of wavy form, where its waviness is described by amplitude (a) and number of undulations (λ). u and v are the velocity components in the direction of x - and y -axes, respectively. The enclosure inclination (φ) is the inclination angle from the horizontal plane to the bottom wall of the enclosure (x -axis). The gravity (g) acts in the vertically downward direction. The left wall of the enclosure is heated with

sinusoidal temperature profile while the right wall is cooled at a constant temperature T_c . The remaining top and bottom walls are thermally insulated. The fluid in the enclosure is having constant properties, incompressible, Newtonian and density variation is negligible except in the buoyancy term (by Boussinesq approximation). Furthermore, the flow is assumed to be steady and laminar, and viscous dissipation is neglected. The porous medium is assumed to be homogeneous, isotropic and in thermal equilibrium with the fluid. Thus, the fluid flow through the porous medium is described by Darcy model. Porous medium with internal heat generation or heat absorption is also considered in the case of $\phi = 0^\circ$. By the laws of conservation for mass, momentum and energy, the governing equations can be written as given by equations (4.1) to (4.4). The boundary conditions of the wavy porous enclosure are;

$$\begin{aligned}
 & \text{on all solid walls} : u = v = 0, \\
 & \text{on } x = 0, 0 \leq y \leq L : T = T_c + (T_{\text{ref}} - T_c) \sin\left(\pi \frac{y}{L}\right), \\
 & \text{on } x = L - aL \left(1 - \cos\left(2\pi\lambda \frac{y}{L}\right)\right), 0 \leq y \leq L : T = T_c, \\
 & \text{on } y = 0 \text{ and } L, 0 \leq x \leq L : \frac{\partial T}{\partial y} = 0,
 \end{aligned} \tag{8.1}$$

where T_{ref} is a reference temperature. It is the average temperature of sinusoidal temperatures applied on the left wall and it is higher than T_c .

Non-dimensional method is employed to reduce the number of variables involved on solving the governing equations with boundary conditions. Apply dimensionless variables (3.40) on the governing equations and boundary conditions (8.1), we get dimensionless governing equations (3.41) and (3.42), and the boundary conditions are,

$$\begin{aligned}
 & \text{on all solid walls} : \Psi = 0, \\
 & \text{on } X = 0, 0 \leq Y \leq 1 : \Theta = \sin(\pi Y), \\
 & \text{on } X = 1 - a(1 - \cos(2\pi\lambda Y)), 0 \leq Y \leq 1 : \Theta = 0, \\
 & \text{on } Y = 0 \text{ and } 1, 0 \leq X \leq 1 : \frac{\partial \Theta}{\partial Y} = 0.
 \end{aligned} \tag{8.2}$$

The rate of heat transfer across the enclosure can be used to determine the significance and efficiency of the system proposed. The dimensionless heat transfer rate is called the Nusselt number. It shows the ratio of convection to conduction heat transfer across the fluid layer. The local Nusselt number at any point on the sidewall and the average Nusselt number are calculated as given by equations (3.45) and (3.46).

8.3 Solution Approach

We intend to use finite difference method to solve the governing equations with the corresponding boundary conditions. However, the wavy nature of the enclosure gives the challenge to impose the wavy boundary on rectangular grids. Hence, grid generation method is used to map the non-rectangular physical domain to a rectangular computational domain. Transformation on the governing equations and boundary conditions is needed to express the governing equations and boundary conditions in the computational coordinate system proposed. In this study, the following algebraic relations will map the enclosure from physical grid system (X,Y) to a rectangular computational grid system (ξ,η) ;

$$\xi = \frac{X}{1 - a(1 - \cos(2\pi\lambda Y))}, \quad \eta = Y. \quad (8.3)$$

After transformation, the governing equations in the computational coordinate system are equations (3.66) and (3.67). The transformed boundary conditions are;

$$\begin{aligned} \text{on all solid walls} & : \Psi = 0, \\ \text{on } \xi = 0, \quad 0 \leq \eta \leq 1 & : \Theta = \sin(\pi\eta), \\ \text{on } \xi = 1, \quad 0 \leq \eta \leq 1 & : \Theta = 0, \\ \text{on } \eta = 0 \text{ and } 1, \quad 0 \leq \xi \leq 1 & : \xi_Y \frac{\partial \Theta}{\partial \xi} + \eta_Y \frac{\partial \Theta}{\partial \eta} = 0. \end{aligned} \quad (8.4)$$

In computational coordinate system, the Nusselt numbers are evaluated as given by equations (3.69) and (3.70).

Finite difference approximations are used to discretize governing equations (3.66), (3.67) and boundary conditions (8.4). Uniform grids in the ξ - and η -directions are used in all computations. Grid test is performed for the wavy enclosure ($a = 0.25$, $\lambda = 5$) and

square enclosure ($a = 0, \lambda = 0$) at $Ra_D = 10^3$. The test uses grid sizes range from 50×50 to 300×300 , and 150×200 grids provide results as good as the finer meshes as presented in Table 8.1. SUR method is used to solve the stream function equation (3.66) and energy equation (3.67). Ψ and Θ in the set of discretized governing equations and corresponding boundary conditions are solved iteratively until convergence is reached as discussed by the numerical procedure in Chapter 3.

Table 8.1: Grid independency test for wavy and square enclosures with sinusoidal heating

Grid size	\overline{Nu}	
	$a = 0.25, \lambda = 5$	$a = 0.00, \lambda = 0$
50×50	10.210	9.336
80×80	11.137	10.329
100×100	11.453	10.690
120×120	11.669	10.927
150×150	11.890	11.170
150×200	11.933	11.181
150×250	11.957	11.185
250×250	12.247	11.567
300×300	12.337	11.667

8.4 Results and Discussion

Natural convection in a wavy enclosure filled with fluid-saturated porous medium is studied numerically. The waviness of the right sidewall is controlled by the amplitude (a) and number of undulations (λ), in the range of $0 \leq a \leq 0.25$ and $0 \leq \lambda \leq 5$. The Darcy-Rayleigh number (Ra_D), which determines the importance of natural convection, is varied from 10 to 10^3 . The internal heat generation/absorption parameter, Q is taken from -5 to 5. The enclosure inclination (ϕ) is taken into account as well, which varies from 0° (heating from side) to 90° (heating from below) of inclination from the horizontal plane.

8.4.1 Effects of Wall Waviness

Figures 8.2 and 8.3 clearly present the effects of waviness of the right sidewall on natural convection in a wavy enclosure when $\phi = 0^\circ$. The isotherms for different amplitudes and number of undulations are shown in Figure 8.2 with $Ra_D = 10^3$, $\phi = 0^\circ$ and $Q = 0$. The temperature contours exemplify the effect of sinusoidal temperature distribution in the enclosure. The isotherms are clustered along heated wall, especially in the middle part, indicating steep temperature gradients occur in horizontal direction at $Ra_D = 10^3$. The isotherms are also indicated that convection is the dominated mode of heat transfer inside the enclosure. The temperature contours are clustered along the top portion of the cold right wall for the enclosure with one undulation on the wavy right sidewall. On increasing the amplitude of the wavy right wall to 0.15 and 0.25, there exists a thermal boundary layer along the top of the right wall. It shows strong convection heat transfer inside the enclosure. When $\lambda = 3$ and 5, the distribution of temperature contours is following the waviness of the right wall, where thermal boundary layer is formed along the wavy wall, and it gradually vanishes along the wall from top to bottom. Thermal boundary boundary layer along the right wall also vanishes as the amplitude increases from 0.05 to 0.25.

The streamlines for different amplitudes and number of undulations of the right sidewall are shown in Figure 8.3 with $Ra_D = 10^3$, $\phi = 0^\circ$ and $Q = 0$. A single clockwise rotating cell is occupying majority of the enclosure with existence of a small recirculating cell on the top-left corner for all cases of amplitude and number of undulations. For a fixed number of undulations, the core region is decreasing in size as the amplitude of the wavy right wall increases. The increase of amplitude reduces the space in the enclosure and thus the main flow is limited by the shape of the right wall. The flow in the enclosure is also affected by the undulations of the right wall, where the flow near the right wall is of wavy form. With higher amplitude and number of undulations, it can be observed that the flow velocity is very low in the hulls of the wavy wall as depicted in the case of $a = 0.25$, $\lambda = 5$.

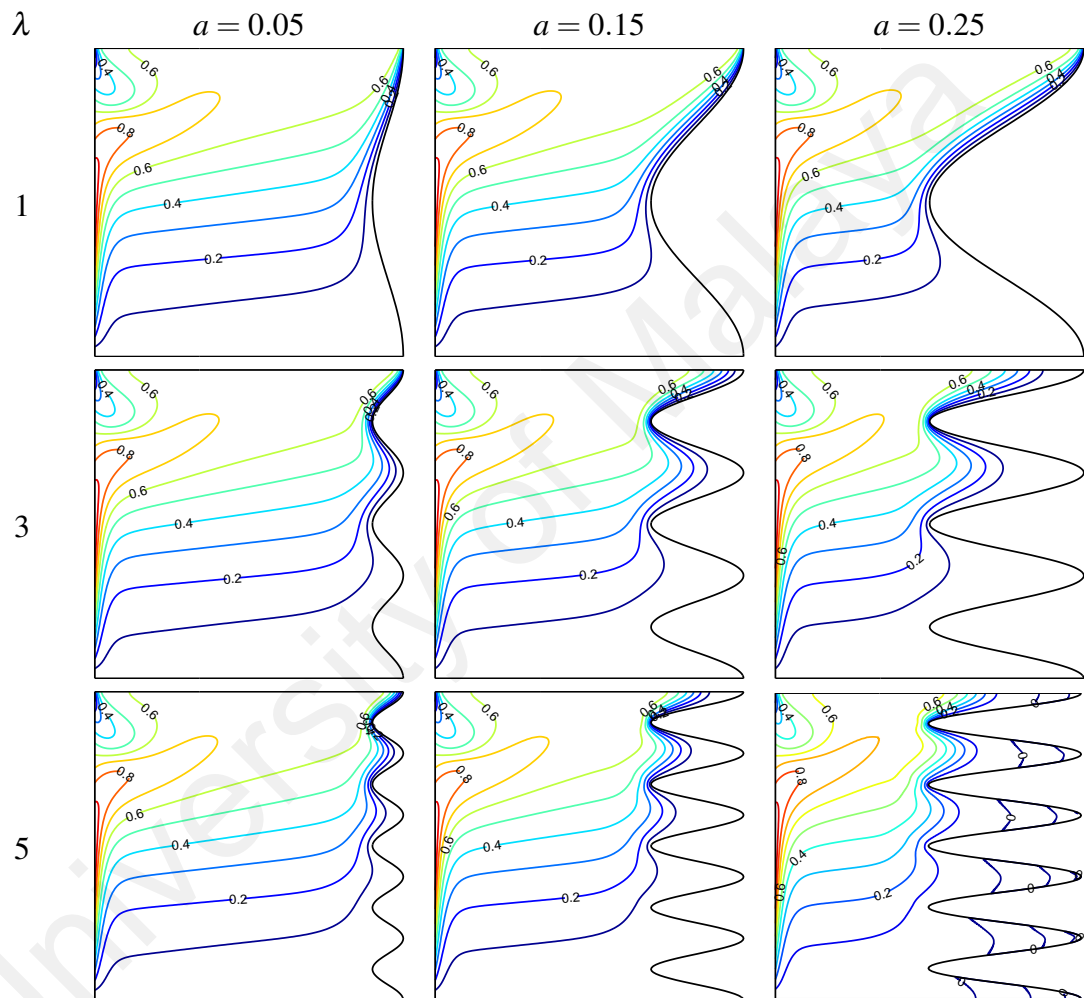


Figure 8.2: Isotherms for various amplitudes and undulations with $\varphi = 0^\circ$ and $Q = 0$ at $Ra_D = 10^3$

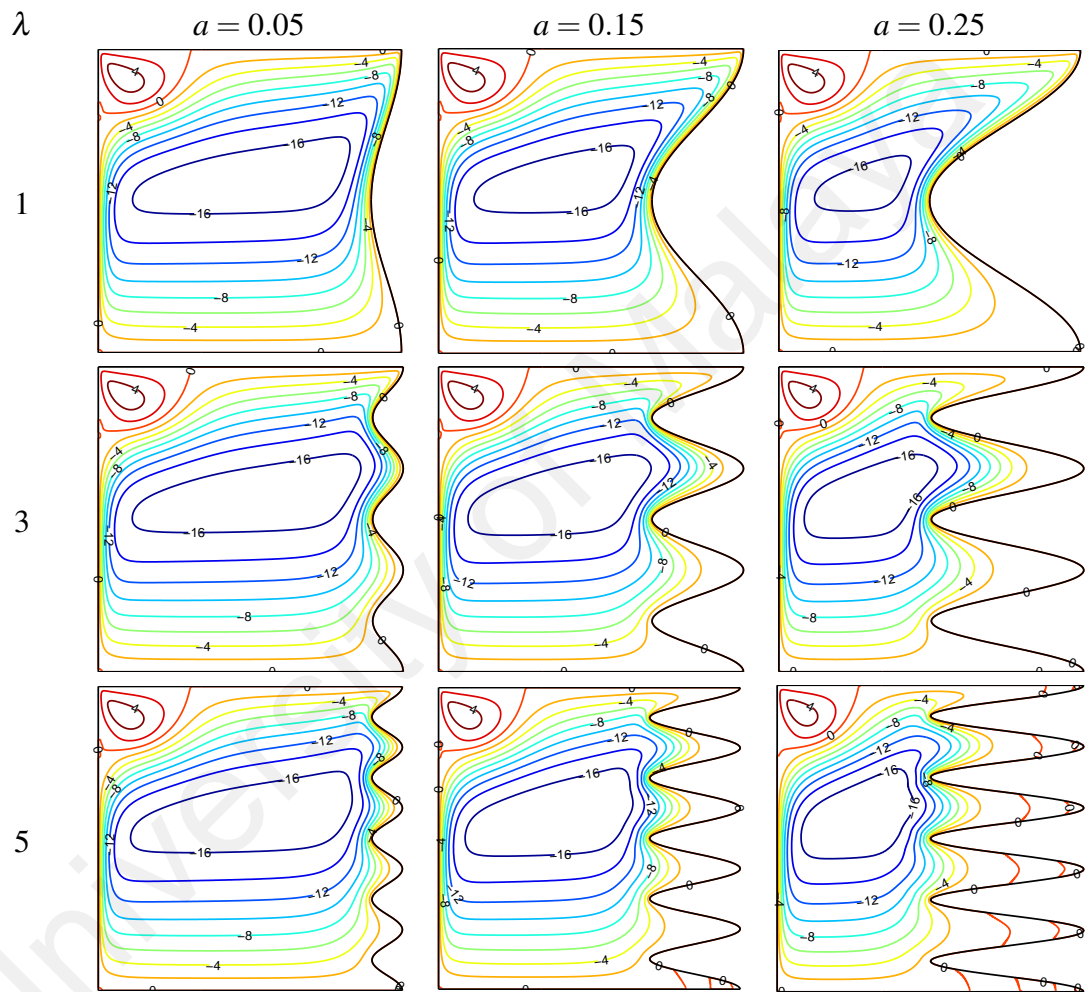


Figure 8.3: Streamlines for various amplitudes and undulations with $\varphi = 0^\circ$ and $Q = 0$ at $Ra_D = 10^3$

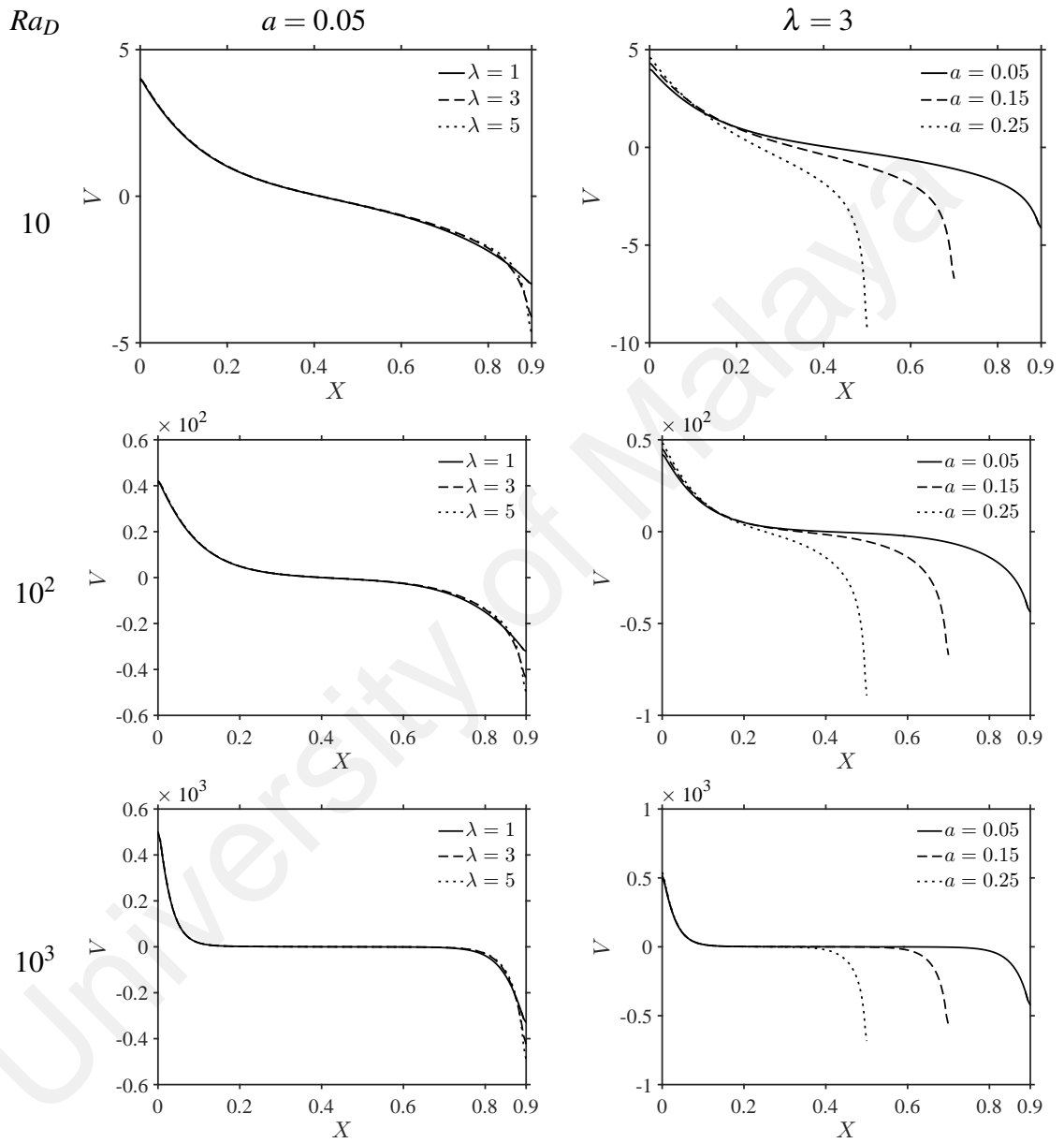


Figure 8.4: Mid-height velocity for different amplitudes and undulations with $\varphi = 0^\circ$ and $Q = 0$ at various Darcy-Rayleigh numbers

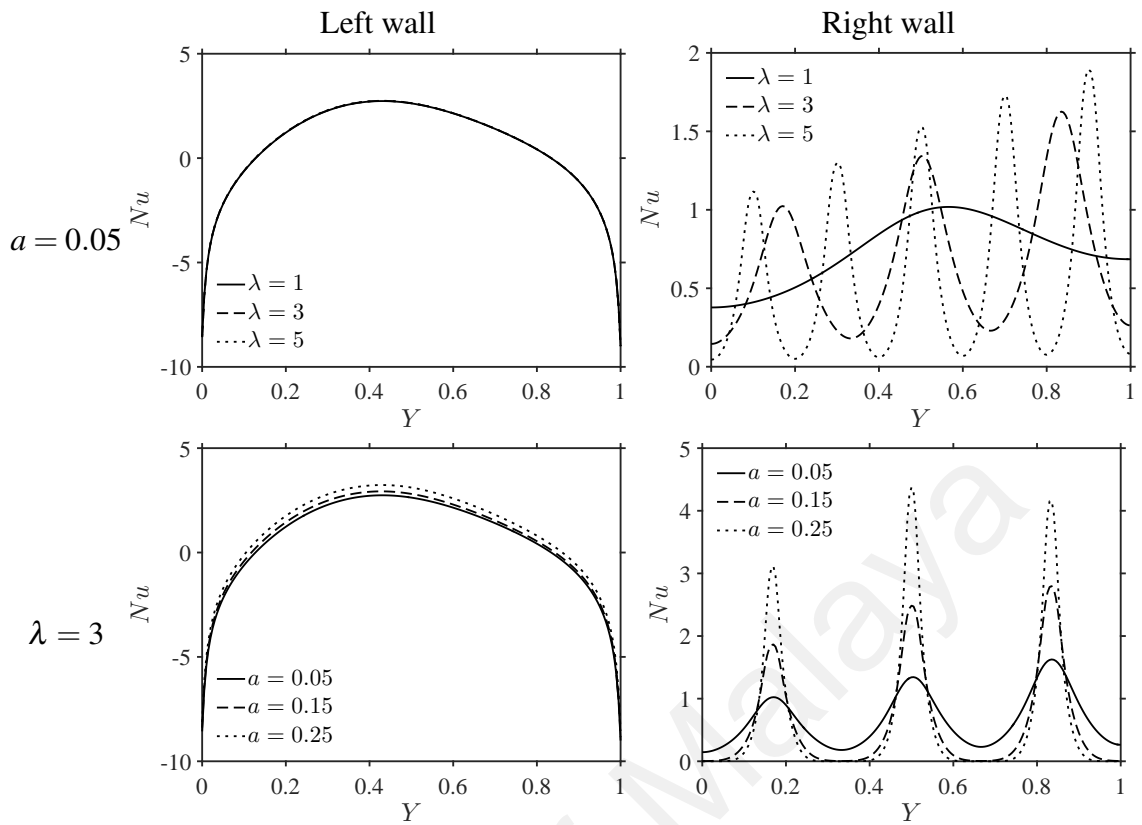


Figure 8.5: Local Nusselt number for different amplitudes and undulations with $\varphi = 0^\circ$ and $Q = 0$ at $Ra_D = 10$

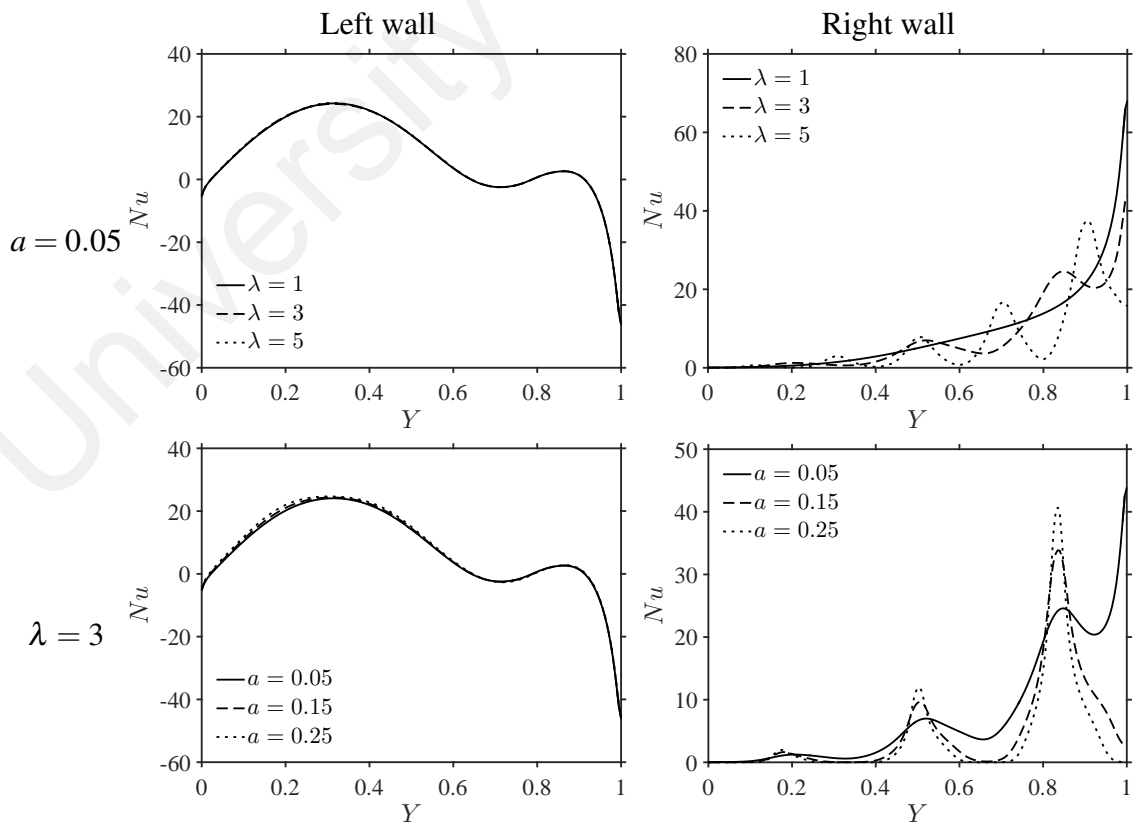


Figure 8.6: Local Nusselt number for different amplitudes and undulations with $\varphi = 0^\circ$ and $Q = 0$ at $Ra_D = 10^3$

The mid-height vertical velocity profiles in the enclosure with different amplitude and number of undulations are plotted in Figure 8.4 for $Ra_D = 10$ to 10^3 . High vertical velocity can be observed near heated wall and it is gradually decreasing along the mid-height plane. The vertical velocity decreases rapidly as reaches the right wall. For a fixed amplitude, enclosure with 5 undulations is having the lowest mid-height vertical velocity as reaches the right wall while the enclosure with 1 undulation is having higher value of mid-height vertical velocity at the right wall. This might be due to higher number of undulations that limit the fluid flow. Instead of flowing closer to the trough of the wavy wall, the fluid is flowing downwards at a higher vertical velocity in the enclosure with 5 undulations. For the case of 3 undulations on the wavy wall, the enclosure with $a = 0.05$ is having higher vertical velocity whereas $a = 0.25$ is having the lowest mid-height vertical velocity as approaching the right wall. Higher amplitude also limits the fluid to flow closer to the trough of the wavy wall. It can be observed that $Ra_D = 10^3$ is having the highest vertical velocity for the fluid among all Darcy-Rayleigh numbers considered. Low vertical velocity is observed in the center of enclosure for all values of Ra_D, a and λ .

Figures 8.5 and 8.6 illustrate the local Nusselt number along the hot and cold walls for different amplitudes and undulations at $Ra_D = 10$ and 10^3 . It can be observed from Figure 8.5 that at $Ra_D = 10$, the local Nusselt number is increasing along the heated wall and reaches maximum around $Y = 0.4$ and then decreases for all amplitudes and number of undulations considered. There is no significant change on the local Nusselt number along the left wall for a fixed amplitude with different number of undulations. However, for a fixed number of undulations, say $\lambda = 3$, heat transfer rate increases with increasing a . The local Nusselt number along the right wall is of wavy form due to the wavy nature of the wall. Higher heat transfer is observed at the crests of the wavy wall while lower heat transfer is obtained at the troughs of the wavy wall. It is interesting to note that the heat transfer for the crests of wavy wall is increasing along the wall from bottom to top for a given amplitude. For a fixed number of undulations, the rise of wall amplitude leads to the increase of the range of heat transfer along the right wall. However, heat transfer

at the third crest is slightly lower than the second crest for $a = 0.25$. This is due to lower fluid velocity for low Ra_D and reduced core region, which causes less heat transfer at higher portion of the right wall.

For $Ra_D = 10^3$, it can be noticed in Figure 8.6 that the local heat transfer of the left wall is increasing up to its global maximum near $Y = 0.3$ and then decreases. The decreasing local Nusselt number rises again near $Y = 0.7$ to local maximum at $Y = 0.9$ and then decreases. Hence, the local Nusselt number behaves non-linearly and shows the direct impact of the temperature boundary condition on it. There is not much difference on the local Nusselt number along the left wall for different values of amplitudes and number of undulations considered. The local Nusselt number of the right wall is increasing along the wall. For $a = 0.05$, the highest heat transfer is obtained at the top of the right wall for $\lambda = 1$ and 3, while $\lambda = 5$ gives highest heat transfer at the crest near the top wall. This difference is due to the high number of undulations causes less space between the top wall and the last hull, lesser fluid is flowing in this area and thus lower the heat transfer. For $\lambda = 3$, the highest heat transfer is obtained at the top of the wall for $a = 0.05$, while the top crest gives the highest local heat transfer for $a = 0.15$ and 0.25. Higher amplitude also causes space limitation between the top wall and the hull near the top wall. Thus, it reduces the flow circulation in the narrow region and results in lower heat transfer at the end of the right wall.

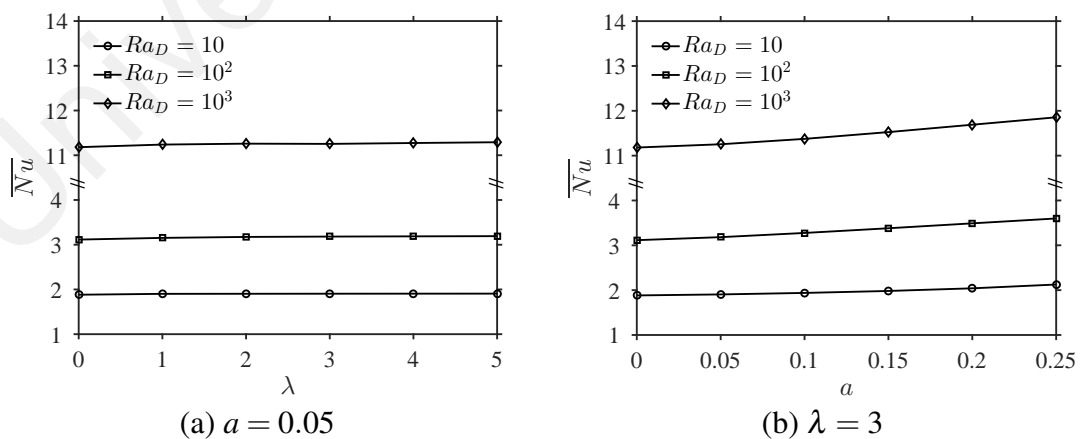


Figure 8.7: Average Nusselt number for various Darcy-Rayleigh numbers with different amplitudes and number of undulations when $\varphi = 0^\circ$

The average Nusselt number for different amplitudes and undulations is shown in Figure 8.7. It is obvious that the heat transfer rate increases on increasing Darcy-Rayleigh number for a given values of a and λ . Figure 8.7(a) presents the variation of average heat transfer with number of undulations at different Darcy-Rayleigh numbers. The heat transfer rate slightly increases upon the increase of number of undulations. The variation of average heat transfer with amplitude is shown in Figure 8.7(b). The heat transfer rate increases as amplitude increases. Thus, it can be seen that increasing the amplitude and number of undulations of the cold wall can increase the average heat transfer of heated wall. Increasing the amplitude of the wavy wall gives more increment on the heat transfer than that of increasing the number of undulations.

8.4.2 Effects of Internal Heat Generation/Absorption

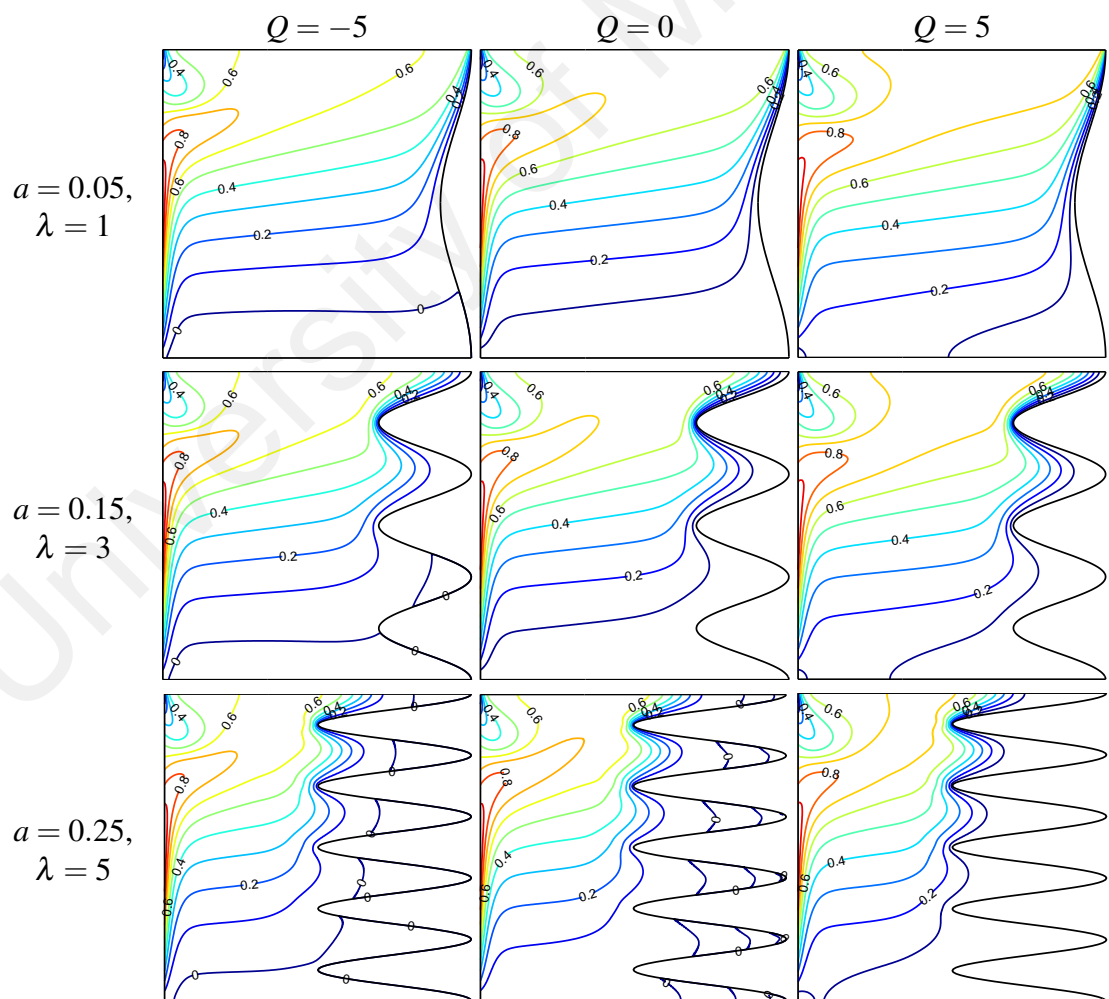


Figure 8.8: Isotherms for various internal heat generation/absorption parameters with different combinations of amplitudes and undulations at $\phi = 0^\circ$ and $Ra_D = 10^3$

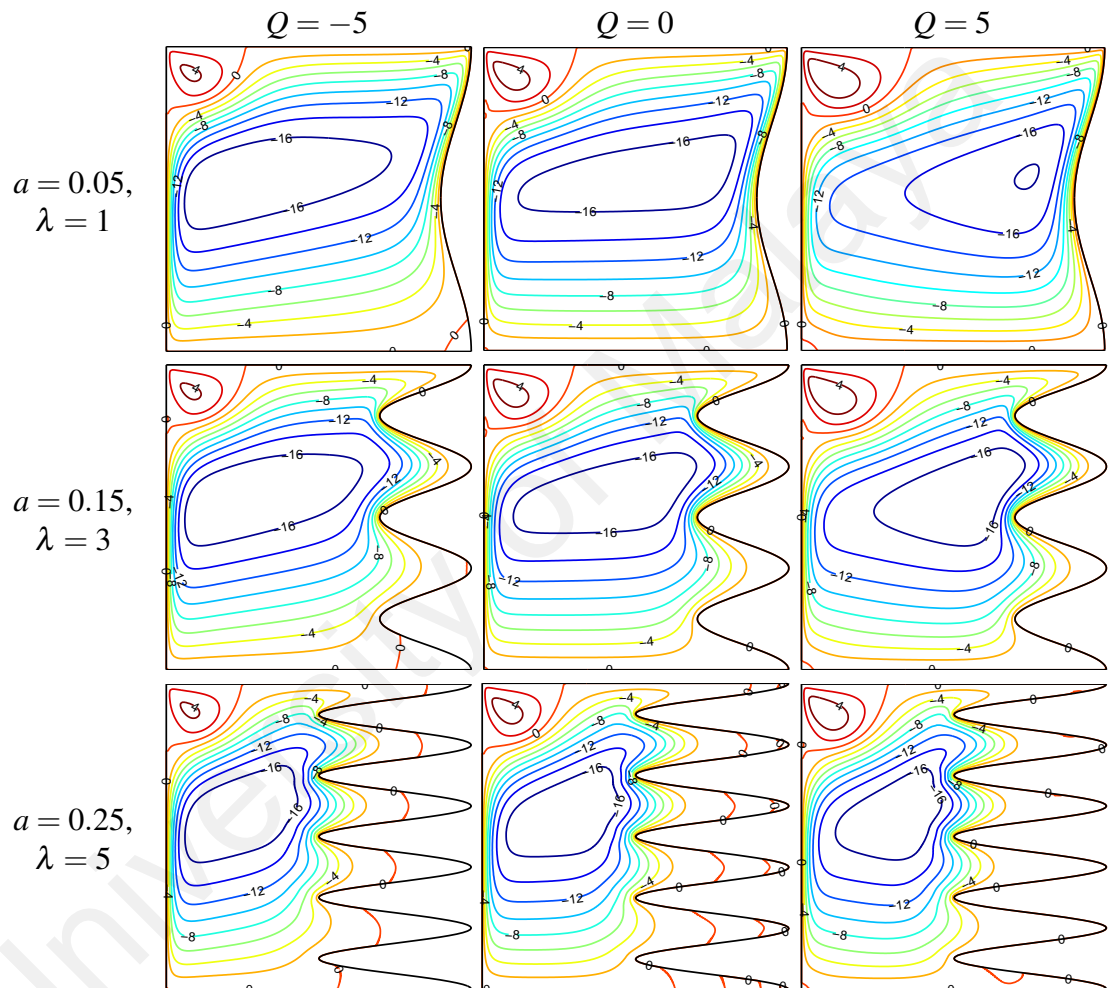


Figure 8.9: Streamlines for various internal heat generation/absorption parameters with different combinations of amplitudes and undulations at $\varphi = 0^\circ$ and $Ra_D = 10^3$

The effect of internal heat generation/absorption on the fluid flow and temperature distribution is illustrated in Figures 8.8 and 8.9 with $Ra_D = 10^3$ for different amplitudes and undulations. The internal heat generation/absorption clearly shows its effect on the temperature distribution inside the enclosure as presented in Figure 8.8. While keeping the internal heat generation parameter at -5, the isotherms are clustered along heated wall and upper portion of cold wall. Temperature lower than the cold wall is observed at the lower part of the enclosure and it shows conduction mode of heat transfer in the bottom portion of the enclosure. As the internal heat generation parameter increases to 5, the isotherms are clustered nearer to heated wall and top portion of cold wall. In the case of $Q = -5$, the fluid is heat absorbing, where heat is required to trigger the fluid motion. Fluid further away from the heat source is absorbing heat from the nearby fluid particles and it is less energized to flow with the main flow. Thus, the temperature distribution is weak in the bottom portion and hulls. While in the case of $Q = 5$, heat is released to the surrounding, thus the clustering of isotherms are near to the cold wall, indicating steep heat transfer occurs.

The streamlines for $Ra_D = 10^3$ with different internal heat generation parameter are shown in Figure 8.9. The enclosure is occupied by clockwise flow with a small recirculating cell on the top-left corner. The fluid is flowing at higher velocity in the enclosure in presence of internal heat generation/absorption. The core region of the cell is nearer to the left wall in the case of $Q = -5$. It is because the heat source on the left wall provides the energy required for fluid flow. Fluid nearer to the left wall is flowing upwards and loses energy when meeting less energized fluid particles as reaches the cold wall, and then descending down along the left wall. In the case of heat-generating fluid, the fluid particles have sufficient energy to flow upwards along the heated wall. Upon meeting the cold wall, the fluid particles are releasing energy to the wall or surrounding fluid. Hence, the core region is flowing nearer to the cold wall in heat-generating case. Also, the fluid velocity is slightly higher in the hulls of the wavy wall in heat-generating case.

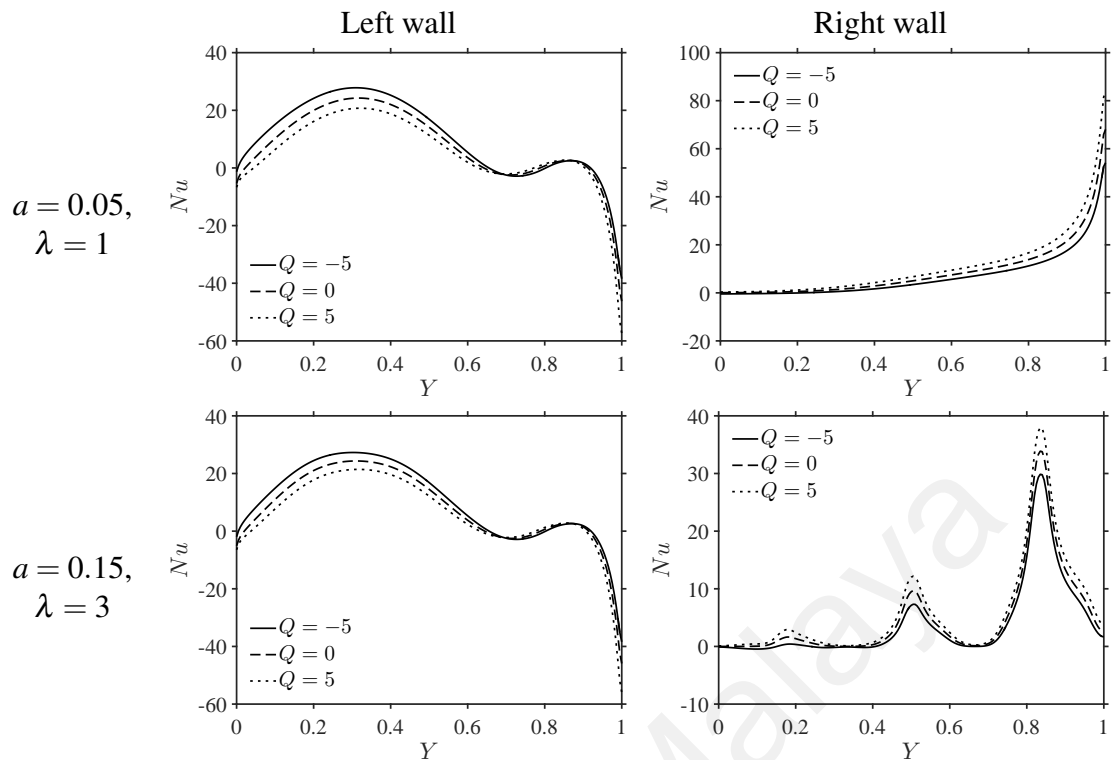


Figure 8.10: Local Nusselt number for various internal heat generation/absorption parameters with different combinations of amplitudes and undulations at $\phi = 0^\circ$ and $Ra_D = 10^3$

The local Nusselt number along the left and right walls for $Ra_D = 10^3$ with internal heat generation/absorption is shown in Figure 8.10. It can be noticed that there is no significant difference in the local heat transfer of left wall between different amplitude and number of undulations for a fixed internal heat generation parameter. However, it can be observed that $Q = -5$ has higher local heat transfer than other heat generating parameter in the range $0 \leq Y \leq 0.7$ and $0.9 \leq Y \leq 1$. In the range mentioned before, $Q = 5$ has the lowest heat transfer but greater than the other heat generating parameter when $0.7 \leq Y \leq 0.9$. The local heat transfer along the right wall is increasing along the wall in the enclosure with $a = 0.05$ and $\lambda = 1$. For wavy enclosure with $a = 0.15$ and $\lambda = 3$, high local heat transfer can be obtained at the crests of the wavy wall and the highest value is located at the crest nearest to the top wall. For the combinations of amplitude and number of undulations considered, enclosure with $Q = -5$ has the lowest local heat transfer while heat generation provides the highest local heat transfer along the right wall.

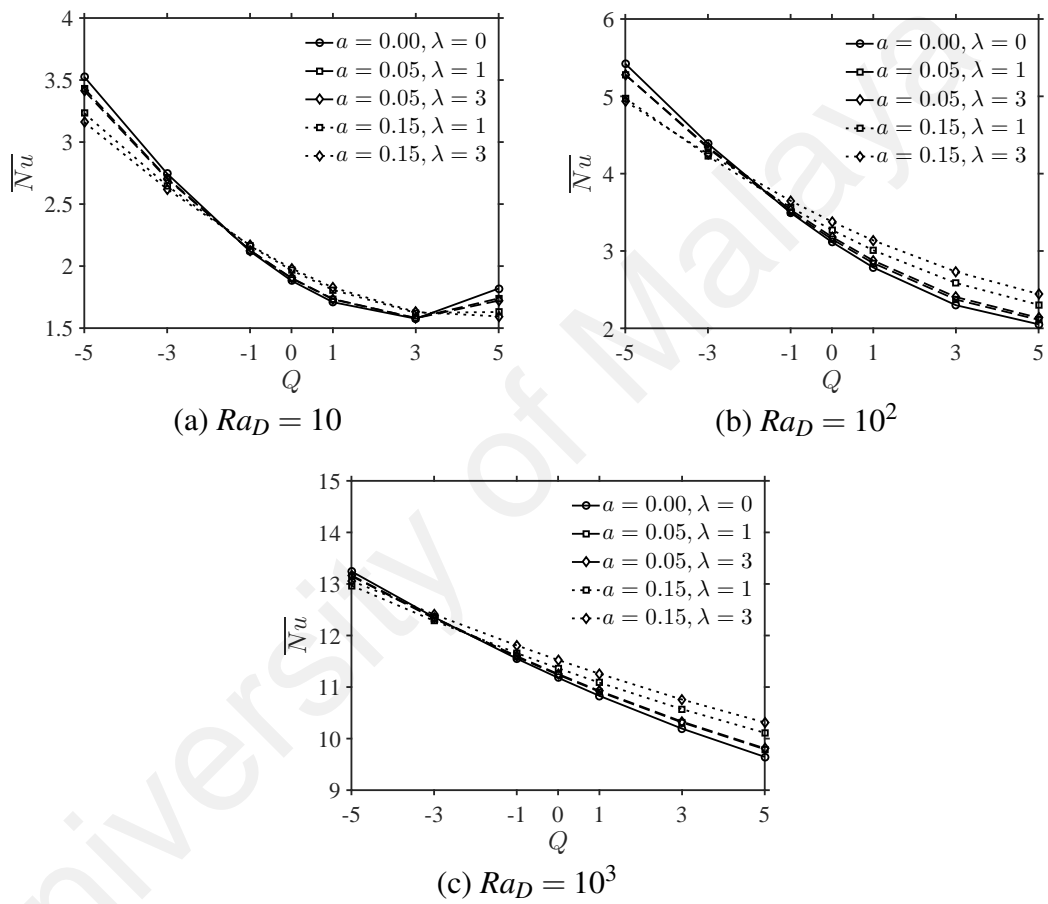


Figure 8.11: Variation of average Nusselt number with internal heat generation/absorption parameters with different combinations of amplitudes and undulations at various Darcy-Rayleigh numbers when $\varphi = 0^\circ$

Figure 8.11 presents the variation of average heat transfer of the left wall with different internal heat generation/absorption parameters and Darcy-Rayleigh numbers. The heat transfer decreases as the internal heat generation parameter increases. The heat transfer rate is high when $Q < 0$, because the fluid in the enclosure is heat absorbing and heat is transferred quickly from the wall to the fluid which gives positive gradient of heat transfer. However, in the case of $Q > 0$, heat is generating in the fluid. Less heat is absorbed and excessive generated heat is transferred from the fluid to the wall which gives negative gradient of local heat transfer. Thus, the overall heat transfer reduces in the enclosure. However, it can be observed that the heat transfer rate increases for high values of heat generating parameter ($Q > 3$) at $Ra_D = 10$. Since convection effect is less significant at low Darcy-Rayleigh number, sinusoidal heating affects the behaviour of flow and heat transfer in the enclosure at high internal heat generation, where recirculation zones and high heat transfer rates can be observed at the top and bottom corners of the left wall.

8.4.3 Effects of Inclination

The effects of enclosure inclination on the fluid flow in the wavy porous enclosure at $Ra_D = 10^3$ are presented clearly in Figure 8.12. For enclosure with $a = 0.05$ and $\lambda = 1$, fluid is flowing in clockwise direction, with recirculating eddy is forming at the top-left corner of the enclosure. On increasing of enclosure inclination, the size of the recirculating eddy decreases. The strength of fluid circulation increases when the enclosure is inclined, and the enclosure of 45° inclination has the highest value of fluid velocity. When the enclosure is inclined with 90° , fluid is rotating in counter-clockwise direction with recirculating eddy at the bottom-left corner. For a fixed amplitude, increasing the number of undulations on the wavy wall affects the fluid flow along the right wall only, where the flow pattern is wavy, following the waviness of the right wall. When the enclosure is heated from below (90°), flow separation occurs for $\lambda = 4$, where fluid is flowing in opposite directions and it is symmetrical about the mid-plane of the enclosure. When the number of undulations on the right wall is fixed, increasing the amplitude has much more effect on the fluid flow inside the enclosure. The core

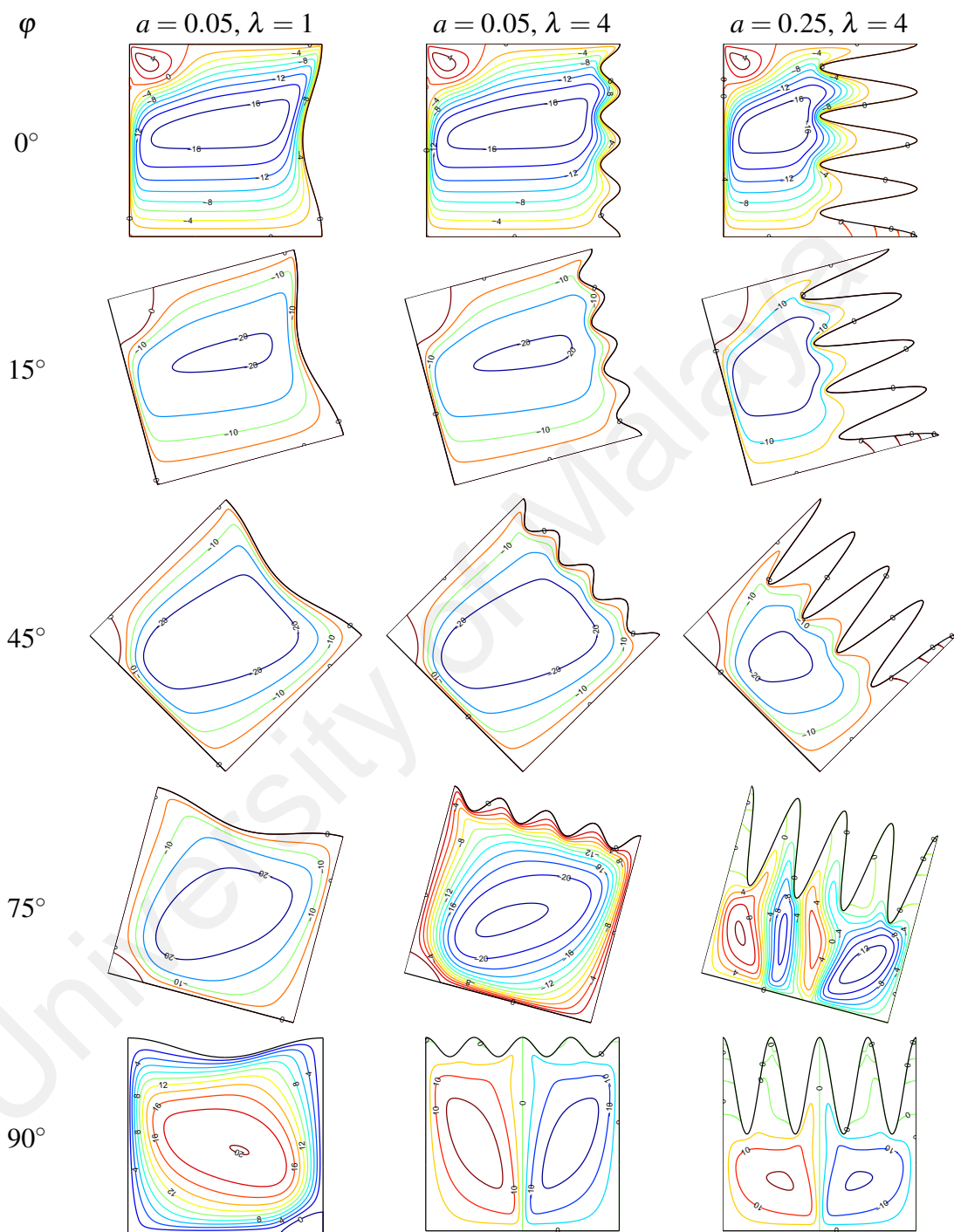


Figure 8.12: Streamlines for various enclosure inclination with different combinations of amplitude and undulation at $Q = 0$ and $Ra_D = 10^3$

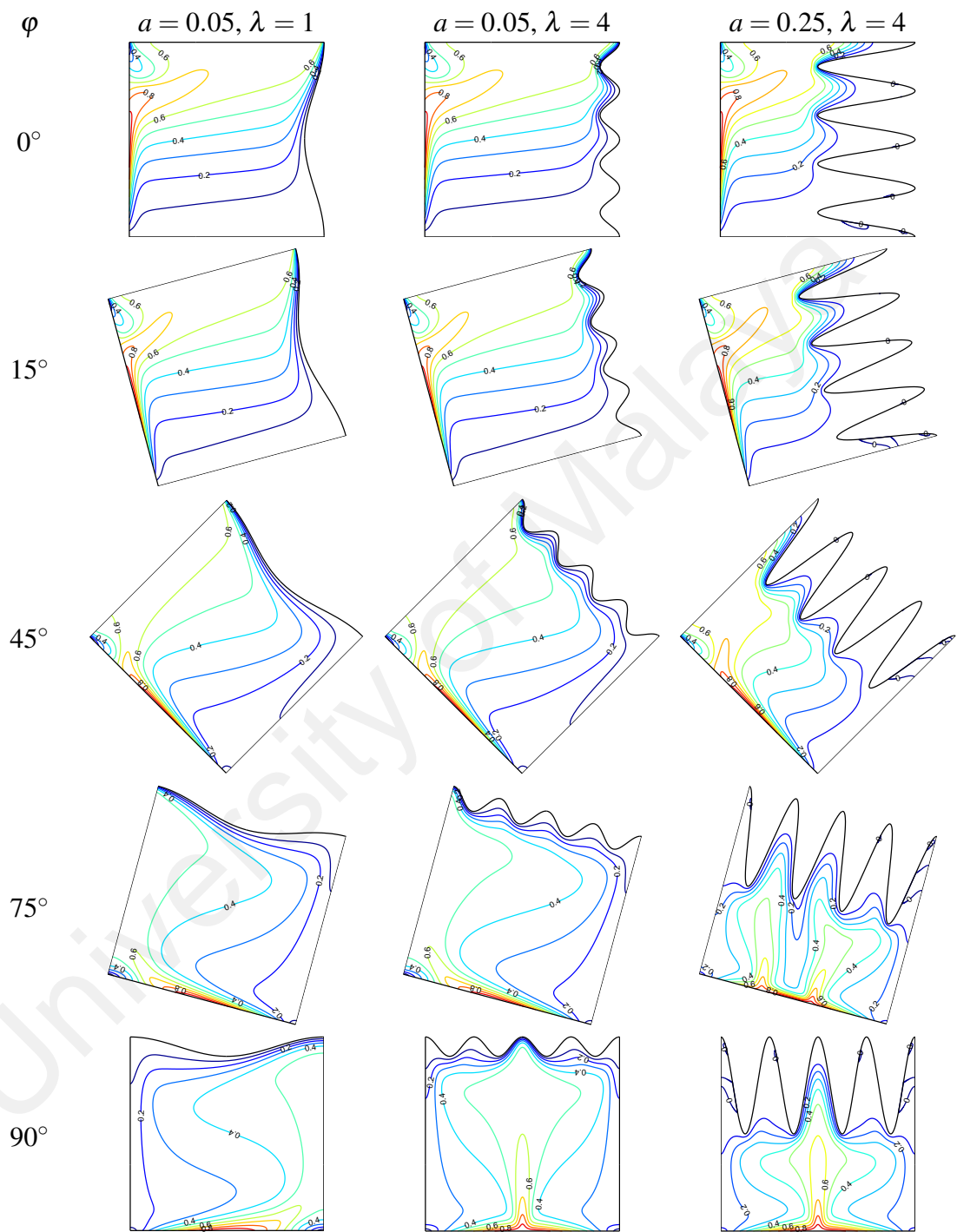


Figure 8.13: Isotherms for various enclosure inclination with different combinations of amplitude and undulation at $Q = 0$ and $Ra_D = 10^3$

region is smaller in size compare to the enclosure with lower amplitude. Increasing the enclosure inclination to 75° gives multiple fluid flow inside the enclosure and 90° shows symmetrical flow inside the enclosure with higher number of undulations.

The isotherms in Figure 8.13 illustrate the effects of enclosure inclination and right wall waviness on the temperature distribution inside the porous enclosure. The temperature contours clearly exemplify the sinusoidal temperature applied on the left wall of the enclosure where higher temperature is observed in the middle of the left wall and lower temperature can be obtained at the top and bottom corners of the left wall. The isotherms cluster along the left wall, especially in the middle section, indicating steep temperature gradients occur in the direction perpendicular the wall at $Ra_D = 10^3$. That is, thermal boundary layers are formed here. The temperature contours also cluster along the top section of the right wall. It indicates that convection is the mode of heat transfer in the enclosure at $Ra_D = 10^3$, as the isotherms are extended from the left wall to the right wall. For enclosure with $a = 0.05$ and $\lambda = 1$, there is no obvious difference on the temperature distribution on increasing the enclosure inclination. When the enclosure is inclined with 90° , the isotherms are clustered at the lower section of the wall. On increasing the number of undulations on the right wall, thermal boundary layer along the right wall is of wavy form, following the waviness of the right wall. Thermal boundary layer along the top-right corner gradually vanishes as the enclosure inclination increases. Thermal boundary layer is formed in the middle undulation when the enclosure is heated from below. The plume like structure of temperature distribution is observed in the middle of hot wall when $\varphi = 90^\circ$. When the number of undulations on the right wall is fixed, increasing the amplitude gives significant effect on the temperature distribution inside the porous enclosure. Thermal boundary layer along the right wall is less obvious, as the thermal penetration from left wall to right wall is obstructed by high waviness of the right wall. Increasing the amplitude of the right wall increases its arc length, thus a large area is cooled with constant temperature. The undulations also hinder thermal penetration as the cold fluid is trapped in the hulls of the right wall. Increasing the enclosure inclination to 90° gives symmetrical temperature distribution in the enclosure along the mid-plane for $\lambda = 4$.

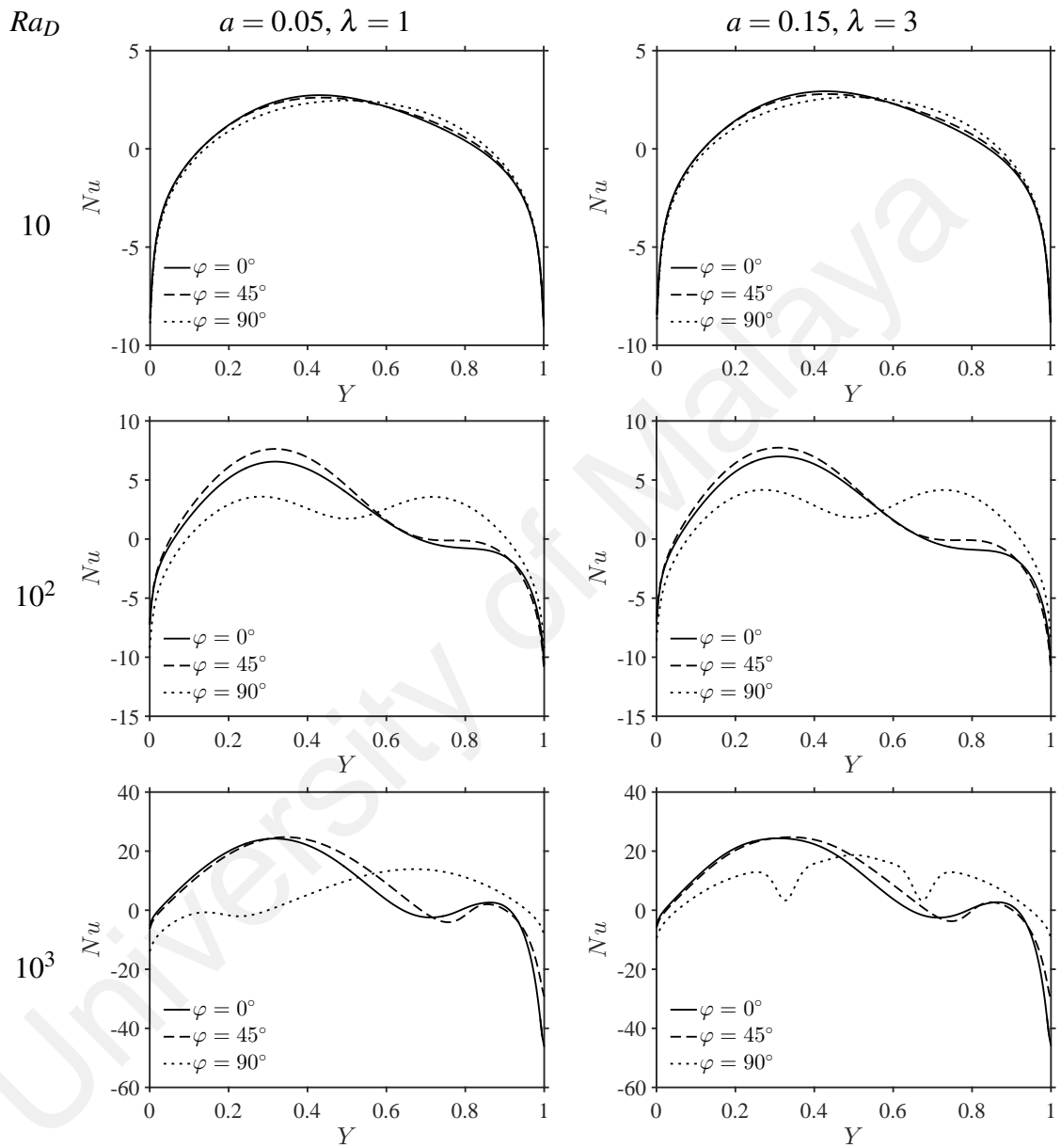


Figure 8.14: Local Nusselt numbers for various enclosure inclination with different combinations of amplitude and undulation at different Darcy-Rayleigh numbers when $Q = 0$

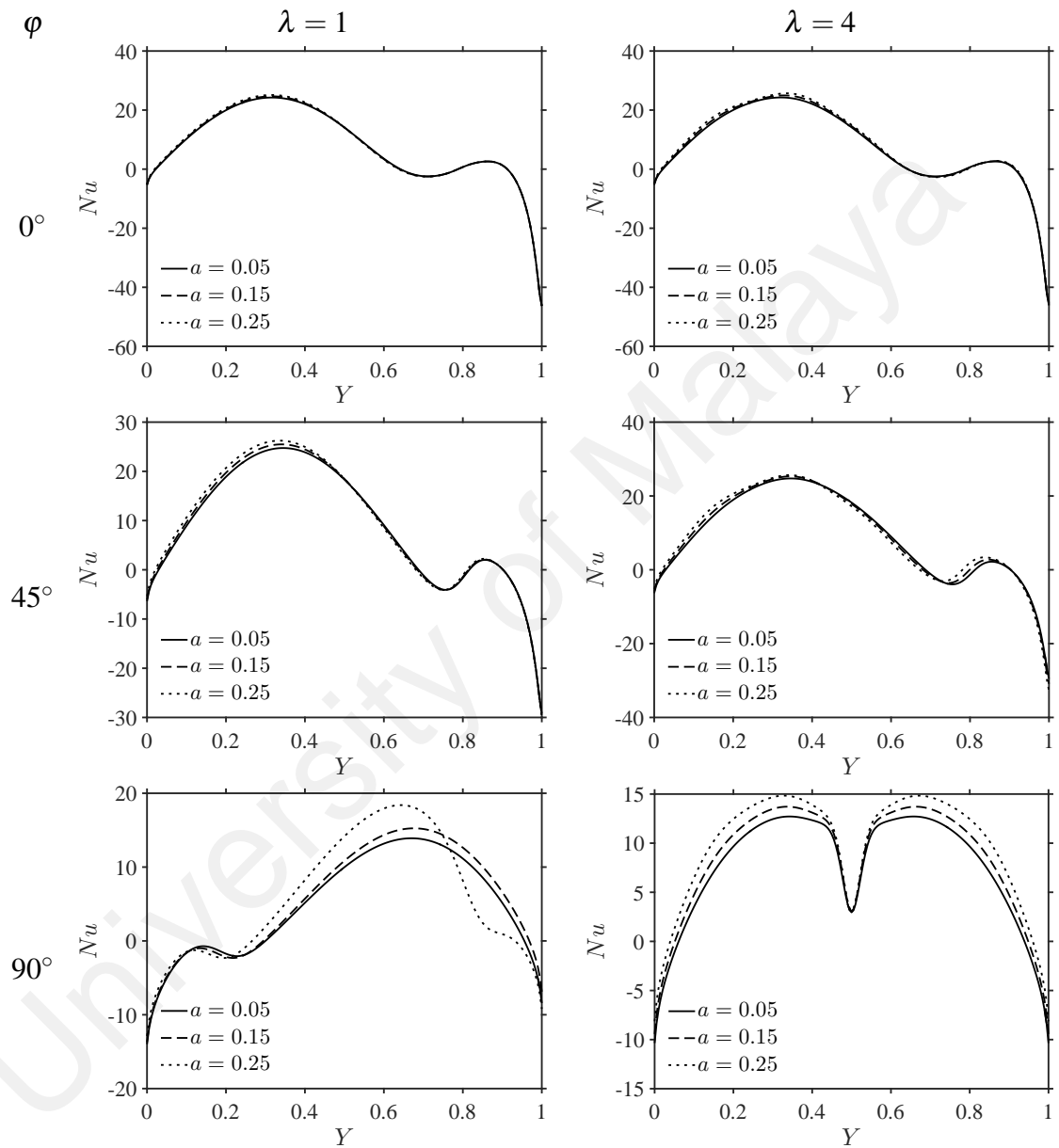


Figure 8.15: Local Nusselt number for various amplitudes with different number of undulations and enclosure inclination at $Q = 0$ and $Ra_D = 10^3$

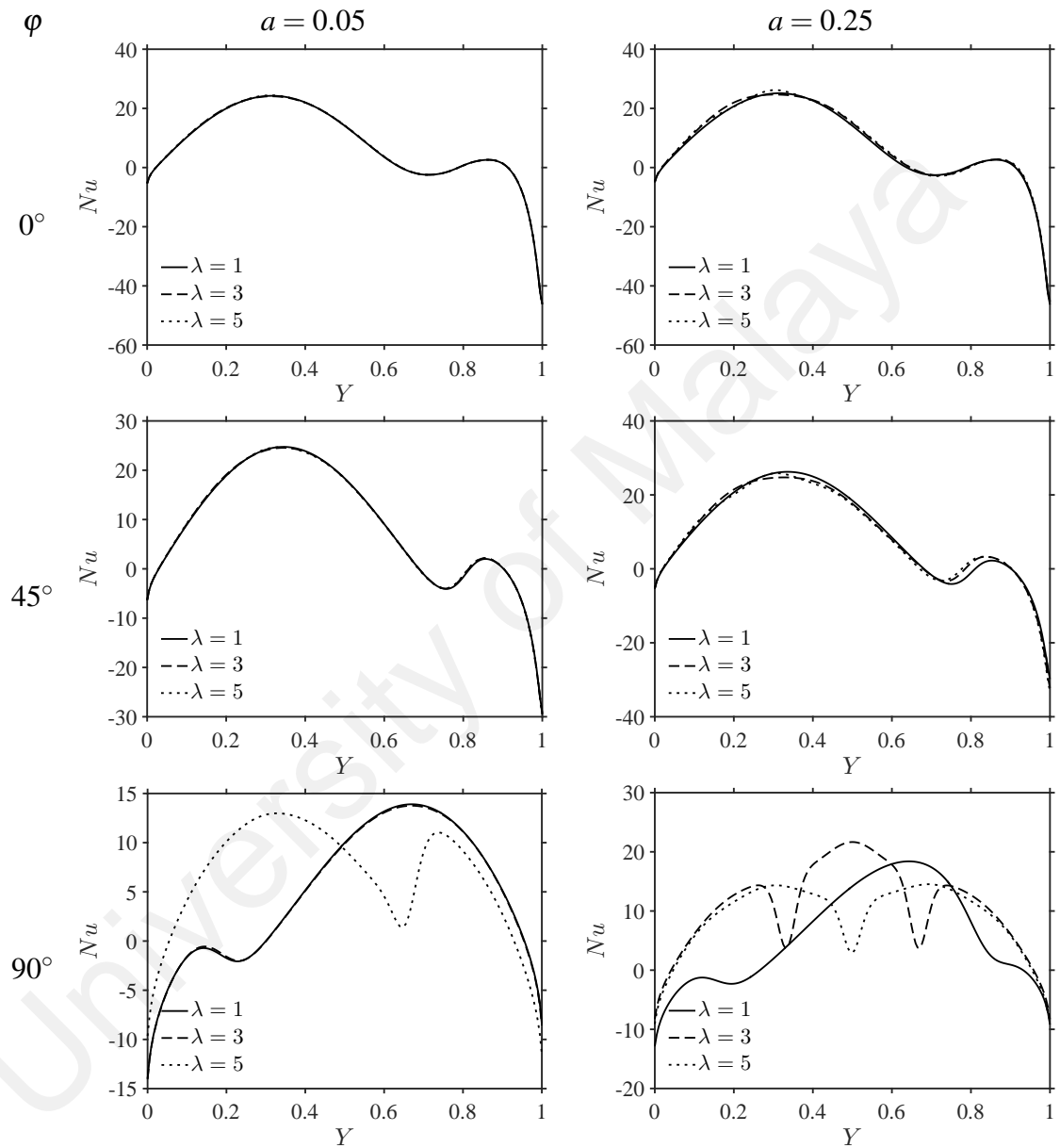


Figure 8.16: Local Nusselt number for various number of undulations with different amplitudes and enclosure inclination at $Q = 0$ and $Ra_D = 10^3$

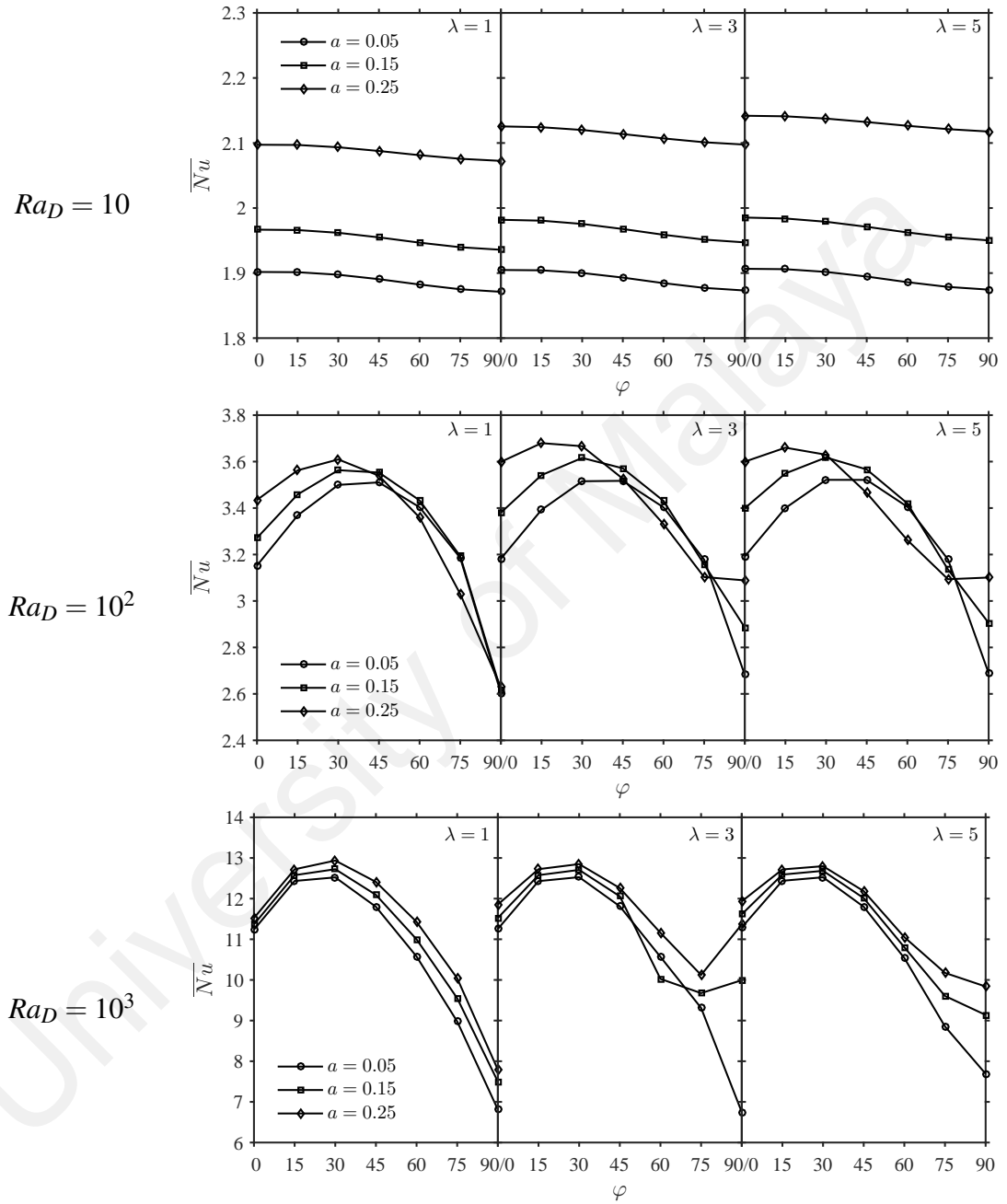


Figure 8.17: Variation of average Nusselt numbers with enclosure inclination for various amplitudes at different Darcy-Rayleigh numbers when $Q = 0$

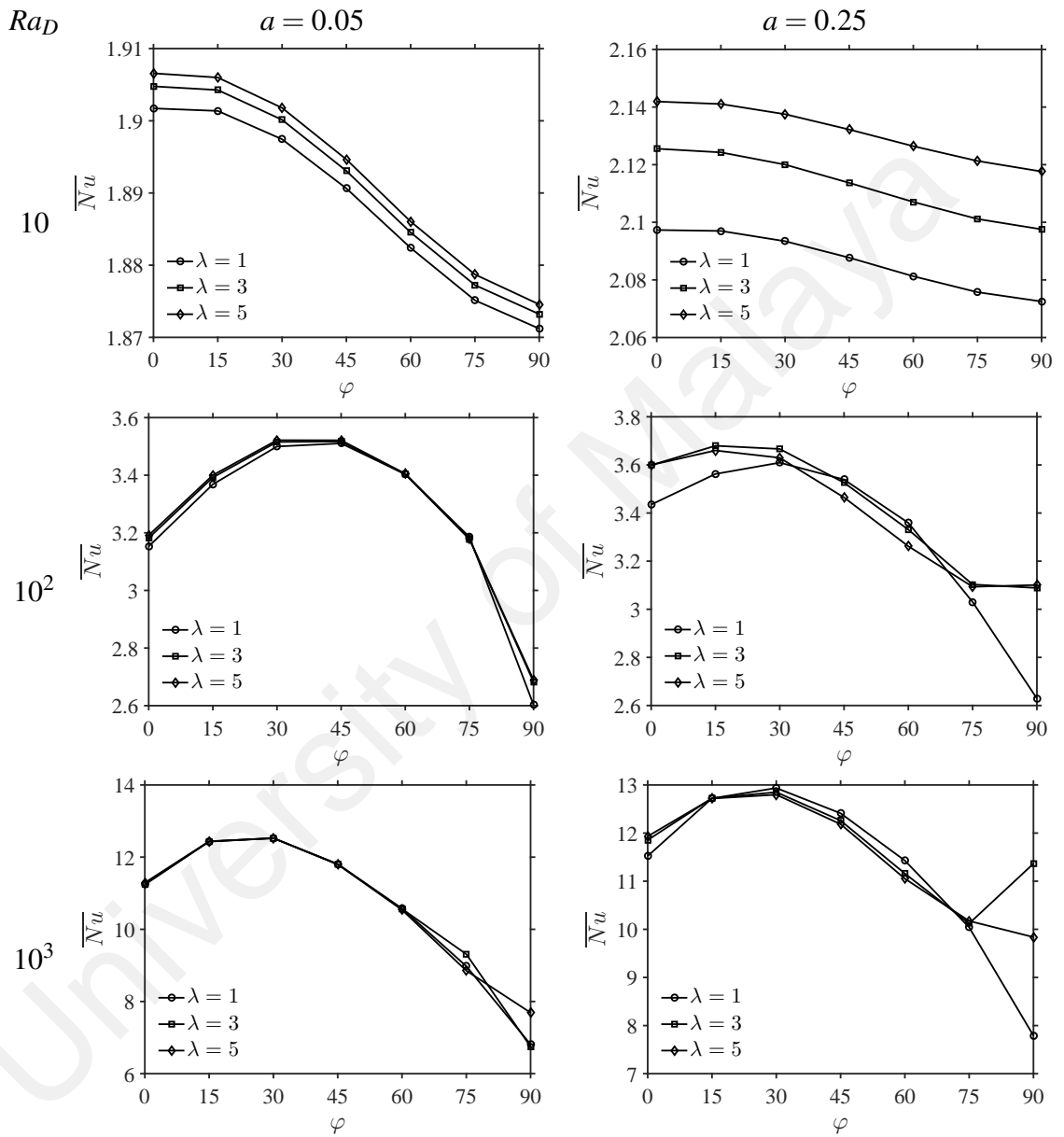


Figure 8.18: Variation of average Nusselt numbers with enclosure inclination for various undulations at different Darcy-Rayleigh numbers when $Q = 0$

The local Nusselt number along the left wall for different Darcy-Rayleigh numbers is presented in Figure 8.14. The local heat transfer along the left wall is of wavy form, clearly shows the effect of sinusoidal temperature applied on the left wall. At $Ra_D = 10$, the distribution of local heat transfer along the left wall is similar for enclosure with two different right wall waviness considered. For 0° and 45° of enclosure inclination, the local heat transfer rises from the bottom to maximum at $Y = 0.4$ and then decreases along the wall. The enclosure with 90° inclination shows symmetrical local heat transfer rate and maximum local heat transfer rate can be obtained at $Y = 0.5$. The raise of Darcy-Rayleigh number alters the waviness of local heat transfer distribution along the left wall. At $Ra_D = 10^2$, maximum heat transfer for 0° and 45° of enclosure inclination can be obtained near $Y = 0.3$. The distribution of heat transfer rate of 90° inclination is symmetric about $Y = 0.5$, with local minimum at $Y = 0.5$ and local maxima of heat transfer rate at $Y = 0.25$ and 0.75 . Similar to the phenomenon at $Ra_D = 10^2$, the local heat transfer for 0° and 45° at $Ra_D = 10^3$ also increases around $Y = 0.7$ to local maximum near $Y = 0.9$ and later decreases as approaching the top-left corner. The porous enclosure with $a = 0.05$ and $\lambda = 1$ shows non-linear behaviour of local heat transfer at 90° whereas the porous enclosure with $a = 0.15$ and $\lambda = 3$ displays symmetrical local heat transfer at $Y = 0.5$. It can be observed that the range of local Nusselt number increases on increasing of Darcy-Rayleigh number.

Figure 8.15 displays the variation of local Nusselt numbers with different right wall amplitudes at $Ra_D = 10^3$. The porous enclosure with 0° and 45° of inclination show similar form of local heat transfer distribution along the left wall with different number of undulations considered. When the enclosure is heated from below, the distribution of local heat transfer for the porous enclosure with $\lambda = 1$, $a = 0.05$ and 0.15 is a reflection of the local heat transfer distribution when the enclosure is inclined 0° and 45° . When the enclosure is having amplitude $a = 0.25$, the local heat transfer in the middle of left wall is slightly higher than other amplitudes considered, with local maximum located near $Y = 0.6$. It can be noticed that the temperature distribution on the left wall is non-symmetrical for low number of undulations regardless of the amplitude. Increasing the number of undulations of the enclosure produces symmetrical distribution of local

heat transfer when the enclosure is heated from below, see Figure 8.15. It is observed that the sudden decrement on the local heat transfer is found at the middle of the wall when $\varphi = 90^\circ$ and $\lambda = 4$ for all values of a , where plume like structure in the isotherms is found. It also can be observed that the local heat transfer increases on the raise of right wall amplitude.

The variation of local heat transfer along the left wall with different number of undulations at $Ra_D = 10^3$ is presented in Figure 8.16. There is not much difference in the local heat transfer distribution along the left wall for different values of undulations with fixed values of amplitude and inclination ($\varphi = 0^\circ$ and 45°). When the porous enclosure is heated from below (90°), the local heat transfer for $a = 0.05$ is non-consistent with the variation of number of undulations as shown in the enclosure inclination. The local heat transfer is symmetrical for porous enclosures with $\lambda = 3$ and 5 , whereas $\lambda = 1$ is the reflection of local heat transfer as the porous enclosure with inclination 0° and 45° when $a = 0.25$. The range of local heat transfer increases on increasing of right wall amplitude. The variation of local heat transfer for the enclosure of inclination 90° shows that the temperature distribution is non-symmetrical when the porous enclosure is having low amplitude regardless of the number of undulations on the right wall.

Figures 8.17 and 8.18 demonstrate the variation of average Nusselt numbers with enclosure inclination for different right wall amplitude, number of undulations and Darcy-Rayleigh numbers. From Figure 8.17, the highest heat transfer rate is obtained when the enclosure is heated from side and enclosure heated from below gives the lowest heat transfer rate at $Ra_D = 10$. The average heat transfer rate decreases on increasing the inclination from 0° to 90° for all a and λ at $Ra_D = 10$. The average heat transfer rate increases when the right wall amplitude and number of undulations increase. The average heat transfer rate increases to its maximum and then decreases with the enclosure inclination at $Ra_D = 10^2$ and 10^3 . At $Ra_D = 10^2$, the highest heat transfer for $a = 0.05$ and 0.15 can be obtained at $\varphi = 45^\circ$ and 30° , respectively regardless of the number of undulations. The porous enclosure with $a = 0.25$ has the highest heat transfer at $\varphi = 30^\circ$ when $\lambda = 1$ and $\varphi = 15^\circ$ for $\lambda = 3$ and 5 . The lowest heat transfer rate can be obtained at 90° of inclination for all values of amplitude and undulations except for enclosure with

$a = 0.25$ and $\lambda = 5$. For the porous enclosure with $a = 0.25$ and $\lambda = 5$, the lowest heat transfer is obtained when the enclosure is inclined with 75° . The variation of average heat transfer rate at $Ra_D = 10^3$ is more consistent as compared to $Ra_D = 10^2$. The highest heat transfer rate is obtained when the enclosure is of inclination 30° for all values of amplitude and undulations. Enclosures with $\lambda = 1$ and 5 have the lowest heat transfer rate when it is heated from below. When $\lambda = 3$, the lowest heat transfer rate is at $\varphi = 90^\circ$ for $a = 0.05$, and $\varphi = 75^\circ$ for $a = 0.15$ and 0.25 . Hence, we can conclude that higher heat transfer rate is obtained when the porous enclosure is slightly inclined from the horizontal plane for the case of sinusoidal heating.

In Figure 8.18, it can be noticed that the behaviour of the variation of average heat transfer rate with inclination is quite similar between different number of undulations for $a = 0.05$. The difference of average heat transfer rate for a fixed enclosure inclination with the number of undulations is small for $a = 0.05$ as compared to $a = 0.25$. Therefore, the average heat transfer rate increases on increasing the amplitude of the wavy wall. From Figures 8.17 and 8.18, it also can be noticed that the average heat transfer rate enhances on raising of the amplitude than that of the number of undulations.

Correlation equations can provide informative relations between pertinent parameters involved in the study. Hence, a set of correlation equations are derived based on the results from this study. We intend to understand the relations of the average Nusselt number at heated wall with the waviness of right wall, a and λ , and enclosure inclination, φ . For square vertical enclosure without internal heat generating/absorbing porous medium ($a = 0, \lambda = 0, \varphi = 0, Q = 0$),

$$\overline{Nu} = 0.077 (Ra_D + 80.25)^{0.71} = a.$$

The effect of internal heat generation/absorption on heat transfer rate in a square porous enclosure is,

$$\overline{Nu} = 0.022Q^2 - 0.29Q + a.$$

When enclosure inclination is considered,

$$Ra_D = 10,$$

$$\begin{aligned}\overline{Nu} &= (0.014\varphi^4 - 0.029\varphi^3 + 0.0074\varphi^2 - 0.0118\varphi) \\ &\quad + (-0.092\varphi^4 + 0.4\varphi^3 - 0.57\varphi^2 + 0.22\varphi) a \\ &\quad + (0.09\varphi^4 - 0.66\varphi^3 + 1.26\varphi^2 - 0.46\varphi) a^2 + (a \times b),\end{aligned}$$

where,

$$\begin{aligned}b &= \frac{(28.28a^3 - 3.44a^2 + 0.96a) \lambda}{\lambda + 1} + (-0.26a^3 + 0.051a^2 - 0.0070a) \lambda^3 \\ &\quad + (3.23a^3 - 0.60a^2 + 0.085a) \lambda^2 + (-13.3a^3 + 2.34a^2 - 0.36a) \lambda + 1.\end{aligned}$$

$$Ra_D = 10^2,$$

$$\begin{aligned}\overline{Nu} &= (-1.37\varphi^4 + 3.21\varphi^3 - 3.07\varphi^2 + 1.71\varphi) \\ &\quad + (0.50\varphi^4 - 1.14\varphi^3 + 0.79\varphi^2 - 0.26\varphi) \lambda \\ &\quad + (-0.064\varphi^4 + 0.15\varphi^3 - 0.11\varphi^2 + 0.033\varphi) \lambda^2 \\ &\quad + (5.46\varphi^4 - 16.23\varphi^3 + 14.43\varphi^2 - 3.9\varphi) a \\ &\quad + (-5.76\varphi^4 + 27.49\varphi^3 - 30.65\varphi^2 + 1.96\varphi) a^2 + (a \times b),\end{aligned}$$

where,

$$\begin{aligned}b &= \frac{(32.13a^3 - 5.97a^2 + 0.061a) \lambda}{\lambda + 2} + (-0.26a^3 + 0.088a^2 + 0.0034a) \lambda^3 \\ &\quad + (3.18a^3 - 1.02a^2 - 0.042a) \lambda^2 + (-14.87a^3 + 4.14a^2 + 0.2a) \lambda + 1.\end{aligned}$$

$$Ra_D = 10^3,$$

$$\begin{aligned}\overline{Nu} &= (-8.64\varphi^4 + 22.09\varphi^3 - 23.14\varphi^2 + 10.22\varphi) \\ &\quad + (6.03\varphi^4 - 13.56\varphi^3 + 8.99\varphi^2 - 2.09\varphi) \lambda \\ &\quad + (-0.88\varphi^4 + 1.95\varphi^3 - 1.25\varphi^2 + 0.26\varphi) \lambda^2 \\ &\quad + (17.9\varphi^4 - 32.09\varphi^3 + 12.21\varphi^2 - 0.51\varphi) a \\ &\quad + (-30.31\varphi^4 + 28.36\varphi^3 + 39.56\varphi^2 - 28.83\varphi) a^2 + (a \times b),\end{aligned}$$

where,

$$\begin{aligned}b &= \frac{(16.43a^3 - 24.21a^2 + 3.13a) \lambda}{\lambda + 3} + (0.047a^3 + 0.060a^2 - 0.0065a) \lambda^3 \\ &\quad + (0.038a^3 - 1.06a^2 + 0.12a) \lambda^2 + (-3.85a^3 + 7.05a^2 - 0.79a) \lambda + 1.\end{aligned}$$

8.5 Conclusion

Natural convection in a wavy enclosure filled with fluid-saturated Darcy porous medium has been numerically studied. The waviness of the right wall of the enclosure is controlled by the amplitude, a and number of undulations, λ . The left wall of the enclosure is heated with sinusoidal temperature while the right wall is cooled at a constant temperature. The waviness of the right wall affects the flow field and temperature distribution in the enclosure. The enclosure is occupied by a clockwise circulating flow and small recirculation at the top-left corner of the enclosure. The raise of Darcy-Rayleigh number increases the strength of fluid circulation and heat transfer rate. The heat transfer is enhanced with higher amplitude and more undulations. However, the raise of right wall amplitude gives more enhancement than the increase of right wall undulations. Thus, wavy porous enclosure provides higher rate of heat transfer than that of square porous enclosure. The heat transfer rate decreases on increasing the internal heat generation/absorption parameter.

The effects of enclosure inclination and waviness of the right wall on natural convective flow and heat transfer characteristics in a wavy Darcy porous enclosure with sinusoidal heating are studied numerically as well. The enclosure inclination affects the flow field and temperature distribution as well as heat transfer in the enclosure. Fluid is flowing in clockwise direction with recirculating eddies at the corners of the hot wall when the enclosure is heated from side or inclined. When the hot wall of the enclosure is approaching or on the horizontal plane, multiple flow exist in the enclosure. Symmetric flow field and temperature distribution can be obtained with appropriate combination of the right wall amplitude and number of undulations. However, it is observed that the fluid flow and temperature distribution are non-symmetrical when $a = 0.05$ or $\lambda = 1$ as the porous enclosure is inclined with 90° . Also, inclined enclosure has higher heat transfer rate than the vertical porous enclosure. Higher heat transfer can be obtained when the enclosure is slightly inclined. When the hot wall is located near or on the horizontal plane, the heat transfer rate is the lowest depending on the right wall waviness.

CHAPTER 9: NATURAL CONVECTION IN A WAVY POROUS ENCLOSURE WITH LOCALIZED HEATING

9.1 Introduction

In previous chapter, porous enclosure with a wavy right sidewall is introduced. Fully heating on the wavy porous enclosure has been reported by several researchers, and partial heating is little. The present chapter considers localized heating on the wavy porous enclosure, that is, the different positions of heater on the vertical left wall will be the main concerns. Constant cooling is applied on the wavy right sidewall and its waviness is taken into account as well.

9.2 Problem Statement

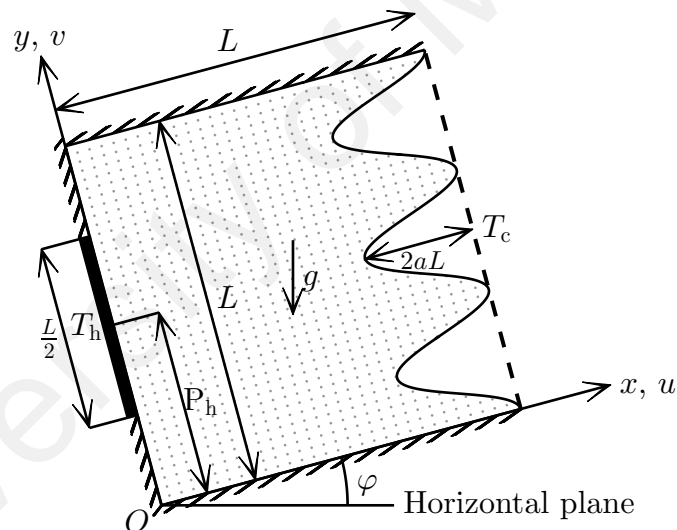


Figure 9.1: Schematic diagram of a wavy porous enclosure with localized heating

Cartesian coordinate system with the schematic of the physical model proposed in the present study is illustrated in Figure 9.1. u and v are the velocity components in the direction of x - and y -axes, respectively and the gravitational acceleration (g) acts in the vertical downward direction. A two-dimensional square enclosure of width and height L with a wavy right sidewall of amplitude a and number of undulations λ is considered. Also, the enclosure is inclined at an angle φ from the horizontal plane. A fixed portion of the left wall ($L/2$) is heated at a higher temperature T_h and the opposite wavy right sidewall is cooled at a constant temperature T_c . Three distinct positions on the left sidewall

are taken as the center of the heater, and it is corresponding to three different heating portions along the left sidewall. Hence, the positions of the heater (P_h) are $L/4$ (bottom heating), $L/2$ (middle heating) and $3L/4$ (top heating). The remaining portion of the left wall, bottom and top walls are adiabatic.

The enclosure is filled with fluid-saturated porous medium. The fluid in the enclosure is incompressible and Newtonian. Furthermore, the fluid is of constant properties and density variation is negligible except in the buoyancy term. That is, Boussinesq approximation is valid for the body force acts on the system, as the buoyancy force is resulting from the density variation with temperature. Fluid flow inside the enclosure is assumed to be laminar, steady and viscous dissipation is also negligible. The porous medium is assumed to be homogeneous, isotropic and in thermal equilibrium with the fluid, and hence Darcy model is used for fluid flow through the porous medium. The governing equations are derived based on the laws of conservation for mass, momentum and energy, and those equations are (4.1) to (4.4) with $q''' = 0$. The boundary conditions of the wavy porous enclosure with localized heating are;

$$\begin{aligned}
 & \text{on all solid walls} : u = v = 0, \\
 & \text{on } x = 0, \quad \left(P_h - \frac{1}{2} \cdot \frac{L}{2}\right) \leq y \leq \left(P_h + \frac{1}{2} \cdot \frac{L}{2}\right) : T = T_h, \\
 & \text{on } x = 0, \quad 0 < y < \left(P_h - \frac{1}{2} \cdot \frac{L}{2}\right) \text{ and } \left(P_h + \frac{1}{2} \cdot \frac{L}{2}\right) < y < L : \frac{\partial T}{\partial x} = 0, \\
 & \text{on } x = L - aL \left(1 - \cos\left(2\pi\lambda \frac{y}{L}\right)\right), \quad 0 \leq y \leq L : T = T_c, \\
 & \text{on } y = 0 \text{ and } L, \quad 0 \leq x \leq L, : \frac{\partial T}{\partial y} = 0,
 \end{aligned} \tag{9.1}$$

where $P_h = L/4, L/2, 3L/4$ are bottom heating, middle heating and top heating, respectively.

The governing equations and boundary conditions are dimensional, and the physical quantities of the variables involved are needed for solving the system of partial differential equations. Appropriate dimensionless variables are able to scale the dimensional governing equations and boundary conditions into dimensionless form, with reduced number of variables that are remained as dimensionless numbers. Hence, the suitable dimensionless variables for the present study are given by equation (3.40). After the substitution of dimensionless variables (3.40) into the governing equations and boundary

conditions (9.1), the dimensionless governing equations are equations (3.41) and (3.42) with $Q = 0$, and the corresponding boundary conditions are,

$$\begin{aligned}
 & \text{on all solid walls} : \Psi = 0, \\
 & \text{on } X = 0, \quad \left(\frac{P_h}{L} - \frac{1}{4}\right) \leq Y \leq \left(\frac{P_h}{L} + \frac{1}{4}\right) : \Theta = 1, \\
 & \text{on } X = 0, \quad 0 < Y < \left(\frac{P_h}{L} - \frac{1}{4}\right) \text{ and } \left(\frac{P_h}{L} + \frac{1}{4}\right) < Y < 1 : \frac{\partial \Theta}{\partial X} = 0, \\
 & \text{on } X = 1 - a(1 - \cos(2\pi\lambda Y)), \quad 0 \leq Y \leq 1 : \Theta = 0, \\
 & \text{on } Y = 0 \text{ and } 1, \quad 0 \leq X \leq 1 : \frac{\partial \Theta}{\partial Y} = 0,
 \end{aligned} \tag{9.2}$$

where $P_h/L = 1/4, 1/2$ and $3/4$ are bottom, middle and top heating respectively.

One of the factors to determine the importance of an energy related model is the heat transfer rate. Therefore, the heat transfer rate is taken as an assessment in the present study. The dimensionless heat transfer rate is the Nusselt number which gives the ratio of convection to conduction heat transfer across the fluid layer. Hence, the local Nusselt number of a point on the sidewall and the average Nusselt number of the heater are given by equations (3.45) and (3.46) with $D = 1/2$.

9.3 Solution Approach

Grid generation method is used to partition the wavy enclosure for numerical simulations. This technique enables the mapping of the wavy physical domain to a square computational domain with regular grids of constant step size. The transformation of the wavy enclosure from the physical coordinate system (X, Y) to a square computational coordinate system (ξ, η) is associated by the algebraic relations (8.3).

In order to perform calculations in the computational domain, the governing equations and boundary conditions are required to be expressed in terms of the computational coordinate system as well. Hence, the transformed governing equations are equations

(3.66) and (3.67), and the corresponding boundary conditions are;

$$\begin{aligned}
& \text{on all solid walls} : \Psi = 0, \\
& \text{on } \xi = 0, \quad \left(\frac{P_h}{L} - \frac{1}{4}\right) \leq \eta \leq \left(\frac{P_h}{L} + \frac{1}{4}\right) : \Theta = 1, \\
& \text{on } \xi = 0, \quad 0 < \eta < \left(\frac{P_h}{L} - \frac{1}{4}\right) \text{ and} \\
& \quad \left(\frac{P_h}{L} + \frac{1}{4}\right) < \eta < 1 : \xi_X \frac{\partial \Theta}{\partial \xi} + \eta_X \frac{\partial \Theta}{\partial \eta} = 0, \quad (9.3) \\
& \text{on } \xi = 1, \quad 0 \leq \eta \leq 1 : \Theta = 0, \\
& \text{on } \eta = 0 \text{ and } 1, \quad 0 \leq \xi \leq 1 : \xi_Y \frac{\partial \Theta}{\partial \xi} + \eta_Y \frac{\partial \Theta}{\partial \eta} = 0.
\end{aligned}$$

Besides that, the Nusselt number in the computational coordinate system is evaluated as given by equations (3.69) and (3.70) with $D = 1/2$.

The transformed governing equations (3.66) and (3.67) with the corresponding boundary conditions (9.3) are now discretized using finite difference approximations. Second order central difference approximation is used for interior points and second order forward and backward approximations are employed for boundary points. SUR method is used to solve stream function equation (3.66) and energy equation (3.67). The process is taken iteratively to solve the equations until the convergence criterion is reached as discussed in the numerical procedure in Chapter 3.

The grids of the computational coordinate system are uniformly spaced in the ξ - and η -directions. The average Nusselt number is used to determine a suitable grid size for simulations. Grid independence tests are carried out for the square ($a = 0$, $\lambda = 0$) and wavy ($a = 0.25$, $\lambda = 5$) enclosures in the case of middle heating with $L_h = L/2$ and L at $Ra_D = 10^3$. Mesh sizes considered are in the range of 60×60 to 300×300 . The results are tabulated in Table 9.1 and it is observed that 150×200 grids are sufficient for simulations.

Table 9.1: Grid independency test for wavy and square enclosures at $Ra_D = 10^3$ with different heating lengths

Grid size	$a = 0, \lambda = 0$		$a = 0.25, \lambda = 5$	
	$L_h = L/2$	$L_h = L$	$L_h = L/2$	$L_h = L$
80×80	18.030	13.122	19.808	14.005
100×100	18.727	13.280	20.388	14.107
150×180	19.812	13.463	21.388	14.265
150×200	19.864	13.469	21.466	14.275
180×180	20.060	13.497	21.554	14.281
200×200	20.240	13.518	21.719	14.297
300×300	20.820	13.572	22.261	14.366

9.4 Results and Discussion

Natural convective flow and heat transfer in a wavy porous enclosure with localized heating on the left wall are investigated numerically. The waviness of the right wall is governed by the amplitude a and number of undulations λ , which are in the range of $0 \leq a \leq 0.15$ and $0 \leq \lambda \leq 3$, respectively. A heater is placed on the left wall and the positions of the heater (P_h) at the left wall are $L/4$ (bottom heating), $L/2$ (middle heating) and $3L/4$ (top heating), respectively. The Darcy-Rayleigh number which determines the importance of convective heat transfer is taken in the range of 10 to 10^3 . Also, the enclosure inclination is investigated in the range of $\varphi = 0^\circ$ to 90° . The flow pattern and temperature distribution in the enclosure are illustrated by plotting the corresponding contours of stream function and temperature inside the enclosure. The heat transfer rate of the enclosure is displayed in terms of local and average Nusselt numbers.

9.4.1 Effects of Heater Location

Figures 9.2 and 9.3 present the effects of heating locations and waviness of the right wall on the temperature distribution and flow field in the wavy enclosure at $Ra_D = 10^3$. The isotherms in Figure 9.2 clearly show that the heating location affects the temperature distribution in the enclosure. For all cases of heating location, it is observed that the isotherms are clustered along the heater. The clustering of isotherms suggests the occurrence of steep temperature gradients in the horizontal direction along the heater,

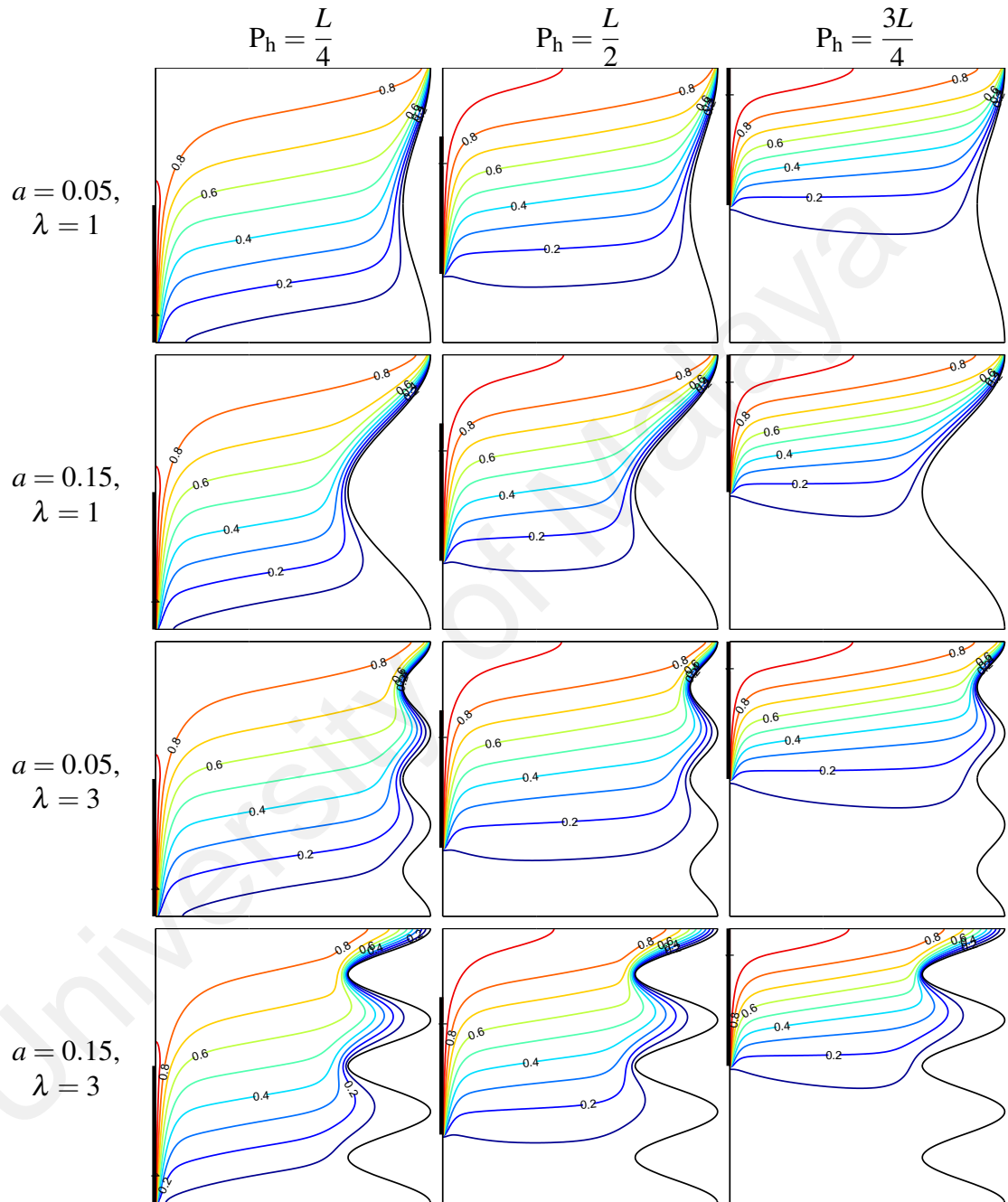


Figure 9.2: Isotherms for various heating locations, amplitude and undulation of the wavy right wall with $\phi = 0^\circ$ at $Ra_D = 10^3$

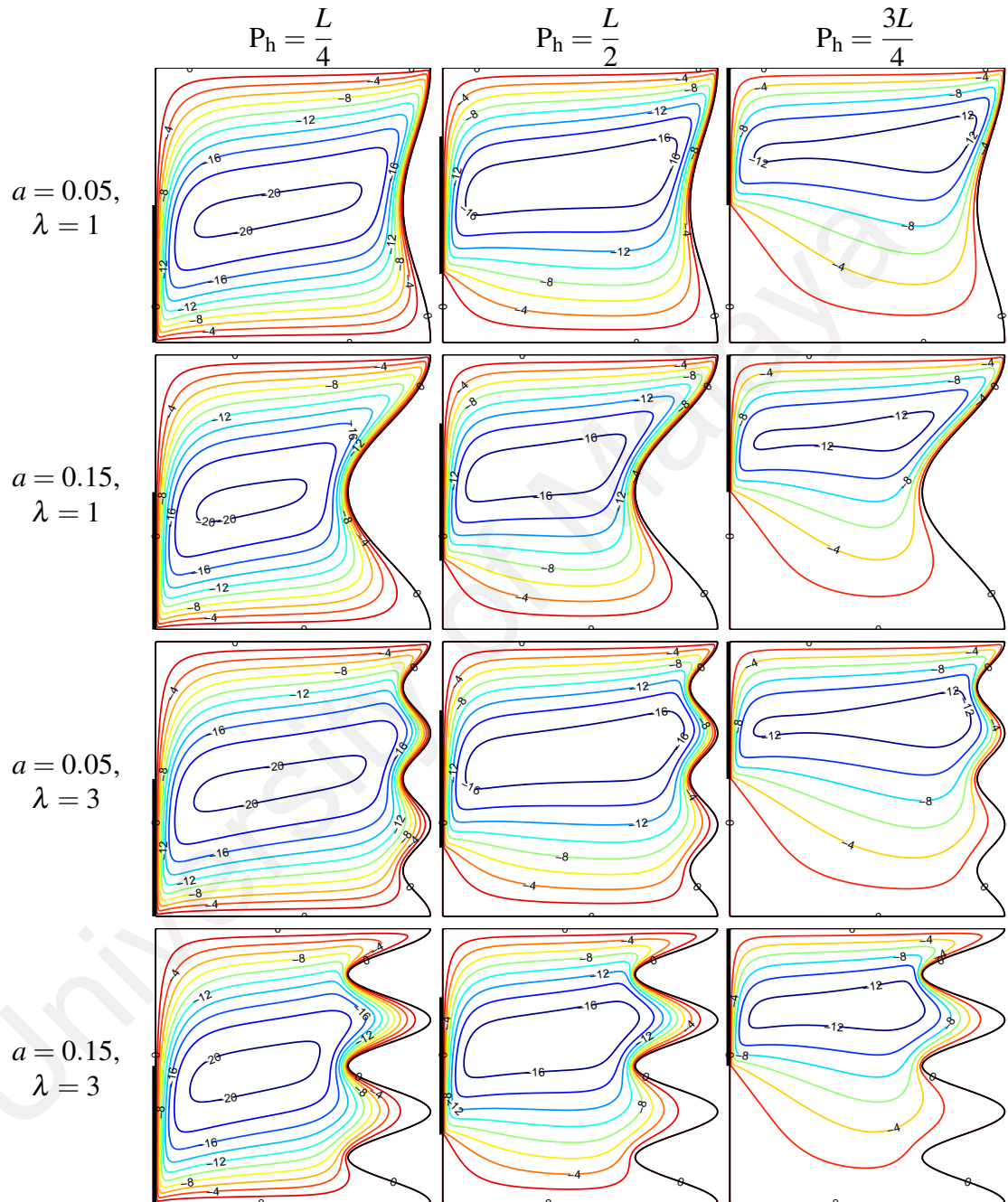


Figure 9.3: Streamlines for various heating locations, amplitude and undulation of the wavy right wall with $\phi = 0^\circ$ at $Ra_D = 10^3$

and it also indicates the development of thermal boundary layer along the heater. The isotherms are also gathered along the upper portion of the right wall, suggests the formation of thermal boundary layer along the top-right corner of the right wall as well. The distributed temperature contours illustrate the thermal stratification from cold region (bottom) to hot region (top) in the enclosure, thus indicate the dominance of convective heat transfer from the heater to the right wall at $Ra_D = 10^3$. When bottom heating is applied on the left wall of the enclosure, the stratification of temperature layers is well distributed in the whole enclosure. As heating location is switched to middle heating, the thermal stratification is begun from one-quarter (position of the leading edge of the heater) of the enclosure, and the lower quarter of the enclosure is filled with isothermal cold fluid only. The same phenomenon can be observed for the case of top heating on the left wall of the enclosure as the thermal stratification occupied the upper portion of the enclosure and the lower half of the enclosure is saturated with isothermal cold fluid. Hence, the variation of heating location affects the thermal distribution in the enclosure, and the area of cold fluid in the lower portion of the enclosure increases as the heating location changes from bottom to top. Also, the heating locations affect the length of thermal boundary layer along the right wall, that is, the thermal boundary layer is extended from the top to center of the right wall when bottom heating is applied and the extension is shorter in the case of top heating.

Figure 9.2 also indicates that the waviness of right wall affects the temperature distribution in the wavy enclosure. The wavy nature of the right wall induces the formation of wavy form of clustered isotherms along the right wall, which is the wavy thermal boundary layer along the right wall. More undulations on the wavy wall increases the number of undulated isotherms along the wall as well. The top undulation is the first area of exposure for heat exchange as hot fluid from the left wall approaches the cold wall. Therefore, thermal boundary layer is appeared along the right wall and gradually vanished along the wall. Hence, the waviness of the right wall affect mostly the temperature distribution along the right wall.

The streamlines in Figure 9.3 show that clockwise circulating flow occupies the whole enclosure when the left wall is heated at the lower half portion (bottom heating). When the heater at the bottom of left wall is constantly heated, the fluid particles adjacent to the heater are constantly receiving heat from the heater and eventually become energize. The energize fluid particles are less dense and begin to rise along the wall. Since the upper section of the left wall is adiabatic, there is no heat exchange in the vertical direction between the wall and the fluid particles as the fluid is rising from the bottom to the top of the enclosure. As the hot fluid reaches the right wall, the fluid particles lose energy to the cold right wall, and become denser and thus sink along the right wall. Hence, clockwise circulating flow is observed in the enclosure for all values of parameters. As the enclosure is experiencing middle and top heating respectively, the streamlines are clustered along the heater, showing that momentum boundary layer is formed along the heater, and it is also inline with the formation of thermal boundary layer as presented in Figure 9.2. The flow is stagnant in the area below the leading edge of the heater, as the lower portion of the enclosure is saturated with cold fluid as shown in the respective isotherms. Also, the main core of the circulating flow is rotating according to the position of the heater placed at the left wall. Moreover, it can be observed that the strength of circulation is getting weaker as the heater position is varied from bottom to top heating.

For a fixed number of undulation, Figure 9.3 shows that a smaller main core is obtained when the wavy enclosure is of higher amplitude. High amplitude on the right wavy wall reduces the space in the enclosure and thus limited fluid flow in the enclosure. On the other hand, when the enclosure is having the same amplitude, higher number of undulations also affect the flow field in the enclosure as the main core is larger when the right wall has more undulations. Momentum boundary layer is observed along the right wall and it is inline with the occurrence of thermal boundary layer as presented in the respective isotherms in Figure 9.2. It appears that the length of momentum boundary layer from the top-right corner is shorter when the wavy wall has more undulations. Stagnation of fluid also occurred in the undulations on the right wall that are close to the bottom wall. It is because the fluid particles are low in energy and dense, thus fluid motion is low at the bottom portion of the undulated right wall.

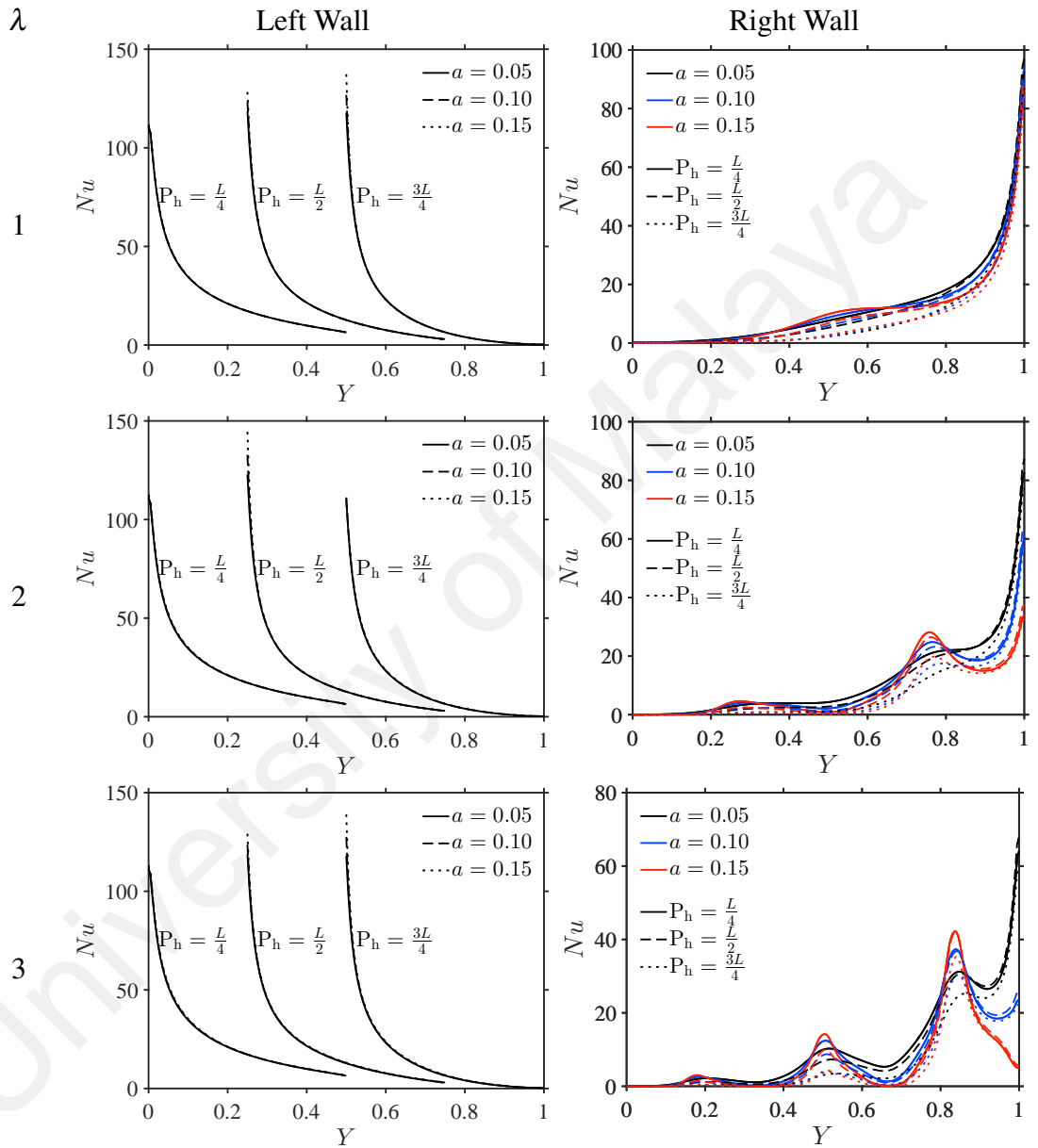


Figure 9.4: Local Nusselt numbers for different heating locations and waviness of right wall when $\varphi = 0^\circ$ at $Ra_D = 10^3$

The local heat transfer along the left and right walls of the enclosure is shown in Figure 9.4. For local heat transfer rate along the left wall, it can be observed that the heat transfer rate is decreasing sharply along the heater. By keeping a fixed heating location and number of undulation, the enclosure with high amplitude has higher heat transfer at the leading edge of the heater. Also, the heat transfer rate at the end of the heater decreases as the heating location changes from bottom to top heating. For heat transfer rate along the right wall, the plot is of wavy form, with the wave number is equal to the number of undulation on the wavy right wall. It can be observed that the local heat transfer along the right wall increases from the leading edge of the right wall, and the peaks and valleys corresponding to the crests and troughs along the wavy wall. On increasing of the amplitude of the wavy wall, the range of heat transfer rate decreases. Also, the heat transfer rate for bottom heating has higher local heat transfer rate along the heater.

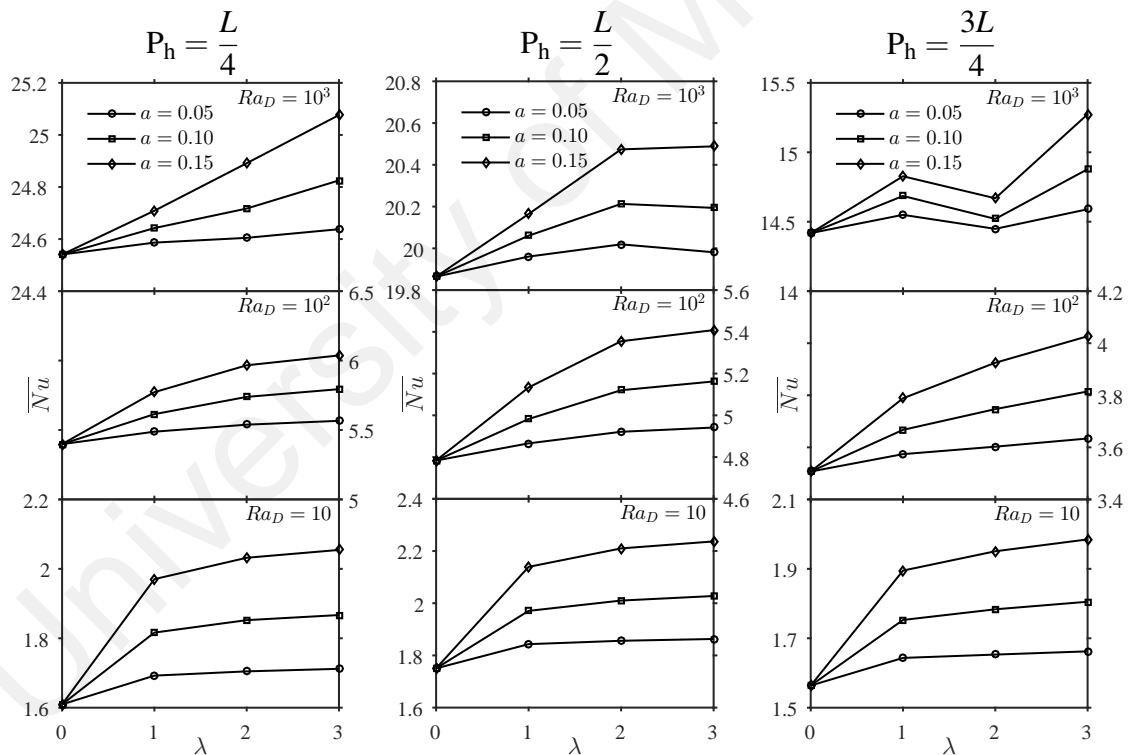


Figure 9.5: Variation of average Nusselt number with different undulations, amplitudes, Darcy-Rayleigh numbers and heating locations when $\varphi = 0^\circ$

The average heat transfer rate along the heater is presented in Figure 9.5. The heat transfer rate increases on increasing of Darcy-Rayleigh number. It is clear that the raise of Darcy-Rayleigh number increases the ratio of buoyancy force to viscous force of fluid in the enclosure. Fluid particles are able to move nearer to the walls, and hence increases the rate of heat exchange between the heater and fluid particles. Also, the average heat transfer rate increases on the raise of amplitude and number of undulations. The undulated right wall increases the surface area for heat exchange between the fluid and the wall, thus increases the rate of heat transfer from the heater into the enclosure. Moreover, it can be observed that bottom heating on the left wall produces higher heat transfer rate compared to other cases of heating location for $Ra_D > 10$. However, middle heating gives higher heat transfer rate than other heating locations when convective strength is low, i.e. at $Ra_D = 10$. Bottom heating triggers the fluid motion from bottom of the wall and the fluid is circulating in the whole enclosure. High Darcy-Rayleigh number reduces the fluid viscosity, and thus higher rate of heat transfer can be achieved when the fluid is flowing along the heater. At low Darcy-Rayleigh number, viscosity of the fluid is high, diffusion will be mode of heat transfer in the enclosure and middle heating is effective in promoting the mixing of fluid in the enclosure.

Correlation equations are derived based on the numerical data obtained to provide the relations between the average Nusselt number and parameters considered in this study. For a square enclosure with a fixed length of heater $L/2$ located at different heating locations on the left wall, the average Nusselt number can be estimated as;

$$\overline{Nu} = 2 \left[\frac{1 + 0.046 Ra_D^{0.71}}{\left(\frac{P_h}{L}\right)^2 - 0.194 \left(\frac{P_h}{L}\right) + 0.507} - 1.535 \left(\frac{P_h}{L}\right)^2 + 3.469 \left(\frac{P_h}{L}\right) - 2.335 \right].$$

It is observed that the behaviours of the variation of average Nusselt number with Darcy-Rayleigh numbers, heating locations and waviness of the right wall are inconsistent.

9.4.2 Effects of Enclosure Inclination

Temperature distributions inside the wavy porous enclosure of waviness $a = 0.15$, $\lambda = 3$ are displayed in Figure 9.6 for different heating locations and enclosure inclinations at $Ra_D = 10^3$. First of all, it is observed that the thermal stratification inside the enclosure is almost parallel to the horizontal plane, and the temperature contours are extended from the heater to the cold wall. This indicates that convection is the dominated mode of heat transfer across the porous enclosure at $Ra_D = 10^3$. Also, it is noticed that the position of heater on the left sidewall determines the region that the temperature field is occupied inside the wavy enclosure. That is, when $\varphi = 0^\circ$, temperature field is well distributed in the whole enclosure during bottom heating. However in the case of middle and top heating, thermal stratification begins from the leading edge of heater, and the region below is saturated with isothermal cold fluid. Furthermore, the enclosure inclination affects the overall temperature distribution inside the wavy porous enclosure. When the enclosure is inclined, the isotherms inside the enclosure are shifted to align with the horizontal plane. For $\varphi = 75^\circ$ and 90° , a plume like structure is appeared on the heater, and the isotherms are now parallel with the adiabatic walls. Thermal boundary layers are formed along the heater, as shown by the clustering of isotherms. The isotherms are also gathered around the top-right corner of the enclosure, or between the second and third undulation of the cold wall. The formation of thermal boundary layers indicates the occurrence of steep temperature gradient in those region.

The streamlines in Figure 9.7 depict the effect of the position of heater on the left sidewall on the flow field inside the porous enclosure as well as the circulation strength of the flow. When $\varphi = 0^\circ$, the flow is circulating in clockwise direction and it is occupying the whole enclosure during bottom heating. In the case of middle and top heating, fluid flow is clockwise, but the momentum boundary layer begins from the leading edge of the heater, and below that, the flow is stagnant, as it is mostly occupied by cold fluid as presented in Figure 9.6. The inner core of the flow is located at the center of the enclosure in the case of middle heating, whereas it is in the mid-height of the heater during middle and top heating. The strength of flow circulation is the highest for bottom heating, and it is gradually decreasing on the rise of heater position on the left sidewall. The flow is

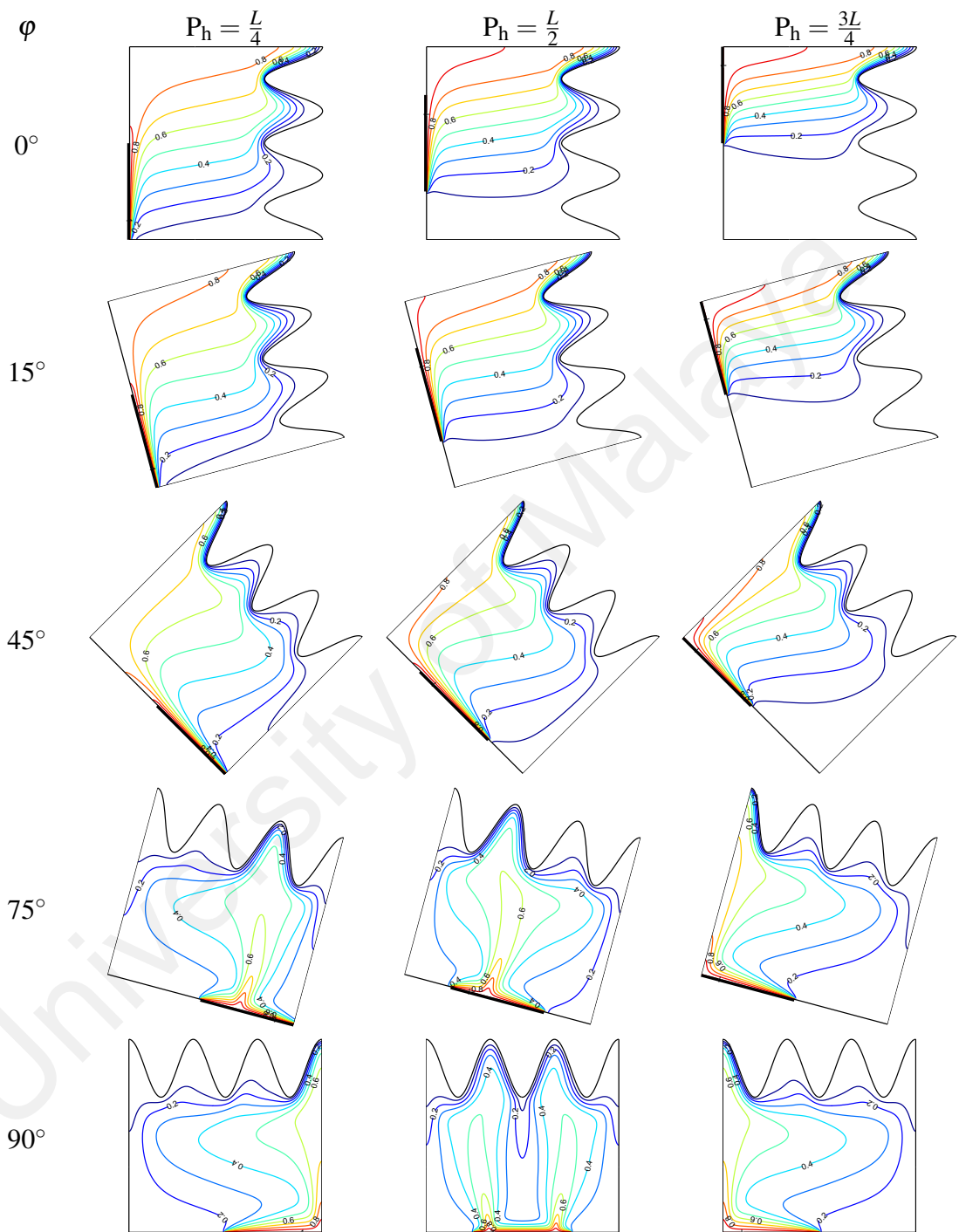


Figure 9.6: Isotherms for various heating locations and enclosure inclinations with $a = 0.15$, $\lambda = 3$ at $Ra_D = 10^3$

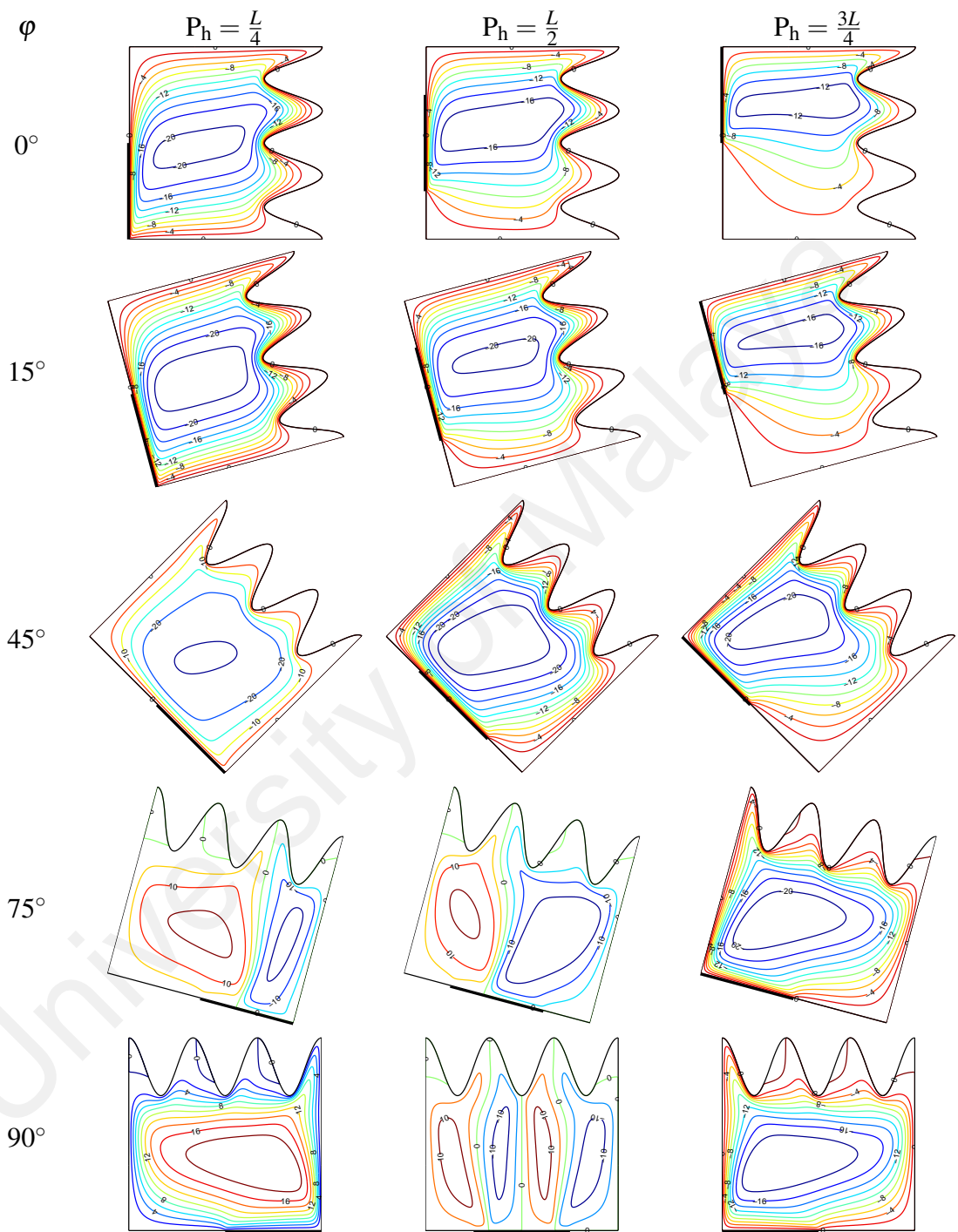


Figure 9.7: Streamlines for various heating locations and enclosure inclinations with $a = 0.15$, $\lambda = 3$ at $Ra_D = 10^3$

unicellular as the enclosure is inclined from 0° to 45° , and dual cell structure is obtained at $\varphi = 75^\circ$ in the case of bottom and middle heating. The flow is multicellular when the heater is parallel with the horizontal plane, that is $\varphi = 90^\circ$ in middle heating case. The formation of multiple flow inside the enclosure is coincided with the appearance of plume like structure in the temperature field as shown in Figure 9.6. Based on the observations, bottom heating on the left sidewall triggers the fluid flow from the bottom of the enclosure as the reduction of density allows the energize fluid particles to raise along the wall until meeting the adiabatic top wall. Hot fluid is cooled along the wavy wall and the fluid particles are now denser, and sink to the bottom of the enclosure. Hence, the fluid flow is clockwise, single cell and it occupies the whole enclosure. In the case of middle and top heating, the heater is only able to heat the fluid near to the heater, and below that, the fluid is remained cold and stagnant. When the enclosure is inclined at 75° and 90° , the heater is almost or parallel to the horizontal plane. In this case, flow separation occurs along the heater, and hence multiple flow is obtained.

The variation of local Nusselt numbers along the heater for different heating locations and enclosure inclinations at $Ra_D = 10^3$ are plotted in Figure 9.8. Based on the overall observation, it is noticed that the heat transfer rate decreases sharply from the leading edge of the heater and it is asymptotically reaching the minimum value at the end of the heater for all heating locations of the porous enclosures with 0° and 45° inclinations. In the case of $\varphi = 90^\circ$, the variation of local Nusselt number is depending on the heating locations. When bottom heating is applied, the heat transfer rate is gradually increasing along the heater. Upon approaching the end of the heater, the heat transfer rate slightly decreases and then it increases rapidly to the end of the heater. The local heat transfer rate of top heating is the reflection of bottom heating case along the mid-height of the porous enclosure, that is, the heat transfer rate decreases rapidly from the leading edge of the heater, and then it slowly decreases to the end of the heater. The local heat transfer rate for middle heating is symmetrical at the mid-height of the porous enclosure. The heat transfer rate is decreasing rapidly from the leading edge of the heater to the mid-length of the heater, and then it is increasing till the end of the heater. It is noticed that the

points with lowest heat transfer of the heater are corresponded to the formation of plume structure in the isotherms shown in Figure 9.6 and flow separation as illustrated in Figure 9.7.

Now, consider the effects of waviness of the right wall on the variation of local Nusselt number. For both $\lambda = 2$ and 3, it can be noticed that the local heat transfer rate along the heater increases on the raise of amplitude for all heating locations, especially at the leading edge of the heater. It is because the raise of amplitude on the wavy wall reduces the distance between the heater and the cold right wall, and hence it promotes better chance of heat exchange between walls. For 2 undulations on the right sidewall, it is noticed that middle heating has higher heat transfer rate at the leading edge of the heater as compared to bottom and top heating. It is also due to the short distance between the edges of the heater and the concave sections of the right sidewall that enhances the heat transfer rate at those sections. However, when the wavy wall has 3 undulations, the leading edge of the heater is always leveled with the convex section of the wavy wall for bottom and middle heating, and concave section for top heating. Hence, the heat transfer rate at the leading edge increases on shifting the heating location from bottom to top. Therefore, it can be noticed that the waviness of the right sidewall also affects of the heat transfer rate of the heater.

Figure 9.9 presents the variation of average Nusselt number of the heater with enclosure inclination, undulations of the right sidewall, heating locations and Darcy-Rayleigh numbers when $a = 0.15$. Based on the overall observation, the average heat transfer rate increases on the raise of number of undulations for all enclosure inclination, heating location and Darcy-Rayleigh number considered. It is because more undulations on the wavy wall increases the surface area of the wall, and hence increases the heat transfer rate from the heater to the cold (right) wall. At $Ra_D = 10$, it can be seen that middle heating has the highest average heat transfer rate, followed by bottom heating, and then top heating. Top heating gives the lowest average heat transfer rate for $\varphi = 0^\circ$ to 45° , and for $\varphi = 60^\circ$ onwards, bottom heating has the lowest average heat transfer rate. For the variation with enclosure inclination, the average heat transfer is slightly increased and then it decreases to minimum at $\varphi = 90^\circ$. The highest heat transfer

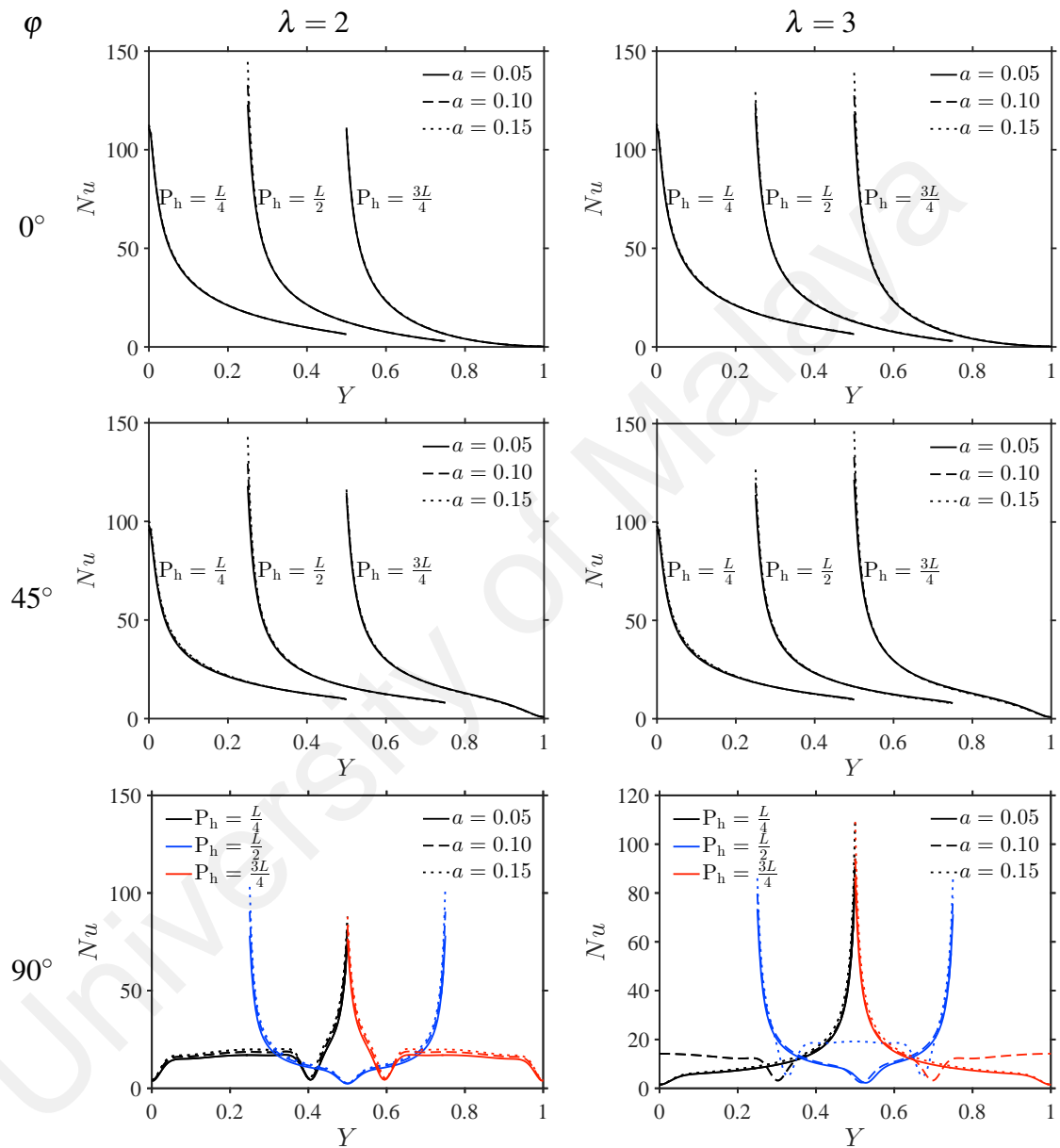


Figure 9.8: Local Nusselt number for different heating locations and waviness of right wall at $Ra_D = 10^3$

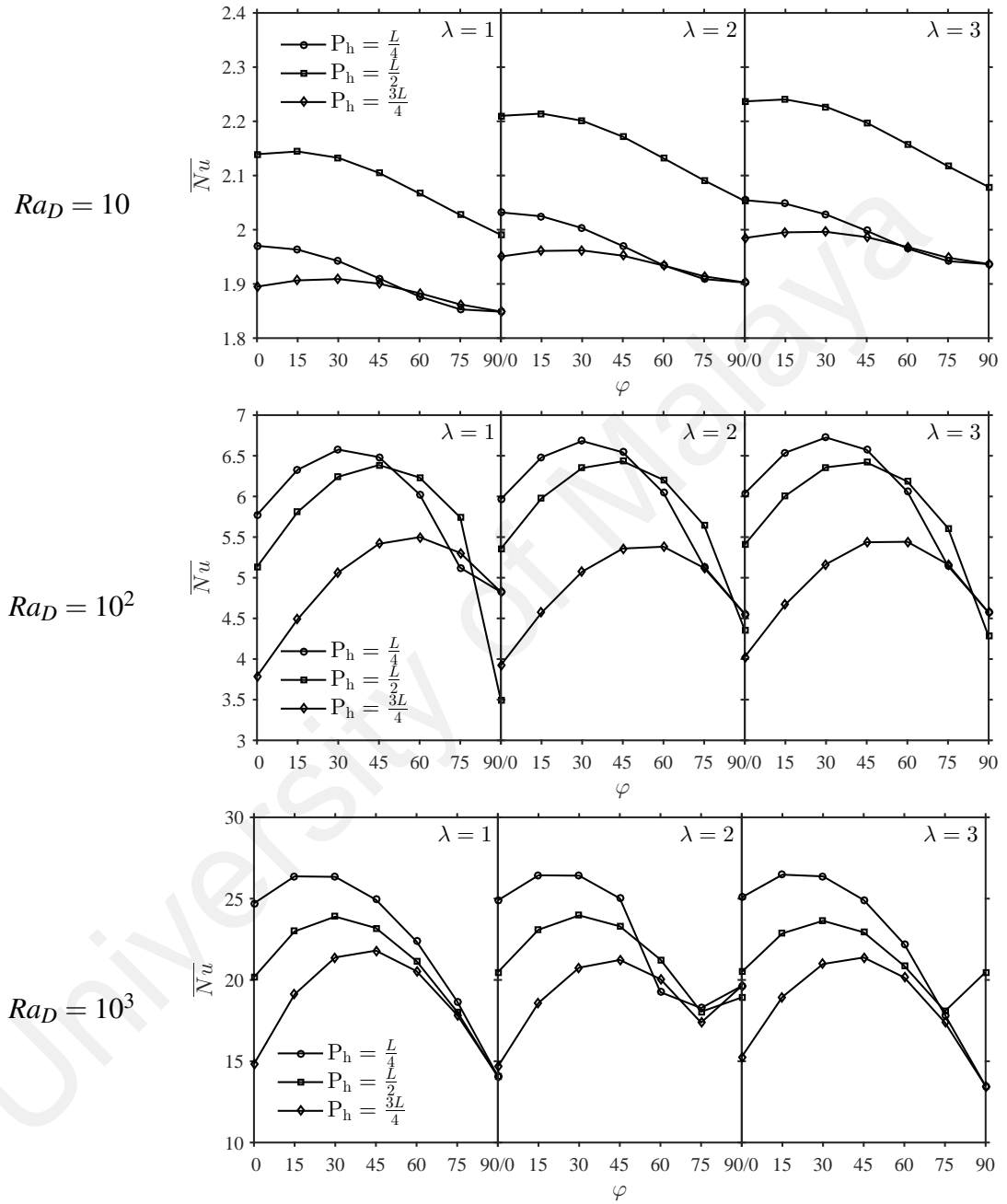


Figure 9.9: Variation of average Nusselt number with enclosure inclination at different heating locations when $a = 0.15$ at various Darcy-Rayleigh numbers

is obtained when $\varphi = 0^\circ, 15^\circ$ and 30° , for bottom, middle and top heating, respectively. When the Darcy-Rayleigh number is low, i.e. $Ra_D = 10$, the ratio of buoyancy to viscous force is low. Since viscosity is high at low Darcy-Rayleigh number, heat is transferred from the heater to fluid particles by conduction, and hence middle heating is able to distribute heat from the heater to the whole domain, and hence, it is the most effective for heat transfer at low Darcy-Rayleigh number. Also, the orientation of hot and cold walls with the gravity is modified when the enclosure is inclined. The porous enclosure has higher heat transfer rate when the enclosure is slightly inclined, that is, the heating direction is slightly slanted from the vertically acting gravity. However, when the heater of the porous enclosure is approaching the horizontal plane, the heating direction is almost parallel to the buoyancy force, flow separation occurs, and thus lower the heat transfer rate along the heater.

When the Darcy-Rayleigh number is increased to 10^2 , bottom heating is now having the highest average heat transfer rate up to $\varphi = 45^\circ$, followed by middle heating and lastly top heating. The highest average heat transfer rate is obtained when the enclosure is inclined at $30^\circ, 45^\circ$ and 60° for middle, bottom and top heating, respectively. However, for the lowest average heat transfer rate, it is obtained at 90° for middle and bottom heating, but it is 0° for top heating. For $Ra_D = 10^3$, middle heating is again having the highest average heat transfer rate, and the lowest is top heating. The enclosure inclination with the highest average heat transfer rate is similar as $Ra_D = 10$, but the lowest average heat transfer is the same enclosure inclination as $Ra_D = 10^2$. Increasing the Darcy-Rayleigh number increases the buoyancy ratio, and lower viscous force between fluid particles. Hence, when partial heating is applied on the left wall, fluid adjacent of the heater is energized and easily raise along the left wall and eventually fluid flow is fully developed inside the porous enclosure. Bottom heating is able to drive the fluid flows from the bottom of the enclosure, and hence gives overall higher strength of fluid flow as presented in Figure 9.7. So, fluid velocity is higher near the heater, and hence increases the rate of heat transfer between heater and fluid.

9.5 Conclusion

Natural convection in a wavy porous enclosure with localized heating was investigated numerically. The position of heater on the left wall affects the flow field and temperature distribution in the enclosure. Also, the waviness of the right wall affects the flow and temperature fields especially along the right wall. A clockwise circulating flow is observed regardless of the position of heater. However, the heating locations affect the location of core region of convective cell. Heat transfer rate is high at the leading edge of heater and low heat transfer rate is obtained at the end of the heater. It is observed that the waviness of the right wall enhances the heat transfer rate into the enclosure. Bottom heating produces highest heat transfer into the enclosure when the convection strength is strong, i.e. $Ra_D \geq 10^2$. Middle heating enhances the heat transfer into the enclosure for low Darcy-Rayleigh number ($Ra_D = 10$).

Numerical investigation has been performed for natural convection in an inclined wavy porous enclosure with localized heating. The enclosure inclination also alters the flow and temperature fields inside the porous enclosure as multiple flows and plume structures are observed when the partially heated left wall is approaching the horizontal plane. Other than that, the waviness of the right sidewall coupled with heating locations and enclosure inclination affect the distribution of local heat transfer rate along the heater. Higher heat transfer rate can be obtained for different heating locations when the enclosure is slightly inclined, but low heat transfer rate is acquired when the partially heated wall is approaching or parallel to the horizontal plane. The present study is useful for providing us better understanding on the design of the solar collection panels and cooling of electronic devices.

CHAPTER 10: SUMMARY AND CONCLUSION

10.1 Summary

Buoyancy-driven flow and heat transfer through porous medium have been greatly attended by many researchers due to the importance to natural phenomena, geosciences, medical sciences and engineering applications. In particular, the modelling of natural convection process inside the porous enclosures is important for the understand of fluid flow and heat transfer of the solar collectors, geothermal reservoirs, blood flow, electronic equipment cooling and other applications. Enclosures with rectangular shape have been common, but to serve different purposes, non-rectangular enclosure sometimes is more practical. The present numerical study focuses on natural convective flow and heat transfer inside the porous enclosures with different geometries. The different enclosure shapes, which are square, trapezoidal, triangular, oblique and wavy have been considered to investigate the variation of flow and heat transfer inside the porous enclosures. Also, different thermal boundary conditions have been applied as well, to examine the effect of different thermal boundary conditions on the flow and heat transfer inside the porous enclosure.

The enclosure under consideration is two-dimensional, and it is filled with fluid-saturated porous medium. Darcy model is adopted for fluid flow through the porous medium. The fluid is Newtonian and it has constant properties, whereas the fluid flow is viscous, laminar and incompressible. Also, Boussinesq approximation is valid for density variation. Based on the mentioned assumptions, governing equations are derived, as well as different boundary conditions with appropriate mathematical formulae. To obtain the solution for a specific problem, the governing equations are required to be solved simultaneously with the respective boundary conditions. The governing equations for natural convective flow are partial differential equations, which can be solved using finite difference method. The square, trapezoidal and triangular porous enclosures in the present study have been solved directly using finite difference method within the respective domains. However, it is noticed that the direct method is not applicable for some domains, such as the wavy enclosure. Hence, grid generation method is introduced

to map the non-rectangular domain to a rectangular domain. The primitive variables, stream function and temperature, are then solved iteratively until the convergence is reached. To ensure the validity of the numerical algorithm, the results obtained are compared with the other results available in the literature. A good agreement is found and so it gave the confidence to implement the algorithm in solving the enclosure problems.

The different enclosure shapes considered are reported from Chapter 4 to 9. Different temperature boundary conditions, which are constant, sinusoidal, linear and discrete heating, are also investigated for the enclosure problems. Other than that, the enclosure inclination which alters the orientation of the thermally active walls is examined as well.

10.2 Conclusion

Based on the overall results of this study, it can be concluded that,

1. The average heat transfer rate increases with Darcy-Rayleigh number, regardless of the enclosure shape, thermal boundary condition, enclosure inclination and internal heat generation parameter.
2. The average rate of heat transfer decreases with the raise of internal heat generation parameter at high Darcy-Rayleigh number.
3. At low Darcy-Rayleigh number, the average rate of heat transfer decreases with the raise of internal heat generation parameter up to $Q = 0$. For $Q > 0$, its behaviour is depending on the enclosure shape considered.
4. The isosceles triangular porous enclosure give better heat transfer rate than the right-angled triangular porous enclosure.
5. The square porous enclosure gives higher heat transfer rate than the right-angled trapezoidal and triangular porous enclosures, but the oblique porous enclosure has higher heat transfer rate than the square porous enclosures when $Ra_D > 10$.
6. Among all enclosure shapes, wavy porous enclosure gives the highest heat transfer enhancement.

7. The heat transfer rate of the wavy porous enclosure increases with the waviness of the right wall of the enclosure. The raise of amplitude gives better enhancement on the heat transfer than that of the undulations on the right wall.
8. Sinusoidal heating and linear wall temperature ($\Theta = 1 - Y$) give multiple flow inside the porous enclosures.
9. Single cell flow has higher heat transfer rate than the porous enclosure with multiple flow in the case of fully heating on the wall.
10. Constant heating gives the highest heat transfer enrichment among all thermal boundary conditions considered.
11. Linear wall temperature ($\Theta = Y$) gives the least heat transfer rate among all thermal boundary conditions.
12. Localized heating with short heater gives higher heat transfer than fully heating on the wall.
13. Localized heating on the left wall with heater placed at the lower section of the wall gives higher heat transfer rate than the heater placed at higher position (middle and top) along the wall.
14. The heat transfer rate behave non-linearly with the enclosure inclination. However, it is noticed that the heat transfer rate is higher when the enclosure is slightly inclined.
15. The heat transfer rate is low when the hot wall is approaching the horizontal plane, that is $\varphi = 75^\circ$ and 90° .

10.3 Future Work

Natural convection inside the porous enclosure has been investigated numerically. This work is useful for the improvement and development on the design of heat dependent devices, such as the solar collectors, geothermal reservoirs, electronic equipment cooling and more. To get better modelling of those engineering applications, the effect of mass diffusion, nano-particles, magnetic field and others are going to be taken into account for further investigation.

REFERENCES

- Adjlout, L., Imine, O., Azzi, A., & Belkadi, M. (2002). Laminar natural convection in an inclined cavity with a wavy wall. *International Journal of Heat and Mass Transfer*, *45*, 2141–2152.
- Ahmed, S. E., Oztop, H. F., & Al-Salem, K. (2014). Natural convection coupled with radiation heat transfer in an inclined porous cavity with corner heater. *Computers and Fluids*, *102*, 74–84.
- Al-Farhany, K. & Turan, A. (2012). Numerical study of double diffusive natural convective heat and mass transfer in an inclined rectangular cavity filled with porous medium. *International Communications in Heat and Mass Transfer*, *39*, 174–181.
- Anandalakshmi, R., Kaluri, R. S., & Basak, T. (2011). Heatline based thermal management for natural convection within right-angled porous triangular enclosures with various thermal conditions of walls. *Energy*, *36*, 4879–4896.
- Anandalakshmi, R. & Basak, T. (2012a). Heatline analysis for natural convection within porous rhombic cavities with isothermal/nonisothermal hot bottom wall. *Industrial and Engineering Chemistry Research*, *51*, 2113–2132.
- Anandalakshmi, R. & Basak, T. (2012b). Analysis of energy management via entropy generation approach using natural convection in porous rhombic enclosures. *Chemical Engineering Science*, *79*, 75–93.
- Anandalakshmi, R. & Basak, T. (2013a). Numerical simulations for the analysis of entropy generation during natural convection in porous rhombic enclosures. *Numerical Heat Transfer; Part A*, *63*(4), 257–284.
- Anandalakshmi, R. & Basak, T. (2013b). Analysis of natural convection via entropy generation approach in porous rhombic enclosures for various thermal aspect ratio. *International Journal of Heat and Mass Transfer*, *64*, 224–244.
- Anandalakshmi, R. & Basak, T. (2013c). Heatline based thermal management for natural convection in porous rhombic enclosures with isothermal hot side or bottom wall. *Energy Conversion and Management*, *67*, 287–296.
- Aounallah, M., Addad, Y., Benhamadouche, S., Imine, O., Adjlout, L., & Laurence, D. (2007). Numerical investigation of turbulent natural convection in an inclined square cavity with a hot wavy wall. *International Journal of Heat and Mass Transfer*, *50*, 1683–1693.
- Badruddin, I. A., Zainal, Z. A., Narayana, P. A. A., & Seetharamu, K. N. (2007). Numerical analysis of convection conduction and radiation using a non-equilibrium model in a square porous cavity. *International Journal of Thermal Sciences*, *46*, 20–29.

- Báez, E. & Nicolás, A. (2006). 2D natural convection flows in titled cavities: Porous media and homogeneous fluids. *International Journal of Heat and Mass Transfer*, 49, 4773–4785.
- Basak, T., Roy, S., Paul, T., & Pop, I. (2006). Natural convection in a square cavity filled with a porous medium: Effects of various thermal boundary conditions. *International Journal of Heat and Mass Transfer*, 49, 1430–1441.
- Basak, T., Roy, S., & Takhar, H. S. (2007). Effect of nonuniformly heated wall(s) on a natural-convection flow in a square cavity filled with a porous medium. *Numerical Heat Transfer, Part A*, 51(10), 959–978.
- Basak, T., Roy, S., & Babu, S. K. (2008a). Natural convection and flow simulation in differentially heated isosceles triangular enclosures filled with porous medium. *Chemical Engineering Science*, 63, 3328–3340.
- Basak, T., Roy, S., Babu, S. K., & Pop, I. (2008b). Finite element simulations of natural convection flow in an isosceles triangular enclosure filled with a porous medium: Effects of various thermal boundary conditions. *International Journal of Heat and Mass Transfer*, 51, 2733–2741.
- Basak, T., Roy, S., Singh, A., & Balakrishnan, A. R. (2009a). Natural convection flows in porous trapezoidal enclosures with various inclination angles. *International Journal of Heat and Mass Transfer*, 52, 4612–4623.
- Basak, T., Roy, S., Singh, A., & Pop, I. (2009b). Finite element simulation of natural convection flow in a trapezoidal enclosure filled with porous medium due to uniform and non-uniform heating. *International Journal of Heat and Mass Transfer*, 52, 70–78.
- Basak, T., Roy, S., Singh, S. K., & Pop, I. (2009c). Finite element simulation of natural convection within porous trapezoidal enclosures for various inclination angles: Effect of various wall heating. *International Journal of Heat and Mass Transfer*, 52, 4135–4150.
- Basak, T., Roy, S., Matta, A., & Pop, I. (2010a). Analysis of heatlines for natural convection within porous trapezoidal enclosures: Effect of uniform and non-uniform heating of bottom wall. *International Journal of Heat and Mass Transfer*, 53, 5947–5961.
- Basak, T., Roy, S., Ramakrishna, D., & Pop, I. (2010b). Visualization of heat transport during natural convection within porous triangular cavities via heatline approach. *Numerical Heat Transfer, Part A*, 57(6), 431–452.
- Basak, T., Gunda, P., & Anandalakshmi, R. (2012). Analysis of entropy generation during natural convection in porous right-angled triangular cavities with various thermal boundary conditions. *International Journal of Heat and Mass Transfer*, 55, 4521–4535.
- Basak, T., Anandalakshmi, R., & Biswal, P. (2013a). Analysis of convective heat flow visualization within porous right angled triangular enclosures with a concave/convex hypotenuse. *Numerical Heat Transfer, Part A*, 64(8), 621–647.

- Basak, T., Anandalakshmi, R., Roy, S., & Pop, I. (2013b). Role of entropy generation on thermal management due to thermal convection in porous trapezoidal enclosures with isothermal and non-isothermal heating of wall. *International Journal of Heat and Mass Transfer*, 67, 810–828.
- Basak, T., Singh, A. K., Richard, R., & Roy, S. (2013c). Finite element simulation with heatlines and entropy generation minimization during natural convection within porous tilted square cavities. *Industrial and Engineering Chemistry Research*, 52, 8046–8061.
- Baytas, A. C. & Pop, I. (1999). Free convection in oblique enclosures filled with a porous medium. *International Journal of Heat and Mass Transfer*, 42, 1047–1057.
- Baytaş, A. C. (2000). Entropy generation for natural convection in an inclined porous cavity. *International Journal of Heat and Mass Transfer*, 43, 2089–2099.
- Baytaş, A. C. & Pop, I. (2001). Natural convection in a trapezoidal enclosure filled with a porous medium. *International Journal of Engineering Sciences*, 39, 125–134.
- Baytas, A. C. & Pop, I. (2002). Free convection in a square porous cavity using a thermal nonequilibrium model. *International Journal of Thermal Sciences*, 41, 861–870.
- Bhardwaj, S. & Dalal, A. (2015). Effect of undulations on the natural convection heat transfer and entropy generation inside a porous right-angled triangular enclosure. *Numerical Heat Transfer, Part A*, 67(9), 972–991.
- Bhardwaj, S., Dalal, A., & Pati, S. (2015). Influence of wavy wall and non-uniform heating on natural convection heat transfer and entropy generation inside porous complex enclosure. *Energy*, 79, 467–481.
- Bhuvaneshwari, M., Sivasankaran, S., & Kim, Y. J. (2011). Effect of aspect ratio on natural convection in a porous enclosure with partially active thermal walls. *Computers and Mathematics with Applications*, 62, 3844–3856.
- Braga, E. J. & de Lemos, M. J. S. (2008). Computation of turbulent free convection in left and right tilted porous enclosures using a macroscopic $k - \epsilon$ model. *International Journal of Heat and Mass Transfer*, 51, 5279–5287.
- Brewster, H. D. (2009). *Fluid mechanics*. Jaipur, India: Oxford Book Company.
- Chamkha, A. J. & Al-Naser, H. (2001). Double-diffusive convection in an inclined porous enclosure with opposing temperature and concentration gradients. *International Journal of Thermal Sciences*, 40, 227–244.
- Chamkha, A. J. & Al-Mudhaf, A. (2008). Double-diffusive natural convection in inclined porous cavities with various aspect ratio and temperature-dependent heat source or sink. *Heat and Mass Transfer*, 44, 679–693.
- Chery, L. & de Marsily, G. (Eds.). (2007). *Aquifer systems management: Darcy's legacy in a world of impending water shortage*. UK: Taylor and Francis/Balkema.

- Chen, Y.-Y., Li, B.-W., & Zhang, J.-K. (2016). Spectral collocation method for natural convection in a square porous cavity with local thermal equilibrium and non-equilibrium models. *International Journal of Heat and Mass Transfer*, *96*, 84–96.
- Chen, Y.-H. & Lin, H.-T. (1997). Natural convection in an inclined enclosure with a fluid layer and a heat-generating porous bed. *Heat and Mass Transfer*, *33*, 247–255.
- Cho, C.-C. (2014). Heat transfer and entropy generation of natural convection in nanofluid-filled square cavity with partially-heated wavy surface. *International Journal of Heat and Mass Transfer*, *77*, 818–827.
- Costa, V. A. F. (2003). Unified streamline, heatline and massline methods for the visualization of two-dimensional heat and mass transfer in anisotropic media. *International Journal of Heat and Mass Transfer*, *46*, 1309–1320.
- Costa, V. A. F. (2004). Double-diffusive natural convection in parallelogrammic enclosures filled with fluid-saturated porous media. *International Journal of Heat and Mass Transfer*, *47*, 2699–2714.
- Dalal, A. & Das, M. K. (2005). Laminar natural convection in an inclined complicated cavity with spatially variable wall temperature. *International Journal of Heat and Mass Transfer*, *48*, 3833–3854.
- Hoffman, K. A. & Chiang, S. T. (2000). *Computational fluid dynamics* (4th ed.). USA: Engineering Education System.
- Hsiao, S.-W. (1998). Natural convection in an inclined porous cavity with variable porosity and thermal dispersion effects. *International Journal of Numerical Methods for Heat and Fluid Flow*, *8*(1), 97–117.
- Hussain, S. H., Jabbar, M. Y., & Mohamad, A. S. (2011). Influence of presence of inclined centered baffle and corrugation frequency on natural convection heat transfer flow of air inside a square enclosure with corrugated side walls. *International Journal of Thermal Sciences*, *50*, 1799–1808.
- Incropera, F. P., Dewitt, D. P., Bergman, T. L., & Lavine, A. S. (2007). *Fundamentals of heat and mass transfer* (6th ed.). Singapore: John Wiley and Sons (Asia) Pte Ltd.
- Kaluri, R. S. & Basak, T. (2010). Heatline analysis of thermal mixing due to natural convection in discretely heated porous cavities filled with various fluids. *Chemical Engineering Science*, *65*, 2132–2152.
- Kaluri, R. S. & Basak, T. (2011a). Entropy generation due to natural convection in discretely heated porous square cavities. *Energy*, *36*, 5065–5080.
- Kaluri, R. S. & Basak, T. (2011b). Role of entropy generation on thermal management during natural convection in porous square cavities with distributed heat sources. *Chemical Engineering Science*, *66*, 2124–2140.

- Kayhani, M. H., Nazari, M., & Shakeri, E. (2011). The effects of fluid-to-solid conductivity ratio, rayleigh number and interstitial heat transfer coefficient on the TNE free convection in a porous enclosure. *Transport in Porous Media*, 87, 625–633.
- Khanafer, K., Al-Azmi, B., Marafie, A., & Pop, I. (2009). Non-Darcian effects on natural convection heat transfer in a wavy porous enclosure. *International Journal of Heat and Mass Transfer*, 52, 1887–1896.
- Khandelwal, M. K., Bera, P., & Chakrabarti, A. (2012). Influence of periodicity of sinusoidal bottom boundary condition on natural convection in porous enclosure. *International Journal of Heat and Mass Transfer*, 55, 2889–2900.
- Kumar, A. & Bera, P. (2009). Natural convection in an anisotropic porous enclosure due to nonuniform heating from the bottom wall. *ASME Journal of Heat Transfer*, 131, 072601-1–072601-13.
- Liu, W., Shen, S., & Riffat, S. B. (2002). Heat transfer and phase change of liquid in an inclined enclosure packed with unsaturated porous media. *International Journal of Heat and Mass Transfer*, 45, 5209–5219.
- Mansour, M. A., Abd El-Aziz, M. M., Mohamed, R. A., & Ahmed, S. E. (2011a). Numerical simulation of natural convection in wavy porous cavities under the influence of thermal radiation using a thermal non-equilibrium model. *Transport in Porous Media*, 86, 585–600.
- Mansour, M. A., Abd-Elaziz, M. M., Mohamed, R. A., & Ahmed, S. E. (2011b). Unsteady natural convection, heat and mass transfer in inclined triangular porous enclosures in the presence of heat source or sink: Effect of sinusoidal variation of boundary conditions. *Transport in Porous Media*, 87, 7–23.
- Mansour, M. A., Abd-Elaziz, M. M., Abdalla, R., & Elsayed, S. (2012). Effect of sinusoidal variations of boundary conditions on unsteady double diffusive convection in a square enclosure filled with a porous medium. *International Journal of Numerical Methods for Heat and Fluid Flow*, 22(1), 129–146.
- Misirlioglu, A., Baytas, A. C., & Pop, I. (2005). Free convection in a wavy cavity filled with a porous medium. *International Journal of Heat and Mass Transfer*, 48, 1840–1850.
- Misirlioglu, A., Baytas, A. C., & Pop, I. (2006). Natural convection inside an inclined wavy enclosure filled with a porous medium. *Transport in Porous Media*, 64, 229–246.
- Moya, S. L., Ramos, E., & Sen, M. (1987). Numerical study of natural convection in a titled rectangular porous material. *International Journal of Heat and Mass Transfer*, 30, 741–756.
- Murthy, P. V. S. N., Rathish Kumar, B. V., & Singh, P. (1997). Natural convection heat transfer from a horizontal wavy surface in a porous enclosure. *Numerical Heat Transfer, Part A*, 31(2), 207–221.

- Ni, J. & Beckermann, C. (1991). Natural convection in a vertical enclosure filled with anisotropic porous media. *ASME Journal of Heat Transfer*, 113, 1033–1037.
- Nield, D. A. & Bejan, A. (2013). *Convection in porous media* (4th ed.). New York: Springer.
- Oosthuizen, P. H. & Naylor, D. (1999). *An introduction to convective heat transfer analysis*. Singapore: WCB/McGraw-Hill.
- Oztop, H. F. (2007). Natural convection in partially cooled and inclined porous rectangular enclosures. *International Journal of Thermal Sciences*, 46, 149–156.
- Oztop, H. F., Varol, Y., & Pop, I. (2009). Investigation of natural convection in triangular enclosure filled with porous media saturated with water near 4°C. *Energy Conversion and Management*, 50, 1473–1480.
- Öztop, H. F., Estellé, P., Yan, W.-M., Al-Salem, K., Orfi, J., & Mahian, O. (2015). A brief review of natural convection in enclosures under localized heating with and without nanofluids. *International Communications in Heat and Mass Transfer*, 60, 37–44.
- Ramakrishna, D., Basak, T., & Roy, S. (2013). Heatlines for visualization of heat transport for natural convection within porous trapezoidal enclosures with various wall heating. *Numerical Heat Transfer, Part A*, 63(5), 347–372.
- Ramakrishna, D., Basak, T., Roy, S., & Momoniat, E. (2014). Analysis of thermal efficiency via analysis of heat flow and entropy generation during natural convection within porous trapezoidal cavity. *International Journal of Heat and Mass Transfer*, 77, 98–113.
- Rathish Kumar, B. V., Murthy, P. V. S. N., & Singh, P. (1998). Free convection heat transfer from an isothermal wavy surface in a porous enclosure. *International Journal for Numerical Methods in Fluids*, 28, 633–661.
- Rathish Kumar, B. V. (2000). A study of free convection induced by a vertical wavy surface with heat flux in a porous enclosure. *Numerical Heat Transfer, Part A*, 37(5), 493–510.
- Rathish Kumar, B. V., Singh, P., & Bansod, V. J. (2002). Effect of thermal stratification on double-diffusive natural convection in a vertical porous enclosure. *Numerical Heat Transfer, Part A*, 41(4), 421–447.
- Rathish Kumar, B. V. & Shalini. (2003). Free convection in a non-Darcian wavy porous enclosure. *International Journal of Engineering Science*, 41(16), 1827–1848.
- Rathish Kumar, B. V. & Kumar, B. (2004). Parallel computation of natural convection in trapezoidal porous enclosure. *Mathematics and Computers in Simulation*, 65, 221–229.
- Rathish Kumar, B. V. & Shalini. (2005). Double diffusive natural convection in a doubly stratified wavy porous enclosure. *Applied Mathematics and Computation*, 171, 180–202.

- Sabeur-Bendehina, A., Imine, O., & Adjlout, L. (2011). Laminar free convection in undulated cavity with non-uniform boundary conditions. *Comptes Rendus Mecanique*, 339, 42–57.
- Saeid, N. H. & Pop, I. (2004). Transient free convection in a square cavity filled with a porous medium. *International Journal of Heat and Mass Transfer*, 47, 1917–1924.
- Saeid, N. H. & Mohamad, A. A. (2005). Natural convection in a porous cavity with spatial sidewall temperature variation. *International Journal of Numerical Methods for Heat and Fluid Flow*, 15(6), 555–566.
- Saeid, N. H. (2005). Natural convection in porous cavity with sinusoidal bottom wall temperature variation. *International Communications in Heat and Mass Transfer*, 32, 454–463.
- Sankar, M., Bhuvaneswari, M., Sivasankaran, S., & Do, Y. (2011). Buoyancy induced convection in a porous cavity with partially thermally active sidewalls. *International Journal of Heat and Mass Transfer*, 54, 5173–5182.
- Sathiyamoorthy, M., Basak, T., Roy, S., & Pop, I. (2007). Steady natural convection flow in a square cavity filled with a porous medium for linearly heated side wall(s). *International Journal of Heat and Mass Transfer*, 50, 1892–1901.
- Selamat, M. S., Roslan, R., & Hashim, I. (2012). Natural convection in an inclined porous cavity with spatial sidewall temperature variations. *Journal of Applied Mathematics*, 2012, 1–10.
- Sheremet, M. A. & Pop, I. (2015a). Natural convection in a wavy porous cavity with sinusoidal temperature distributions on both side walls filled with a nanofluid: Buongiorno's mathematical model. *ASME Journal of Heat Transfer*, 137, 072601-1–072601-8.
- Sheremet, M. A. & Pop, I. (2015b). Free convection in a triangular cavity filled with a porous medium saturated by a nanofluid: Buongiorno's mathematical model. *International Journal of Numerical Methods for Heat and Fluid Flow*, 25(5), 1138–1161.
- Sheremet, M. A., Pop, I., & Bachok, N. (2016). Effect of thermal dispersion on transient natural convection in a wavy-walled porous cavity filled with a nanofluid: Tiwari and Das' nanofluid model. *International Journal of Heat and Mass Transfer*, 92, 1053–1060.
- Singh, A. K., Paul, T., & Thorpe, G. R. (2000). Natural convection in a non-rectangular porous enclosure. *Forschung im Ingenieurwesen*, 65, 301–308.
- Singh, S. & Bhargava, R. (2014). Numerical study of natural convection within a wavy enclosure using meshfree approach: Effect of corner heating. *The Scientific World Journal*, 2014, 1–18.
- Sivasankaran, S., Do, Y., & Sankar, M. (2011). Effect of discrete heating on natural convection in a rectangular porous enclosure. *Transport in Porous Media*, 86, 261–281.

- Sivasankaran, S. & Bhuvaneshwari, M. (2013). Natural convection in a porous cavity with sinusoidal heating on both sidewalls. *Numerical Heat Transfer, Part A*, 63(1), 14–30.
- Sojoudi, A., Saha, S. C., Khezerloo, M., & Gu, Y. T. (2014). Unsteady natural convection within a porous enclosure of sinusoidal corrugated side walls. *Transport in Porous Media*, 104, 537–552.
- Sultana, Z. & Hyder, M. N. (2007). Non-Darcy free convection inside a wavy enclosure. *International Communications in Heat and Mass Transfer*, 34, 136–146.
- Sun, Q. & Pop, I. (2011). Free convection in a triangle cavity filled with a porous medium saturated with nanofluids with flush mounted heater on the wall. *International Journal of Thermal Sciences*, 50, 2141–2153.
- Sun, Q. & Pop, I. (2014). Free convection in a titled triangle porous cavity filled with Cu-water nanofluid with flush mounted heater on the wall. *International Journal of Numerical Methods for Heat and Fluid Flow*, 24(1), 2–20.
- Tiwari, A. K., Singh, A. K., Chandran, P., & Sacheti, N. C. (2012). Natural convection in a cavity with a sloping upper surface filled with an anisotropic porous material. *Acta Mechanica*, 223, 95–108.
- Vafai, K. (Ed.). (2000). *Handbook of porous media*. USA: Marcel Dekker, Inc.
- Vafai, K. (Ed.). (2005). *Handbook of porous media* (2nd ed.). USA: CRC Press, Taylor and Francis Group.
- Vafai, K. (Ed.). (2010). *Porous media: Applications in biological systems and biotechnology*. USA: CRC Press, Taylor and Francis Group.
- Varol, Y., Oztop, H. F., & Varol, A. (2006). Free convection in porous media filled right-angle triangular enclosures. *International Communications in Heat and Mass Transfer*, 33, 1190–1197.
- Varol, Y. & Oztop, H. F. (2007). Buoyancy induced heat transfer and fluid flow inside a tilted wavy solar collector. *Building and Environment*, 42, 2062–2071.
- Varol, Y., Oztop, H. F., & Varol, A. (2007). Free convection heat transfer and flow field in triangular enclosures filled with porous media. *Journal of Porous Media*, 11(1), 103–115.
- Varol, Y. & Oztop, H. F. (2008). A comparative numerical study on natural convection in inclined wavy and flat-plate solar collectors. *Building and Environment*, 43, 1535–1544.
- Varol, Y., Oztop, H. F., & Avcı, E. (2008a). Estimation of thermal and flow fields due to natural convection using support vector machines (SVM) in a porous cavity with discrete heat sources. *International Communications in Heat and Mass Transfer*, 35, 928–936.

- Varol, Y., Oztop, H. F., Mobedi, M., & Pop, I. (2008b). Visualization of natural convection heat transport using heatline method in porous non-isothermally heated triangular cavity. *International Journal of Heat and Mass Transfer*, *51*, 5040–5051.
- Varol, Y., Oztop, H. F., & Pop, I. (2008c). Numerical analysis of natural convection for a porous rectangular enclosure with sinusoidally varying temperature profile on the bottom wall. *International Communications in Heat and Mass Transfer*, *35*, 56–64.
- Varol, Y., Oztop, H. F., & Pop, I. (2008d). Influence of inclination angle on buoyancy-driven convection in triangular enclosure filled with a fluid-saturated porous medium. *Heat and Mass Transfer*, *44*, 617–624.
- Varol, Y., Oztop, H. F., & Pop, I. (2008e). Numerical analysis of natural convection in an inclined trapezoidal enclosure filled with a porous medium. *International Journal of Thermal Sciences*, *47*, 1316–1331.
- Varol, Y., Oztop, H. F., & Pop, I. (2009a). Natural convection in right-angle porous trapezoidal enclosure partially cooled from inclined wall. *International Communications in Heat and Mass Transfer*, *36*, 6–15.
- Varol, Y., Oztop, H. F., & Pop, I. (2009b). Entropy analysis due to conjugate-buoyant flow in a right-angle trapezoidal enclosure filled with a porous medium bounded by a solid vertical wall. *International Journal of Thermal Sciences*, *48*, 1161–1175.
- Varol, Y., Oztop, H. F., & Pop, I. (2009c). Entropy generation due to natural convection in non-uniformly heated porous isosceles triangular enclosures at different positions. *International Journal of Heat and Mass Transfer*, *52*, 1193–1205.
- Varol, Y., Oztop, H. F., & Pop, I. (2010). Maximum density effects on buoyancy-driven convection in a porous trapezoidal cavity. *International Communications in Heat and Mass Transfer*, *37*, 401–409.
- Varol, Y. (2012). Natural convection for hot materials confined within two entrapped porous trapezoidal cavities. *International Communications in Heat and Mass Transfer*, *39*, 282–290.
- Wendt, J. F. (Ed.). (2009). *Computational fluid dynamics: An introduction* (3rd ed.). Berlin: Springer-Verlag Berlin Heidelberg.
- Whitaker, S. (1986). Flow in porous media I: A theoretical derivation of Darcy's law. *Transport in Porous Media*, *1*, 3–25.
- Zahmatkesh, I. (2008). On the importance of thermal boundary conditions in heat transfer and entropy generation for natural convection inside a porous enclosure. *International Journal of Thermal Sciences*, *47*, 339–346.
- Zeng, M., Yu, P., Xu, F., & Wang, Q. W. (2013). Natural convection in triangular attics filled with porous medium heated from below. *Numerical Heat Transfer, Part A*, *63*(10), 735–754.

- Zhao, F.-Y., Liu, D., & Tang, G.-F. (2007). Free convection from one thermal and solute source in a confined porous medium. *Transport in Porous Media*, 70, 407–425.
- Zhao, F.-Y., Liu, D., & Tang, G.-F. (2008). Natural convection in a porous enclosure with partial heating and salting element. *International Journal of Thermal Sciences*, 47, 569–583.
- Zheng, W., Robillard, L., & Vasseur, P. (2001). Convection in a square cavity filled with an anisotropic porous medium saturated with water near 4°C. *International Journal of Heat and Mass Transfer*, 44, 3463–3470.

University of Malaya

LIST OF PUBLICATIONS AND PAPERS PRESENTED

Publications:

1. Cheong, H. T., Sivasankaran, S., & Bhuvanewari, M. (2017). Natural convection in a wavy porous cavity with sinusoidal heating and internal heat generation. *International Journal of Numerical Methods for Heat and Fluid Flow*, 27(2), 287–309. (ISI)
2. Cheong, H. T., Siri, Z., & Sivasankaran, S. Natural convection in an inclined porous triangular enclosure with various thermal boundary conditions. *Thermal Science*. (Accepted, ISI)
3. Cheong, H. T., Sivasankaran, S., & Siri, Z. (2016) Natural convection in an oblique porous cavity with non-uniform heating. *AIP Conference Proceedings 1750*, 030010-1–030010-7. (ISI)
4. Cheong, H. T., Sivasankaran, S., Bhuvanewari, M., & Siri, Z. (2015). Effects of various thermal boundary conditions on natural convection in porous cavities. *AIP Conference Proceedings 1682*, 020007-1–020007-7. (ISI)

Papers Presented:

1. Cheong, H. T., Sivasankaran, S., & Siri, Z. (2015, November). Natural convection in an oblique porous cavity with non-uniform heating. Paper presented at the 23rd National Symposium on Mathematical Sciences, Johor Bahru, Malaysia.
2. Cheong, H. T., Sivasankaran, S., Bhuvanewari, M., & Siri, Z. (2014, November). Effects of various thermal boundary conditions on natural convection in porous cavities. Paper presented at the 22nd National Symposium on Mathematical Sciences, Shah Alam, Malaysia.